Diese Dissertation haben begutachtet:

....

TECHNISCHE
UNIVERSITÄT
WIEN

VIENNA
UNIVERSITY OF
TECHNOLOGY

Dissertation

Studies for the Silicon Tracking System of the International Large Detector at the International Linear Collider

ausgeführt zum Zwecke der Erlangung des akademischen Grades eines Doktors der technischen Wissenschaften unter der Leitung von

Univ.Doz. Dipl.-Ing. Dr.techn. Manfred Krammer

Institut für Hochenergiephysik
der Österreichischen Akademie der Wissenschaften
und
Atominstitut der Österreichischen Universitäten

eingereicht an der Technischen Universität Wien
Fakultät für Physik

von

Dipl.-Ing. Stephan Hänsel

Matrikelnummer: 9726687
Lilienberggasse 12/5
1130 Wien

Wien am 14.02.2011

Abstract

The International Large Detector (ILD) is one of the proposed detector concepts for the future International Linear Collider (ILC), which will extend and complement the physics program of the Large Hadron Collider (LHC). One of the perceived priorities of an ILC detector is the reconstruction of charged particle momenta with a precision of $\sigma(\Delta p_t/p_t^2) \leq 2 \cdot 10^{-5}(\mathrm{GeV/c})^{-1}$, required for the use of the particle flow concept. Only with the particle flow approach the needs on jet-energy resolution can be satisfied. The ILD meets this requirement with a central tracking system consisting of a TPC combined with silicon strip detectors. In the barrel region, the silicon tracking system is composed of three double layers of silicon strip detectors. Two of these layers, located between vertex detector and TPC, form the Silicon Internal Tracker (SIT) and the third layer surrounds the TPC, the Silicon External Tracker (SET). In the forward region the silicon tracking system is completed with the End-cap Tracking Detector (ETD), two times three layers of silicon strip detectors just outside the TPC End Plates, and the Forward Tracking Detector (FTD), two times seven discs of silicon detectors, covering the very forward region.

After a short description of the International Linear Collider and its possible physics program, the International Large Detector, its tracking system and especially silicon strip sensors are examined in more detail. Based on simulations, presented in this thesis, it could be verified that the high demands on the resolution of charged particle momenta can only be satisfied with the inclusion of precise measured space points just outside the TPC volume. These simulations led to the inclusion of the Silicon External Tracker into the ILD baseline design. It was understood, that the resolution of the SET along the TPC must be in the order of $50\,\mu$m and that its resolution in $r\varphi$ must be below $10\,\mu$m.

At the HEPHY two different silicon strip sensors, a multi-geometry and a big area sensor, were designed with the purpose to provide a deeper insight into the definition of the ILD tracking system. These two sensors could be implemented on one silicon wafer which was produced by Hamamatsu Photonics, Japan.

Each of the multi-geometry sensors contains 256 readout strips arranged in 16 zones with different strip geometries and a readout pitch of $50\,\mu$m, which is the lower limit for reliable mass production of silicon strip detectors, as needed for large scale detector systems. These sensors were designed to determine the optimal geometry in terms of spatial resolution, taking the different charge collection efficiencies and signal to noise ratios into account. After the quality of these

sensors was verified at the institute, they were connected to front end electronics, designed by the electronic group of the HEPHY Vienna, and integrated into detector modules. After the functionality of the modules was tested in Vienna, they were used in a test beam at the Super Proton Synchrotron (SPS) at CERN. About 500k events were recorded with a $120\,\mathrm{GeV/c}$ pion beam providing enough statistics to reliably determine the spatial resolution of all different geometries. The achieved results are presented and were included into the simulations of the ILD tracking system.

The big area micro-strip sensors have a size of $91.5\,\mathrm{mm}^2$ and a readout pitch of $50\,\mu\mathrm{m}$. After their quality was verified at the HEPHY, those sensors were used to build detector modules which could be integrated into a test beam experiment at DESY, Hamburg, where the Large TPC Prototype (LP), a first large scale prototype for the ILD TPC, is installed in a superconducting magnet. This test beam campaign, dedicated to deliver data with different TPC readout systems in a time period of four years, is an important step towards the optimization of the ILD tracking system. At first, the complete silicon system, including the data acquisition system used for the test beam, was verified during a stand-alone test with cosmic muons in IEKP, Karlsruhe. Afterwards, in November 2009, the system was installed into the setup at DESY. In a first combined test beam of the LP and the silicon detectors without magnetic field more than 80k events were recorded with a $5.6\,\mathrm{GeV/c}$ electron beam. The results of this first experiment and a simulation study for the operation with magnetic field show, that all systems work as expected and that useful insights can be gained with the LP setup.

Based on the knowledge gained in the test beams and the simulations an optimal design for the Silicon External Tracker is developed. For cost reasons single sided silicon strip sensors, optimized for the needed resolutions, will be arranged in a double layer with orthogonal readout strips to provide the optimal spatial resolution for both measured coordinates. Next to the spatial resolution the minimization of the material budget of the silicon tracker is most important, because of multiple scattering and the production of unwanted secondary particles. Different possibilities to achieve this goal are discussed, like the thinning of the sensors and the readout chips and the inclusion of on-sensor pitch adapters. It should also be possible to redundantise the need for cooling pipes, a major contributor to the material budget in former silicon tracking systems, with the development of low power front end electronics making forced air-cooling sufficient.

Kurzfassung

Der International Large Detector (ILD) ist eines der vorgeschlagenen Vielzweck-Experimente am geplanten International Linear Collider (ILC), der es ermöglichen wird unser physikalisches Wissen über die Grenzen des Large Hadron Collider (LHC) zu erweitern. Eine der wichtigsten Anforderungen an die Detektorsysteme am ILC ist die sehr präzise Vermessung der Flugbahn geladener Teilchen, wobei der sogenannte Tracker (von engl. Track, Spur) eine Genauigkeit von $\sigma(\Delta p_t / p_t^2) \leq 2 \cdot 10^{-5} (\text{GeV/c})^{-1}$ für die Messung des transversalen Impulses dieser Teilchen erreichen muss. Der ILD Tracker, bestehend aus einer großen Zeitprojektionskammer (Time Projection Chamber, TPC) die von Silizium Detektoren umgeben ist, kann diese Anforderung erfüllen. Im zentralen, zylinderförmigen Bereich ist das Silizium Tracking System aus drei Doppellagen mit Silizium Streifensensoren aufgebaut. Zwei davon befinden sich zwischen Vertex Detektor und TPC, der Silicon Internal Tracker (SIT), und die dritte Doppellage ummantelt die TPC, der Silicon External Tracker (SET). An den Stirnseiten wird der zylinderförmige Bereich des Trackers mit dem End-cap Tracking Detector (ETD), jeweils drei Lagen Silizium Streifensensoren gleich außerhalb der TPC Endplatten, und dem Forward Tracking Detector (FTD), jeweils sieben scheibenförmige Detektorlagen im Vorwärtsbereich, abgeschlossen.

Einleitend werden die wichtigsten Merkmale des ILC und dessen physikalisches Programm, der Aufbau des ILD und die Grundlagen der Halbleitertechnologie vorgestellt, notwendig um die Anforderungen an den Detektor und die Funktionsweise des ILD und von Silizium Streifensensoren verstehen zu können. Anschließend wird anhand von Simulationen gezeigt, dass die hohen Ansprüche an die Messung des transversalen Impulses geladener Teilchen nur mit der Aufnahme des Silicon External Trackers in das ILD Tracking System erfüllbar sind. Diese Simulationen haben dazu geführt, dass der SET zu einem fixen Bestandteil des ILD wurde. Weiterführende Simulationen zeigen, dass die Sensoren des Silizium Trackers eine Auflösung von zirka $50 \, \mu$m in Richtung der TPC Achse und von unter $10 \, \mu$m in $r\varphi$ benötigen.

Um ein tieferes Verständnis für die Definition des ILD Tracking Systems zu erlangen wurden am HEPHY zwei unterschiedliche Silizium Streifensensoren entwickelt. Diese Sensoren, ein kleiner Multigeometriesensor und ein großflächiger Streifensensor, konnten auf einem Silizium Wafer untergebracht werden, der von Hamamatsu Photonics, Japan produziert wurde.

Die 256 Auslesestreifen der Multigeometriesensoren haben einen Abstand von

$50\,\mu$m und sind in 16 Zonen mit unterschiedlicher Streifengeometrie unterteilt. Das spezielle Design der Sensoren ermöglicht es die optimale Streifengeometrie hinsichtlich örtlicher Auflösung zu ermitteln. Nach der Qualitätskontrolle im Reinraum des Instituts wurden acht der Sensoren zu Detektormodulen verbaut um sie mit einem am HEPHY entwickelten Datenerfassungssystems auslesen zu können. Mit Hilfe eines speziellen Testaufbaus konnte die Funktionsweise dieser Detektoren noch am HEPHY verifiziert werden. Danach wurden sie in einem Teststrahl Experiment am Super Proton Synchrotron (SPS) am CERN verwendet. Mit dem Teststrahl, bestehend aus Pionen mit einem Impuls von $120\,$GeV/c, wurden etwa eine halbe Million Events aufgenommen und das örtliche Auflösungsvermögen der 16 Zonen ermittelt. Diese Studie zeigt, dass es möglich ist im ILD Tracker Silizium Streifensensoren mit einer Auflösung von unter $6\,\mu$m zu verwenden. Dieses Ergebnis wurde in den Simulationen dieser Arbeit berücksichtigt.

Die großflächigen Silizium Streifensensoren besitzen eine Fläche von $91{,}5\,$mm^2 und einen Ausleseabstand von $50\,\mu$m. Nach intensiven elektrischen Tests wurden jeweils drei Sensoren in zwei Detektormodule verbaut. Diese Module wurden speziell für die Integration in das Large TPC Prototype (LP) Teststrahl Experiment entwickelt. Dieses Experiment befindet sich am DESY in Hamburg wo der LP, der erste große TPC Prototyp für die ILD TPC, in einem supraleitenden Magneten eingebaut ist. In einem Zeitraum von 4 Jahren können mithilfe dieses Aufbaus unterschiedliche TPC Auslesetechnologien getestet und so die ideale Technologie ermittelt werden. Dabei spielen die Silizium Streifendetektoren eine wichtige Rolle, die den genauen Vergleich erst ermöglichen und außerdem die Entwicklung einer gemeinsamen Datenanalyse forcieren. Nach einem abschließenden Test mit kosmischen Muonen am IEKP in Karlsruhe wurde das Silizium System, bestehend aus den Silizium Sensor Modulen, dem Datenerfassungssystem und der notwendigen Halterung, in das LP Experiment integriert. In einem ersten gemeinsamen Test ohne Magnetfeld konnten über 80.000 Events mit $5{,}6\,$GeV/c Elektronen aufgezeichnet werden. Die ersten Resultate in Kombination mit einer Simulationsstudie für den Betrieb mit Magnetfeld zeigen, dass alle Systeme einwandfrei funktionieren und wertvolle Erkenntnisse mit dem Testaufbau gewonnen werden können.

Die Ergebnisse der beschriebenen Experimente werden verwendet um, mit Hilfe von Simulationen, das Layout des Silizium Tracking Systems zu optimieren. Aus Kostengründen sollen einseitige Silizium Streifensensoren, die für die notwendige hohe Auflösung optimiert sind, in Doppellagen mit orthogonal angeordneten Auslesestreifen verwendet werden. Abgesehen von der örtlichen Auflösung ist die Minimierung des Materials im Tracker am wichtigsten, um die Mehrfachstreuung und die Produktion von Sekundärteilchen zu reduzieren. Mehrere Lösungsansätze werden diskutiert, wie zum Beispiel die Verwendung dünnerer Silizium Sensoren und Auslesechips und die Verwendung der Chips direkt auf den Sensoren. Eine gewaltige Reduktion des Materials kann durch die Verwendung eines Kühlsystems basierend auf Gas erzielt werden, was durch die zeitliche Struktur der ILC Kollisionen und die Entwicklung spezieller Ausleseelektronik ermöglicht wird.

Contents

Chapter 1

Introduction

The goal of physicists is to understand the world surrounding us. In theory, all things in the universe can be explained by their basic properties, which describe the ways they act and interact with other things. Physics does not only want to describe, but also to predict the outcome of an event with the help of numerical quantities characterising these properties. Two complementing approaches to increase our knowledge exist. The first is to develop theories which describe observations of natural phenomena. The second is to develop theories predicting specific phenomena, which can be proven or negated with the help of experiments. Our knowledge is gathered with a mix of both ways, but always aware that it is approvable to only reject but never possible to absolutely verify a theory.

To understand the microcosm, the smallest parts of our world, ever since physicists looked closer and closer to the matter surrounding us. Some define the beginning of particle physics with the discovery of the electron in 1897. In the following decades one new particle after the other was discovered, mostly with cosmic ray experiments, at that time the only available source of high energetic particles. In the middle of the 20th century the subject really blossomed, following the discovery of new elementary particles in cosmic rays, and pushed the developments of high energy accelerators. With the help of the intense and controlled beams of known energy provided by the accelerators it was possible to reveal the quark substructure of matter and put the subject on a sound basis.

In the beginning, the structure of the atomic nucleus was investigated with, at that time, high energetic particles with an energy of a few MeV. Since then, different generations of particle accelerators have been used, following two different approaches: fixed target experiments and colliders. In the first case a particle beam is directed onto a stationary target and the second technique uses two accelerated beams of particles which are accelerated against each other. In the generated high energetic collisions, it is not only possible to resolve the structure of matter, but with higher and higher energies also massive particles can be created. The properties of these particles can be studied with the help of huge detector systems build around the interaction point.

In all observations, the spatial resolution of the available image forming devices

is the determining criteria for what can be made visible. The resolution is limited by two factors: aberration and diffraction. These two phenomena are unrelated and have different origins. Imprecision due to aberration are in principle only affected by the quality of the system. Diffraction, on the other hand, is dependent on the ratio between the size of the looked at object and the wavelength of the particle used to resolve it. Assuming the probing particles are pointlike, the resolution is limited by the de-Broglie wavelength λ_{dB} of these particles, which is $\lambda_{dB} = h/p$. We see that λ_{dB} is indirectly proportional to the particle momentum p with the Planck's constant h. Therefore the higher the momentum of the particle used as probe, the smaller its wavelength and thus, the higher the achievable spatial resolution. This is the fundamental idea for the development of particle accelerators. Each increase in the momentum of the probing particle opens the possibility to investigate new territories.

1.1   History of Particle Accelerators and Particle Detectors

The duty of particle accelerators is to speed up and increase the energy of charged particles and to provide an intense and controlled beam of known energy. In the last decades accelerators have grown from the 13 cm diameter cyclotron invented by E. Lawrence, figure 1.1, to the Large Hadron Collider (LHC) [1], figure 1.2, with a circumference of 27 km. While the first cyclotron could accelerate protons to an energy of 80 keV, the LHC is able to accelerate two beams of protons to 7 TeV each and will produce collisions at a centre of mass energy of 14 TeV in the near future. Nevertheless, the basic principle has remained the same: the particles are accelerated with electric fields and steered and focused with magnetic fields.
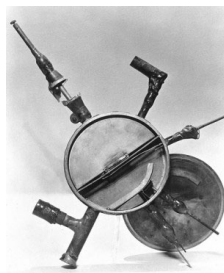
Fig. 1.1: 13 cm diameter cyclotron constructed by E. Lawrence (1931).

Fig. 1.2: LHC at CERN with a circumference of 27 km (2009).

The Livingston chart, figure. 1.3, named after its originator S. Livingston, shows the historical increase of energies reached by particle accelerators. The slope of the asymptotic dashed line indicates a rise in the obtained energies by an order of magnitude roughly every seven years. This development could only be accomplished by the introduction of new accelerator technologies, indicated with green

lines drawn down to the time axis. Since 1960, or 1970 if one counts collider as new technology, there was no new accelerator technology developed, and afterwards the only really new invention was the introduction of superconducting magnets. The red line shows the centre of mass energies of colliders. To indicate the equivalent energies of hypothetical single beams on stationary targets, for colliders also twice the centre of mass energies are plotted.
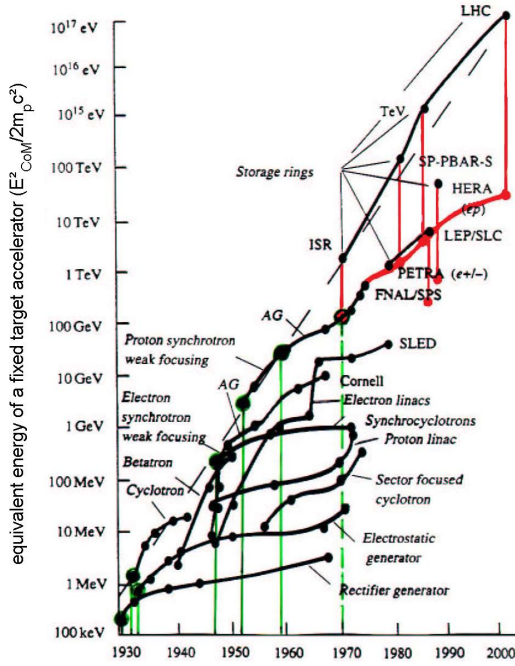
Fig. 1.3: Livingston chart [2].
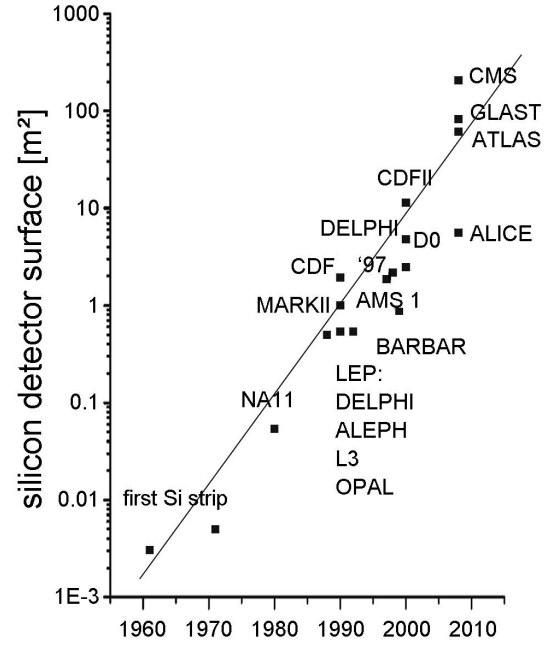
Fig. 1.4: Area covered with silicon [3].

To gain knowledge from the high energetic collisions provided by the accelerators, the generated processes have to be visualised. This is done with the help of particle detectors, which measure the characteristics and identities of the involved particles. Modern detector systems are composed of different sub-detectors as described in chapter 3. With the historical increase of the collision energies, also the size of the particle detectors scaled up. Figure 1.4 illustrates this behaviour for the area covered with silicon sensors for detectors used in the past decades. A similar plot for the number of channels, or the power consumption of the silicon tracking system, would show the same behaviour. From the plot it is clearly visible, that the construction of particle detectors expanded to huge projects which can only be accomplished within worldwide collaborations.

1.2   The Standard Model

The Standard Model (SM) of particle physics [4] was built up through decades of intensive dialogue between theory and experiments at both hadron and electron

	1st	2nd	3rd	em. charge	spin
lepton (mass)	e neutrino ν_e (< 3 eV)	μ neutrino ν_μ (< 0.19 MeV)	τ neutrino ν_τ (< 18.2 MeV)	0	1/2
	electron e (511 keV)	muon μ (105.7 MeV)	tau τ (1.777 GeV)	-1	1/2
quark (mass)	up ($1.5 - 3.3$ MeV)	charm (1.27 GeV)	top (171.2 GeV)	+2/3	1/2
	down ($3.5 - 6$ MeV)	strange (104 MeV)	bottom (4.2 GeV)	-1/3	1/2

Tab. 1.1: Fermions described in the Standard Model [4].

colliders and has proven to be a successful theory to describe nature. The Standard Model perfectly accounts for practically all of the very precise experimental observations done so far. The three generations of quarks and leptons, postulated by the SM, have been detected and their properties were measured with great accuracy. Table 1.1 shows the three generations of fermions, six leptons and six quarks, the elementary particles of matter. Each fermion has an antimatter counterpart of equal mass but opposite charge. Only the matter particles of the first generation and the three neutrinos are stable in time. All higher generation particles decay into first generation particles, namely the electron, the up and the down quark. Unlike leptons, quarks do not exist as free particles and can only be observed in groups of three quarks, so-called baryons, or in bound states of quark-antiquark pairs, so-called mesons.

In the last century, it was also proven that the three fundamental forces described in the Standard Model are mediated by the gauge bosons, namely photons, W- and Z-bosons, and eight gluons. It has been verified that the apparently very different electromagnetic and weak forces are just different manifestations of one, the electroweak, force. Table 1.2 summarizes the bosons described in the SM with their associated fundamental forces. While fermions have half integer spins bosons have integer spin. The table also lists the higgs boson which does not mediate a force but is introduced into the SM to explain the appearance of mass as explained in section 1.2.2.

The dynamics of the SM particles is described in terms of quantised fields while the forces are derived from the gauge invariance principle. With the help of the mathematical framework of the SM it is possible to calculate the cross section of particle interactions, which is the most important observable in high-energy physic experiments.

force	boson	mass [GeV/c^2]	em. charge	spin
strong	gluon g	0	0	1
electromagnetic	photon γ	0	0	1
weak	$W^{\pm}$	80	± 1	1
	Z^0	91	0	1
(mass)	higgs	> 114.4	0	0

Tab. 1.2: Bosons described in the Standard Model [4].

1.2.1 Problems of the SM

Even though the Standard Model perfectly accounts for practically all of the very precise experimental observations done so far, there are still some open gaps in our understanding. One central part of the Standard Model, the higgs mechanism [4], has not been confirmed experimentally. The corresponding higgs boson is already an inherent part of the SM, meaning, that if it is not found in the expected mass window, the probability interpretation of the SM calculations would break down at energies above 1 TeV. Furthermore, the SM contains too many free parameters to make it a candidate for a 'theory of everything' and does not include the neutrino masses nor the fourth fundamental force of nature, the gravitational force. Another open issue is that dark matter and dark energy comprise about 20 % and 75 % of our universe, which leave only approximately 5 % to matter describable with the Standard Model. Also the question about the large excess of matter over antimatter is unanswered.

Many theoretical ideas have been developed which extend the standard model to answer some of these open problems. Most of these attempts have in common that they predict some new phenomena at energies of a few hundred GeV, which is based on the mechanism of the electroweak symmetry breaking. For example, if a light higgs boson exists, the large gap between the low electroweak scale and the high grand unification scale can be stabilized by extending the SM with supersymmetry. Then the Standard Model could naturally be embedded in a grand unified theory. If no fundamental higgs boson exists, or if the higgs boson is very heavy, unification predicts new strong interactions between the electroweak gauge bosons at the TeV scale. When looking at this and other theories it gets obvious, that accelerators producing collisions in the TeV energy range will uncover the structure of physics beyond the Standard Model known today.

1.2.2 Higgs Mechanism

Until now, we have no direct evidence for the generation of the masses of gauge bosons and fermions. The standard model predicts that these masses are generated by the higgs mechanism [4]. If this mechanism is realised in nature, it would manifest itself in the existence of the yet undiscovered higgs boson and a new
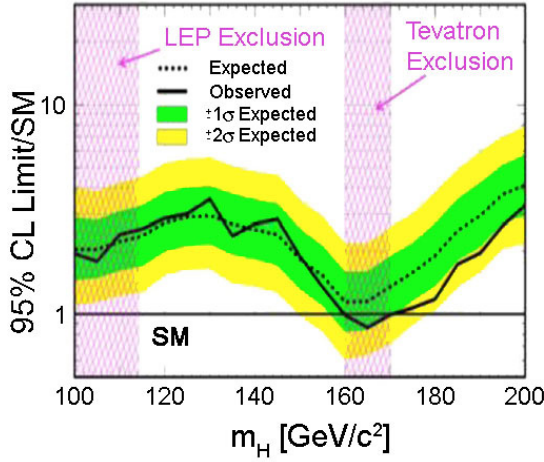
Fig. 1.5: Current situation of the SM higgs search, including preliminary results from the Tevatron Run II with $\mathcal{L} = 0.9\text{-}4.2\,\text{fb}^{-1}$ [5].
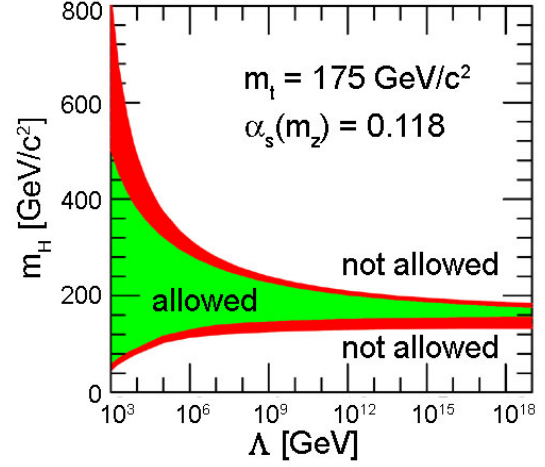
Fig. 1.6: Theoretical upper and lower bounds on the higgs mass from the assumption that the SM is valid up to the cut-off scale Λ_{GUT} [6].

fundamental field, the higgs boson field. This postulated field does not, like all other fields, vanish in the lowest energy state and is omnipresent, meaning that it spontaneously breaks the electroweak symmetry. By the interaction with this field the masses of the quarks, $W^{\pm}$- and Z-bosons and leptons are generated, while the photon stays massless. Within the standard model the properties of the higgs particle and all couplings are theoretically well defined. The only free parameter is the mass of the higgs boson itself. Since the higgs boson was not discovered yet, only limitations on its mass, determined with former experiments, exist. Figure 1.5 summarises the current knowledge of the SM higgs boson search. The lower limit for the higgs mass of $114{,}4\,\text{GeV/c}^2 \lesssim m_H$ was established at the Large Electron Positron (LEP) collider with a 95 % confidence level [7]. With the data recorded at the Tevatron it is possible to exclude the area between $162\,\text{GeV/c}^2 \lesssim m_H \lesssim 166\,\text{GeV/c}^2$ with a 95 % confidence level [8]. Figure 1.6 shows the range of the higgs mass when the SM is extended to the scale of the Grand Unified Theory with $\Lambda_{GUT} \sim 10^{16}\,\text{GeV}$, including the effect of top quark loops on the running coupling [5]. When following this approach the higgs mass should be smaller than $180\,\text{GeV/c}^2$. In every theory beyond the SM, that is required to be weakly interacting up to the GUT scale, the higgs boson should be lighter than $m_H \lesssim 200\,\text{GeV/c}^2$. At the ILC such a higgs boson could be produced already at a centre of mass energy of $E_{CoM} \sim 300\,\text{GeV}$, but to cover the entire higgs mass range possible in the SM, centre of mass energies close to $1\,\text{TeV}$ are required.

1.3 Physics at the ILC

The basic e^+e^--processes of the SM are e^+e^--annihilation to pairs of fermions and gauge bosons. Their cross sections for polar angles between $10° < \Theta < 170°$ in the final state are displayed in figure 1.7. It will be very important to study these processes to be able to suppress them in novel reactions where they are unwanted background. In addition precision measurements of these processes at high energies can be used to accurately determine the properties of the particles of the Standard Model and to detect, or set limits to, irregularities.
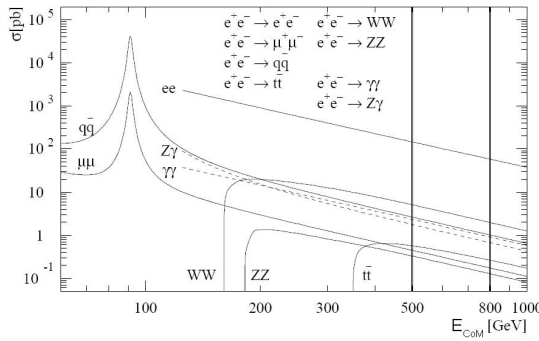

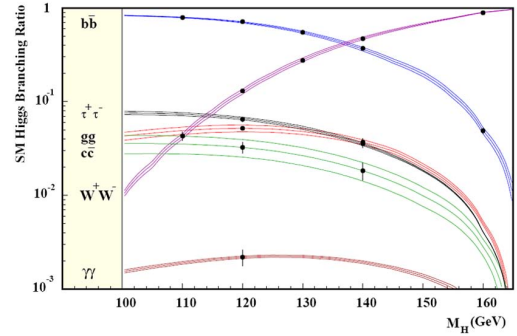Fig. 1.7: Basic e^+e^--processes of the Standard Model [9].

Fig. 1.8: Predicted branching ratios for a light SM higgs boson [6].

1.3.1 Higgs Measurements

If the higgs boson exists, it is almost certain that it will be detected at the LHC. The higgs mass will be measured but it will be difficult for the LHC experiments to measure also its spin and parity and thus to establish its essential nature. This will be possible with high precision measurements at the ILC. If there is more than one decay channel the ratio of branching fractions and the couplings to quarks and vector bosons can be measured accurately at the few percent level. Thus the ILC will be able to reveal whether the higgs is a simple Standard Model object, or something more complex.

Several studies investigating the branching ratios for a light Standard Model higgs boson were done, and, although based on slightly different assumptions on detector performance and centre of mass energy, show consistent results. The predicted probabilities of the different decay channels for the Standard Model higgs particle as a function of the higgs mass are shown in figure 1.8. The points with error bars indicate the expected experimental accuracy obtainable with the anticipated sensitivity of the ILC experiments at a centre of mass energy of 350 GeV and a luminosity of $500\,\text{fb}^{-1}$ [6].

The predicted main mechanism for the production of higgs bosons at the ILC is $e^+e^- \rightarrow ZH \rightarrow \ell^+\ell^- X$. In this process it is possible to measure the higgs mass by its recoil from the Z-boson. To clearly separate this resonance from
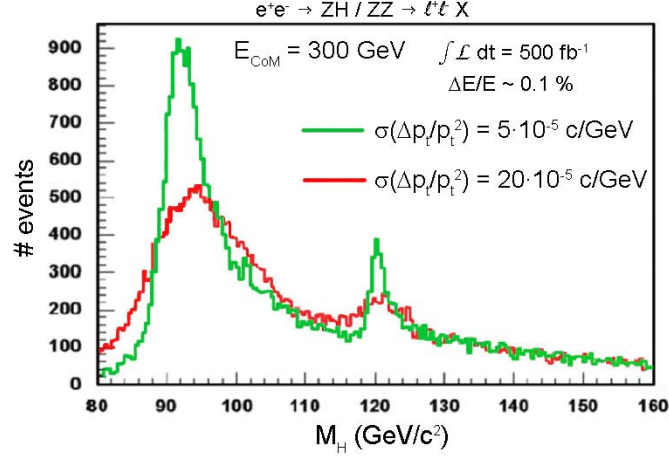
Fig. 1.9: Higgs recoil mass spectra for $500\,\mathrm{fb}^{-1}$ at $\mathrm{E}_{CoM} = 300\,\mathrm{GeV}$ for a higgs mass of $120\,\mathrm{GeV/c^2}$ and two different momentum resolutions [10].

backgrounds, the ILC detectors must be able to measure the mass of the Z-boson $\mathrm{m}_Z \approx 91\,\mathrm{GeV/c^2}$ with a precision of about $50\,\mathrm{MeV/c^2}$. This requires a measured resolution of charged particle momenta of $\sigma(1/p_t) = 5 \cdot 10^{-5}\,(\mathrm{GeV/c})^{-1}$, as indicated in figure 1.9.

1.3.2   Couplings of Gauge Bosons

The Standard Model prescribes, within the non-abelian gauge symmetry, the form and the strength of the triple couplings $WW\gamma$, WWZ and quartic couplings of the electroweak gauge bosons. The triple gauge boson couplings define the electroweak charges, the magnetic dipole moments and the electric quadrupole moments of the $W^{\pm}$-bosons. These interactions have been measured before, but not down to the precision of a few per mill as possible with the ILC. Even a small deviation from the predicted values of these parameters will destroy the unification cancellations of the gauge theories in the SM. These possible deviations will be magnified with increasing energy and the bounds will tighten considerably, enabling their experimental study. From the measurement of the angular distribution of the W-decay the most stringent bounds on anomalous couplings can be derived. Because of the energetic neutrino in the final state a precise measurement of the missing energy and thus sufficient detector hermeticity is utterly important for such measurements.

1.3.3   Top Quark Physics

The mass of the top quark is much larger than the masses of all the other quarks and leptons, and even of the electroweak gauge bosons, making it the heaviest elementary particle of the Standard Model. Therefore it is the particle most strongly

coupled to the electroweak symmetry breaking sector and expected to play a fundamental role in the dynamics behind the symmetry breaking mechanism. With the analysis of the $t\bar{t}$ threshold region at the ILC it is expected that the top mass can be measured with a statistical uncertainty of about $40\,\text{MeV}$. This should be possible even with a 'quick' scan of $10\,\text{fb}^{-1}$, which would take a small fraction of a year at typical design luminosities [6]. This accuracy will be a significant improvement compared to former measurements, for example at the Tevatron the top quark mass was measured to $m_t = 172.6 \pm 1.4\,\text{GeV/c}^2$ [11].

The top quark is also special because it is so short-lived that it decays before hadronisation takes place, and long before its spin can flip. For the other heavy quarks depolarisation effects during fragmentation wash out the quark helicity, whereas the polarisation of the top quark at production is reflected in its decay products. In the decay $t \rightarrow bW$ followed by $W \rightarrow c\bar{s}$, the polarisation of the top quark can be measured from the angular distribution of the $\bar{s}$ jet with respect to the top flight direction. Furthermore the study of open top production $e^+e^- \rightarrow t\bar{t}$ at high energies will be another powerful pointer to new physics.

1.3.4   Supersymmetry

SM bosons	spin	SUSY partner	spin
W$^\pm$ H$^\pm$	1	charginos: $\widetilde{\chi}_1^\pm$, $\widetilde{\chi}_2^\pm$	1/2
g, Z, h^0, H^0, A^0	1	neutralinos: $\widetilde{\chi}_1^0$, $\widetilde{\chi}_2^0$, $\widetilde{\chi}_3^0$, $\widetilde{\chi}_4^0$	1/2
g$_i$	1	gluinos: $\widetilde{g}_i$	1/2
graviton: G	2	gravitino: $\widetilde{G}$	3/2
SM fermions	**spin**	**SUSY partner**	**spin**
leptons: ℓ	1/2	sleptons: $\widetilde{\ell}_L$, $\widetilde{\ell}_R$	0
neutrinos: ν_ℓ	1/2	sneutrinos: $\widetilde{\nu}_\ell$	0
quarks: u, d, s, c, b, t	1/2	squarks: $\widetilde{q}_L$, $\widetilde{q}_R$	0

Tab. 1.3: SUSY particles in the MSSM.

Supersymmetry (SUSY) is the most popular extension of the Standard Model today. It offers solutions to many theoretical and experimental problems of the SM and can be introduced with total agreement to all performed precision measurements. This theory postulates symmetry between bosons and fermions: for each known particle with spin j of the SM a supersymmetric partner with spin j-1/2 is predicted, as shown in table 1.3. The gauginos are the supersymmetric spin-1/2 partners of the gauge bosons, while quarks and leptons are associated with scalar supersymmetric particles, the squarks and sleptons. The minimal supersymmetric standard model (MSSM), the minimal extension to the SM that realizes SUSY, is based on the symmetry group $SU(3) \times SU(2) \times U(1)$ of the SM. To preserve
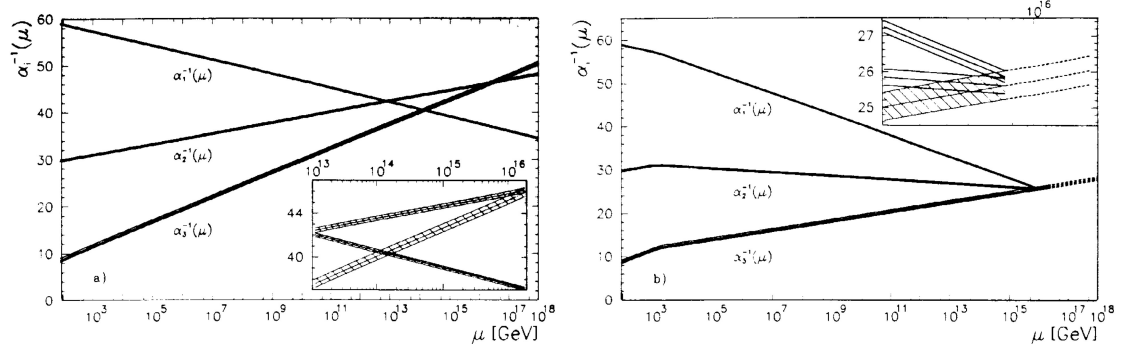
Fig. 1.10: Extrapolation of the inverse of the three coupling constants in the Standard Model (left) and in the Minimal Supersymmetric Standard Model (right) - the small figures show enlargements of the area of intersection [12].

supersymmetry and to keep the theory free of inconsistencies the higgs spectrum of the MSSM consists of five particles: $H^{\pm}$, h^0, H^0 and A^0. In general charged and neutral higgsinos mix with the non-colored gauginos and form charginos and neutralinos. Since R-parity conservation is postulated, supersymmetric particles are generated in pairs and the lightest supersymmetric particle (LSP) has to be absolutely stable. The LSP is often assumed to be the lightest neutralino $\widetilde{\chi}_1^0$ which is an end-product in a lot of predicted reactions where supersymmetric particles are involved. The LSP can only be detected indirectly via the missing energy of a collision, thus hermeticity of the detector system is essential for SUSY discoveries.

As example, the introduction of supersymmetry provides a bridge from the presently explored energy scale to the scale of Grand Unified Theories close to the Planck scale, where gravity becomes important. This can be achieved without conflict to existing data. In the Standard Model, with the present errors, the extrapolations of the inverse of the coupling constants of the weak (α_2), the electromagnetic (α_1) and the strong (α_3) force towards high energies reveal, that within the SM no unification of the three forces can be obtained. This is visualised in the left plot of figure 1.10 where the extrapolation of α_3^{-1} misses the crossing point of α_1^{-1} and α_2^{-1} by more than 8 standard deviations. The right plot in figure 1.10 shows, that the MSSM gives unification of the three independent coupling constants close to $\Lambda_{GUT} \sim 10^{16}$ GeV. This occurs due to contributions in loop corrections, introduced by the new particles that modify the energy dependences of the force couplings. This is even valid if the SUSY contribution to the running of the coupling constants becomes only effective for energies above the masses of the SUSY particles.

At the ILC the lightest CP-even higgs particle h^0, if it exists, could be produced in the entire range of the MSSM parameter space, either via the higgs-strahlung process $e^+e^- \rightarrow h^0 Z$, where the higgs boson is radiated from a Z-boson, or via pair production $e^+e^- \rightarrow h^0 A^0$.

Chapter 2

International Linear Collider

2.1 Motivation for a Linear e^+e^--Collider

In the coming years the Large Hadron Collider (LHC) will give access to energy regions never reached before. It started operation in the beginning of 2010 and provided proton-proton collisions with a centre of mass energy of $E_{CoM} = 2 \times 3.5\,\text{TeV}$ for the experiments. The machine works perfectly and already achieved the goal for 2010, an integrated luminosity above $10^{32}\,\text{cm}^{-2}\text{s}^{-1}$. This corresponds to approximately ten trillion proton-proton collisions, of which only a small fraction contains events interesting enough to record for later analysis, and of these, only a tiny fraction yields data relevant for physics. Nevertheless this first phase delivered enough data across all the potential discovery areas to firmly establish the LHC as the world's foremost facility for high-energy particle physics.

The International Linear Collider will extend and complement the physics program of the LHC, as shortly described in section 1.3. The comparable clean environment of a lepton collider is ideally suited for high precision measurements, like the determination of the spin and parity of the higgs boson. The physics program of the LHC reaches from the deeper understanding of the Charge-Parity (CP) violation and the quark-gluon plasma, as described within quantum chromodynamics (QCD), to the search for the higgs boson and supersymmetric (SUSY) particles, always with the openness to experience the complete unexpected. Keeping this in mind it is rather difficult to anticipate the full physics program at a new facility before the physics of the energy regime where it will operate is known.

2.1.1 Why do we need an ILC when we have the LHC?

The answer to this question is quite simple: "the Large Hadron Collider is a circular proton-proton collider while the International Linear Collider is a linear electron-positron collider".

A circular collider provides high energies and luminosities at the expense of precision. It is qualified to find new physical effects and particles as a "discovery machine". On the other hand a linear e^+e^--collider provides high precision and
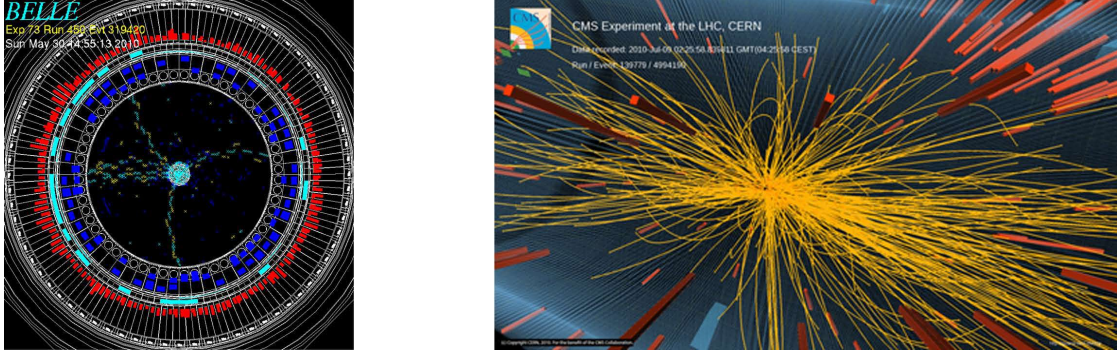
Fig. 2.1: Event displays from the BELLE (left) and the CMS (right) experiment, [13] and [14].

exactly known initial state conditions at the expense of energy and luminosity. With such a "precision machine" it is possible to very accurately measure the properties of particles and effects found at a "discovery machine", and is thus the logical complement to a circular collider.

2.1.1.1   Lepton versus Hadron Collider

Leptons, in comparison to hadrons, are fundamental, pointlike particles, what makes, in terms of precision, lepton-lepton colliders superior to colliders using hadrons. Since leptons are pointlike, the initial state in lepton-lepton collisions is precisely known and the full beam energy is used for particle creation: $E_{CoM} \approx 2 \times E_{beam}$. Because of their inner structure only a fraction of the protons, composed of quarks and gluons, collide and the centre of mass energy of the collisions is much smaller than twice the beam energy: $E_{CoM} << 2 \times E_{beam}$. Since it is not possible to foresee which sub-particles of the protons really hit each other, it is impossible to know the exact initial kinematic configuration of the collisions and thus the total energy of the created particles is unknown.

Second, in hadron-hadron collisions, the processes are defined by the strong interaction, which leads to the production of an immense background. This effect can be seen in figure 2.1, which shows an event display of an e^+e^--collision recorded by the Belle experiment at the national Japanese particle physics centre KEK on the left and a p^+p^+-event recorded with the CMS experiment at the LHC. Because of their very different centre of mass energies these two events are not really comparable but visualise the trend. In lepton-lepton collisions beam bremsstrahlung produces a background of photons, e^+e^--pairs and hadrons mainly in the forward directions, but in terms of complexity it is not comparable to the background at a hadron collider. For this reason particles at lepton-lepton colliders can be observed closer to the collision point allowing high precision measurements of secondary vertices, the decay points of short-lived particles.

2.1.1.2   Circular versus Linear Collider

The crucial difference between the acceleration of charged particles along a straight and a curved line is synchrotron radiation. It is generated during every acceleration of a charged particle and the permanent change of direction in a circular collider leads to an energy loss proportional to γ^4, with $\gamma = E/m$. Thus the energy loss in a circular collider scales with the mass m of the accelerated particle by $1/m^4$. When comparing the invariant mass of electrons $m_e \approx 0.511\,\mathrm{MeV/c^2}$ and protons $m_p \approx 938\,\mathrm{MeV/c^2}$, it is obvious that it is not desirable to use electrons in a circular accelerator. Ideas for muon‑muon colliders are under development [15], which would have the advantage of using pointlike particles with high mass $m_\mu \approx 105\,\mathrm{MeV/c^2}$. One of the unsolved problems of this idea is the short lifetime of the muon $\tau_\mu \approx 2.2\,\mu\mathrm{s}$, which is too short for the use with existing technologies.

The downside of linear accelerators is, that they are so‑called one shot machines, where particles pass every accelerating radio frequency (RF) cavity only once. Therefore, to reach high centre of mass energies, the accelerating distance has to be quite long. Furthermore it is not possible to reuse bunches after the collision, like it can be done in circular colliders. Therefore, to obtain a high luminosity in a linear collider, extreme demands on beam profile and bunch intensity exist.

2.1.1.3   Collision Rate

One big advantage of lepton‑lepton colliders is that the production rates for events containing standard physics and new physics are comparable. For example the higgs production rate is expected to be similar to other processes with the same topology [16].

At hadron‑hadron colliders very high collision rates are needed, because the probability for events containing new physics is quite low. Therefore tremendous amounts of data are produced by the experiments. With existing technologies it is impossible to save the data from each collision and only a small fraction of events can be recorded. The decision, if an event is interesting enough to be recorded, has to be made in a very short time and requires a hard‑coded trigger logic. The discarded data is lost forever, making it very delicate to define the trigger decisions for the search of new particles and unknown processes. As example, for the nominal LHC design luminosity of $10^{34}\,\mathrm{cm^{-2}s^{-1}}$ each LHC experiment will see an event every 25 ns. Each of these events will contain on average 20 collisions, leading to up to 1000 tracks in the detectors. The trigger logic of the CMS experiments has to immediately reduce the average produced data rate of about $10^9\,\mathrm{Hz}$ to $100\,\mathrm{Hz}$, which is the maximum rate that can be handled by the online computer farm of the experiment [17].

In comparison the expected time integrated collision rate at the International Linear Collider is around 15 kHz. Due to the small number of tracks per event, this leaves enough time to use a very open, software based trigger system and to store the data of most events for later analyses.
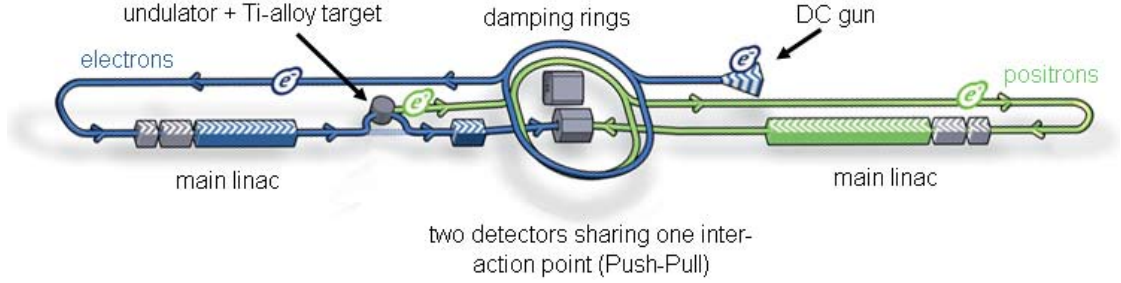
2.2 Baseline Design of the ILC

Fig. 2.2: Basic layout of the International Linear Collider [18].

The International Linear Collider (ILC), sketched in figure 2.2, will have a total length of about 31 km. The parameters of the baseline machine are listed in table 2.1.

centre of mass energy range	$200\,\mathrm{GeV} \leq \mathrm{E}_{CoM} \leq 500\,\mathrm{GeV}$
peak luminosity*	$2 \cdot 10^{34}\,\mathrm{cm}^{-2}\mathrm{s}^{-1}$
average beam current in pulse	$9.0\,\mathrm{mA}$
pulse rate	$5.0\,\mathrm{Hz}$
pulse length (beam)	$\sim 1\,\mathrm{ms}$
number of bunches per pulse	1000 - 5400
charge per bunch	$1.6 - 3.2\,\mathrm{nC}$
accelerating gradient*	$31.5\,\mathrm{MV/m}$
pulse length	$1.6\,\mathrm{ms}$
beam power (per beam)*	$10.8\,\mathrm{MW}$
typical beam size at IP $(h \times v)$*	$640 \times 5.7\,\mathrm{nm}^2$
total AC power consumption*	$230\,\mathrm{MW}$

Tab. 2.1: Design parameters of the ILC baseline machine (values with * are given for a centre of mass energy of $500\,\mathrm{GeV}$ [6].

The collider will be able to produce electron - positron collisions at all centre of mass energies in the range of $200\,\mathrm{GeV} \leq \mathrm{E}_{CoM} \leq 500\,\mathrm{GeV}$. It will also be possible to make energy scans with relative short down times needed for the change of energy. This flexibility is important, since today the energies of interest are not exactly known and will be strongly influenced by the discoveries made at the LHC. At all energies the beam stability and precision are required to be below the tenth of percent level. The same accuracy is needed for the measurement of the beam energy and the differential luminosity spectrum. The possibility for a later

upgrade to a centre of mass energy of $2 \times 500\,\mathrm{GeV}$ is already embedded in the baseline design and can be achieved by extending the length of the accelerators, while it is possible that higher gradient cavities are needed.

For particle accelerators, next to the centre of mass energy, the second most important figure of merit is the luminosity $\mathcal{L}$. It describes the number of particles brought to collision per unit time and area and multiplied with the cross section σ of a given physic process it determines its rate $n = \mathcal{L} \cdot \sigma$. It is possible to calculate the specific cross section of a process from its Feynman diagram. For example, many supersymmetric processes have theoretical cross sections in the order of a few ten femtobarn, with $1\,\mathrm{fb} = 10^{-39}\,\mathrm{cm}^2$. With a centre of mass energy of $\mathrm{E}_{CoM} = 500\,\mathrm{GeV}$ and a peak luminosity of $\mathcal{L} = 2 \cdot 10^{34}\,\mathrm{cm}^{-2}\mathrm{s}^{-1}$ the ILC will be able to produce an integrated luminosity of $\int \mathcal{L}\,dt = 500\,\mathrm{fb}^{-1}$ within the first 4 years of operation, excluding the need of one commissioning year beforehand. This corresponds to roughly 200 petabytes of data which has to be stored and analysed. Within two additional years it should be possible to double the integrated luminosity to a total of 1 inverse attobarn, with $1\,\mathrm{ab} = 10^{-42}\,\mathrm{cm}^2$. For an operation at lower energies it is assumed that the luminosity scales as $\mathcal{L} \sim \mathrm{E}_{CoM}$. As example, the actual integrated luminosity $\int \mathcal{L}\,dt$ produced at a centre of mass energy of $\mathrm{E}_{CoM} = 250\,\mathrm{GeV}$ would be half of that generated at $\mathrm{E}_{CoM} = 500\,\mathrm{GeV}$ [19].
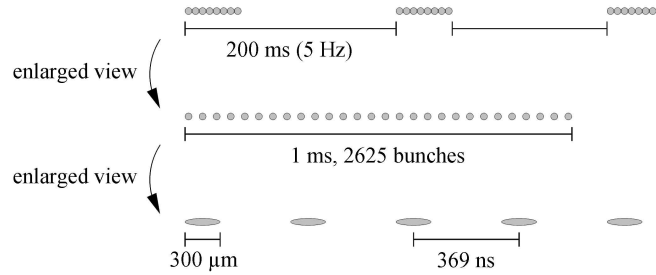

Fig. 2.3: Beam structure of the ILC.

The nominal beam structure of the ILC is displayed in figure 2.3. The electron and positron beams will be pulsed with bunch trains, composed of 2625 bunches over 1 ms, repeated every 200 ms. The interval between the bunches, with a length of approximately $300\,\mu\mathrm{m}$ each, is 369 ns. These parameters result in a burst collision rate of about 3 MHz, and a time-integrated collision rate of 15 kHz. To enhance signals and to suppress backgrounds it will be possible to polarise the electron and positron beams to $80\,\%$ and $60\,\% - 65\,\%$, respectively.

The physics results obtained in the first few years of running, together with the results from LHC, will then define the schedule for possible upgrades of the baseline machine or for the running with other modes of operation, like described in section 2.4.
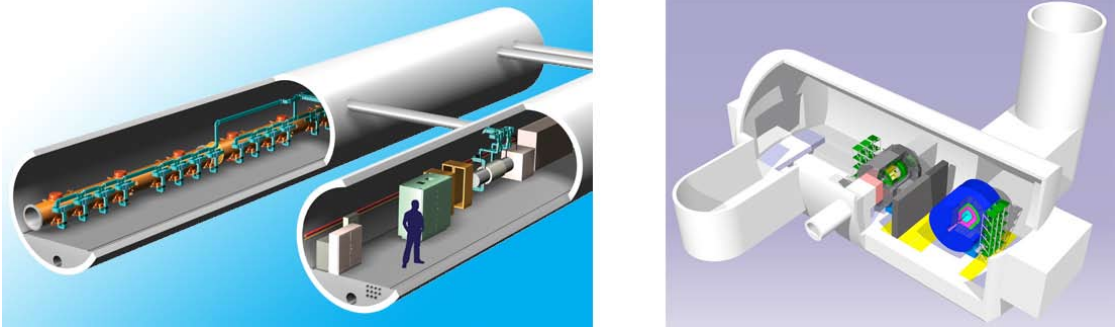
Fig. 2.4: Artist's impressions of the two ILC tunnels and the push‑pull scenario [20].

2.3   Accelerator Chain

The electrons for the e$^-$‑ beam of the ILC are created with a DC gun, with a laser illuminating a photocathode. A fraction of the electrons is extracted from the main linac and pass a 150 m long helical undulator in an offset beam line to create photons with an energy of 10 MeV. These photons are directed onto a rotating titanium alloy target to produce a beam of e$^+$e$^-$‑ pairs, whereof the positrons are extracted.

As first acceleration stage, both beams are accelerated to 5 GeV in supercon‑ ducting linacs. The resulting electron and positron beams have a large transversal and longitudinal emittance, which is reduced in two damping rings (DR), with a circumference of 6.7 km. The DR are located in a common tunnel at the centre of the machine complex, as visible in figure 2.2. The superconducting radio fre‑ quency (RF) system in the damping rings is operated at 650 MHz, and provides 24 MV for each ring. After the bunches in the damping rings are filled, they are extracted and transported via two, about 15 km long lines to the upstream ends of the main linacs. In these lines the polarization of the leptons can be rotated from the vertical to any arbitrary angle desired at the collision point.

In the two 11 km long main linacs the beams are accelerated to their final energies with the help of about 17,000 superconducting radio frequency (SCRF) cavities. These SCRF cavities operate at a frequency of 1.3 GHz and provide an average gradient of 31.5 MV/m, with a pulse length of 1.6 ms. In order to reach superconductivity, these cavities have to be operated at a temperature of 2 K. The components of the main linacs are housed in two tunnels, an accelerator and a service tunnel as sketched in figure 2.4, each with an interior diameter of around 4.5 meters.

A 4.5 km long beam delivery system brings the two beams to the collision point with a crossing angle of 14 mrad. For cost reasons only one interaction region is foreseen, which will be shared by two different detector systems alternately. The use of two detector systems is essential to enable the measurements of critical pa‑ rameters independently and complementary. In this so‑called push‑pull scenario,

as sketched in figure 2.4, the detectors and their supports have to be designed in a way, that the detector changeover can be accomplished in approximately 1 week. This puts extreme demands on the components and alignment strategies of the detector systems.

2.4 Possible Options

After a few years of operation in the baseline configuration, the ILC could be upgraded to higher energies or also be slightly modified to enable one of the options described below. This cannot be decided now, but is dependent on the scientific findings obtained till then.

2.4.1 Energy Upgrade

An energy upgrade to enable centre of mass energies up to $E_{CoM} = 1\,\text{TeV}$ would open the door to even greater discoveries. This upgrade is already considered in the baseline design and demands the extension of both main linacs, and their beam transport lines, by approximately 11 km. In addition some components in the beam delivery system would need to be upgraded or replaced.

2.4.2 Giga - Z

Running at the Z^0-resonance with a luminosity of $\mathcal{L} = 10^{33}\,\text{cm}^{-2}\text{s}^{-1}$ would produce 10^9 hadronic Z-decays within a year of operation and enable studies of the Z-boson with unprecedented precision. For this option positron polarisation and frequent flips of the polarisation states are essential. In addition energy stability and calibration accuracy below the tenth of percent level would be needed. Running at the Z^0-resonance for a short time after a push-pull operation is also one of the most popular scenarios for a quick track based alignment of the detector systems, because $Z^0 \rightarrow \mu^+\mu^-$ provides stiff tracks from a resonance with a well known initial state.

2.4.3 Mega - W

The world's most precise determination of the W-mass with an accuracy in the order of $10\,\text{MeV/c}^2$ would be possible with one year of data taking at the W^+W^--threshold with a luminosity of about $\mathcal{L} = 10^{33}\,\text{cm}^{-2}\text{s}^{-1}$. However, since this measurement would require about one year of operation at a centre of mass energy of 160 GeV, where not many physics issues can be addressed, this option is rather unlikely.

2.4.4   e⁻e⁻- Collider

For some physics measurements, like for example the measurement of the selectron mass, if the supersymmetric partner of the electron exists in the ILC energy range, running as an e⁻e⁻- collider would be interesting. This is in principal possible for all energy values up to the maximum energy of the e⁻e⁺- collisions, although with reduced luminosity.

2.4.5   e⁻γ - and γγ - Collider

Colliding electrons with a very intense laser beam close to the interaction point can produce a high energetic photon beam of high quality. Hence, with two electron beams it is possible to set up an e⁻γ - or γγ- collider which would allow to obtain additional information about the triple gauge couplings. This mode would require a larger crossing angle than the baseline e⁺e⁻- operation and also the installation of a large laser system.

2.5   Requirements for an ILC Detector

In order to achieve the physic goals described in section 1.3, stringent demands on the performance of the ILC detectors are set. In the following the requirements on the different sub - detector systems are described.

2.5.1   Vertex Detector

To enable high precision measurements of low - momentum tracks within dense jets and to achieve excellent flavour identification, the required impact parameter resolution for both coordinates is [21]:

$$\sigma_{r_{ip}} = \sigma_z = 5\,\mu m \oplus \frac{10}{p\,(GeV/c)^{-1} \cdot sin^{3/2}\vartheta}\,\mu m \qquad (2.1)$$

To measure the charge of produced quarks the association of even low momentum tracks to the correct decay vertex is essential. This demands, that the innermost vertex layer should be as close to the interaction point as possible. Studies have shown that the radius of the innermost vertex layer should not be above 15 mm [22]. To minimise multiple scattering in the vertex region, the thickness of the beryllium beam pipe is foreseen to be below 0.4 mm and the radiation length of the individual layers of the vertex detector should not exceed 0.1 % X_0.

  Another critical issue for the vertex detector is its readout speed because of the immense beam radiation background produced by the ee⁺- pairs in the intense electromagnetic fields of the colliding bunches. The required readout rate, if it is necessary to read out once the occupancy of the vertex detector reaches 1 %, would be about 20 kHz per 1 MegaPixel frame, which is orders of magnitude higher than achievable with currently available solutions. Different approaches to reduce

the occupancy to a manageable level are under investigation, as described in [23]: continuous readout, data sparsification with time‑stamping of individual hits, in‑situ storage with delayed readout during the time without collisions and also the use of a super‑fine segmentation.

2.5.2 Tracking System

As already described in section 1.3, one of the perceived priorities of an ILC detector is the reconstruction of the transversal momentum p_t of charged particles with a precision of [10]:

$$\sigma(\Delta p_t / p_t^2) = 5 \cdot 10^{-5} \, (GeV/c)^{-1} \tag{2.2}$$

which by far exceeds the performance of former tracking systems, as for example that of the CMS detector at the LHC described in [24]. This requirement is especially driven by the predicted main mechanism for the higgs production at the ILC: $e^+ e^- \to ZH \to \ell^+ \ell^- X$, and allows the measurement of the higgs mass with a precision of better than $\Delta m_H \sim 100 \, \text{MeV}$ [6]. To preserve lepton identity and high performance calorimetry the material budget inside the tracking volume has to be minimised. Full solid angle coverage for tracks with energies ranging from the beam energy to very low momenta is required for particle flow calorimetry and missing energy measurements. More details about the tracking system are given in section 3.2.2.

2.5.3 Calorimeter System

A lot of the interesting physics processes at the ILC will appear in multi‑jet final states, often accompanied by charged leptons and missing energy. The goal for the jet energy resolution is [25]:

$$\frac{\sigma_{E_{jet}}}{E_{jet}} = \frac{\alpha}{\sqrt{E_{Jet} \, / \, GeV}} \oplus \beta \leq \frac{30 \, \%}{\sqrt{E_{jet} \, / \, GeV}} \tag{2.3}$$

which is defined by the demand to efficiently identify and distinguish between $W \to q\bar{q}$ and $Z \to q\bar{q}$ decays. To ensure an effective $3.6\,\sigma$ separation of the corresponding mass peaks a di‑jet mass resolution $\sigma_m/m \sim \alpha \, / \, \sqrt{E_{jj}}$ comparable to the gauge boson widths $\Gamma_W/m_W \sim \Gamma_Z/m_Z \sim 2.7\,\%$ is needed. For interesting physics processes at the ILC the energy of the di‑jet system E_{jj} is typically in the range of $150 \, \text{GeV}$ to $350 \, \text{GeV}$, defining the stochastic term α. The constant term β encompasses a variety of effects and is typically in the order of a few percent.

With a traditional approach to calorimetry this is unlikely to be achievable, but with the introduction of the particle flow concept, the full reconstruction of the four‑momentum vector of each particle in the detector with the optimal set of sub‑detector measurements, the needed energy resolution gets possible. Simulation studies revealed, that with the introduction of the particle flow concept a jet energy resolution of better than $3.8\,\%$ is reachable for jets with an energy between $40 \, \text{GeV}$ and $400 \, \text{GeV}$ [25].

2.5.4   Very Forward Region

In the very forward region of the detector system, due to beam related backgrounds, radiation hardness is an important issue. In particular e^+e^-- pairs created by beam - beam interactions emerge at relatively shallow angles in beam direction, while spiralling along the magnetic field lines parallel to the beam axis z. These pairs form a dense cone, starting from the collision point at $z = 0$ with a radius roughly proportional to $\sqrt{z/B}$, with an expected flux of electromagnetic radiation even exceeding the estimations for the LHC. At the position of the beam calorimeter the expected total energy deposit in the order of $10\,\mathrm{TeV}$ per bunch crossing leads to a total annual dose of about $10\,\mathrm{MGy}$ [10]. This cone of high background defines the upper limit for the length of the vertex detector [27], which is unable to cope with the flux in this region. With increasing centre of mass energies events get more isotropic and topologies in which an event is contained solemnly in the barrel region get less and less probable. Therefore tracking in the forward region becomes essential for higher energies [28].

2.5.5   Push - Pull

It is foreseen that the interaction point is shared by two detector systems in a so - called push - pull scenario, as sketched in figure 2.4. To share one interaction point both detector systems must be mounted on movable platforms, which can transport the detectors out of the beam line. Since even the smallest vibrations during this operation could cause dislocations at the sub - mm level this idea puts stringent demands on the stability and the alignment strategies for the detector systems. Also the detector services need to be designed for a moving detector, which is a very tricky task, especially for the liquid helium needed to cool the solenoid coils of the experiments.

2.6   Costs, Status and Near Future Steps

Only with fascinating results from the Large Hadron Collider it will be possible to explain the need of an International Linear Collider to participating agencies and governments. A preliminary cost analysis has been performed for the ILC Reference Design Report[6], where the total costs for the ILC was estimated to 4.79 billion 2007-USD[1] with an additional 1.83 billion 2007-USD to provide the infrastructure required to site the machine. Approximately 24 million person - hours will be required to support the construction project, including administration and project management, installation and testing. This is comparable to the largest present day projects, the Large Hadron Collider (LHC) and the International Thermonuclear Experimental Reactor (ITER).

---

[1] 1 2007-USD = 0.83 2007-Euro = 117 2007-Yen

For the moment the strategies and priorities for the work of hundreds of scientists and engineers at universities and laboratories all around the world are defined within a Global Design Effort [29]. For the ILC Reference Design Report [6] three sample sites, one each in America, Asia and Europe, were evaluated, but till now no decisions were made. The near future goal is to produce an ILC Technical Design Report by the end of 2012, which will be used to decide the future of the ILC project.

Chapter 3

International Large Detector

The International Large Detector (ILD) was developed from the merged efforts for the Large Detector Concept (LDC) [30] and the Global Large Detector (GLD) [31]. The tracking systems of both detectors were based on silicon devices combined with a large Time Projection Chamber (TPC) and both concepts anticipated to use a calorimetry system designed for particle flow. Most of the main parameters of the ILD, such as the magnetic field and dimensions of the sub-detectors, are motivated by extensive simulation studies based on variants of both, the GLD and the LDC.

To be able to fully exploit the physics at the ILC the ILD is based on the concept of particle flow, which foresees the reconstruction of the full four-momentum vector of each single particle produced inside the detector. This implies that for the event reconstruction the data of all sub-detectors must be combined. Measurements at LEP revealed, that on average, after the decay of short-lived particles, roughly 62 % of the energy is carried by charged particles, 27 % by photons, 10 % by long-lived neutral hadrons and about 1.5 % by neutrinos [25]. The momenta of charged particles are measured in the tracking system, leaving the energy measurement of photons and neutral hadrons to the calorimeters. The concept of particle flow sets stringent demands on the performance of the detector system:

- the detector must be as hermetic as possible to minimise the number of particles leaving the detector system unidentified

- the tracking system must be highly efficient and enable a precise momentum measurement of all charged particles

- the material budget of the tracking system must be as small as possible to minimise multiple scattering and the conversion of particles before they reach the calorimetry system

- the calorimeter must be very fine grained for both electromagnetic and hadronic showers to allow the correct correlation of calorimeter clusters to particles, which is especially important in jets with high particle densities
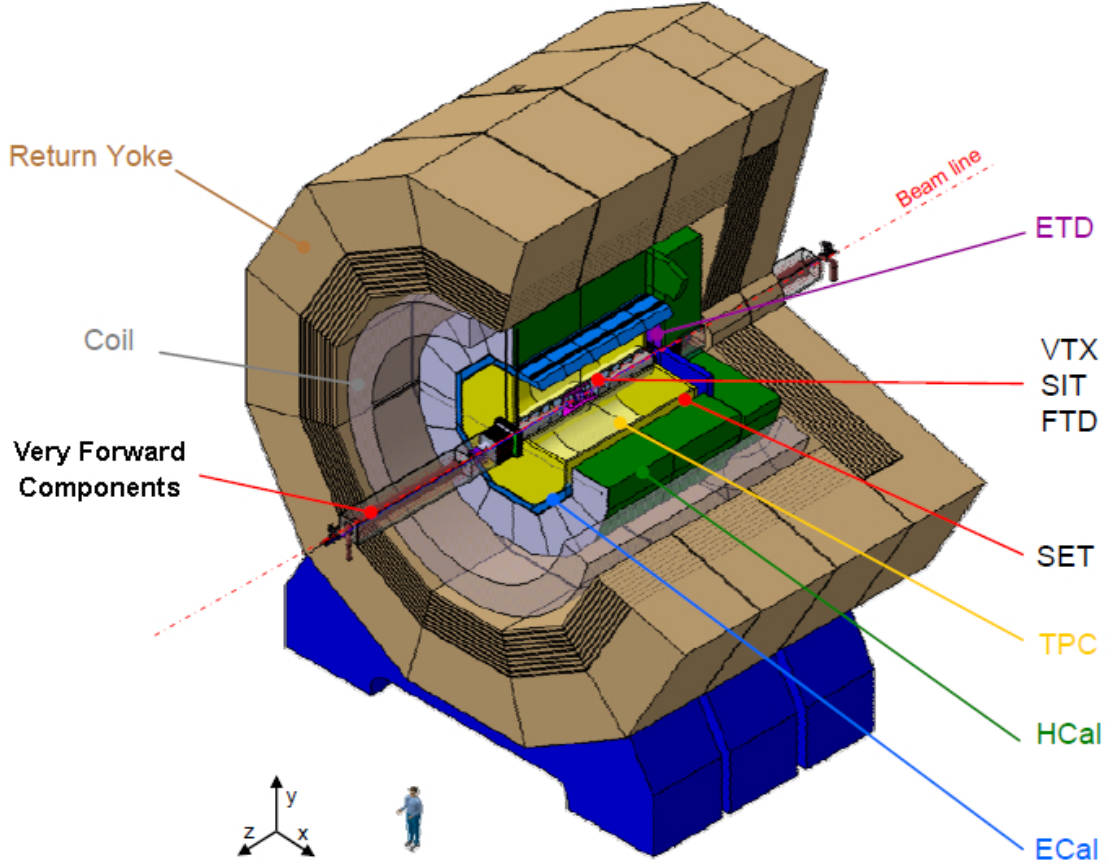
Fig. 3.1: The International Large Detector (ILD) [32].

To fulfil these requirements, the ILD is designed as a multi‑purpose detector composed of different sub‑systems arranged in an onion like structure around the collision point of the ILC, as displayed in figure 3.1. Starting from the centre, the components of the ILD are: Vertex Detector (VTX), Silicon Internal Tracker (SIT), Time Projection Chamber (TPC), Silicon External Tracker (SET), End‑cap Tracking Detector (ETD), Electromagnetic Calorimeter (ECAL), Hadronic Calorimeter (HCAL), Superconducting Solenoid (Coil) and the Return Yoke including the muon detector system. In the very forward region these sub‑detectors are completed with the Forward Tracking Detector (FTD), luminosity detector (LumiCal), Pair Monitor and the beam calorimeter (BCAL).

Altogether, the ILD will have a length and diameter of about 14 m each and a total mass of approximately 14,000 tonnes. The superconducting solenoid surrounding the tracking and calorimeter systems will provide a nominal magnetic field of 3.5 Tesla. But, at the momentary stage, the design of the ILD is far from being determined. Different promising technologies for the sub‑systems are currently under development with the goal to finalise the Technical Design Report (TDR) in the end of 2012.

3.1 Working Principle

The purpose of a detector system operating at a particle collider is to visualise and record the particles created in the collisions. The work particle physicists do, to identify the particles that pass through the detector system, is similar to the way someone would study the tracks or footprints left by animals in snow. The characteristics of the prints, like size and shape, length of stride, overall pattern, direction and depth can reveal the type, size and speed of the animal that came past. Instead of footprints, particle detectors are able to measure different properties of traversing particles, which can be deciphered by physicists. These characteristics are the particle's trajectory, momentum, velocity, energy and electric charge. From these properties physicists are able to calculate the masses of the particles, recover intermediate processes and decays, and to finally identify all the particles initially created during the collision in the heart of the detector.

Since it is not possible to acquire all needed information with just one detector technology, modern particle detectors are designed as multi-purpose detector systems. They consist of multiple layers of different sub-detectors, each specialised to measure a particular type or characteristic of the traversing particles, as shown in figure 3.2. In principle, each multi-purpose detector consists of the following five sub-systems:

- **vertex detector - visualises the vertices of charged particles**
  Most of the numerous known particles do not live long enough to leave tracks in the detector and therefore it is only possible to measure them indirectly via their decay products. These so-called secondary particles originate from a secondary vertex a short distance away from the collision point. The identity of the short living particles can then be calculated from kinematic relations.

- **tracking system - reveals the tracks of charged particles**
  The tracking system measures very precisely the path of traversing charged particles. Due to the external magnetic field these tracks are bent and it is possible to calculate the momenta of the particles from the curvature of their trajectories. From the direction of the curvature, with respect to the magnetic field, the sign of the particle's electric charge can be determined.

- **calorimeter system - measures the energy of particles**
  Calorimeter are composed of layers of a dense material interleaved with layers of an active medium. Particles interacting with the material of the calorimeter lose their energy and give rise to a cascade of charged secondary particles, which can be detected by the active layers. From the reached depth and the amount of the secondary particles it is possible to calculate the total energy of the initial particle. Since the electromagnetic interaction of $e^{\pm}$ and photons is very different to the strong interaction of hadrons, the calorimeter system is split into two parts using different absorber materials, the electromagnetic and the hadron calorimeter.

- **superconducting solenoid - provides a magnetic field**
  A huge superconducting solenoid, surrounding the tracking and calorimeter systems, provides a strong magnetic field which bends the trajectories of charged particles. In addition, the magnetic field reduces the low energy background because it prevents charged particles with low momenta from reaching the sensitive layers. For example at the ILD the magnet provides a magnetic field of 3.5 Tesla and only charged particles with an transverse momentum above 17 MeV/c (170 MeV/c) reach the first layer of the vertex (tracking) system, located at a radius of 16 mm (162 mm).

- **muon system - identifies muons**
  Muons and neutrinos are the only particles of the Standard Model reaching behind the calorimeters and the magnet. Since all measurable particles are stopped in the calorimeters, every particle that produces a signal in the muon system has to be a muon.
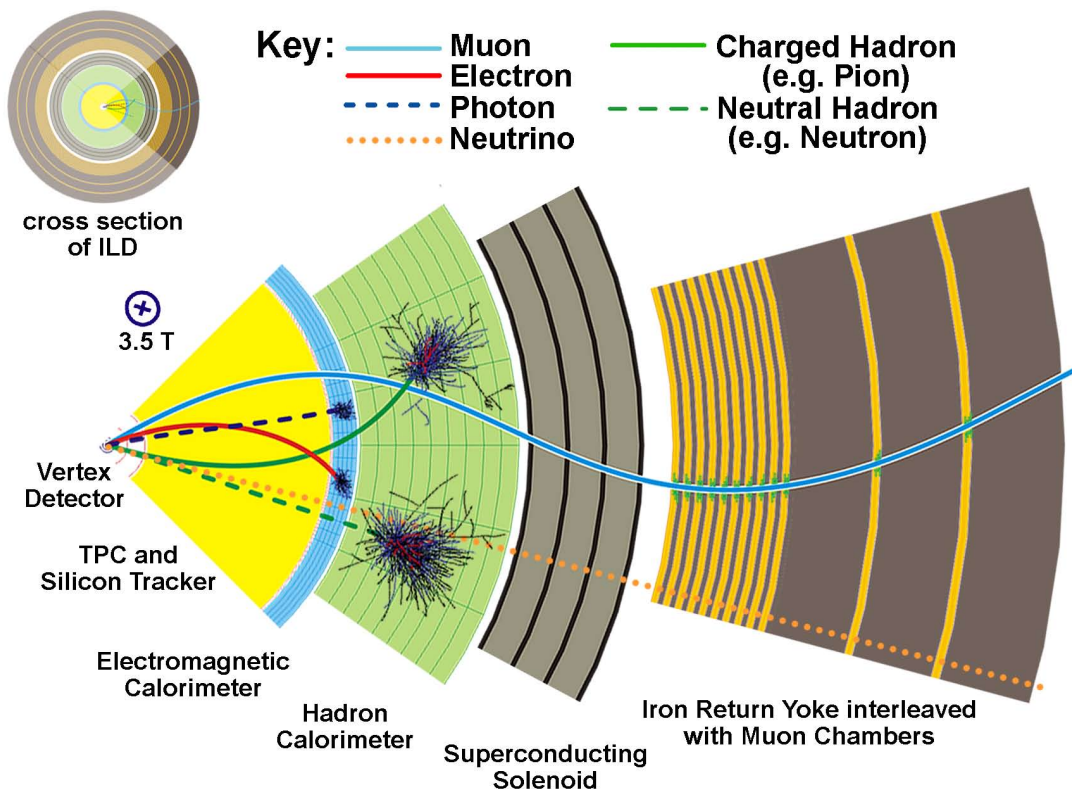

Fig. 3.2: Working principle of the ILD detector - particles with dashed tracks are invisible for the sub-detector.

Since each of the different sub-detectors measures different characteristics of different particles, the information of all systems has to be combined to identify all particles created in the collisions. As indicated in table 3.1 and figure 3.2, only

	e$^\pm$	γ	p$^\pm$	n	$\mu^\pm$	ν
tracker	X		X		X	
ECAL	X	X	X		X	
HCAL			X	X	X	
muon system					X	

Tab. 3.1: Particles that can be measured with the different sub‑detectors are marked with a 'X'.

the following long‑lived particles, produced directly in the collisions or in decays of short lived particles, can be identified by a multipurpose detector:

- **photons** are unique to leave signal only in the electromagnetic calorimeter

- **electrons and positrons** can be seen in the vertex and tracking system and deposit their whole energy in the electromagnetic calorimeter.

- **hadrons** deposit most of their energy in the hadron calorimeter. Charged hadrons are also visible to the vertex and tracking detectors.

- **muons** pass through matter almost undisturbed and therefore pass through all materials of the detectors. Since they are charged they can be seen by all active sub‑detectors.

Neutrinos interact only weakly with matter so that they leave no measurable signal in any sub‑detector. Therefore they can only be measured indirectly via missing energy, the difference between the collision energy and the total measured energy, which requires full detector hermeticity.

3.2   ILD Reference Detector

In this section the different sub‑systems of the ILD Reference Detector are presented as defined in the ILD Letter of Intent [21] with updates done by the ILD joint steering board [33]. The design of the silicon tracking system was prepared by the Silicon for the Linear Collider (SiLC) Collaboration [34] and [35].

3.2.1   Vertex Detector

Simulations have shown, that, in order to achieve the desired flavour tagging performance, the first layer of the vertex detector has to be as close as possible to the collision point, with a maximal radius of 15 mm [22]. For the vertex detector, the major technical challenge is the beam‑related background, which increases rapidly when going closer to the interaction point. Therefore it is clear that silicon pixel
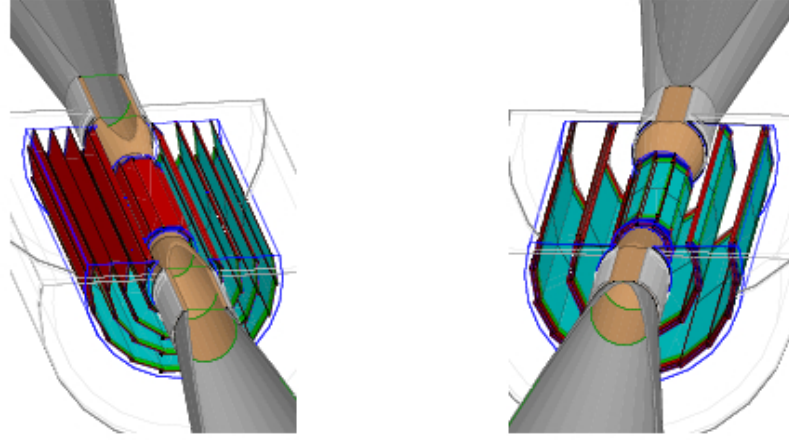
Fig. 3.3: Proposed geometries of the ILD vertex detector - VTX - SL with five single layers (left) and VTX - DL with three double layers (right) [21].

detectors are the only possible option, whereas the exact technology and readout architecture are still undefined.

Based on the present understanding, a design with extended cylinder layers reduces the material budget in comparison to a shorter barrel part complemented with end cap disks, like used for example for the vertex detector of the CMS experiment. At the moment two different layouts of the cylindrical vertex detector are under investigation, as displayed in figure 3.3 and table 3.2. The first layout, VTX - SL, uses five single layers, whereas the second, VTX - DL, is a geometry with three double layers of silicon pixel detectors. The VTX - SL is cheaper because it is technically less challenging to build and contains one pixel layer less. On the other hand the VTX - DL performs slightly better regarding the impact parameter resolution, as shown in section 9.1, and allows for the implementation of additional electronics which could correlate the hits in the two sensor layers of one double layer and would then be more robust against low momentum background. To minimise the number of background hits in the innermost layer, in both designs the first vertex layer is only half the length of the other and covers the collision point down to a polar angle of $\vartheta = 6.84\,°$ (VTX - SL) and $\vartheta = 14.36\,°$ (VTX - DL).

The pixel sensors are envisaged to provide a single point resolution of $2.8\,\mu m$ over the whole sensitive vertex area. A review of the different pixel sensor technologies under investigation for the ILC can be found in [36]. Most of them are currently under development and need at least a couple of years to fulfil the required specifications. Within the ILD groups the technologies of interest are CMOS sensors, DEPFETs, FPCCDs and ISIS.

Two different readout modes are under investigation: continuous readout and readout which is delayed to the time after a bunch - train. For the approach using continuous readout the goal is to achieve very low noise at a high readout frequency while keeping the power consumption at an affordable level. For the innermost

layer	VTX‑SL		VTX‑DL	
	radius [mm]	length [mm]	radius [mm]	length [mm]
layer 1	15.0	125.0	16.0 / 18.0	125.0
layer 2	26.0	250.0	37.0 / 39.0	250.0
layer 3	37.0	250.0	58.0 / 60.0	250.0
layer 4	48.0	250.0		
layer 5	60.0	250.0		

Tab. 3.2: Radius and ladder length for each layer of the two vertex detector geometries [33].

layers a readout time of about $25\,\mu\text{s} - 50\,\mu\text{s}$ is required. The ultimate goal for the average power dissipation of the vertex system is a few tens of watts, which could be reached if the concept of power cycling, described in section 5.2.1, is possible.

Interactions of traversing particles with the material inside the volume of the vertex system lead to the production of secondary particles and to trajectory kinks. Therefore it is important to minimise the material budget of the beam pipe and the vertex detector. The beam pipe around the collision point is assumed to be made of $250\,\mu\text{m}$ thick beryllium with a radiation length (RL) of $0.07\,\%\,X_0$, covered with a $25\,\mu\text{m}$ thick titanium foil with $0.07\,\%\,X_0$ to reduce the background from synchrotron radiation. The radiation length of the single layers of the VTX‑SL is foreseen to be smaller than $0.11\,\%\,X_0$. Each double layer of the VTX‑DL is envisaged to be below $0.16\,\%\,X_0$. These values can be reached when using pixel sensors with a thickness of $50\,\mu\text{m}$ and a lightweight support structure. The whole vertex detector will be enclosed with an approximately $500\,\mu\text{m}$ thick cylindrical beryllium support at a radius of $65\,\text{mm}$ with a RL of $0.14\,\%\,X_0$. Together with a light foam cryostat with $0.05\,\%\,X_0$ and a $500\,\mu\text{m}$ thick aluminium foil with $0.56\,\%\,X_0$, which acts as a Faraday cage, this wrapping adds up to a radiation length of $0.75\,\%\,X_0$.

3.2.2   Tracking System

The ILD tracking system, shown in figure 3.4, is a combination of a large Time Projection Chamber (TPC) surrounded by silicon strip detectors. The most stringent requirement of the tracking system is the ability to measure the transversal momentum of charged particles with an accuracy of $\sigma(\Delta p_t/p_t^2) \leq 2 \cdot 10^{-5}\,(\text{GeV/c})^{-1}$, as outlined in section 1.3. In addition a full angular coverage and high hermeticity are needed. Due to the comparable low particle rates outside the very forward region, radiation hardness of the sensors and their appropriate readout electronics is not a crucial issue. This enables to operate the silicon sensors at room temperature with a relaxed temperature gradient of about $\Delta T = \pm 5\,^\circ$. In addition long shaping times between $1\,\mu\text{s}$ to $3\,\mu\text{s}$ and the use of readout strips with a length of up to $50\,\text{cm}$ in the silicon layers are possible. To enable the monitoring of the TPC
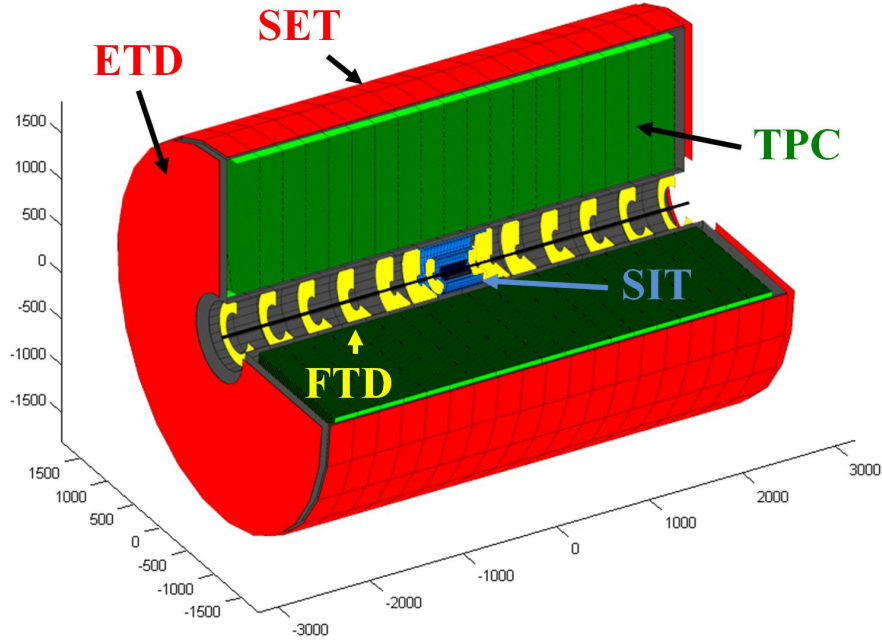
Fig. 3.4: Tracking system of the ILD.

it is necessary that the silicon detectors are able to provide a time stamping of the events. The concept of particle flow tightens the demands on material budget, which is an object of ongoing R&D studies. The bunch structure of the ILC beam allows to use the concept of power cycling, described in section 5.2.1, which immensely decreases the need of cooling systems, one of the major contributors to the material budget of former tracking systems. The need of the push - pull scenario, compare section 2.5.5, sets highest demands on the rigidity and also the alignment strategy of the tracking system.

3.2.2.1   Time Projection Chamber

The ILD contains a big Time Projection Chamber (TPC) as the main tracking component. This offers several advantages, like the continuous measurement of a large number of true, three - dimensional space points, which compensates for the moderate point and double track resolution. Since the TPC is mainly a huge gas volume, it presents a minimum amount of material, which is utterly important to allow particle flow calorimetry. Thanks to the continuous measurement of the particle tracks a good particle identification via the specific energy loss is provided, with a dE/dx - resolution of about 5 %.

The performance goals and design parameters of the Linear Collider Time Projection Chamber (LCTPC) are summarised in table 3.3. To measure more than 200 space points of the track with a spatial resolution of 100 μm or better in the whole drift volume of 2.2 m, the TPC must be read out with Micro Pattern Gas Detectors (MPGD). The required resolutions are not obtainable with Multi - wire Pro-

outside dimensions	diameter $= 3.6\,\mathrm{m}$
	length $= 4.3\,\mathrm{m}$
momentum resolution (3.5 T)	$\sigma(1/p_T) \sim 9 \times 10^{-5}\,\mathrm{GeV}^{-1}$ (TPC only)
	$\sigma(1/p_T) \sim 2 \times 10^{-5}\,\mathrm{GeV}^{-1}$ (VTX + tracking)
material budget	chamber gas $\sim 1\,\%\,X_0$
	inner field cage $\sim 1\,\%\,X_0$
	outer field cage $\sim 3\,\%\,X_0$
	end‑caps $\sim 15\,\%\,X_0$
number of measured points	≥ 200
point resolution	$\sigma_{point}(r\varphi) < 100\,\mu\mathrm{m}$
	$\sigma_{point}(rz) \sim 500\,\mu\mathrm{m}$
two hit resolution	in $r\varphi \sim 2\,\mathrm{mm}$
	in $rz \sim 6\,\mathrm{mm}$
dE/dx resolution	$\sim 5\,\%$
Performance ($p_T > 1\,\mathrm{GeV}$)	$> 97\,\%$ efficiency for TPC only
	$> 99\,\%$ efficiency for tracking system

Tab. 3.3: Goals for performance and design parameters of the LCTPC, [21] and [33].

portional Chambers (MWPC) like used in former experiments. Currently different readout options are under investigation with the goal to understand their properties and to evaluate the best possible point resolution. The focus of the LCTPC collaboration lies on two technologies, Micromesh Gas Detectors (Micromegas) [37] and Gas Electron Multipliers (GEMs) [38], as described in section 7.4.2. The choice of the TPC gas is crucial for efficient and stable operation. The gas influences the transverse diffusion and the number of ionisation electrons produced by a traversing particle. Both factors are important to achieve the required position‑ and dE/dx‑resolution. The strong magnetic field of the surrounding magnet is beneficial for the resolution of the TPC, because it compresses the transverse diffusion of the drift electrons to the order of $1\,\mathrm{mm}$. To limit the needed voltage at the central cathode and to minimise event overlaps, the chamber gas must ensure a drift velocity of around $5\,\text{-}\,10\,\mathrm{cm}/\mu\mathrm{s}$ at a drift field of a few $100\,\mathrm{V/cm}$. To distinguish between tracks from different bunch crossings, or from cosmic radiation, the timing of the TPC has to be around $2\,\mathrm{ns}$. This is also important to ensure a two hit resolution of $2\,\mathrm{mm}$ in the $r\varphi$‑plane and $6\,\mathrm{mm}$ in the rz‑plane.

3.2.2.2 Silicon Tracking System

In the barrel region, the silicon tracking system is composed of three double layers of silicon strip sensor modules, two between vertex detector and TPC, the Silicon Internal Tracker (SIT), and one layer just outside the TPC, the Silicon External Tracker (SET). The radii and proposed lengths of these silicon layers are given in table 9.1. Each double layer of the SIT and SET is build of silicon detectors containing up to five daisy‑chained single sided silicon strip sensors, described in section 5.1. The foreseen sensors have a thickness of 200 μm and will be processed on 6 inch wafers, resulting in a size of $95.5 \times 95.5 \,\mathrm{mm}^2$. If possible even 8 inch wafers will be used, dependant on their availability and costs at the time the mass production will start. These silicon strip sensors will most likely have a readout pitch of 50 μm, containing one intermediate strip, providing a spatial resolution of 6 μm, as determined in a test beam campaign described in chapter 6. To min-imise the material budget, the layers of the silicon strip tracker must not exceed $0.5\,\% \, X_0$, which should be no problem when using 200 μm thick silicon sensors with integrated pitch adapters, as described in section 5.4.

To ensure hermeticity, the silicon tracking system is completed in the forward region with the End‑cap Tracking Detector (ETD) and the Forward Tracking Detector (FTD), as shown in table 9.2. The three layers of the ETD will use the same silicon strip sensors as the barrel layer. The first three layers in the FTD will contain silicon pixel sensors, most probably similar to the vertex detector. The outer four layers will be made of trapezoidal silicon strip sensors forming disks, as used in the forward regions of present LHC tracking systems.

The readout chips for the silicon strip sensors are still under development and foreseen to be processed in 90 nm deep CMOS technology. They should have at least 512 channels and support the concept of power cycling. Presently first pro-totypes in 130 nm technology are under investigation, as described in section 5.2.

3.2.2.3 Alignment of the Tracking System

To enable measurements with the desired momentum resolution of $\sigma(\Delta p_t/p_t^2) = 2 \cdot 10^{-5}\,(\mathrm{GeV/c})^{-1}$, the tracking system must be aligned to the order of a few μm. Temperature variations, fluctuations in the atmospheric pressure, inhomogeneities in the electric and magnetic fields and the foreseen push pull scenarios make the alignment of the system a very challenging task. To perform an initial alignment of the TPC a laser system and the monitoring of the B‑field by a matrix of Hall plates and Nuclear Magnetic Resonance (NMR) probes are foreseen. After each tracking detector is aligned internally the fine alignment of the TPC with the SIT and the SET will be done with a subset of data. This will then be iterated until the correct momentum measurement for $\mathrm{Z} \to \mu\mu$ events is achieved. Simulations have shown that about $10\,\mathrm{pb}^{-1}$ of data at the Z‑peak is needed during commissioning and typically $1\,\mathrm{pb}^{-1}$ after each push‑pull operation [39].

3.2.3 Calorimeter System

The calorimeter system is composed of the electromagnetic calorimeter (ECAL) surrounded by the hadronic calorimeter (HCAL), as shown in figure 3.1. Both are divided into a barrel part enclosed with two end caps. To ensure the best possible hermeticity a set of special calorimeters are foreseen in the forward region of the ILD, which are able to cope with the harsh radiation there.

The design of the calorimeters is dictated by the particle flow approach. In principal the primary performance limitation of the calorimeter comes from failures in the assignment of the energy deposits to the associated particles. To minimise these failures the ILD calorimeters aim for a very fine transversal and longitudinal segmentation. Different technologies are studied within the CALICE, CALorimetry for the ILC, collaboration [40]. At the moment, a silicon‑tungsten ECAL [41] and a steel‑scintillator HCAL [42] are proposed for the ILD.
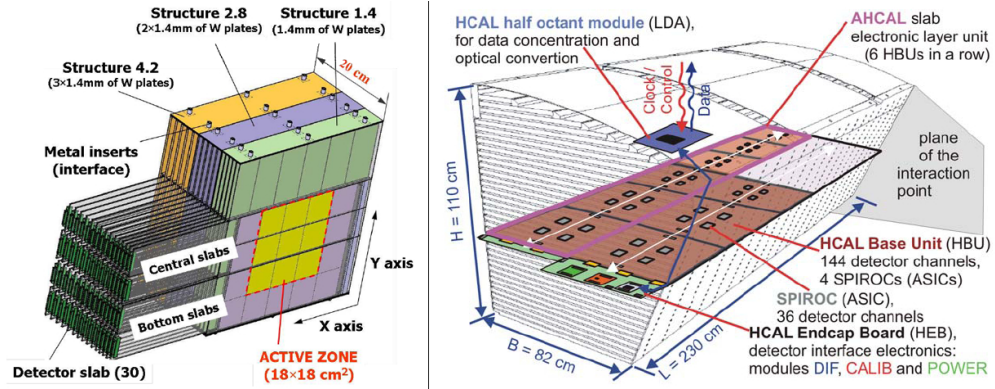

Fig. 3.5: ILD calorimeter - schematic view of a silicon‑tungsten ECAL module (left) [41] and a half sector of the proposed steel‑scintillator HCAL (right) [42].

3.2.3.1 ECAL

The silicon‑tungsten electromagnetic calorimeter, as displayed in figure 3.5, is longitudinally segmented into around 30 tungsten layers interleaved with silicon sensors. Tungsten is chosen as absorber material because of its beneficial properties: radiation length $X_0 = 3.5\,\text{mm}$, Molière Radius $R_M = 9\,\text{mm}$ and interaction length $\lambda_I = 99\,\text{mm}$. The small Molière Radius allows for a compact design with a depth of roughly $24\,X_0$ within $20\,\text{cm}$ thickness and, compared to other materials, it provides a very good separation of electromagnetic showers generated by near‑by particles. The sensitive part of the ECAL will be build of high resistivity ($5\,\text{k}\Omega/\text{cm}$) silicon sensors with a thickness of $320\,\mu\text{m}$. These sensors are segmented into individual PIN‑diodes with a size of $5 \times 5\,\text{mm}^2$, leading to approximately 10^8 readout cells on the active area of about $2{,}500\,\text{m}^2$.

Test beam measurement with a first silicon‑tungsten prototype revealed an energy resolution of $(16.6 \pm 0.1)\,/\,\sqrt{E(GeV)} \oplus (1.1 \pm 0.1)\,\%$ with a signal over noise

ratio of S/N ~ 7.5 for minimum ionising particles [41]. At the moment, optimisation studies of the longitudinal profile of the ECAL are performed, which lead in a direction to use varying thicknesses for the silicon and tungsten layers, which could reduce the costs and is beneficial for the lateral spread and energy resolution.

3.2.3.2   HCAL

In particle flow the HCAL plays a crucial role in separating and measuring the energy deposits of charged and neutral hadrons. The hadronic calorimeter will be designed as a sampling calorimeter composed of stainless steel absorber layers interleaved with either scintillator tiles (analogue HCAL) or gaseous devices (digital HCAL) as active medium. Stainless Steel is non‑magnetic and can therefore be used inside the magnet and, in contrast to heavier materials used in other experiments, has a moderate ratio of hadronic interaction length $\lambda_I = 17\,\mathrm{cm}$ to electromagnetic radiation length $X_0 = 1.8\,\mathrm{cm}$. This allows a fine longitudinal sampling in terms of X_0, with a reasonable number of layers in a given total hadronic absorption length, keeping the detector volume and number of needed readout channels small. The total hadronic absorption length of the HCAL corresponds to a minimum of $5.5\,\lambda_I$ in addition to the ECAL [21], with the muon system acting as tail catcher. The arrangement of the active layers with internal and external electronics components is sketched in figure 3.5.

At the moment, R&D activities focus on the barrel part, where two geometries are compared. The first uses long barrel modules, subdivided only once in z, with electronics and service connections at the end faces and the second idea investigates 5 rings with interfaces located at the outside of the barrel.

3.2.3.3   Forward Calorimeter

A set of special calorimeters is needed in the forward region of the ILD. These have to cope with the harsh radiation introduced from beam related backgrounds, as described in section 2.5.4, which requires special front‑end electronics and data transfer equipment. The following list gives a short description of the foreseen forward calorimeters:

- the **LumiCal** enables a precise luminosity measurement using Bhabha scattering, $e^+e^- \rightarrow e^+e^-(\gamma)$, as gauge process

- the **BeamCal** is positioned just outside the final focusing quadrupoles and will provide a fast estimation of the bunch‑by‑bunch luminosity by measuring the energy deposit of e^+e^-‑pairs originating from beam radiation

- the **LHCal** extends the coverage of the HCAL end‑cap to small polar angles

- the **GamCal** is located about $100\,\mathrm{m}$ downstream of the detector and will assist the beam‑tuning

- a **pair monitor**, composed of a layer of pixel sensors, positioned just in front of the BeamCal will measure the distribution of beam radiation pairs and give additional information of specific beam parameters

At the moment first prototypes are build which will be tested in near future test beams.

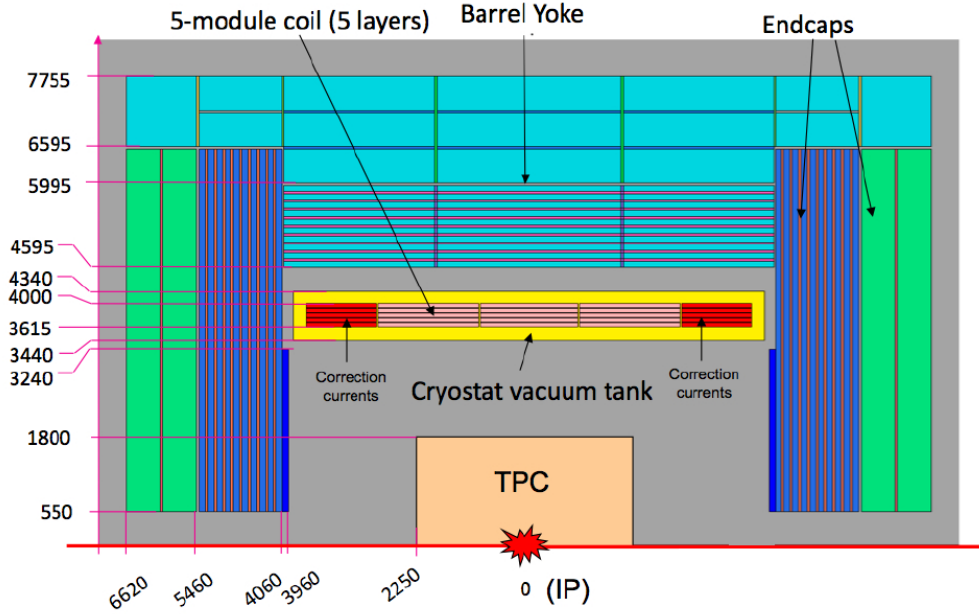## 3.2.4 Superconducting Coil and Return Yoke

Fig. 3.6: Magnet system of the ILD [21].

To obtain good momentum resolution and to suppress low momentum backgrounds, the superconducting magnet, surrounding the tracking and calorimeter systems, will provide a magnetic field of 3.5 Tesla. As shown in figure 3.6, the magnet system consists of the superconducting solenoid, including correction coils, and the iron return yoke. The coil of the solenoid will be divided into five modules, which are electrically and mechanically connected. The conductor will consist of a superconducting cable embedded inside a low electrical resistivity stabiliser and mechanically reinforced with a high-strength aluminium alloy. The coil will be cooled using liquid helium with a temperature of 4.5 K. At a current of 18.2 kA the magnet will provide a maximal central field of 4.0 T, comprising a stored energy of 2.0 GJ. The design of the coil must assure a high field homogeneity within the TPC volume and very small fringe fields of around 40 Gauss in a radial distance of 15 m.

The iron return yoke will have a total weight of about 13.400 t and is divided into a barrel yoke and two end-cap yokes. They consist of 13 and 12 layers of iron

plates for the barrel part and the end - caps, respectively. The inner ten layers will have a thickness of 100 mm followed by the outer plates with a thickness of 560 mm. These absorber layers are interleaved with Resistive Plate Chambers (RPC) for tail catching and muon detection.

3.2.5   Muon System

Muons are the only particles that can be measured outside the magnet coil and therefore quite easy to identify. Due to the magnetic field only muons with a momentum above 3.6 GeV can reach the muon system. Muons with lower momenta have to be identified with the tracker and the calorimeter. In addition, the muon system can act as a tail catcher for very late developed hadronic showers.

Due to the relative clean nature of the e^+e^- - collisions there is no need to trigger on muon tracks. When compared to the requirements at hadron colliders, this drastically lowers the demands on the muon system. Because of the significant amount of multiple scattering at the location of the muon detectors, a spatial resolution in the order of a few cm is sufficient. The two options under consideration are Resistive Plate Chambers (RPC), with a strip pitch of $3-4$ cm, and extruded plastic scintillator strips, containing embedded wavelength shifting fibres read out on both ends with silicon photomultipliers.

Chapter 4

Silicon Strip Sensors

4.1 Basic Properties of Silicon

Silicon (Si) is the second most common element in the upper crust of our earth. It rarely occurs in its elemental state, but mostly in the form of silicon dioxide and complex silicates. The fundamental properties of silicon are summarised in table 4.1.

parameter	symbol	value
atomic number		14
relative atomic weight		$28.0855\,\mathrm{g/mol^3}$
crystal structure		diamond cubic
lattice constant	a_0	$5.4307\,\text{Å}$
density	ρ	$2.328\,\mathrm{g/cm^3}$
relative permittivity	ϵ_{Si}	11.68
atomic concentration		$5 \cdot 10^{22}\,\mathrm{atoms/cm^3}$
intrinsic carrier density	n_i	$1.45 \cdot 10^{10}\,\mathrm{cm^{-3}}$
band gap energy @ $300\,\mathrm{K}$ ($0\,\mathrm{K}$)	E_g	$1.124\,\mathrm{eV}$ ($1.170\,\mathrm{eV}$)
energy to create an e^-h-pair	E_I	$3.63\,\mathrm{eV}$
drift mobility electrons	μ_e	$1450\,\mathrm{cm^2/Vs}$
drift mobility holes	μ_h	$450\,\mathrm{cm^2/Vs}$
intrinsic resistivity		$235\,\mathrm{k\Omega cm}$
radiation length	X_0	$9.36\,\mathrm{cm}$

Tab. 4.1: Fundamental properties of silicon.

4.1.1   Intrinsic Properties of Silicon

In its pure form silicon has a diamond cubic crystal structure formed by four covalent bonded electrons. It is a semiconductor which isolates at low temperatures and shows a specific conductance of $10^2 - 10^{-9}\,\Omega^{-1}\mathrm{cm}^{-1}$ at higher temperatures.

The electrical conductance can be explained by the electronic band structure of silicon. In classic crystalline semiconductors, the electrons can have energies only within certain energy levels separated by regions of forbidden energies. The highest energy band of the atom filled with electrons at a temperature of $T = 0\,K$ is the valence band, and the lowest energy band that is not occupied with electrons at $T = 0\,K$ is the conducting band. The forbidden region in between, the band gap, has a height equal to the energy difference between the conductive and the valence band, which is $E_g = E_C - E_V = 1.12\,\mathrm{eV}$ for silicon at $300\,K$. While electrons are bound in the valence band, electrons in the conduction band can move freely between atoms and can be handled like quasi free particles with an effective mass $m_e^* = 1.09\,m_e$. In silicon, bound electrons can be excited, raised from the valence band to the conducting band, by the introduction of an energy above the threshold energy $E_I = 3.63\,\mathrm{eV}$. During this process, called carrier generation, also a so-called electron hole h is generated. An electron hole is the conceptual and mathematical opposite of an electron, describing the lack of an electron at a position where one could exist in an atom. Similar to electrons in the conducting band holes in the valence band can be handled like quasi free particles with the effective mass $m_h^* = 0.56\,m_e$. The difference between the band gap E_g and the threshold energy E_I comes from the fact that silicon is an indirect semiconductor, where the maximum energy of the valence band and the minimum energy of the conduction band are located at different crystal momenta. This implies that during carrier generation and recombination also the absorption or emission of a phonon must be involved. Phonons are quasi-particles used to describe lattice vibrations, which have a momentum equal to the difference between the momenta of the involved electron and hole.

The number of free charge carriers in silicon is dependent on the temperature and can be calculated with the Fermi-Dirac statistics. It describes the probability for the occupancy of one state in the band structure at the energy E for the temperature T in thermal equilibrium:

$$f(E, T) = \frac{1}{exp\left(\frac{E - E_F}{k_B T}\right) + 1} \tag{4.1}$$

Where k_B is the Boltzmann constant and E_F is the Fermi energy which is defined as the energy where the occupation probability is one half. In intrinsic silicon the Fermi energy is exactly in the middle of the band gap and, due to the global charge neutrality at equilibrium, the concentration of electrons n in the conduction band and that of holes p in the valence band are equal to the intrinsic carrier

concentration n_i:

$$n_i = n = p = \sqrt{N_C N_V} \cdot exp\left(-\frac{E_g}{2k_B T}\right) \tag{4.2}$$

with $n_i \sim 1.45 \cdot 10^{10}\,\text{cm}^{-3}$ for silicon at $T = 300\,\text{K}$. Here N_C and N_V are the effective state densities in the conduction and the valence band. They can be calculated with:

$$N_C = 2 \cdot \left(\frac{2\pi m_e^* k_B T}{h^2}\right)^{\frac{3}{2}} \text{ and } N_V = 2 \cdot \left(\frac{2\pi m_h^* k_B T}{h^2}\right)^{\frac{3}{2}} \tag{4.3}$$

where m_e^* and m_h^* are the effective masses of the quasi-free electrons and holes and h is the Planck's constant. The factor 2 comes from the two possible spin states of the electrons.

4.1.1.1   Including an External Electric Field

Without electric field the average displacement of a charge carrier is zero. When applying an external electric field $\vec{E}$, the free charge carriers will drift according to their charge and the field orientation. The concept of the effective mass: in most cases the charge carriers can be handled like quasi free particles with the effective masses $m_e^* = 1.09\,\text{m}_e$ and $m_h^* = 0.56\,\text{m}_e$, eases the calculation of the drift velocities for electrons $\vec{v}_e$ and holes $\vec{v}_h$. It has to be differentiated between the cases where a weak and a strong external electrical field $\vec{E}$ are present:

- For **weak electric fields**, the drift velocities are linearly proportional to the applied field:

$$\vec{v}_{e,h} = \mu_{e,h} \cdot \vec{E} \tag{4.4}$$

  The mobility of electrons μ_e and holes μ_h can be calculated with:

$$\mu_{e,h} = \frac{q\widehat{\tau}_s}{m_{e,h}^*} \tag{4.5}$$

  For silicon at $300\,\text{K}$ these are $\mu_e \sim 1450\,\text{cm}^2/\text{Vs}$ and $\mu_h \sim 450\,\text{cm}^2/\text{Vs}$. $\widehat{\tau}_s$ is the mean free time between two scattering processes, occurring on imperfections and defects of the crystal lattice and, in the extrinsic case, on impurities like doping atoms.

- In **electric fields above $10^4\,\text{V/cm}$** the velocity dependence deviates from the linear relationship because of the increasing number of collisions between the charge carriers and the crystal lattice atoms. These lead, for sufficient strong external electric fields, to a saturation of the average velocity [43]:

$$\vec{v}_e = \frac{\mu_e \vec{E}}{\sqrt{1 + \left(\frac{\mu_e \vec{E}}{v_{e,sat}}\right)^2}} \text{ and } \vec{v}_h = \frac{\mu_h \vec{E}}{1 + \frac{\mu_h \vec{E}}{v_{h,sat}}} \tag{4.6}$$

  The saturation velocities for electrons and holes are $v_{e,sat} \sim 1.1 \cdot 10^7\,\text{cm/s}$ and $v_{h,sat} \sim 9.5 \cdot 10^6\,\text{cm/s}$.

4.1.1.2 Including an External Magnetic Field

The presents of an external magnetic field $\vec{B}$, in addition to an external electric field, affects the movements of the free charge carriers. This so called Hall effect leads to a Lorentz shift, a change in the direction of the charge carriers, described by the Lorentz angle ϑ_L:

$$\vartheta_L = \mu_H \vec{B} \ \text{ with } \ \mu_H = \mu_{e,h} \cdot r_H \tag{4.7}$$

where the Hall mobility μ_H differs from the conduction mobility $\mu_{e,h}$ by the Hall scattering factor r_H. Since the mobilities of electrons and holes are different, also their deflections are different. Measurements inside a magnetic field of 4 Tesla revealed Lorentz angles of $31\,°$ and $8\,°$ for electrons and holes, respectively, inside a $300\,\mu$m thick silicon sensor [44]. This corresponds to a Lorentz shift of up to $200\,\mu$m for electrons. To minimize the influence of the Lorentz shift in detector systems, it is possible to mechanically tilt the silicon sensors relative to the external magnetic field.

4.1.2 Extrinsic Properties of Silicon

It is possible to alter the electric properties of silicon by replacing silicon atoms from the crystal lattice with foreign atoms. For such a doping two possibilities exist:

- **p‑doping:**
  A silicon atom is replaced with an acceptor atom, an atom with only three valence electrons like boron. Thus one electron is missing in the covalent bonds and a hole is created. This change of the lattice structure is accompanied by the creation of localised, permitted energy levels in the band gap, just above the valence band.

- **n‑doping:**
  Here a silicon atom is replaced with a donator, an atom containing five valence electrons like phosphor. This additional valence electron increases the number of free electrons in the silicon. Donors introduce allowed energy levels just below the lower boarder of the conduction band.

The Fermi level E_F of a doped semiconductor is shifted towards the conduction band in n‑type material and towards the valence band in p‑type material. This can be explained when looking at the product of the densities of electrons n_e and holes n_h in a semiconductor, which always equals the quadratic intrinsic charge carrier concentration n_i:

$$n_e \cdot n_h = n_i^2 \tag{4.8}$$

It is obvious that an increase in the number of majority charge carriers must always be accompanied by a decrease in the number of minority carriers. In the case of n‑type material the majority carriers are electrons and for p‑type material electrons

are the minority charge carriers; and vice versa for holes. In good approximation, for all practical temperatures, the majority charge carrier concentration can be assumed to be identical to the doping concentration. Therefore the resistivity of extrinsic silicon is defined by the doping concentration and the mobility of the majority charge carriers:

$$\rho = \frac{1}{q\mu_e N_D} \quad \text{for n-type silicon} \tag{4.9}$$

$$\rho = \frac{1}{q\mu_h N_A} \quad \text{for p-type silicon} \tag{4.10}$$

Here N_D and N_A are the doping concentrations of n-type and p-type silicon and again μ_e and μ_h are the mobilities for electrons and holes. This behaviour is only valid for medium temperatures and changes for higher temperatures $k_B T \gtrsim E_g$, where the intrinsic electron concentration is increased by thermal excitation so that the intrinsic conduction outbalances the extrinsic conduction. While the resistivity of intrinsic silicon is about $\rho \sim 230\,\text{k}\Omega\text{cm}$, silicon used for strip sensors must have a specific resistivity between $1\,\text{k}\Omega\text{cm} \le \rho \le 10\,\text{k}\Omega\text{cm}$.

4.2 Energy Loss in Silicon

When a photon or charged particle traverses silicon it loses a part of its energy due to the generation of electron-hole e^-h-pairs. Compared to gaseous detectors, where approximately $30\,\text{eV}$ are required to ionise a gas molecule, silicon sensors have a nearly 10 times improved intrinsic energy resolution because for every $3.6\,\text{eV}$, released by a particle crossing silicon, one e^-h-pair is produced. The mechanism for energy loss in silicon is different for photons, charged hadrons, electrons and positrons, as described below.

4.2.1 Electrons and Photons

Electrons and positrons with an energy below few tens of MeV primary lose their energy due to ionisation, although other processes, like Møller scattering, Bhabha scattering and e^+-annihilation also contribute, as visible in figure 4.1. As displayed, at small energies the loss rates due to ionization rise logarithmically with energy, while the loss rates due to bremsstrahlung rise nearly linearly and begin to dominate above a few tens of MeV in most materials. For electrons and positrons with energies above a few tens of MeV basically all energy loss happens due to bremsstrahlung and is nearly proportional to their energy.

The energy loss of low energetic photons is dominated by the photoelectric effect and photons with an energy larger than the band gap can excite electrons from the valence into the conduction band. High energetic photons lose their energy due to e^+e^--pair production.
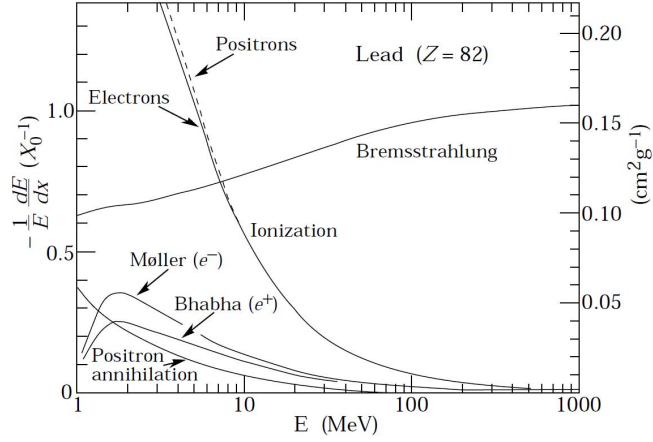
Fig. 4.1: Fractional energy loss of electrons and positrons in lead per radiation length as a function of their energy [4].

The energy loss of high energetic, electromagnetic - interacting particles is characteristic for each material and can be described with the characteristic radiation length X_0, which is:

- the mean distance along which a high energetic electron loses all but $1/e$ of its energy by bremsstrahlung

- 7/9 of the mean free path for e^+e^- - pair production from a high energetic photon

- the appropriate scale length for describing high energetic electromagnetic cascades

4.2.2   Other Charged Particles

The Bethe - Bloch equation describes the energy loss of charged particles, heavier than the electron, for the energy region of approximately $0.1 < \beta\gamma < 1000$, with $\beta = v/c$ and $\gamma = (1 - \beta^2)^{-\frac{1}{2}}$, in materials with intermediate atomic numbers, with an accuracy of a few % [4]:

$$\left\langle -\frac{dE}{dx} \right\rangle = Kz^2 \frac{Z}{A} \frac{1}{\beta^2} \left[\frac{1}{2} ln \left(\frac{2m_e c^2 \beta^2 \gamma^2 T_{max}}{I^2} \right) - \beta^2 - \frac{\delta(\beta\gamma)}{2} \right] \qquad (4.11)$$

with

$$K = 4\pi N_A r_e^2 m_e c^2 \quad \text{and} \quad T_{max} = \frac{2m_e c^2 \beta^2 \gamma^2}{1 + \frac{2\gamma m_e}{M} + \left(\frac{m_e}{M} \right)^2} \qquad (4.12)$$

N_A, Z and A are the Avogadro's constant, the atomic number and the atomic mass of the traversed matter, m_e and r_e are the electron mass and its classical radius and z_e is the incident particles charge. T_{max} is the maximum kinetic energy which

can be transferred to a free electron in a single collision, I is the mean excitation energy and M is the mass of the incident particle. $\delta(\beta\gamma)$ is the correction to the density effect, which describes that the electric field of an incident particle results in the polarisation of individual atoms of the material, which in turn shields the electric field of the particle.
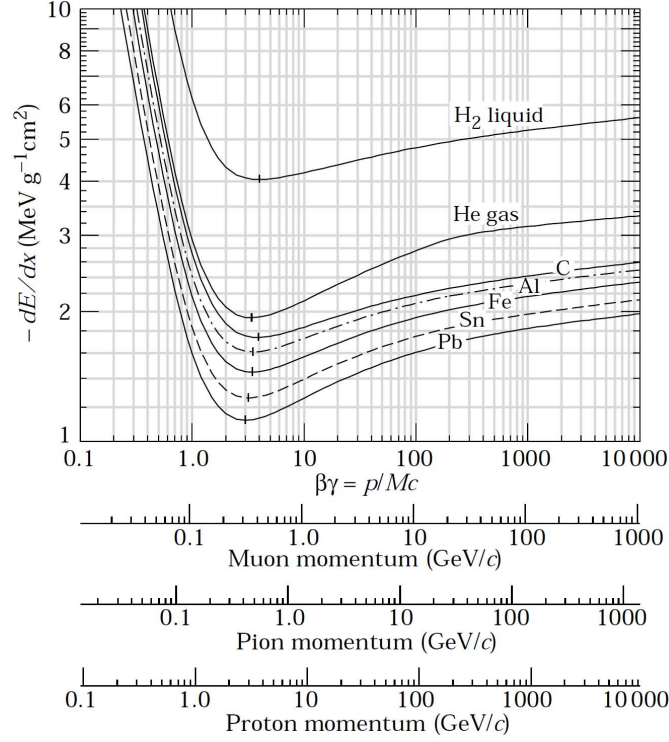

Fig. 4.2: Mean energy loss rate in different materials for charged particles heavier than electrons - radiative effects, relevant for muons and pions are not included [4].

Figure 4.2 shows the function 4.11 computed for pions in different materials. At low energies various corrections must be made and at high energies, dependent on the atomic number, radiative processes become more important than ionization for all charged particles. But, nevertheless, for all practical purposes in high energy physics the energy loss dE/dx in a given material is a function only of β. Particles of the same velocity have similar rates of energy loss in different materials, except for hydrogen, with a slow decrease in the rate of energy loss with increasing Z. The visible difference in the behaviour of the stopping power in gas and in other materials at high energies comes from the density effect correction.

The small vertical lines on the curves in figure 4.2 indicate the minimum of deposited energy in the material, which is approximately at $\beta\gamma = 3$. This energy is very important for particle detectors, because every detector must be able to keep its noise well below this energy to be able to detect such Minimum Ionizing Particles (MIPs).

4.3 Silicon Strip Sensors

This section gives a short overview of the working principle and layout of silicon strip sensors. The most important properties and characteristics are briefly described and more details can be found in literature, for example in [3].
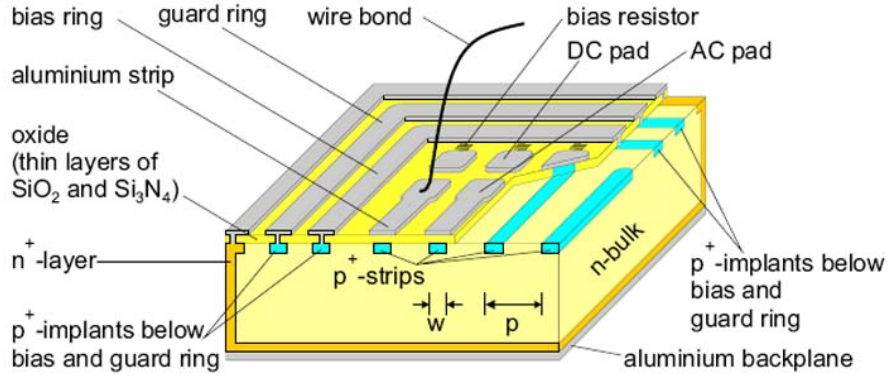
4.3.1 Layout and Working Principle

Fig. 4.3: Layout of an AC - coupled silicon strip sensor as used in high energy physic experiments.

The main part of the silicon sensor, as shown in figure 4.3, is the n - doped bulk, which has p^+- doped strips on the front side and an n^+- doped layer surrounding the other surfaces[1]. At AC - coupled sensors the p^+-strips on the front side are isolated from the aluminium readout strips deposited on the sensor surface by a thin layer of oxide[2]. The strips are surrounded by a bias ring, a p^+- implant which is directly connected to an aluminium ring on top and to each p^+-strip via a bias resistor. The bias ring is surrounded by one or more guard rings. The n^+- doped back side of the sensor is covered with an aluminium layer.

When the sensor is reverse biased, meaning that the bias ring and the p^+-strips lie on negative and the aluminium back plane on positive potential, the pn - junctions between the n - bulk and the p^+-strips form a depleted zone, a zone without free charge carriers, as described in more detail in section 4.3.3. With increasing voltage this zone expands and above the full depletion voltage V_{FD} the whole sensor volume is free of charge carriers. When an ionising particle traverses

---

[1] For silicon sensors in high energy physics experiments this p - on - n structure is the classical layout and this notation will be used for the whole chapter. Nevertheless, also sensors using n - on - p, n^+- on - n and p^+- on - p structures are studied.

[2] It is also possible to directly connect the p^+-strips to the aluminium strips. Such a DC - coupling has the advantage that the production of the sensors involves fewer process steps and is therefore cheaper, but the disadvantage that the readout electronics sees the small DC current of the pn - junctions in the order of a few nA, rising with irradiation up to μA, and therefore has to be protected by intern current compensating circuits.

a fully depleted sensor, along its track electron‑hole pairs are produced which drift along the electric field, generated by the bias voltage, to the electrodes: holes drift to the p^+‑doped strips and the electrons drift to the n^+‑layer at the backplane. The generated charge can be measured via the induced current coming from the movements of the charge carriers to the electrodes. The induced current at the aluminium readout strips, which are directly connected with wire bonds to the charge preamplifier of the associated channel on the readout chip, reveals the position where the particle traversed the sensor.

4.3.2 Signal Production in Silicon Sensors
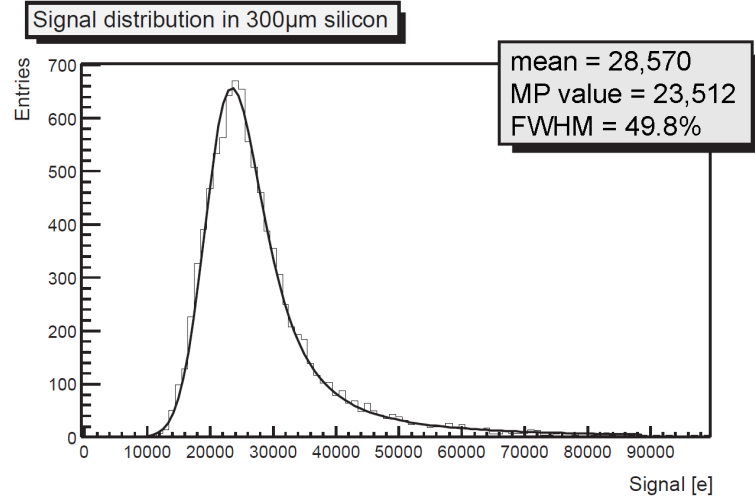
Fig. 4.4: Measured signal distribution of pions in a $300\,\mu$m thick silicon sensor [45].

The energy loss due to ionization of charged particles traversing silicon is statistically distributed around its mean value. For thick absorbers this is a Gaussian distribution which develops an asymmetry and a tail towards high energies for decreasing material thickness. Silicon sensors used in high energy experiments have a thickness of maximal $500\,\mu$m, and are therefore considered as very thin absorbers. Ionising particles are not absorbed in the silicon sensors, but pass them while losing only a small part of their energy. Figure 4.4 shows a measurement of the signal distribution of pions traversing a silicon detector with a thickness of $300\,\mu$m. The fitted curve is a convolution of a Landau distribution describing the signal and a Gaussian distribution caused by electronic noise and statistical detector fluctuations. The Landau tail, the very long asymmetric tail towards high energy deposits, comes from rare events with large single‑collision energy deposits, so‑called δ‑rays or δ‑electrons. Because of these highly energetic δ‑electrons it is not easy to obtain a dependable value for the mean energy loss even with a large number of measurements. Far better, and more easy to measure, is the most probable (MP) energy loss, the visible peak of the distribution, which is at a clearly

lower signal than the mean value. A minimum ionising particle traversing a silicon sensor with a thickness of $300\,\mu$m has a mean energy loss of about $78\,$keV. Since the needed energy to create an e^-h - pair in silicon is $E_I = 3.63\,$eV this corresponds to $72\,e^-h$ - pairs$/\mu$m. The most probable energy loss in $300\,\mu$m silicon is $118\,$keV, resulting in an average of $108\,e^-h$ - pairs$/\mu$m.

For a silicon sensor diode with a surface of $A = 1\,$cm^2 and a thickness of typically d $= 300\,\mu$m the signal of a MIP can be calculated to

$$\frac{dE/dx \cdot d}{E_I} = \frac{387\,eV/\mu m \cdot 300\,\mu m}{3.63\,eV} \sim 3.2 \cdot 10^4\,e^-h\text{-pairs} \qquad (4.13)$$

Measurements of the most probable collected charge with a $300\,\mu$m thick silicon strip sensor revealed about 22,500 electron - hole pairs [45]. This is lower than the theoretical value, which caused by losses due to recombination and losses in the readout electronics. In comparison, the number of free charge carriers, thermally produced in intrinsic silicon of the same size, at $300\,$K is:

$$n_i \cdot d \cdot A = 1.45 \cdot 10^{10}\,\text{cm}^{-3} \cdot 0.03\,\text{cm} \cdot 1\,\text{cm}^2 \sim 4.35 \cdot 10^8\,e^-h\text{-pairs} \qquad (4.14)$$

This is four orders of magnitude higher than the number of e^-h - pairs produced by a MIP. Therefore the number of free charge carriers has to be reduced by several orders of magnitude to make a MIP signal visible. This is possible by either cooling the silicon to very low temperatures, which is not affordable for large devices, or by depleting the silicon volume of free charge carriers, which is possible when the silicon is used as a reverse biased pn - junction, as described in the next section.

4.3.3   pn - Junction and Full Depletion Voltage

A pn - junction is the interface of p - doped and n - doped silicon. Due to diffusion electrons near the pn - interface move into the p region and leave positively charged ions, so - called donors in the crystal lattice of the n - region. Similarly, holes near the pn - junction diffuse into the n - type region and leave negatively charged ions, so - called acceptors. This is the reason why in equilibrium, without external electric field, the regions nearby the pn - interfaces lose their neutrality and become charged, forming a depleted region. The electric field created by this space charge region opposes the diffusion process for both, electrons and holes, and establishes an equilibrium when the region reaches a certain width.

By applying a reverse bias voltage, positive at the n - side and negative at the p - side, the electrons in the n - type region and the holes in the p - type region are pulled away from the junction, increasing the width of the depletion zone with increasing reverse bias voltage until the sensor reaches full depletion when the full depletion voltage V_{FD} is applied. When a sensor is fully depleted, the electric field is zero at the backplane and linearly increases to its maximum E_{max}. If an ionising particle traverses such a full depleted sensor, the only free charge carriers are the e^-h - pairs created by the particle and the generated charge can be

measured with a reasonable S/N ratio. In most experiments, silicon sensors are operated over depleted, always aware that at high bias voltages beyond a critical level an electrical breakdown is observed. At this breakdown voltage the current through the sensor starts to increase dramatically. This can be caused either due to charge multiplication in the collisions of the charge carriers with the lattice atoms, a so-called avalanche breakdown, or by the Zener breakdown, which is based on the quantum mechanical tunnel effect.

For practical reasons, in silicon strip sensors the pn-junction is very asymmetric with a light doped n-type silicon bulk, with typically doping concentration of about $N_{bulk} \sim 10^{12}\,\mathrm{cm}^{-3}$, and a heavy doped small p^+ surface layer, with approximately $N_{SL} \sim 10^{15}\,\mathrm{cm}^{-3}$. The high doped p^+-layer is very thin compared to the width of the depleted zone.

4.3.3.1 $\mathbf{V}_{FD,diode}$

The full depletion voltage of a diode scales with the square of its thickness d and the inverse resistivity ρ of the silicon. The voltage needed to fully deplete a diode can be estimated with:

$$V_{FD,diode} \sim \frac{d^2}{2\,\rho\,\mu_e\,\epsilon_0\,\epsilon_{Si}} \tag{4.15}$$

Here μ_e is the mobility of electrons, the majority charge carriers in an n-type bulk, and ϵ_0 and ϵ_{Si} are the vacuum permittivity and the relative permittivity of silicon. With equation 4.9 this can also be written as:

$$V_{FD,diode} \sim \frac{N_{bulk}\,e\,d^2}{2\,\epsilon_0\,\epsilon_{Si}} \tag{4.16}$$

showing that V_{FD} is dependent on the effective doping concentration N_{bulk} of the bulk material, explaining the change of V_{FD} with radiation damage, which is important to consider for the design of silicon detector systems used in high radiation environments. Typically high-resistivity diodes can be fully depleted with a reverse bias voltage between 30 V to 600 V, depending on their thickness d and specific resistivity ρ.

4.3.3.2 $\mathbf{V}_{FD,strips}$

In contrast to diodes, silicon strip sensors do not have a homogeneous p^+-doped front side, but only thin p^+-doped strips, as shown in figure 4.3, that are usually extended over the full sensor length. When the sensor is fully depleted these strips are electrically isolated from each other and charge, produced by an ionising particle, is only seen by a few of them. This gives a one-dimensional information about where the particle passed through the sensor.

Due to the segmentation of the p^+-layer we now have not only one pn-junction, but many. Edge effects at the strips make the electric field inside the bulk non-linear and the solutions for the Poisson equation describing the voltage drop are

more complicated than for an ideal diode. The solution for the full depletion voltage of a strip sensor $V_{FD,strips}$, with a p^+-strip width w and a strip pitch p, is given by [46]:

$$V_{FD,strips} = V_{FD,diode} \left(1 + 2 \cdot \frac{p}{d} \cdot f(w/p)\right) \tag{4.17}$$

with

$$
\begin{aligned}
f(w/p) = - &\; 0.00111 \cdot (w/p)^{-2} + 0.0586 \cdot (w/p)^{-1} + \\
&+ 0.240 - 0.651 \cdot (w/p) + 0.355 \cdot (w/p)^2
\end{aligned}
\tag{4.18}
$$

The finite pitch and width of a strip sensor increases the full depletion voltage in comparison to a diode. This comes from the fact that the equipotential lines inside the sensor are encircling the strips and start to be parallel to the surfaces only at a depth of about the strip pitch p.

4.3.3.3 Sensor Capacitance

When comparing the capacitance of a fully depleted diode, which in principle is a parallel plate capacitor of size A and thickness d:

$$C_{tot,diode} = \epsilon_0 \, \epsilon_r \cdot \frac{A}{d} \tag{4.19}$$

with the capacitance of a sensor with a segmented strip side [46]:

$$C_{tot,strips} = \epsilon_0 \, \epsilon_r \cdot \frac{p}{d + p \cdot f(w/p)} \tag{4.20}$$

it gets visible, that the effect of the finite pitch and width of a strip detector results in a decrease of the body capacitance C_{tot}.

4.3.4 Spatial Resolution

When an ionising particle passes silicon, the produced e^-h-pairs are initially localised around the particle track within a distance of about $1\,\mu$m. Due to diffusion the charge cloud widens during the drift to the electrodes. The rms-width of the charge distribution σ_D after a drift time τ is given by:

$$\sigma_D = \sqrt{2\,\tau\,D_{diff}} \;\; \text{with} \;\; D_{diff} = \frac{k_B\,T}{e}\,\mu_{e,h} \tag{4.21}$$

where D_{diff} is the diffusion coefficient, e the elementary charge, k_B the Boltzmann constant, T the temperature and $\mu_{e,h}$ the mobility of the free charge carriers. σ_D is equal for electrons and holes, since $D_{diff} \propto \mu_{e,h}$ and $\tau \propto 1/\mu_{e,h}$. Equation 4.21 shows that the width of the charge distribution increases with the drift time. When assuming analogue readout, measuring the heights of the signals, this is a positive effect, because it is then possible to take advantage of charge sharing between

neighbouring strips and the centre of gravity of the charge distribution can be calculated. Therefore the resolution of a strip sensor increases when the charge can be seen by two or three strips and spatial resolutions in the order of μm get possible.

The defining parameter for the spatial resolution of a silicon strip sensor is the pitch p of its p^+-strips. The binary or digital resolution of a sensor, when the created charge can only be seen by one readout strip, is:

$$\sigma_x \sim \frac{p}{\sqrt{12}} \text{ with position: } x \qquad (4.22)$$

But when the charge is visible by more strips, the measurement of the signal heights h_i at the strip positions x_i allow the calculation of the centre of gravity of the charge distribution. The obtainable resolution then scales with the signal to noise ratio S/N of the sensor [47]:

$$\sigma_x \sim \frac{p}{S/N} \text{ with position: } x = \frac{\sum h_i x_i}{\sum h_i} \qquad (4.23)$$

The size of the readout pitch is limited, not only by geometrical reasons but also because more readout strips need more electronic readout channels, needing more power and cooling and therefore increasing the material budget and the costs of the silicon detector system. One possibility to increase the resolution without increasing the number of readout channels is the use of so-called intermediate strips. These are intermediate p^+-implants between the readout strips, which improve the resolution by capacitive coupling. This is discussed in more detail in chapter 6, where the spatial resolution of different sensors with a readout pitch of $50\,\mu$m, including different numbers of intermediate strips, are investigated.
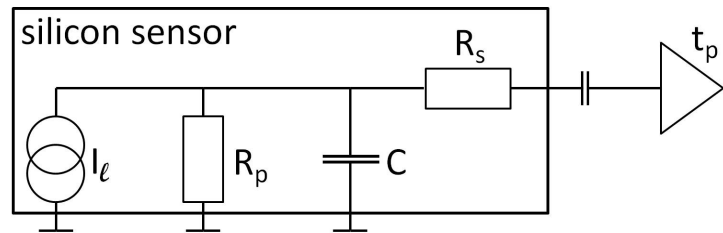
4.3.5 Electrical Noise

Fig. 4.5: Noise sources of a readout strip in a silicon detector including that of the readout amplifier.

As described in the previous section, the electrical noise of a silicon detector directly influences the obtainable spatial resolution. Since the signals produced by ionising particles are very small, it is important to know the contributions of each

effect in detail to allow the optimization not only of the sensor design, but of the whole system.

Noise is mostly expressed as Equivalent Noise Charge (ENC) which gives the number of electrons that contribute to the noise and is composed of different effects:

$$ENC = \sqrt{ENC_C^2 + ENC_{I_\ell}^2 + ENC_{R_p}^2 + ENC_{R_s}^2} \qquad (4.24)$$

Obviously only the parts connected to the readout electronics contribute to the noise of the specific channel, as sketched in figure 4.5:

- **strip capacitance**
  The main part of the electronic noise is caused by the capacitive load of the readout strip C, connected to the readout electronics:

$$ENC_C = a + b \cdot C \qquad (4.25)$$

  where a and b are preamplifier-specific parameters. The total strip capacitance C is composed by of the interstrip capacitance C_{int}, the coupling capacitance C_{ac} and the backplane capacitance C_{back}.

- **shot noise from leakage current**
  The leakage or dark current I_ℓ of the silicon sensor contributes to the noise with the peaking time t_p of the readout chip:

$$ENC_{I_\ell} = \frac{\mathfrak{e}}{2}\sqrt{\frac{I_\ell \cdot t_p}{e}} \qquad (4.26)$$

  where $\mathfrak{e}$ is the Euler number and e the elementary charge.

- **parallel thermal noise**
  The bias resistor of each strip contribute to the noise with

$$ENC_{R_p} = \frac{\mathfrak{e}}{e}\sqrt{\frac{k_B\,T \cdot t_p}{2\,R_p}} \qquad (4.27)$$

- **serial thermal noise**
  The serial line noise of the strip is dominated by the resistance of the metal strip overlaying the p$^+$-strip:

$$ENC_{R_s} = \frac{\mathfrak{e}\,C}{e}\sqrt{\frac{k_B\,T \cdot R_s}{6\,t_p}} \qquad (4.28)$$

Therefore the signal to noise ratio can be increased by:

1. increasing the parallel resistance

2. decreasing the leakage current of the sensor

3. decreasing the series resistance

4. decreasing the load capacitance which is proportional to the length of the sensor strips

Furthermore, the design choices are significantly influenced by the frequency dependence, defined by the readout method. One example for the different needs on the noise contributors at detectors used for different particle accelerators is the shaping time of the readout. Detectors at the International Linear Collider (ILC), will use a comparable long shaping time, which will be sensitive to low resistor values and shot noise from leakage current. On the other side, detectors at the LHC need very short shaping times of 50 ns to cope with the high bunch crossing rate and therefore the noise is maximal affected by the contribution from the load capacitance. Also the operating temperature T is an important factor for both the leakage current and thermal noise of the serial and parallel resistors.

Chapter 5

Baseline Choices for the Silicon Strip Detectors

This chapter explains the baseline design and possible future improvements of the silicon strip detectors, as proposed for the silicon tracking system of the ILD. The basic design choices for the sensors are based on the experiences gathered during the design and quality assurance of the silicon strip sensors that are currently used in the CMS experiment, which was also subject of my diploma thesis [48]. Due to the different requirements at the ILC some adjustments are introduced, as for example the much higher bias resistors needed to operate up to five daisy-chained sensors in one detector. Based on these design choices two different types of prototype sensors were designed, which were used in the two test beam experiments described in the chapters 6 and 7. The silicon detectors developed for the LP experiment, see chapter 7 for details, are a first prototype for the silicon double layers and, although build with state of the art technologies, verify that the requirements on the silicon layers in terms of radiation length can be met. Nevertheless some possible future improvements for the design of the detectors are also illustrated, which are subject of ongoing R&D activities.

The principal duty of silicon strip detectors in high energy physics is the very precise and efficient measurement of charged particle tracks, ideally without any disturbance of the track itself. This requires the optimization of the following parameters: low noise, high signal, low mass, fast response, low power and high radiation tolerance. Unfortunately some of these requirements point towards opposite directions, like for example, the reduction of mass and high radiation tolerance can be achieved with thin detectors, which on the other hand provide a low signal that demands low noise which can be established when using higher power, which introduces additional mass in cabling and cooling and therefore more mass. Although most of the requirements are similar, the optimization of silicon strip detectors is not a general task, but something which is specific for each single experiment in high energy physics. The most crucial requirements for the silicon strip detectors of the ILD tracking system are the high resolution and the minimisation of the material budget.

5.1   Silicon Sensors

In the last years a baseline sensor design for the ILD tracking system has been established within the Silicon tracking for the Linear Collider (SiLC) collaboration [34]. It is used for the production of test sensors and eases the comparison of different sensor vendors. These parameters are called baseline design because they describe only the electric parameters, leaving the process parameters up to the producer. For the ILD tracking system it is anticipated to use, as far as possible, the same sensor technology for the SIT, SET and ETD, described in section 3.

Sensor Material

The base material of the sensors will be float zone silicon with a $\langle 100 \rangle$ crystal lattice orientation. It was verified in test beams, mainly performed during the CMS R&D phase, that $\langle 100 \rangle$ - silicon, in comparison to $\langle 111 \rangle$ - silicon, shows decreased detector capacitances and a smaller increase of the full depletion voltage after irradiation, as described in [49] and [50].

The sensor material is agreed to be p - on - n silicon, implying p^+ - doped strips implanted into an n - doped bulk material. The bulk material should have a high resistivity of approximately $5 - 10\,\mathrm{k\Omega cm}$ to ensure a full depletion voltage of below $100\,\mathrm{V}$.

Sensor Size

For the moment the standard sensors are processed on 6 inch wafers, allowing a maximal sensor size of $95.5 \times 95.5\,\mathrm{mm^2}$. Nevertheless it is possible that the final sensors will be processed on 8 inch or even 12 inch wafers, depending on availability and costs at the time the mass production will start.

Sensor Thickness

To minimise the material budget of the silicon layers the silicon sensors should be between $100\,\mu\mathrm{m}$ and $300\,\mu\mathrm{m}$. The lower limitation comes from the fact that ionising particles traversing less silicon produce less signal and therefore the signal to noise ratio and the spatial resolution is reduced. Also the rigidity of the silicon sensors has to be considered, because thicker sensors assist more to the support of the silicon detectors.

Single Sided

Single sided sensors give only one dimensional information, but their production is much cheaper compared to double sided sensors, described in section 5.3.7. This is the reason why for the large surface of the Silicon External Tracker, which is about $54\,\mathrm{m^2}$, two layers of single sided sensors will be used. For the Silicon

Internal Tracker this decision was not made and must be verified with full detector simulations. One requirement for the single sided sensors is, that the bow of the sensor, originating from the single sided processing, is less than $100\,\mu$m.

Readout Pitch

A readout pitch of $50\,\mu$m is chosen as a compromise between the need for the best possible spatial resolution and the increased complexity of the detector assembly for small pitches. In the test beam campaign described in chapter 6 it was evaluated, that sensors with a readout pitch of $50\,\mu$m, with one intermediate strip in between, can provide a spatial resolution of below $6\,\mu$m. As investigated in chapter 9 this resolution is sufficient to ensure the required transversal momentum resolution with the ILD tracking system.

AC-Coupled Sensors

Although DC-coupled sensors require lesser steps in the production and are therefore cheaper, AC-coupled sensors are beneficial because they protect the amplifier of the readout electronics from the leakage current of the sensor. In AC-coupled sensors the p^+-strips and the aluminium readout lines are separated by a dielectric layer which forms the integrated capacitor between the bias circuit and the readout circuit. Deviating from figure 5.1 it is proposed to use the same sandwich design of silicon dioxide SiO_2 and silicon nitride Si_3N_4 as used for the CMS sensors. The inclusion of the Si_3N_4 is utterly important to improve the mechanical behaviours of the sensor, because pure SiO_2 is too brittle and even small mechanical faults in the dielectric layer can lead to electrical problems [51].

Bias Scheme

There are three different possibilities to bias the p^+-strips of an AC-coupled sensor, as displayed in figure 5.1: poly-silicon, punch-through (PT) and FOXFET technique. For the LHC experiments poly-silicon resistors where used to bias the p^+-implants because this technique can withstand higher radiation doses than the other, and is therefore the current standard. PT and FOXFET techniques are easier to produce and since radiation hardness is not an issue, except for the very forward regions of the ILC detectors, they will be evaluated.
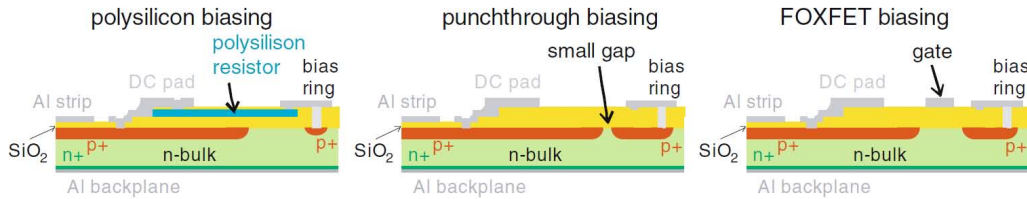

Fig. 5.1: Biasing schemes for AC-coupled silicon strip sensors [3].

The bias resistors of daisy‑chained sensors are connected in parallel and, due to the advantage regarding the material budget, up to five sensors will be daisy‑chained in one silicon detector. Therefore very high values for the bias resistors, in the order of $20-50\,\mathrm{M\Omega}$, are needed for all three biasing schemes.

Dark Current

The beam structure of the ILC allows for long shaping times and therefore the detector noise is mostly influenced by the leakage current of the sensors. To ensure a good signal to noise ratio the silicon sensors must have a very low dark current of below $1\,\mathrm{nA}$ per strip.

Aluminium Thickness

To ensure that the aluminium metallisation of the electrodes has only a small contribution to the noise, its resistance must be low and the aluminium layer is required to be greater than $1{,}2\,\mu\mathrm{m}$.

Metal Overhang of the Aluminium

It is foreseen to make the aluminium, covering guard and bias rings and the p^+‑strips of the sensor about $15\,\%$ wider than the width of the implants underneath. This design significantly increases the HV stability of the sensor because it moves the maximum electric field density from the silicon into the dielectric layer. Due to the small number of free charge carriers the dielectric layer has a much higher breakdown voltage than the silicon.

Bias Ring

As sketched in figure 4.3 the bias ring surrounds the whole active area of the sensor and ensures that all individual isolated p^+‑strips are on the same potential. The different biasing schematics for AC‑coupled sensors used to connect each strip individually to the bias ring are shown in figure 5.1.

Multi Guard Ring Structure

Multiple guard rings are foreseen to surround the bias ring. The aluminium rings on the surface are directly connected to implanted p^+‑rings, with the same doping concentration as the strip implants, by multiple vias in the dielectric layer. This structure shapes the field inside the sensitive area so that also the p^+‑implants at the edges of the sensor have a homogeneous potential. It is either possible to connect the guard rings to a certain potential or to use one or more of these rings floating to discretely adapt the potential, which is important especially for high depletion voltages. Studies are ongoing to minimize the area needed and to design so‑called edgeless sensors, as described in section 5.3.2.

Reference Marks

In the non‑active region on the front side of the sensor a series of reference marks will be drawn for assembling and mechanical survey purposes. A consecutively numbering of the readout strips helps to find specific strips under the microscope, which is important when a specific readout strip has to be disconnected from the readout electronics.

n^+‑doped Edge

To reduce the sensibility of the silicon sensor edges to cracks caused during the cutting of the silicon wafer an n^+‑implant is introduced along the edges of the sensor. This design prevents the space charge region inside the sensor from reaching the cutting edge and protects the active area from charge injections originating in this heavily damaged region. This n^+‑edge is floating and follows the potential applied to the sensor backplane and is usually connected to the outermost guard ring on the sensor surface.

Sensor Backplane

The backside of the sensors is uniformly metallised with an approximately $2\,\mu$m thick aluminium‑silicon‑alloy which allows to apply the HV bias voltage and ensures a homogeneous potential at the backplane. To provide an ohmic contact between the n‑bulk and the aluminium a several μm thick layer of n^+‑ or even n^{++}‑doped silicon is implemented in between. This layer acts as a barrier for minority carriers coming from the depleted bulk and for majority carriers injected from the metal contact and therefore keeps the overall leakage current very low.

Sensor Passivation

To protect the sensor from mechanical damage and chemical reactions with the environment, the front side of the sensors are covered with a thin layer of approximately $1\,\mu$m thick silicon dioxide. This passivation‑layer must be etched off areas where the metal layer of the sensor has to be contacted, like for example at the bonding pads.

5.1.1   Prototype Silicon Wafer

A 6 inch silicon wafer containing a first large silicon strip sensor prototype and a set of mini‑sensors was designed and developed from HEPHY in collaboration with Hamamatsu Photonics (HPK), Japan. HPK produced a batch of theses wafers which was delivered in October 2007.

The layout of the wafer is shown in figure 5.2. The different test structures surrounding the sensors, labelled with small letters in the left figure, are briefly described below and in more detail in [52] and [53]. The main silicon strip sensors

are used for the Large TPC Prototype experiment at DESY and are described in detail in chapter 7. The "Test AC" sensors are described in chapter 6 and were specially developed for a test beam campaign organised to determine the ideal strip geometry for silicon strip sensors with a readout pitch of $50\,\mu$m. The "Test DC" sensors have the same geometric layout as the "Test AC" sensors, except that the aluminium readout strips are DC-coupled and not separated from the p^+-implants by a dielectric layer. This has the advantage of a cheaper production, but has the problem that the readout chips see the total strip current which increases the demands on the readout chip. These sensors are foreseen to be used with readout chips developed for this biasing scheme. The other two mini sensors were designed with the two other AC-coupled biasing techniques, namely FOXFET and punch-through, explained in figure 5.1. These can be used to compare them with the standard poly-silicon biasing scheme used for the "Test AC" sensors. As subject of this work only the main and the "Test AC" sensors were examined in detail and used in test beams.
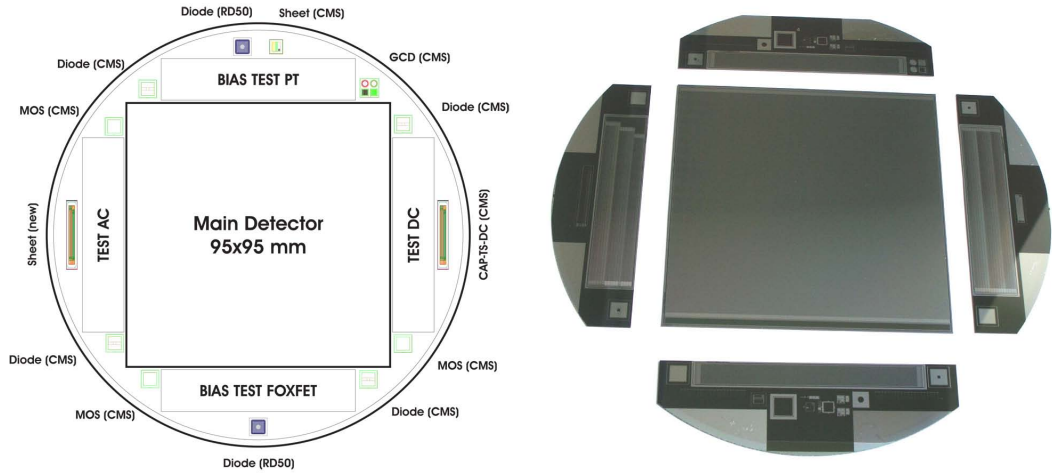
Fig. 5.2: Prototype silicon wafer containing different test structures and sensors - left: schematic with labelled components, right: photo of the wafer after cutting.

5.1.2 Test Structures

The silicon wafers containing the silicon sensors host additional devices, so-called test structures, as indicated in the left picture of figure 5.2. These structures are designed in a way, that they only occupy very small areas on the wafer, which are not used for the actual sensor. Their layouts enable the measurement of sensor parameters which are not accessible at the strip sensor or involve destructive tests and irradiation campaigns. These structures are an essential tool to assess the quality of the manufacturing process during the commissioning of a new vendor and to monitor the quality of the wafers during mass production, as needed for the construction of a large scale tracking system. Such test structures were extensively

used for example during the production of the silicon strip tracker of CMS, as described in [51]. These test structures were adopted from CMS and reworked and improved at the HEPHY, as described in [54]. As initially desired, these test structures found acceptance in the high energy physics community and are now used for a variety of production runs involving different manufacturers which allows the comparison of the different vendors. The following list shortly describes these test structures and the accessible sensor parameters:

- Sheet (CMS)
  It contains nine superficial structures, namely three implant strips, three aluminium strips and three poly‑silicon resistors. They provide access for resistivity measurements of the implanted and deposited materials.

- GCD (CMS)
  This structure contains four Gate Controlled Diodes which are built of comb‑shaped p^+‑ implanted strips intertwined with comb‑shaped metal‑oxide‑semiconductor strips. By measuring the leakage currents conclusions about oxide contaminations can be drawn. The improved version, not implemented on this wafer, contains only two GCDs with larger surfaces which increase the reverse bias current and therefore the measurement reliability of the extracted signals.

- Diode (CMS)
  A simple diode, surrounded by one guard ring, enables the measurement of the full depletion voltage and the bulk resistivity.

- Diode (RD50)
  Similar to "diode (CMS)" with altered design to ensure high voltage stability during irradiation tests with very high doses. These changes were developed within the RD50 collaboration [55] and include rounded corners, multiple guard rings and the introduction of metal overhangs.

- Cap‑Ts‑DC
  On this device the interstrip resistance R_{int} can be measured with high accuracy. It contains nine strips with the same layout as used on the main sensor with the difference that they are not connected to the bias line and therefore completely isolated.

- MOS (CMS)
  By applying a rising bias voltage to its backplane of this Metal‑Oxide‑Semiconductor device it is possible to measure the flatband voltage. With the help of this structure it is possible to measure the trapped positive charges in the oxide and its thickness.

- Sheet (new)
  Similar to the "sheet (CMS)" with two improvements: the length of the

aluminium meanders was increased to raise the absolute resistance and ease the resistance measurements and the contact pad size was increased to enable four‑wire measurements.

- Ts‑Cap
  This structure contains an array of 26 AC‑coupled strips with the same dielectric composition as the main sensor, with the difference that these strips are directly connected to the bias ring. The lack of the bias resistors allows a direct measurement of the coupling capacity of the dielectric layer.

The other structures which can be seen on the photo on the right side of figure 5.2 are test structures designed and used by the manufacturer to monitor the different production steps.

5.2   Front End and Readout Electronics

It is important that the readout system does not degrade significantly the intrinsic detector performance. The requirements on the readout electronics of the silicon strip detectors for an ILC detector are [56]:

- The preamplifier‑specific parameters, compare equation 4.25, must ensure a very low noise. For silicon strips with a capacitance of about $50\,\mathrm{pF}$ the target value for the signal to noise ratio of a Minimum Ionising Particles at a shaping time of $3\,\mu\mathrm{s}$ is 25.

- At the end of each bunch train the chips must provide a continuous stream of loss‑less compressed digital data.

- The readout electronics must be able to use the concept of power cycling, as described in section 5.2.1, to ensure that only a minimum of power is needed.

- To minimise the material budget the chips should be thinned to a minimum.

- The reliability of the whole system must be ensured for the lifetime of the experiment for all channels.

5.2.1   Power Cycling

When looking at the beam structure of the ILC, displayed in figure 2.3, it is clearly visible that there are only short periods where data taking is necessary. For the detectors it is in principle only required to be active during the short periods of $1\,\mathrm{ms}$ where collisions take place, while they could be switched off during the long periods of $199\,\mathrm{ms}$ in between. Following this idea it is possible to reduce the integrated power consumption of the readout chips by a factor of up to 200. One of the biggest problems is the introduction of mechanical oscillations. These could be minimised when the chips, or even channels, are not switched on and off all at

the same time but individually by introducing different delays. Unfortunately this leads again to a longer operation time of the electronics and reduces the savings in the power consumption.

The analogue and digital part of a readout chip enabling power cycling must be separated and individually operable. The signals are processed in the analogue part, which comprises amplifier, shaper and analogue pipeline. The digital part is necessary for monitoring and configuration purposes and, if desired, for the digitisation of the signals which would avoid the delivery of the analogue signals to the off-detector electronics.

5.2.2 Current Development

Within the SiLC collaboration a set of new readout chips, together with the associated readout electronics, are currently under development. The first test chip, SiTR-180, was produced in 180 nm CMOS technology and has been positively tested [57]. Results have been encouraging concerning the main specifications such as noise and power. The power consumption of the pre-amplifier and the shaper is 0.3 mW/channel, proving that a power dissipation below 1 mW/channel, even without power cycling, for the whole system of the front-end chain is achievable.
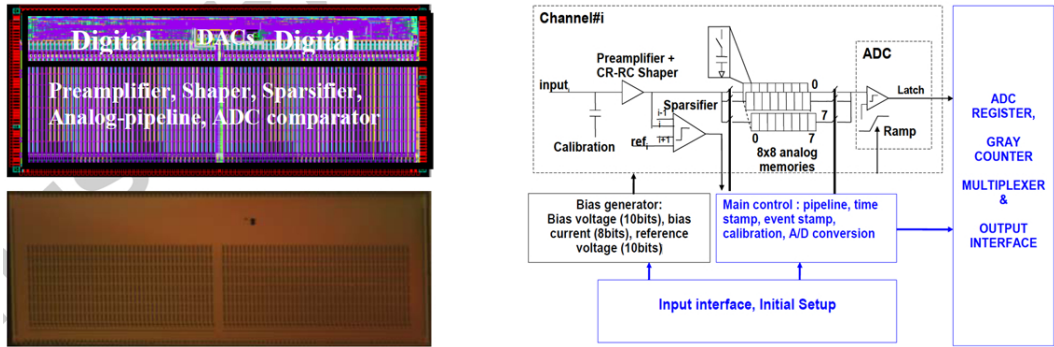
Fig. 5.3: The 88-channel readout chip [58].

Figure 5.3 shows the layout of the SiTr-130 chip, which was already processed using 130 nm CMOS technology and contains 88 readout channels. The two pictures on the left show the layout and a photo of the chip. The right side displays the architecture of one readout channel and its dedicated digital block. This readout chip is at the moment in the prototype stage and was submitted to United Microelectronics Corporation (http://www.umc.com). The chip is a mixed analogue-digital front-end and readout chip that fully processes the analogue signal and has a long shaping time of $1\,\mu$s. On chip digitisation and a high level of digital processing will allow full programmability of the chip. Its total size is $5 \times 10\,\mathrm{mm}^2$, whereof $10 \times 3.5\,\mathrm{mm}^2$ is covered by the analogue part, $1 \times 0.3\,\mathrm{mm}^2$ by the bias generators (DACs) and the remaining space by the digital part. Each readout channel comprises

- a low‑noise charge pre‑amplifier with a gain of 30 mV per Minimum Ionizing Particle (MIP) and a typical signal to noise ratio between 20 and 25

- a pulse shaper capable of operation with shaping times between 0.5 and 2 μs, which allows the use with various readout strip lengths

- a two dimensional structure of an 8×8 analogue sampler, which is capable to store up to eight successive events with eight samples per event

- the analogue sampler is triggered by a sparsifying analogue section which sums up three adjacent channels from the output of the shaper

- finally a 12‑bit parallel analogue‑to‑digital converter (ADC) converts the samples

- the bias conditions of the circuit are controlled by a set of digital‑to‑ analogue converters (DAC)

The digitized samples are read out serially in 40‑bit data words containing charge, time, channel number and event information. The static consumption of the chip was simulated to 1.1 mW per channel in the active mode and 145 μW per channel in the power down mode [58], leading to an integrated power dissipation per channel of about 0.15 mW.

The next generation, a 128 channel‑version on 130 nm CMOS technology will be submitted to a foundry from IBM with a 64 channel‑based modular archi‑ tecture. The total area will be decreased despite more test structures will be implemented. The roadmap for the electronics of the SiLC R&D collaboration includes [35]:

- increasing from 128 to 256 channels per chip

- going from 130 nm to 90 nm CMOS technology

- thinning the chips down to 50 nm

- develop a layout that enables a direct connection of the readout channels to the readout strips of the silicon sensors

5.3   Strategies to minimise the Material Budget

The anticipated material budget of $0.5\,\% X_0$ per silicon layer is easily reachable with the use of 200 μm thick silicon sensors containing integrated pitch adapters, as outlined in section 5.4. This section describes the state of the art technologies and some future improvements which are an issue of ongoing R&D tasks to decrease the material budget of the ILD silicon tracking system.

5.3.1 Long Readout Strips

To make the material budget as small as possible it is obvious that the readout strips of the silicon sensors should be as long as possible. With increasing length of the strips the overall number of needed electronic channels decreases. Fewer channels not mean less material but also less power, leading to a decrease in the amount of cables and the need for cooling.

5.3.1.1 $r\varphi$ - Measurement

For the silicon sensors resolving the $r\varphi$ - coordinate, containing strips parallel to the z - axis, it is rather straight forward to form long readout strips by connecting the readout strips of a few sensors and read out the combined strip length. The maximal strip length, defined by the number of such daisy - chained sensors, is dictated by the signal to noise ratio and the particle density at the radius of a given layer. For such a configuration it is important to choose big enough values for the bias resistors, because the resistors of the combined strips are connected in parallel. The design of such long sensor ladders should also foresee a sensor overlap, as visible in figure 5.6, so that the whole ladder surface is sensitive to traversing particles. For the $\text{SIT}_{r\varphi}$ - layer it is anticipated to use up to five daisy - chained sensors, providing readout strips with a length of close to 50 cm.

5.3.1.2 z - Measurement

As evaluated in section 9.4, a spatial resolution of $50\,\mu\text{m}$ is sufficient for the z - coordinate. This can be obtained with sensors containing strips arranged orthogonal to the z - axis with a readout pitch of $200\,\mu\text{m}$, containing one intermediate strip, as determined in [59]. Even larger readout pitches could be possible, which is beneficial because a large pitch effectively reduces the number of needed readout channels.

The use of daisy - chained sensors for the resolution in z is not as easy as for the resolution in $r\varphi$ and different possibilities have to be evaluated:

Stereo Angle

In former silicon tracking systems the z - coordinate was measured with silicon detectors containing sensors which were tilted by a stereo angle α with respect to the z - axis. For example for the CMS tracker a stereo angle of $5.73\,°$ for the strip sensors measuring the second coordinate was used. The size of this angle determines not only the maximal number of daisy - chained sensors usable for a given radius, but also the spatial resolution along the strip axis, as described in section 9.6. To provide a spatial resolution of $50\,\mu\text{m}$ in z, a sensor with a nominal resolution of $6\,\mu\text{m}$ must be tilted by at least $9.7\,°$. Because of the small available space, even with the use of such high resolution sensors, for the SIT_z - layer it is very challenging to use this concept even for two daisy - chained sensors.

Convex Ladder

Another possibility would be to develop a technique that allows the production of convex silicon ladders, where the readout strips of the sensors are connected with wire bonds "round the corner". Such a wire bonding "round the corner" should in principle be possible with the development of a luffing bonding jig. Nevertheless the production of such ladders would be quite tricky, and maybe too difficult for mass production.

Second Metal Layer Routing

Maybe the best solution would be the design of silicon strip sensors with an implemented second metal layer, as visible at the top surface of the sensor illustrated in figure 5.7. This second metal layer is located on top of the first metal layer, the aluminium readout strips of the sensor, and isolated by an additional dielectric layer. Its aluminium strips are arranged orthogonal to the readout strips of the first metal layer. Each strip of the second metal layer is connected by a via to exactly one strip of the first layer and routes the signals to the sensor sides parallel to the first layer strips. The disadvantage of this concept is the cross‑talk between the routing lines and the crossed readout strips underneath, which can degenerate the signal quality. To minimise this effect a very thick dielectric layer between the two metal layers is needed, which is very challenging in the sensor production. This concept was already successfully used for single strip sensors, as for example at the DELPHI microvertex detector [60] and the BELLE silicon vertex detector [61].

With such a second metal layer routing it would be possible to transfer the signals of one sensor over the second metal layer of another sensor. Then, when assuming a sensor readout pitch of $200\,\mu$m and a pitch of $50\,\mu$m for the second metal strips, four daisy‑chained sensors can be connected to one set of readout chips. The disadvantages of this concept are the need of four different sensor geometries, because of the different second metal layer routings, and the increased noise caused by the longer strip lengths. This increases not only the costs of the sensor production, but also the single strip resistance and the capacitive load connected to the channels of the readout chips. On the other hand this concept solves all technical problems for the use of long readout strips for the measurement of the z coordinate.

5.3.2 Edgeless Sensors

Standard silicon strip sensors have a multi guard ring structure surrounding the active sensor area to smooth the electric fields, which is also called Voltage Terminating Structure (VTS) and displayed in figure 5.4. The idea of so‑called edgeless sensors is to reduce this inactive area to the absolute minimum. Ideally these sensors are sensitive to the edges, which would allow to mount the silicon sensors seamlessly without the need for overlaps. This would ease the design and
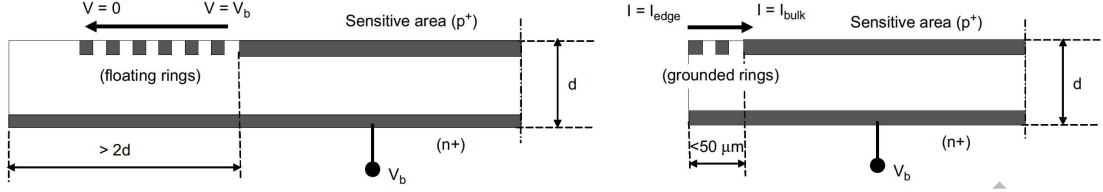
Fig. 5.4: Voltage terminating structure (left) and current terminating structure (right) [62].

production of the detectors and the whole tracking system and allow to reduce the material budget. For example, with the introduction of Current Terminating Structures (CTS) instead of the traditionally used VTS the inactive band at the sensor edges can be reduced from about 2 times the sensor thickness d, as needed for VTS, to less that $50\,\mu$m, as shown in figure 5.4. Although, the performance of devices using the CTS has been confirmed in many tests, studies are ongoing to investigate the origin of key properties, such as the potential distribution across the cut side of the detectors sensitive edge, as described in [62].

5.3.3 Thinning the Sensors

The most obvious thing to reduce the material budget is the use of very thin silicon sensors, which is the main contributor. The biggest problem is that the signal of the sensor scales linearly with its thickness. A reduction of the sensor thickness worsens the signal to noise ratio and thus the spatial resolution of the sensors, as visible from equation 4.23. Since there are no technologies for the direct production of ultra-thin wafers, handle wafers have to be used or standard wafers with a thickness around $300\,\mu$m have to be thinned. Another problem for sensors thinner than $100\,\mu$m is that they get bendable and additional support structures are needed. One approach to solve the rigidity problem is the use of a thinning procedure based on the Silicon On Insulator (SOI) wafer bonding technique, which was developed at the MPI Semiconductor laboratory [63]. Here the active areas of the silicon sensor can be etched down to $50\,\mu$m while a surrounding "handle frame" of thicker silicon ensuring mechanical stability.

5.3.4 Forced Gas Cooling

At former experiments the cooling system, needed to keep the silicon sensors at feasible temperatures, is one of the major contributors to the material budget. For the ILD tracker the goal is to avoid a dedicated liquid cooling system, and to use a forced gas system. This is possible at the ILC for two reasons, the beam structure of the machine and the low radiation level. The bunch structure of the ILC allows the concept of power cycling, described in section 5.2.1, which foresees that the majority of the devices are not constantly powered, but only during the short periods they are needed. This concept reduces the integrated

power consumption and therefore the need for cooling. Due to the relative low radiation levels at the ILC, it is possible to operate the silicon sensors at room temperature. This immensely reduces the demand on cooling when compared to the LHC experiments, where, due to the high radiation, the silicon sensors must be cooled to a temperature of -10°.

The total integrated power dissipation of the ILD silicon tracking system can be approximated as follows. When we assume an integrated power dissipation of 0.15 mW per readout channel, which is anticipated with the newly developed readout chip described in section 5.2.2, and use the values for the number of readout strips as approximated in section 3.2.2, summing up to 4.3 million channels in the barrel part and 1.2 million channels in each forward region, we get a total integrated power consumption of about 640 W in the barrel and 175 W in each end-cap. This is over a factor 60 smaller than the power consumption of the CMS tracker, which is in the order of 60 kW [64]. This could even be lowered with the use of the 1024-channel KPiX chip as described in [65], which has a power consumption of only 20 mW per chip, or 0.02 mW per channel.

However, more detailed studies have to be made, especially regarding the possible oscillations introduced by the air flow and also the switching of the analogue power of several thousand readout chips.

5.3.5   Integrated Pitch Adapter
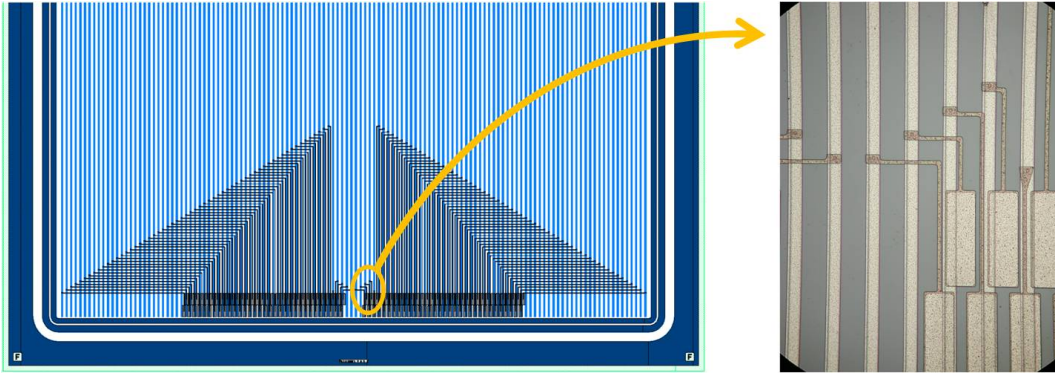
Fig. 5.5: Silicon strip sensor with integrated pitch adapter.

As shown in table 5.2, one glass pitch adapter, used to connect the readout pitch of the sensor to the readout pitch of the readout chips, increases the material budget of a detector containing two daisy-chained sensors by about 4.3%. Since the radiation length is averaged over the sensor surface this influence decreases with the number of sensors. With the introduction of a second metal layer on top of the aluminium readout lines of the sensor it is possible to integrate the pitch adapter into the sensor and make an external pitch adapter obsolete. This not only decreasing the material budget, but also halves the needed amount of wire bonds. A first run of test-sensors with integrated pitch adapters was designed by

the HEPHY and produced at ITE Warsaw[1] [66]. Figure 5.5 shows one of these silicon strip sensors, where the pitch adapter is integrated on a second metal layer (dark blue). The additional metal layer used for signal routing is isolated from the aluminium readout lines by a second dielectric layer, except for small via connections.

A first test beam with detectors containing these sensors was performed at CERN. The results were compared to test‑sensors with similar layout, but without second metal layer and the use of a "traditional" glass pitch adapter, and described in [53]. For such a design, careful attention has to be taken on signal loss and cross‑talk introduced by the signal routing.

5.3.6   Chip on Sensor
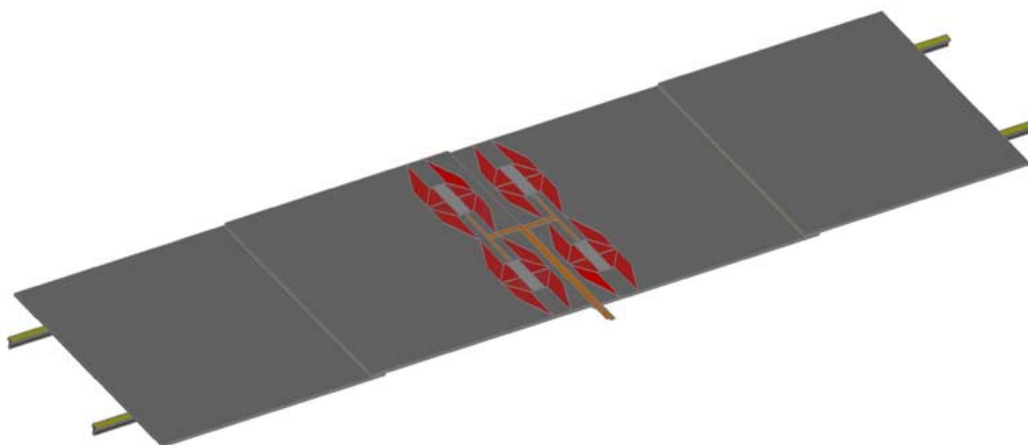
Fig. 5.6: Chip on sensor schematic.

With the introduction of an integrated pitch adapter, it is also possible to directly mount the readout chip onto the silicon sensor. The chip on sensor concept reduces the radiation length by about 20% compared to a detector module with pitch adapter and front‑end hybrid, as outlined in table 5.2. In this concept, special care has to be taken on the heat dissipation of the chip to the sensor and the capacitive couplings.

Figure 5.6 shows a conceptual drawing of two such highly integrated silicon detectors, each consisting of two silicon strip sensors. The high density readout chips (light grey) are directly bump bonded on top of the sensors with an integrated pitch adapter (red) that connects the readout channels of the chips with the strips of the silicon sensor. The power and control lines are brought to the readout chips with the help of thin Kapton foils (orange) with integrated signal lines, which can be glued directly onto the sensor. The same Kapton foils can be used to route the data of the chips to external front‑end electronics for further processing. In the

[1]Instytut Technologii Elektronowej, Al. Lotnikow 32/46, 02-668 Warszawa

drawing one additional silicon strip sensors is daisy-chained to each of the sensors containing the integrated pitch adapter. In the SET it is foreseen to connect up to five sensors to decrease the needed number of electronic readout channels. The silicon sensors are arranged with an overlap, which is necessary to avoid gaps between the sensitive sensor regions when conventional and not edgeless sensors are used.

Using Wire Bonds

To connect the sensor to conventional readout chips via wire bonds, a thin layer of thermally and electrically isolating material is needed between the chips and the sensor. Such a design was already proven by studies with the so-called origami prototype module [67], developed for the upgrade of the BELLE II experiment at KEK in Tsukuba, Japan.

Using Bump Bonds

With the so-called flip-chip technique it is possible to connect a readout chip face-down directly onto the bond pads of the sensor with the help of tiny solder balls. This technique is very challenging and till now was only used for pixel sensors. A drawback of this method is that the sandwich compound cannot easily be repaired but would give the advantage that the connections cannot be destroyed by handling failures, which was a non negligible problem during the production of the silicon detectors for the CMS tracker end-caps. During this production the wire bonds on 6 % of the total assembled detectors were damaged by handling failures, as described in [48].

5.3.7   Double Sided Silicon Sensors

It is possible to also implement readout strips at the backside of a silicon sensor. Such double sided silicon strip sensors give two dimensional information about a traversing ionising particle. The advantage is, that the number of silicon sensors needed to measure two coordinates halves. The drawback is the much more expensive sensor production, since a processing of both sensor sides is needed and all planar process machines in industrial semiconductor production are designed for single-sided processing only. Thus the complexity in the production rises and lowers the production yield.

Figure 5.7 shows such a sensor with orthogonal readout strips on the sensor backplane. This sensor has an n-bulk with p^+-implants on the bottom side and n^+-implants on the top side. These n^+-strips have to be isolated from each other by p^+-implants surrounding them, so-called p^+-stops. This is necessary, because otherwise an electron accumulation layer builds up between the n^+-strips which electrically connects them. A second metal routing on the top enables that both sensor sides can be read out from the same edge of the sensor.
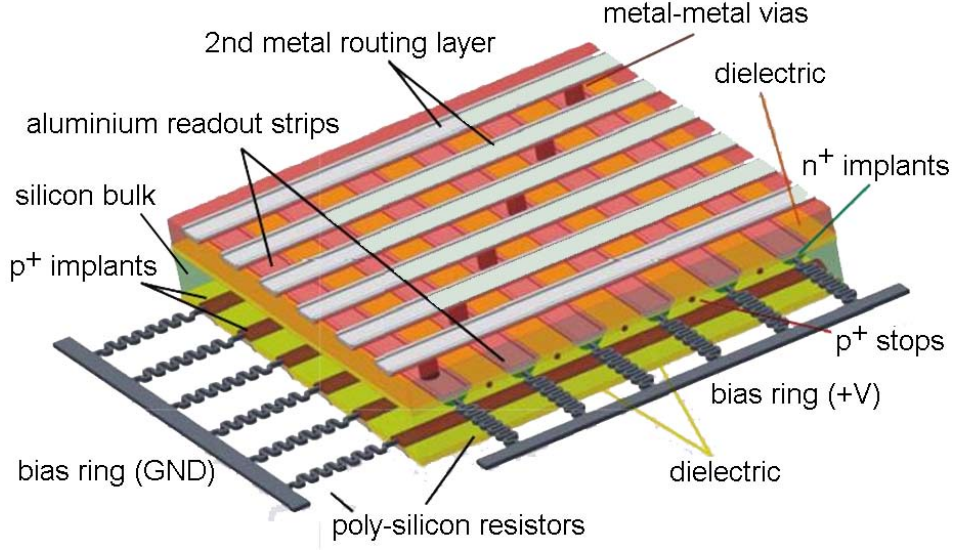
Fig. 5.7: Double sided silicon strip sensor.

5.4   Radiation Length of the Silicon Detectors

5.4.1   Radiation Length of raw Materials

The radiation length of raw materials is only dependant on the atomic number Z and the mass number A of the material, and can be calculated with:

$$X_0 = \frac{716.4 \cdot A}{Z(Z+1) \cdot ln(287/\sqrt{Z})} \; \mathrm{g/cm^2} \qquad (5.1)$$

which is a compact fit to measurements and agrees to better than $2.5\,\%$ with the measured data for all elements except for helium [4].

5.4.2   Radiation Length of composite Materials

For compound materials the radiation length has to be calculated in a weighted sum from the radiation lengths of the elements in the compound $X_{0,element}$:

$$X_{0,material} = \left(\sum_i \frac{\omega_i}{X_{0,element,i}} \right)^{-1} \text{ with the weights } \omega_i = \frac{n_i A_i}{\sum_j n_j A_j} \qquad (5.2)$$

The weight factor ω_i for an element is determined by the molecular composition of the material, where n_i is the isotopic abundance of the specific atom i in the compound molecule and A_i the corresponding atomic number. The weight is normalised by the sum over the whole molecule.

To determine the total radiation length of a device made of different materials, for example a detector layer, one has to sum up the radiation lengths of each involved material $X_{0,material}$. In addition, since the majority of the involved

materials in such an object have different surfaces $A_{material}$, it is only possible to calculate the average radiation length $X_{0,av}$ of such an object:

$$X_{0,av}\,[\%] = \sum_{materials} \frac{100 \cdot d_{material}}{X_{0,material}} \cdot \frac{100 \cdot A_{material}}{A_{total}}\,\% \qquad (5.3)$$

where the radiation length of each involved material is weighted by its individual surface $A_{material}$ and thickness $d_{material}$. A_{total} is the surface of the whole device.

5.4.3   Radiation Length of the used Materials

Table 5.1 displays the radiation lengths of the materials contained in the silicon detector modules as produced for the LP experiment, described in chapter 7.   The

material	X_0 [cm]
silicon	9.37
carbon fibre	23.00
Kapton foil	30.00
hybrid PCB	17.40
copper	1.43
ceramic (AIN)	8.40
araldite glue	23.50
silicone glue	23.50
glass (D263)	12.70
aluminium	8.90

Tab. 5.1: Radiation lengths of the used materials.

elements that make up the materials are not always clear defined by their names. Here is what is used as best guess:

- Kapton is a polyimide: $C_{22}H_{10}N_2O_5$

- the hybrid PCB is assumed to be FR4, which is made of epoxy and glass in the ratio 44:56 by volume

- in the ATLAS [68] collaboration a large number of hybrid flexes were cut and the thickness of layers measured, with the conclusion that the copper layer thickness is around 17 μm rather than the nominal 15 μm

- the araldite glue is treated as phenol epoxy: C_6H_6O

- the silicone glue is assumed to have the same properties as the araldite glue, but in fact it is silicone rubber: SiH_2

material	thickness [μm]	$\% X/X_0$	silicon detector containing one sensor			silicon detector containing two sensors		
			$\sim$ area [mm²]	% of Si area	$\% X/X_0$ (rel)	$\sim$ area [mm²]	% of Si area	$\% X/X_0$ (rel)
silicon	320	0.342	9120.25	100.00	0.342	18240.50	100.00	0.342
carbon fibre ($0.5 \times 3\,\text{mm}^2$)	500	0.217	978.00	10.72	0.023	1548.00	8.49	0.018
carbon fibre ($3 \times 0.5\,\text{mm}^2$)	3000	1.304	163.00	1.79	0.023	258.00	1.41	0.018
araldite glue	2	0.001	978.00	10.72	9.13E-05	1548.00	8.49	7.22E-05
silicone glue	2	0.001	573.00	6.28	5.35E-05	1146.00	6.28	5.35E-05
Kapton foil	100	0.033	4767.00	52.27	0.017	4767.00	26.13	0.009
copper on Kapton	17	0.119	1517.40	16.64	0.020	1517.40	8.32	0.010
hybrid PCB	400	0.230	1500.00	16.45	0.038	1500.00	8.22	0.019
copper in hybrid	17	0.119	377.20	4.14	0.005	377.20	2.07	0.003
six APV25 chips	350	0.374	345.06	3.78	0.014	345.06	1.89	0.007
ceramic supporting hybrid	400	0.476	1950.19	21.38	0.102	1950.19	10.69	0.051
ceramic supporting PA (CMS)	400	0.476	322.50	3.54	0.017	322.50	1.77	0.008
two pitch adapter (D263)	550	0.433	1911.00	20.95	0.091	1911.00	10.48	0.045
wire bonds (Al)	25	0.028	5.86	0.06	1.80E-05	5.86	0.03	9.02E-06
SUM (LP experiment)					0.692			0.530
silicon (200 μm)	200	0.213	9120.25	100.00	0.213	18240.50	100.00	0.213
14 APV25 chips (thinned)	200	0.213	805.14	8.83	0.019	805.14	4.41	0.009
one pitch adapter (D263)	550	0.433	955.50	10.48	0.045	955.50	5.24	0.023
SUM (state of the art)					0.506			0.374
7 SiTr - chips (thinned)	50	0.053	350.00	3.84	0.002	350.00	1.92	0.001
SUM without pitch adapter					0.444			0.342
Kapton to chips	100	0.033	1000.00	10.96	0.004	1000.00	5.48	0.002
copper on Kapton	17	0.119	333.33	3.65	0.004	333.33	1.83	0.002
SUM without hybrid nor PA					0.308			0.274

Tab. 5.2: Estimations for the radial length of the silicon detectors, containing one and two silicon sensors, used for the LP experiment and for possible further detector improvements.

- the glass D263 of the pitch adapters is made of SiO_2, B_2O_3, Na_2O in the ratio 80:12:5 with 3 % other materials, based on the information from Schott GmbH[2]

5.4.4   Radiation Length of the Prototype Detectors

Table 5.2 gives an estimation for the radiation length of the silicon detectors, containing one and two silicon sensors, as used for the Large TPC Prototype experiment described in chapter 7. Due to their minimal thickness and their alikeness in radiation length with the silicon sensor, the aluminium $X_0 = 8.9$ cm, the aluminium oxide Al_2O_3 $X_0 = 7.03$ and the silicon dioxide SiO_2 on the sensor surfaces are neglected. For the six APV25 readout chips, with a size of $7.1 \times 8.1 \times 0.32$ mm^3 each, the radiation length of silicon was used. But, it should be noted that with six APV25 it is not possible to read out all 1792 readout strips of the sensor, but only 768. The detectors contain two different pieces of ceramic (AlN), one supports the CMS hybrid and the other supports the CMS pitch adapter. The column $\% X/X_0$ shows the radiation lengths of the materials of the used thickness and $\% X/X_0$ (rel) shows them normalised to the area of the silicon sensors. The detector containing one and that containing two silicon sensors, which were build for the LP experiment, have a relative radiation length of $0.69 \% X/X_0$ and $0.53 \% X/X_0$, respectively, whereof the radiation length of the sensors are $0.34 \% X/X_0$.

5.4.5   Radiation Length of the Baseline Design

When taking the absence of a liquid cooling system for granted, it is possible, with the state of the art technology, to build the silicon tracking system for the ILD with the required radiation length of $0.5 \% X/X_0$ per layer of silicon detectors. The upper part of table 5.2 gives an estimation for the radiation length of the prototype silicon detectors as used for the Large TPC Prototype (LP) experiment described in chapter 7 and for a state of the art detector. The two different detectors layouts at the LP setup contain one and two silicon sensors with a thickness of 320 μm and, for the reasons explained in chapter 7 also two glass pitch adapters. When we take the detector containing two silicon sensors, remove the unnecessary parts and replace the used parts with state of the art technology, using 200 μm thick sensors, 14 APV25 readout chips, to readout all 1792 readout strips of the sensor, thinned down to 200 μm, as already done at the HEPHY, and only one pitch adapter we get a relative radiation length of $0.37 \% X/X_0$. Now, if we look at a state of the art silicon sensor ladder, containing four daisy-chained sensors, as proposed for the ILD tracking system, the relative radiation length decreases to $0.31 \% X/X_0$. This leaves $0.19 \% X/X_0$ for power and signal cables reaching from the silicon detectors to the outside of the tracking system which should be relatively easy to meet. Of course this is only true if the readout chips are able to operate with the concept of power cycling and forced gas cooling is sufficient.

---

[2]Schott GmbH: www.schott.com

The lower part of table 5.2 shows estimations for the relative radiation length of detectors containing one and two silicon sensor with the introduction of the new technologies described in this chapter:

- With the replacement of the 14 APV25 chips with seven SiTr‑chips, containing 256 readout channels on a size of $5 \times 10 \times 0.05\,\text{mm}^3$ each, and the removal of the external pitch adapter, using a pitch adapter integrated as a second metal layer onto the silicon sensor, we get a silicon detector with a relative radiation length of $0.34\,\%\,X/X_0$. Extending this to a detector containing four daisy‑chained sensors leads to a relative radiation length of $0.30\,\%\,X/X_0$.

- For the ultimate future goal, the chip on sensor concept, without front‑end hybrid nor pitch adapter, but an additional Kapton foil to carry the electrical copper lines for power and signals, the relative radiation length is further decreased to $0.27\,\%\,X/X_0$ for a two sensor detector and to $0.26\,\%\,X/X_0$ for a detector ladder containing four silicon sensors.

When comparing the material budget of detectors containing two sensor with detectors containing four sensors is the reduction in readout channels. Also keep in mind, that these are only estimations and do not include additional support which could be necessary due to the vibrations possibly introduced by power cycling, the gas flow or push‑pull operations.

Chapter 6

Determination of the ideal Strip Geometry

In June 2008 single‑sided silicon strip sensors with a readout pitch of $50\,\mu$m were tested in a high energetic pion beam at the SPS at CERN (www.cern.ch). The goal of this study was the evaluation of the ideal strip geometry for silicon strip sensors with a readout pitch of $50\,\mu$m in terms of spatial resolution. For this purpose sensors with a multi‑geometry layout were designed. The varying parameters, strip width and number of intermediate strips, influence the strip capacitance and the charge sharing ability of the strips, both basic properties that contribute to the spatial resolution of the sensor. The experimental setup and the results are subject of this chapter.

A readout pitch of $50\,\mu$m was chosen, because this is the smallest pitch feasible for large scale module production needed for future silicon trackers, and therefore the proposed pitch for the layers of the ILD silicon tracker which need the highest possible spatial resolution. A smaller readout pitch leads to complications during the integration of the sensors into detector modules, mainly because of the reduced size of the probe and bonding pads.

6.1 Multi‑Geometry Sensors

The multi‑geometry silicon strip sensors were designed at the HEPHY and manufactured by Hamamatsu Photonics, Japan. They are the so‑called "Test AC" sensors which were produced on the wafers described in section 5.1.1.

The sensors are single sided with a thickness of $320\,\mu$m and an active area of $14 \times 64\,\mathrm{mm}^2$. The bulk resistivity of $6.7\,\mathrm{k\Omega cm}$ ensures that the sensors are fully depleted at a voltage below $100\,\mathrm{V}$. The p^+‑implants have a length of $64\,\mathrm{mm}$. The 256 AC‑coupled aluminium readout strips on top of these p^+‑strips have a pitch of $50\,\mu$m and a metal overhang of $2\,\mu$m if the width of the p^+‑strip is a integer number and $2.25\,\mu$m if else. The dielectric structure between the aluminium strips and the p^+‑implants is a superposition of silicon oxide SiO_2 and silicon nitride $\mathrm{Si}_3\mathrm{N}_4$.
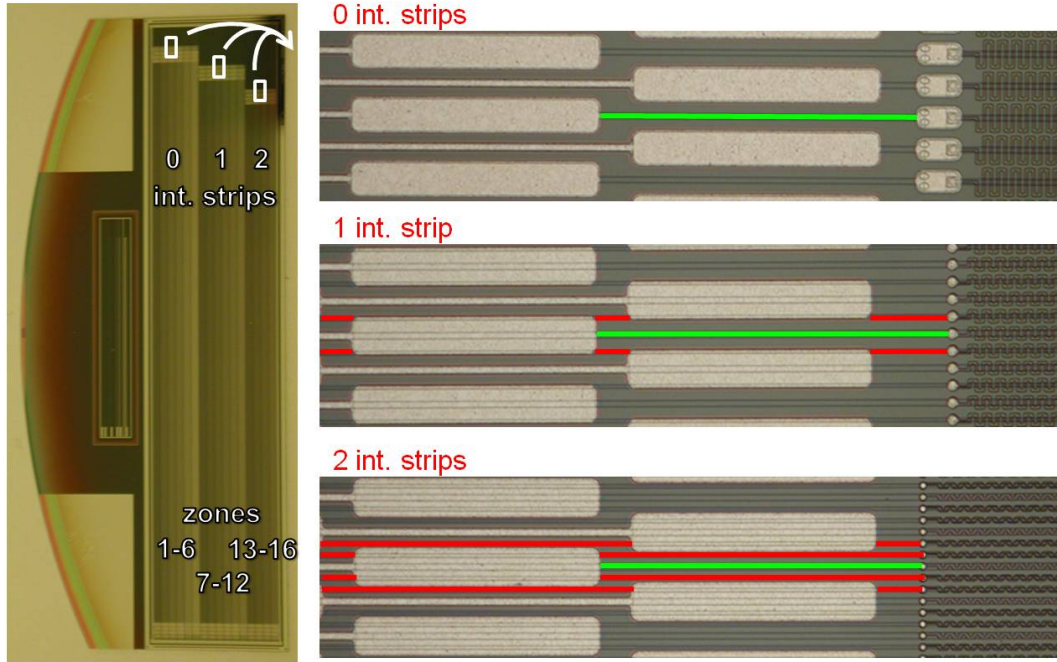
Fig. 6.1: Multi - geometry sensor. The three enlarged cut - outs show the AC - pads and poly - silicon resistors of zones with 0, 1 and 2 intermediate strips (red) between the strips (green) which are AC - coupled to an aluminium readout strip.

There are 16 zones containing p^+- strips with different widths and 0, 1 or 2 intermediate strips, as shown in table 6.1. The intermediate strips are p^+- implants with a constant width of $5\,\mu$m and without aluminium strip on top. The zones are separated from each other by a gap of one missing strip. Each zone consists of 16 readout strips which are individually biased with $20\,\text{M}\Omega$ poly - silicon resistors, clearly visible in the blow - ups in figure 6.1. The resistivity is defined by the length of the poly - silicon, which is shaped in meanders to decrease their effective length. For the three regions with different numbers of intermediate strips, the available width for the poly - silicon meanders is different, leading to different lengths of the aluminium readout strips which are 6.1965 cm, 5.998 cm and 5.733 cm for the zones with zero, one and two intermediate strips, respectively.

The aluminium readout strips can be contacted on both sides via AC - pads, regions where the aluminium is broadened, which are used to connect the sensor strips to the channels of the readout electronics. The p^+- implants below the aluminium are accessible individually via two DC - pad, which are connected to the implants by vias through the dielectric. The p^+- implants of the intermediate strips can be contacted via one very small probe bad also visible in figure 6.1.

strip zone	1	2	3	4	5	6
strip width [μm]	6.0	10.0	12.5	15.0	20.0	25.0
# int. strips	0	0	0	0	0	0

strip zone	7	8	9	10	11	12
strip width [μm]	6.0	7,5	10.0	12.5	15.0	17.5
# int. strips	1	1	1	1	1	1

strip zone	13	14	15	16
strip width [μm]	6.0	7.5	10.0	12.5
# int. strips	2	2	2	2

Tab. 6.1: Zone properties of the multi‑geometry sensors.

6.1.1   Electrical Tests

Prior to the integration of the sensors into detector modules all sensors were electrically tested at the HEPHY setup described in section 7.6.1. The eight sensors showing the best results were assembled and used during the test beam.

IV Measurements

IV‑curves measured up to 500 V showed a stable behaviour for all used sensors far below any critical values, as visible in the left graph of figure 6.2. The IV measurements were the main criterion for the selection of the sensors, since the currents varied and some of the unused sensors showed a current breakdown between 150 V and 400 V.

CV Measurements

The total detector capacitances were measured and, as shown in figure 7.16, from the $1/C^2$ curves the full depletion voltage V_{FD} of the sensors can be determined. The measurements, displayed in the right graph of figure 6.2, revealed full depletion voltages between 50 V and 60 V. This is in good agreement with the measurements done by Hamamatsu Photonics, Japan.

Interstrip Capacities

The interstrip capacities were measured for two different sensors at full depletion, revealing similar behaviours. The measurements were done at the AC‑pads of the aluminium readout strips with the available 4285A Precision LCR Meter in Cp‑Rp mode at a frequency of 1 MHz. As expected and visible in figure 6.3, the interstrip capacities rise linearly with increasing strip width over pitch ratio, which reflects
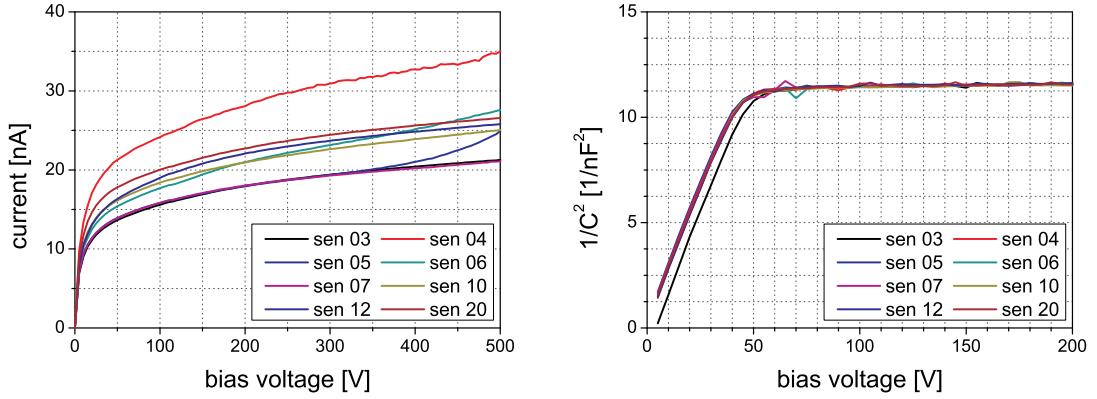
Fig. 6.2: IV and CV measurements of the multi-geometry sensors.

the decreasing distance between the strips. Unexpected was, that the measurements show a varying offset depending on the number of intermediate strips since former measurements of the interstrip capacity for sensors with constant readout pitch and a varying number of intermediate strips did not show this behaviour. For example [59] describes such measurements for silicon strip sensors with a constant readout strip pitch of $200\,\mu$m and 0, 1, 2 and 3 intermediate strips, displayed in figure 6.4. For the regarded multi-geometry sensors, the behaviour most probably comes from the varying overlaps of the bonding pads and the implants, as visible in the blow-ups on the right side of figure 6.1. In the zones with one intermediate strip the aluminium readout pads of two adjacent strips both overlap the same intermediate strip, which increases the interstrip capacity. For the strips in zones with two intermediate strips this is no longer true and the interstrip capacity decreases again.
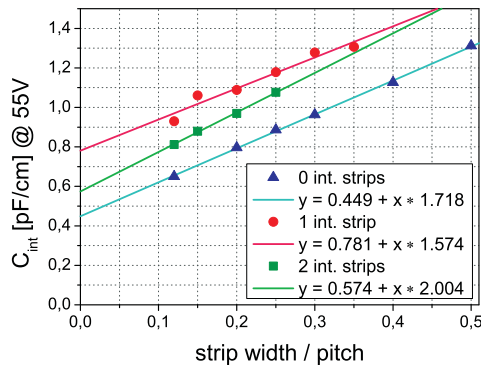
Fig. 6.3: Interstrip capacities of a multi-geometry sensor.
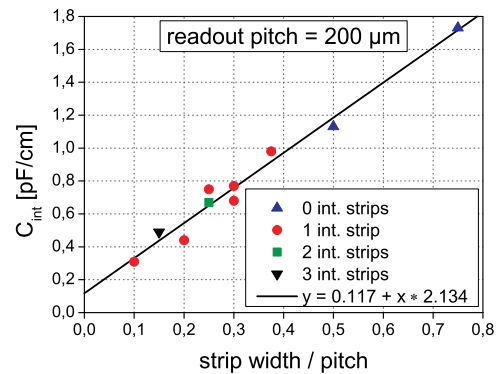
Fig. 6.4: Interstrip capacities of sensors with a readout pitch of $200\,\mu$m [59].

6.2 Detector Modules

In total eight identical detector modules were designed, build and electrically tested in the HEPHY. Each detector module is build of an Isoval®11 support frame and a cover made of the same material, as visible in figure 6.5 and figure 6.6. To minimize multiple scattering and to enable tests with a radioactive source, the support frame and the top cover have openings on the front and back side.
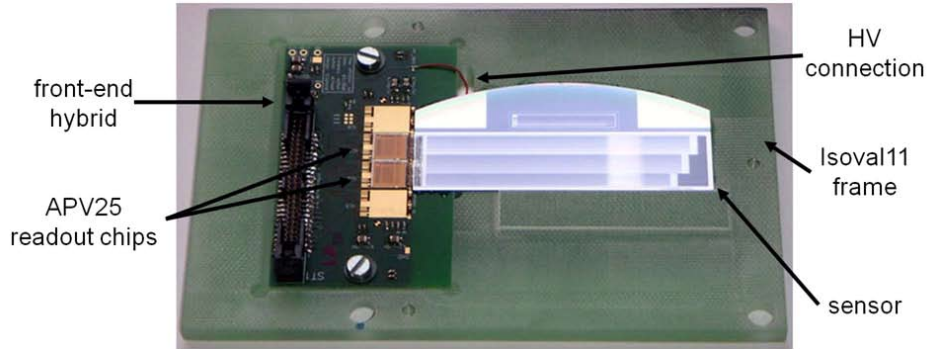
Fig. 6.5: Detector module without top cover.
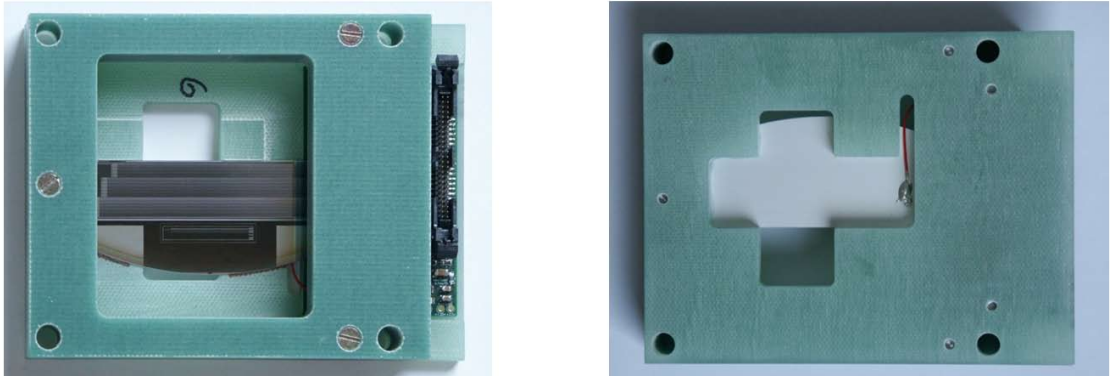
Fig. 6.6: Closed detector module without light‑tight adhesive foil.

The front‑end hybrid can be adjusted in the countersink on the hybrid frame and is fixed with two screws. Although the hybrid, which was also developed at our institute, was designed to carry four APV25 readout chips [69], for the 256 readout strips of the multi‑geometry sensors only two are needed. The sensor is glued to the support frame, which contains a heightened bar to enable a precise alignment of the sensor in the direction orthogonal to the readout strips.

All modules were electronically tested at the HEPHY with the APVDAQ system as described in section 6.3. These tests include IV scans and the measurements of the pedestals and noise of each readout strip. The tests revealed, that there were no faults introduced during the module assembly and that the detector modules are perfectly usable for the test beam.

6.3   Data Acquisition System

For the data acquisition the Vienna APVDAQ system, as shown in figure 6.7, was used. It was developed in the HEPHY to read out the APV25 chip and has proven its reliability in various test beams in the past.

The data of the APV25 readout chips, directly connected to the sensor strips, is read out by the Repeater Boards (REBO) sitting on the so-called DOCK box. Then the data gets transferred via 30 m long cables to two 9U VME Boards housing several FADC modules with built-in processing capabilities, which digitise the data. The 9U VME also contains a single controller (NECO) board and a fan-out unit (SVD3_Buffer). The DAQ PC is connected to the VME crate via a VME controller from National Instruments.

The DAQ PC, running LabWindows, can be used for online monitoring and stores the data. The online monitoring allowed an easy live adjustment of the timing and was especially helpful for the alignment of the sensors with the help of the available xyz-rotation-stage to the correct position inside the beam line.

For the test beam in 2008, the APVDAQ system was adapted to be compatible with the data acquisition of the EUDET pixel telescope [70] and the EUDET Trigger Logic Unit (TLU) [71]. This ensured, that the time stamp and the trigger signals from scintillators, centrally distributed from the TLU to both DAQ systems, could be directly included into the VME hardware of the system.
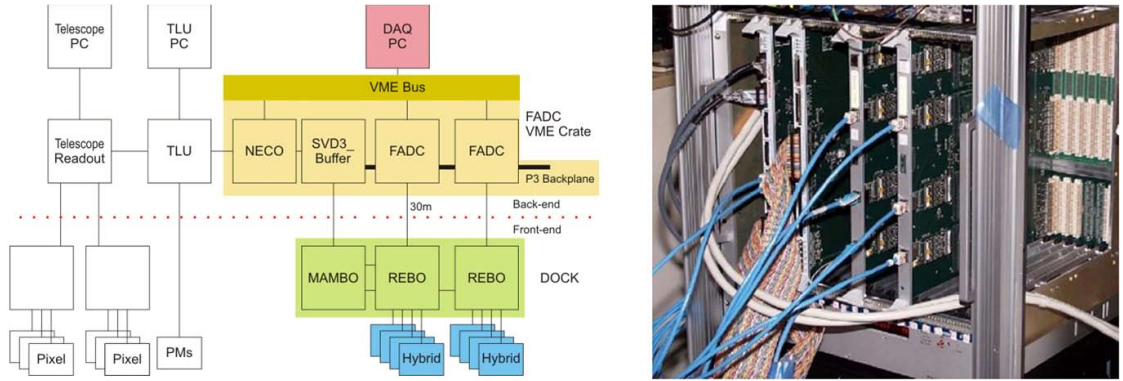
Fig. 6.7: Schematic of the APVDAQ system (left) and picture of the VME crate housing the APVDAQ boards (right).

6.4   Test Beam

The test beam took place from 30.05 - 5.06.2008 at the SPS - H6B area at CERN. For the test beam eight detector modules were screwed together forming a module stack, shown in figure 6.8. The silicon sensor planes are precisely aligned due to their high precision frames and have a distance of 2 cm between each other. The use of eight detector modules at the same time allowed to increase statistics during
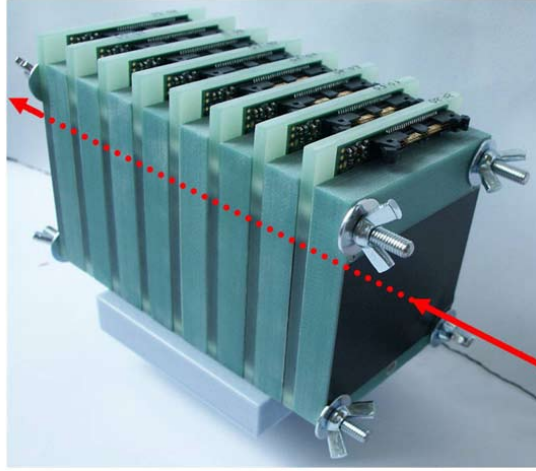
Fig. 6.8: Stack of eight detector modules.

the test beam and enables autonomous tracking, which means, that it is possible
to analyse one sensor while the remaining seven sensors are used as "telescope".
This was important since we have not been absolutely confident if the EUDET
telescope was ready or still under development at the time of the test beam.
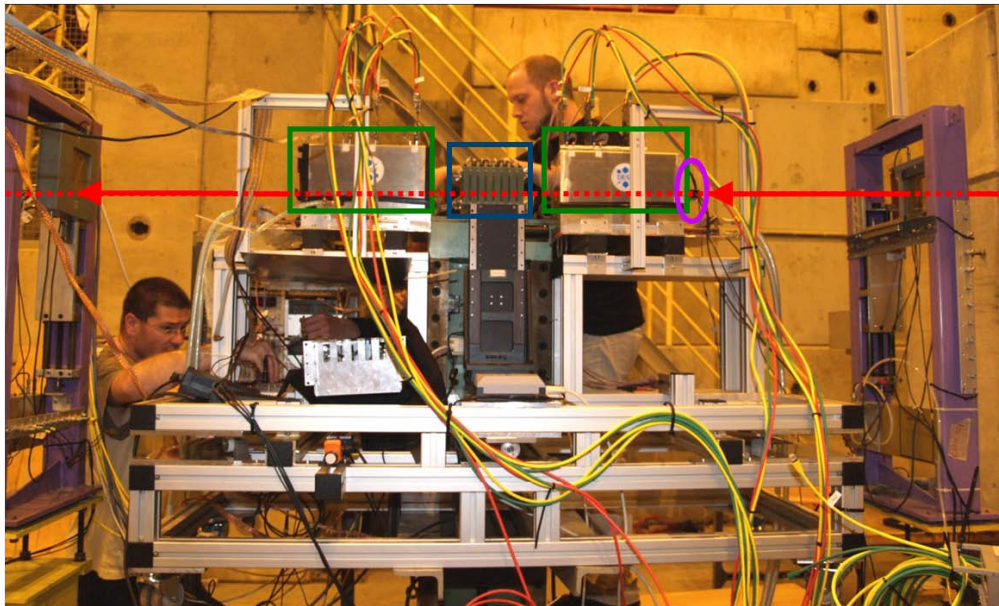
Fig. 6.9: Test beam setup.

Figure 6.9 shows the setup during data taking. The module stack (dark blue
rectangle) was mounted on a xyz-rotation-stage between the two times three
CMOS pixel sensors of the EUDET telescope (dark green rectangles) inside the
beam line (red). Since the Isoval®11 frame is not sufficient to protect the sensors
from ambient light, during data taking the module stack had to be wrapped into a

light‑tight cloth. The coincidence signal of two crossed scintillators (violet ellipse) in front of the setup was used as trigger signal.

The SPS provided a beam with $55.67\,\%$ pions, $38.95\,\%$ protons and $5.38\,\%$ kaons with an energy of $120\,\mathrm{GeV}$ on a beam spot of $4\times2\,\mathrm{cm^2}$. The beam was not continuous, but consisted of spills of $5\,\mathrm{sec}$ with pauses of 20‑$40\,\mathrm{sec}$ in between. Although the APVDAQ was used in raw mode with a trigger rate of $50\,\mathrm{Hz}$ we decided to minimize the beam intensity to reduce the event‑multiplicity in the EUDET telescope.

6.4.1   Measurement Runs

Three different sets of runs were performed, whereas except for the HV scan the sensors were biased with constant $100\,\mathrm{V}$:

Spatial Resolution - three times 100k events

For the measurement of the spatial resolution of the different sensor zones it was important to use the module stack as described before. This ensured the best possible alignment of the sensors to ease the tracking. Because the telescope's pixel sensors only cover an area of $7\times7\,\mathrm{mm^2}$ we had to reduce the visible size of the scintillators. Since this is smaller than the width of $13\,\mathrm{mm}$ of the multi‑geometry sensors, the resolution run had to be performed three times with different module positions, as displayed in the left picture of figure 6.10. A malfunction of the xyz‑rotation‑stage lead to a rotation of $3\,°$ of our module stack, which hampered the analysis. The results obtained with this run are described in section 6.6
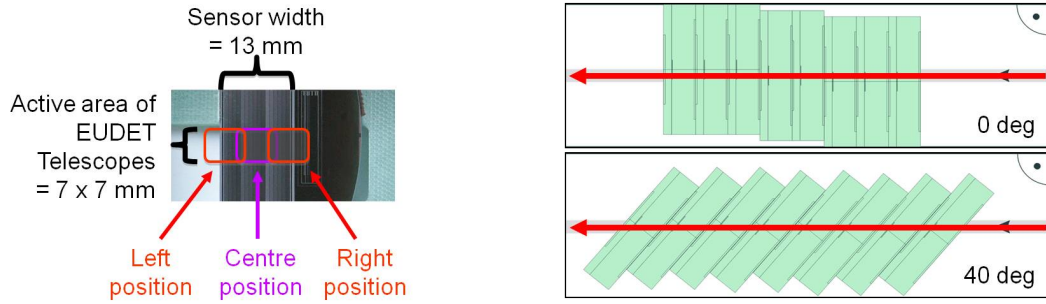
Fig. 6.10: Measurement runs - left: the three positions during the resolution run; right: staggered stacks for a simultaneous measurement in all three sensor areas during the HV and the angle scan.

Voltage Scan - 13 times 10k events

A high voltage scan was performed to examine the dependence of the detector signal on different sensor operation voltages. Since the alignment of the sensors was not important for this analysis, it was possible to use a staggered stack of the

detector modules, as shown in the right picture of figure 6.10. The staggered stack enabled the collection of data in all 16 zones of the multi-geometry sensors at the same time. In total 13 runs with voltages varying between 10 V and 200 V were performed. The data of the voltage scan clearly shows that the cluster width and the signal to noise ratio rapidly increase with the bias voltage until a plateau is reached at full depletion, as shown in section 6.6.2.

Angle Scan - seven times 10k events

This run was performed to answer the question if it is possible to measure the incident angle of particles, traversing a silicon strip sensor with a readout pitch of 50 μm, solely from the measured cluster width. This question arose from the demands on the tracking systems operating at the possible luminosity upgrade of the LHC, where the tracker has to deliver information about the transversal momentum of traversing charged particles to the level one trigger. For these runs the detector modules were also arranged staggered, to collect data of all zones within one position of the xyz-stage, as displayed for the 40°-measurement in figure 6.10. During the angle scan we took data for seven different angles from 0° to 60° in steps of 10° between the beam line and the sensor planes. The results of this scan are described in detail in [72], [73] and [74]. The determination of the incident angle of a traversing particle via the measurement of the produced signal cluster width is possible. Due to the reduced charge sharing and capacitive coupling between adjacent strips, sensors without intermediate strips are suited better for such measurements than sensors containing intermediate strips.

6.5   Data Analysis

The first 600 events of each run are taken with random trigger, ensuring that no particle signals are collected. The first 200 of these are used to calculate the pedestal corrections. With the remaining 400 the common mode noise is calculated by averaging the signals of groups of 32 strips. The standard deviation of each corrected channel gives then the single strip noise N_{ss} of that channel.

6.5.1   Cluster Finding

After the common mode noise is subtracted from the raw data, a standard algorithm is used to search for strips with signals exceeding one or all of the following thresholds:

- seed threshold
  If a strip signal is above 5 times the single strip noise N_{ss} a new cluster is initialized around this seed strip.

- neighbour threshold
  Strips with a signal exceeding 3 times the single strip noise N_{ss} are added to a seed strip as neighbour strip which extends the existing cluster.

- cluster threshold
  A group of strips is only accepted as cluster if the sum of their signals is bigger than the cluster threshold of typically 5 times the cluster noise N_{cl}, which is defined by $N_{cl} = \sqrt{\sum N_{ss}^2}$.

These thresholds worked well except for the analysis of the angle scan data where problems arise when the clusters start to split at high incident angles.

6.5.2 Estimation of the Spatial Resolution

After all hit clusters of each event in the sensors are determined, the final hit position of the particle creating a specific cluster can be found by calculating the centre of gravity of the charge distribution. Since these positions are measured in the coordinate system of each individual sensor it is possible to make an alignment of all sensors with a simple straight track model. Straight tracks can be assumed because deviations caused by multiple scattering in the silicon sensors can be neglected for a beam energy of 120 GeV. For a first crude alignment events with exactly one hit in each sensor are used, which can then be further improved by adding events with multiple tracks. Since the spatial resolution of the different sensor zones are unknown in the beginning, for the first iteration a binary resolution was assumed. Then, after the estimation of the real resolutions the alignment of the sensors must be repeated with the track fits using the correct covariance matrices. Without the data from the EUDET pixel telescope, which was not available at the time the analysis was performed, the alignment of the sensors is only possible in the direction orthogonal to the strips. This can be done quite easily looking at the histograms of the residuals of every detector module and then adding the mean of each histogram to the measurements of the sensor. This procedure is repeated until all shifts fall below $0.05\,\mu$m, which was chosen as threshold. Important to mention is, that with this procedure it is only possible to align the eight used sensors with respect to each other and gives no clue about the location in the global coordinate system. In the test beam setup, the track finding is rather easy, since all tracks can be assumed to be straight because no magnetic field is present and multiple scattering can be neglected. In addition there was no interest for the analysis of single events, but only to find out if a track hits five or more sensors. Below this threshold the chance for ghost hits rise considerably and such tracks were not used for the analysis. The spatial resolution can then be determined using the least square method [75], which defines the residuals as the deviation of the measurements from the estimated track coordinates. A deeper look into the analysis of the test beam data is given by [74]. Because the data of the EUDET pixel telescope was not available at the time of this analysis an approach was used, where the spatial resolutions are calculated by iteratively estimating the residuals

of a single sensor plane in the centre of the module stack, using the other seven strip sensors as "telescope".

6.6   Results

For the analysis, the three runs dedicated to the measurement of the spatial resolutions were used. Since the module stack was slightly rotated with respect to the beam not every event shows a hit in all eight sensors and the average number of hits in each zone is reduced to about $62{,}000 \pm 1{,}000$.

6.6.1   Signal to Noise Ratio

The cluster signal to noise ratios can be calculated with

$$SNR = \frac{S_{MP}}{N_{avg} \times \sqrt{CW}} \tag{6.1}$$

where S_{MP} is the most probable signal, N_{avg} the average noise and CW is the average cluster width. The average cluster width shows no significant variations for the different strip widths, but slightly increases with the number of intermediate strips. The average for zones with the same amount of intermediate strips is 1.94, 2.19 and 2.26 for 0, 1 and 2 intermediate strips, respectively.
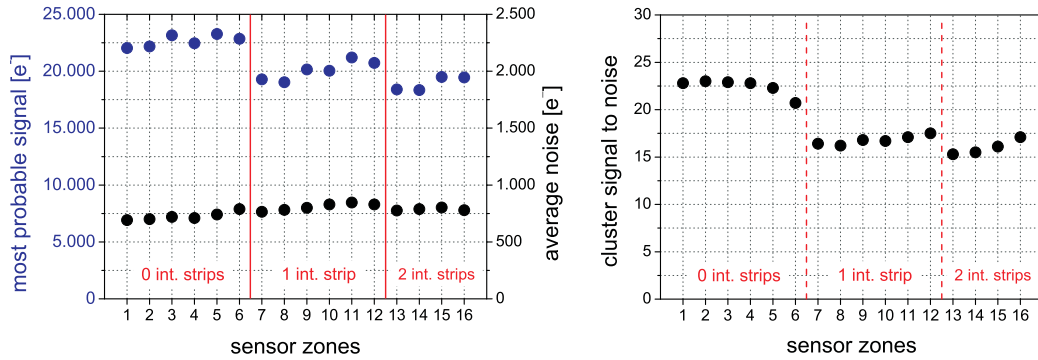
Fig. 6.11: Most probable signal and average noise (left) and cluster signal to noise ratio (right).

The signal to noise ratio is nearly constant for zones with the same number of intermediate strips, and decreases with the number of intermediate strips, as shown on the right plot of figure 6.11. This behaviour can be explained by the fact, that the intermediate strips do not pass the total collected charge to the adjacent readout strips, which lessens the collected signal, as visible in the left plot of figure 6.11. Also the average strip noise slightly rises with the number of intermediate strips and with increasing strip width. The comparison of the average signal to noise ratio of zones with zero (31.28) and one (24.82) intermediate strips

show a decrease of about 25.2 %. The difference between the zones with one and two intermediate strips is only 4.7 %.

6.6.2 Voltage Scan

Apart from here all data presented in this chapter are recorded with a reverse bias voltage of 100 V. Figure 6.12 shows the mean cluster width (left) and signal to noise ratio (right) of the 16 sensor zones as functions of the bias voltage. The mean cluster width of the signals rises until the sensor is fully depleted and slightly decreases again with the degree of over-depletion, especially in zones containing intermediate strips. This is caused by the increased electric field in the sensor bulk, which increases the drift velocity of the charge carriers, compare equation 4.4, resulting in a decrease of their drift time that reduces the final width of the charge cloud, as shown in equation 4.21. Also the signal to noise ratio of the different sensor zones rapidly increases with the bias voltage until a plateau is reached with full depletion voltage. This reflects the behaviour of the sensor capacitance, as visible in the CV measurements shown in the right plot of figure 6.2.
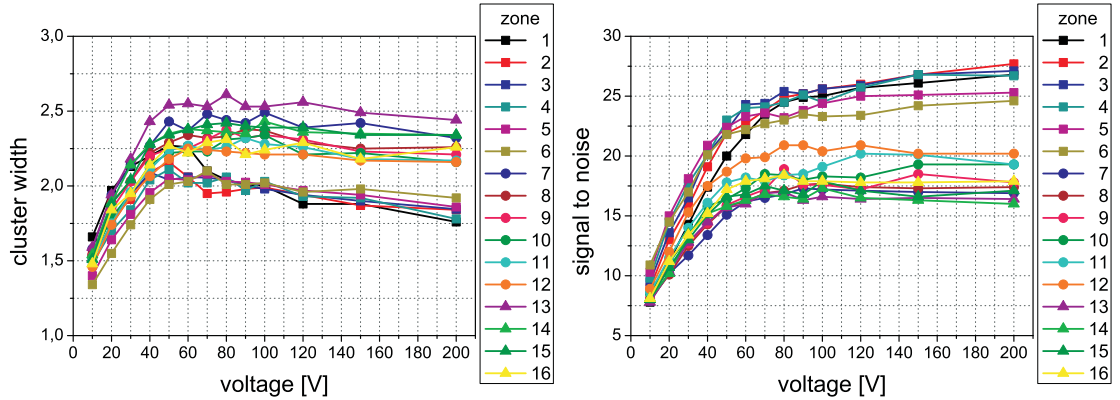
Fig. 6.12: Mean cluster width (left) and signal to noise ratio (right) as functions of the bias voltage.

6.6.3 Capacitive Coupling

To achieve spatial resolutions better than the binary resolution it is necessary that the charge generated by a traversing particle is shared between more than one strip. Then it is possible to calculate the centre of gravity from the signal heights of adjacent strips. This is the basic idea of intermediate strips, which should decrease the probability of single strip clusters. According to [76] the capacitive coupling is defined as the fraction of signal charge that is transferred from a signal strip, crossed by the ionising particle, to each of its neighbours. For perpendicular tracks the value of the capacitive coupling CC in % of the strip signal can be

expressed with:

$$CC = \frac{Q_l + Q_r}{2 \cdot (Q_s + Q_l + Q_r)} \tag{6.2}$$

where Q_s, Q_l and Q_r indicate the charge of the seed strip of the cluster and the charges of its left and right neighbours. This distribution is well modelled by a Gaussian plus a tail at positive value, which comes from the charge sharing with further strips. Figure 6.13 shows the calculated charge couplings for the different zones of the sensor. The coupling of strips without intermediate strips is relatively constant at 3 %, which agrees with the measurements of [76], while it increases to approximately 4 % and 5 % for zones with one and two intermediate strips, respectively.
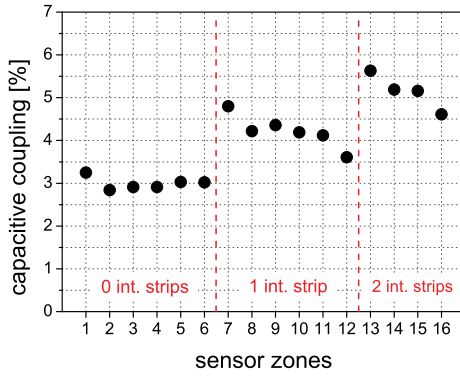
Fig. 6.13: Capacitive coupling of the different sensor zones.
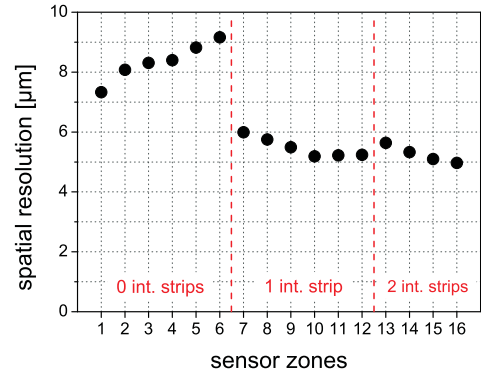
Fig. 6.14: Spatial resolutions of the different sensor zones.

6.6.4 Spatial Resolution

The spatial resolution for each sensor zone is plotted in figure 6.14. Remember, that due to the size of the EUDET telescope three runs with different positions had to be performed. For the zones 3 to 15 where data was collected in more than one run, the estimated resolutions are averaged. Because of the large amount of data the errors on the resolutions are between $0.03\,\mu$m and $0.05\,\mu$m and therefore the error bars are not visible in the plot.

From the results it is clearly visible that the introduction of intermediate strips improves the spatial resolution of the sensors. This is caused by the enhanced capacitive coupling and charge sharing ability in zones with intermediate strips. Zones with a width to pitch ratio between 0.25 and 0.35, corresponding to a p$^+$-strip width of $12.5\,\mu$m and $17.5\,\mu$m, show the best spatial resolutions.

6.7 Recommendation for ILD

The results of this test beam experiment clearly show, that it is possible to fulfil the requirements on the silicon tracking system of the ILD regarding the spatial resolution of the silicon strip sensors. When introducing one or two intermediate strips a readout pitch of $50\,\mu$m is sufficient for the critical measurement of the $r\varphi$-coordinate, as verified with simulations in section 9.4. Although the highest spatial resolution can be achieved with the geometry of zone 16, two intermediate strips and a strip width of $12.5\,\mu$m, due to the better signal to noise performance, a geometry with only one intermediate strip and a strip width of $12.5 - 17.5\,\mu$m, corresponding to zones $10 - 12$, is preferable. When comparing the capacitive couplings in these zones it is visible that the capacitive coupling of zone 12, with a strip width of $17.5\,\mu$m, is comparable lower than that of zones 10 and 11. Therefore the ideal geometry of the silicon strip sensors for the ILD tracker is a readout pitch of $50\,\mu$m, containing one intermediate strip and a strip width in the region of $12.5\,\mu$m to $15\,\mu$m. With such a configuration a spatial resolution below $6\,\mu$m is achievable.

Chapter 7

Design & Construction of the Large TPC Prototype Experiment

Within the R&D of the Linear Collider TPC (LCTPC) collaboration the current focus lies on two different technologies, namely Micromesh Gas Detectors (Micromegas) [37] and Gas Electron Multipliers (GEMs) [38]. The effort is driven by the fact, that with the use of Multi‑Wire Proportional Chambers (MWPC), the standard in former experiments, it is not possible to obtain the required resolution. Therefore a TPC at the International Large Detector must be read out using Micro Pattern Gas Detectors (MPGD). In the past years these readout technologies have been extensively tested with small TPC prototypes with diameters in the range of 30 cm. These tests included various gas mixtures and different magnetic field configurations. To enable tests on a larger surface, the Large TPC Prototype (LP) was designed and built [77].

The LP is designed to fit into a persistent current, superconducting magnet (PCMAG) [78] installed in test beam area T24 at the DESY, the "Deutsches Elektronen‑Synchrotron" in Hamburg [79]. From the beginning contact to the Silicon tracking for the Linear Collider (SiLC) collaboration [34] was establish to push towards a silicon envelope for the Large TPC Prototype. The addition of the silicon sensors improves the ability to compare the different TPC readout technologies under investigation and will help to define the ideal TPC readout electronics for the ILD. Due to the limited space of 35 mm between the LP and the surrounding magnet, as visible in figure 8.1, only one double layer of silicon strip modules on either side of the TPC could be installed. This makes the setup comparable to a half SIT and the SET of the ILD concept and enables first alignment and resolution studies. It is foreseen to merge the data analysis of the silicon layers with the TPC analysis framework, which is a very important step towards a future ILD slice tests. Finally, since the magnet does not have a return yoke, and therefore provides significant field inhomogeneities, it is possible to evaluate different correction techniques for E‑ and B‑field distortions. This chapter describes the

test beam setup and the silicon prototypes.

Starting with the conceptual formulation I took the responsibility for the design and construction of the silicon envelope for the LP experiment. The layout of the silicon sensors and their quality tests were done at the HEPHY Vienna. Every nut, bolt and screw of the silicon detectors and the moveable silicon support structure was designed in 3D with the help of AutoCAD. The construction of the detector parts, their assembly and the final functionality tests were also done at the HEPHY. The data acquisition system for the silicon envelope could be provided with the help of IEKP[1]. After a final functionality test with cosmic muons the silicon envelope was successfully installed at the LP experiment at DESY.

7.1   Overview
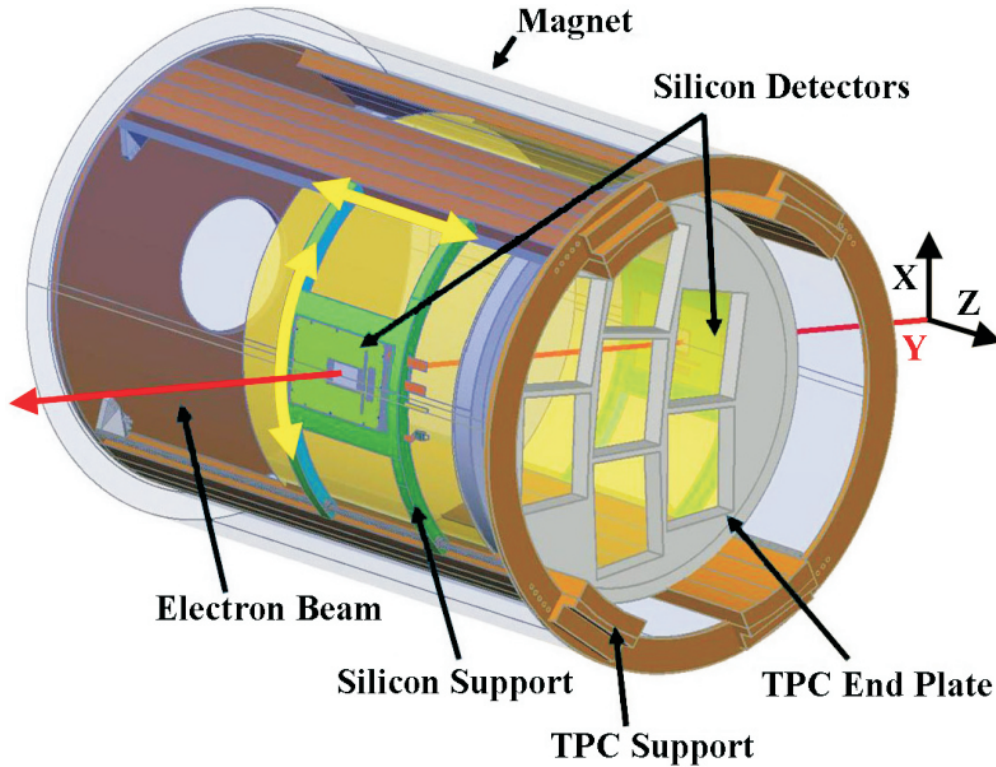
Fig. 7.1: Large TPC Prototype setup.

The Large TPC Prototype setup, as displayed in figure 7.1, is installed in area T24 at DESY, Hamburg, where an electron beam with an adjustable momentum of 1 to 6 GeV/c is available (red line). The estimated spread of the beam is about 2 % with a divergence of 2 mrad and average rates of 250 Hz for 6 GeV/c. The TPC,

---

[1]Institut für Experimentelle Kernphysik (IEKP) at the Karlsruhe Institute of Technology (KIT): http://www-ekp.physik.uni-karlsruhe.de/

magnet inner bore (measured min.)	$850\,mm$ ($846\,mm$)
silicon layers	$2 \times 35\,mm$ on radius
clearance inside of the silicon layers	$780\,mm$
extra clearance	$2 \times 5\,mm$
outer diameter of the field cage	$770\,mm$
field cage wall	$2 \times 25\,mm$
inner diameter of the field cage	$720\,mm$

Tab. 7.1: Radial distances of the LP setup.

with a diameter of $770\,mm$ and a length of $610\,mm$, is designed to fit into the available persistent current, superconducting magnet (PCMAG) [78], which can provide an inhomogeneous magnetic field of up to 1.25 Tesla. The TPC end-plate has seven geometric identical cut-outs, where the different TPC readout-panels can be mounted. As shown in figure 7.8, the LP end-plate is designed as a circular subsection of a TPC with a diameter of $3.6\,m$, as included in the ILD letter of intent [21]. The magnet is mounted on a moveable stage, displayed in figure 7.3, which enables beam tests with different drift distances and also with the beam crossing the TPC volume under different angles. Since the sensitive areas of the silicon sensors have to stay in the beamline, the silicon support has to compensate for all movements of the magnet.

7.2   DESY Test Beam Line
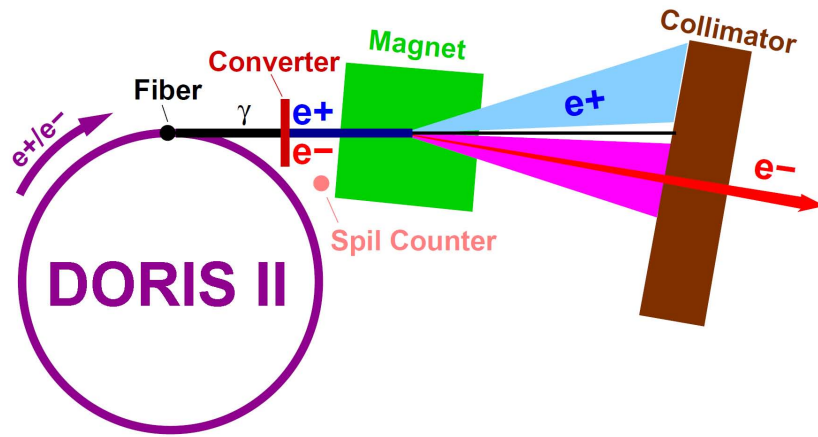
Fig. 7.2: Schematic layout of the test beam at DESY [79].

The LP experiment is installed at the beam line T24 at DESY. The electrons reaching the area are produced as follows: a bremsstrahlung beam is generated by a carbon fibre located inside the e^-e^+-synchrotron DORIS II. The photons are

converted to e$^-$e$^+$- pairs with a metal plate and the desired electron momentum can be selected with the help of dipole magnets. The final beam reaching the test beam area gets cut out of the electron fan with a collimator. The electrons available at the experiment have an adjustable momentum between 1 and 6 GeV/c, a spread of approximately 5 % and a divergence of about 2 mrad [79].

The fibre target, located inside DORIS II, can be moved from the accelerator control room and its position defines the beam intensity at T24. The currents in the magnets, the choice of the target and the positions of the 4 jaws defining the collimator opening are controlled by the user.

7.3   Superconducting Magnet
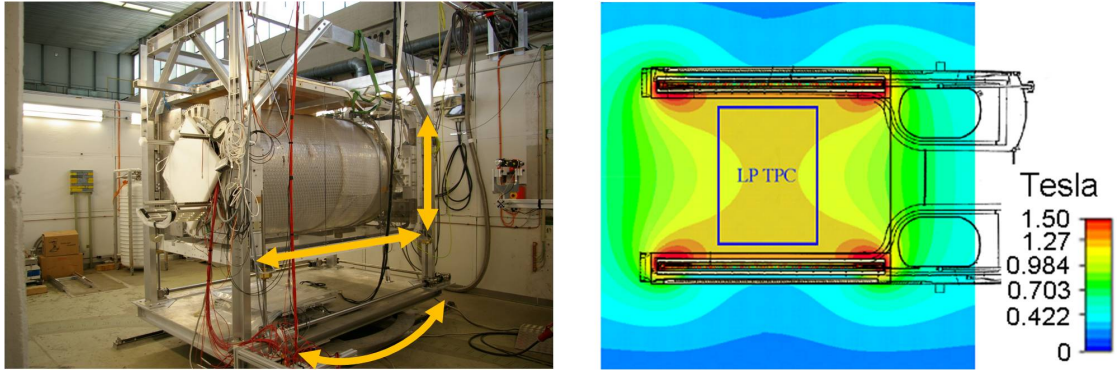
Fig. 7.3: Superconducting magnet in moveable stage (left) and magnetic field calculation (right) [79].

A persistent current, superconducting magnet (PCMAG) [78] built at KEK[2] was installed inside the DESY test beam area in December 2006 and in 2007 its field was measured. Figure 7.3 shows a picture of the magnet and a calculation of its field distribution. Because of the missing return yoke the field of the magnet is very inhomogeneous and can provide a maximum of about 1.25 T in its centre. The magnet is cooled with liquid Helium and needs about 1200 litres for one fill and a refilling of another approximately 500 litres every two weeks of operation. The magnet together with its slow control is mounted into a moveable stage which enables the movement in all directions including rotations of the whole setup, as indicated in the left picture of figure 7.3. This installation allows to collect electron tracks at different drift distances and heights with respect to the field cage. Also events with the beam crossing the TPC volume under different angles can be recorded.

---

[2]High Energy Accelerator Research Organization KEK: http://www.kek.jp

7.4   Large TPC Prototype

The Large TPC Prototype (LP) is designed as a subsection of the Time Projection Chamber foreseen for the ILD concept. With a length of 610 mm and an inner diameter of 720 mm it enables the measurement of tracks with up to 125 space points using pad readout [80].

7.4.1   Working Principle of a TPC

The concept of the Time Projection Chamber (TPC) was first proposed by D. R. Nygren in 1975 [81] and was established for the first time at the PEP-4 collider at SLAC[3]. TPCs have been and are running in a variety of high energy physics detectors, ranging from ion beam experiments with high multiplicity events, as shown in figure 7.4 for the STAR detector[4] [82] to detectors of low rate neutrino experiments like for example the T2K[5] experiment [83].
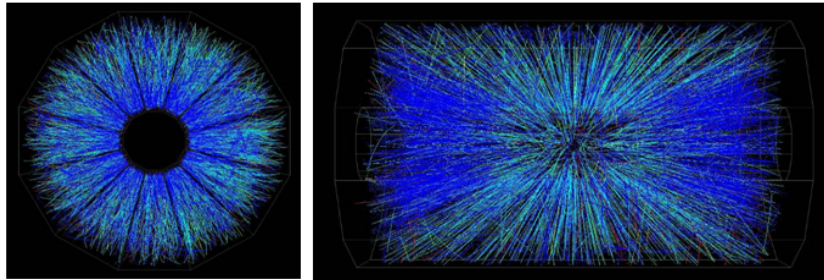
Fig. 7.4: Ion collision recorded with the LBL STAR TPC [84].

The sensitive gas volume of a TPC is located inside a cylindrical field cage between two parallel electrodes, as shown on the left in figure 7.5. Most TPCs are split into two halves by a central high-voltage electrode disc and have one segmented anode on both ends, the so-called end-plates. The electric field inside the gas volume, between the cathode and the anodes, is in the order of some 100 V/cm. To maximise the field homogeneity in the TPC volume, which is one of the most crucial parameters for the TPC resolution, conductive rings, so-called field strips, are attached to the inside wall of the field cage. The field strips are connected in series with equal resistors that apply them with stepwise descending potentials and produce a linear decreasing electric potential along the inside wall of the field cage.

The right picture in figure 7.5 illustrates the measurement principle. When a charged particle traverses the sensitive gas volume, it ionises the gas along its trajectory. Driven by the electric field, the gas ions drift towards the cathode

---

[3]SLAC National Accelerator Laboratory: http://slac.stanford.edu/

[4]Solenoidal Tracker at RHIC (Relativistic Heavy Ion Collider) in Brookhaven National Laboratory, United States

[5]Tokai to Kamioka in Japan
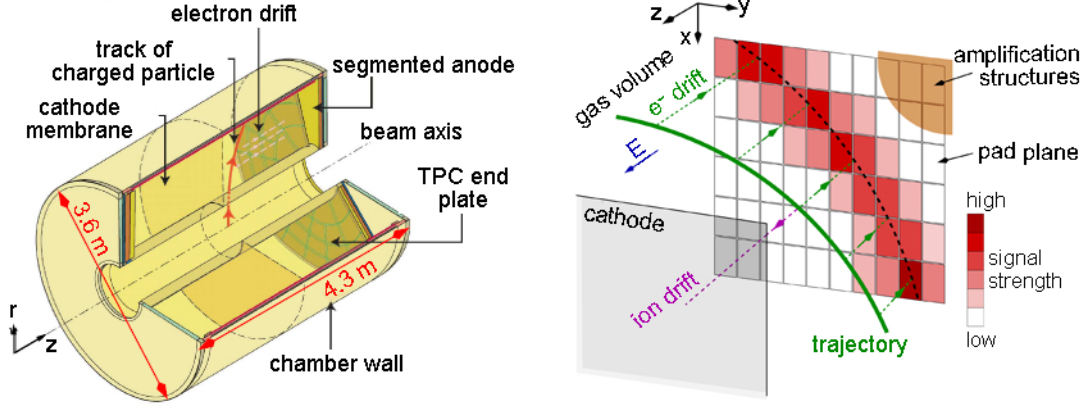
Fig. 7.5: Basic layout of a TPC with the dimensions of the ILD TPC in red (left) and the basic working principle of a TPC (right) [85].

and the electrons drift towards the anode end‑plate. This means that the electric field shifts a projection of the charged particles trajectory in the $r\varphi$‑plane to the readout plane. The third dimension, the z‑coordinate Δz, can be calculated from the electron drift velocity in the gas v_{drift} and the drift time t_{drift} of the electrons:

$$\Delta z = v_{drift} \cdot t_{drift} = v_{drift} \cdot (t_1 - t_0). \tag{7.1}$$

The starting time t_0 must be provided by an external trigger that starts a clock, measuring the time until the electrons arrive at the readout pads, which defines the drift time t_1. The drift velocity $\vec{v}_{drift}$ can be expressed as a function of the electric and magnetic field $\vec{E}$ and $\vec{B}$, the Larmor frequency $\omega = eB/m$ and the mean collision time τ between electrons and molecules [4]:

$$\vec{v}_{drift} = \frac{e}{m}\frac{\tau}{1+\omega^2\tau^2} \cdot (\vec{E} + \frac{\omega\tau}{B}(\vec{E}\times\vec{B}) + \frac{\omega^2\tau^2}{B^2}(\vec{E}\cdot\vec{B})\vec{B}) \tag{7.2}$$

When the $\vec{E}$‑ and $\vec{B}$‑fields are parallel $\vec{E}\times\vec{B} = 0$ and the equation gets simplified to [85]:

$$\vec{v}_{drift} = \mu_e\vec{E} \ \ \text{with} \ \ \mu_e = \frac{e\tau}{m} \tag{7.3}$$

where μ_e is the electron mobility. The electron mobility, and therefore the drift ve‑ locity, strongly depends on different gas parameters like the composition, pressure and the water content. Typical electron drift velocities are in the order of $5\,\text{cm}/\mu\text{s}$ and hence t_{drift} is in the range of some $20\,\mu\text{s}$ for drift lengths of about one metre.

A random diffusive movement, which broadens the charge cloud, is superim‑ posed to the average motion of the electron clusters. This diffusion is caused by the interaction of the created electrons with the TPC gas and their initial energy from the ionisation process. These effects cause an initial point‑like cluster to adopt a Gaussian shape after a certain drift length. Therefore the spatial resolution of a Time Projection Chamber is depending on the drift distance Δz and defined by

two parameters, the resolution in the transversal plane parallel to the pad plane $\sigma_{r\varphi}$ and the resolution in drift direction σ_z:

$$\sigma_{r\varphi}^2 = \sigma_{r\varphi,0}^2 + (C_{r\varphi}/N_{eff})^2 \cdot \Delta z \tag{7.4}$$

$$\sigma_z^2 = \sigma_{z,0}^2 + (C_z/N_{eff})^2 \cdot \Delta z \tag{7.5}$$

Here $\sigma_{r\varphi,0}$ is the lateral resolution at the TPC end-plate and $\sigma_{z,0}$ the drift time resolution converted to the longitudinal resolution. $C_{r\varphi}$ and C_z are the lateral and longitudinal diffusion constants, respectively, and N_{eff} is the number of effective electrons on the readout pads [86]. It is also important to mention, that in the presence of an external magnetic field, oriented parallel to the electric field, the electrons spiral around the magnetic field lines and it their transversal movements are reduced by up to a factor of 10 [4]. Therefore the lateral resolutions improve with the strength of the external magnetic field.

7.4.1.1   Advantages and Disadvantages

+ TPCs are used in collider experiments because of their quasi continuous three dimensional tracking capabilities. With the use of a Micro Pattern Gas Detectors (MPGD) it is possible to measure up to 200 points of ionizing particle tracks inside the ILD TPC.

+ The amount of ionization along the length of the track depends on the velocity of the particle. Therefore, with an external magnetic field it is not only possible to derive the particle's momentum, but with the inclusion of an ionization measurement the mass of the particle and therefore its identity can be determined, as shown in figure 7.6.

+ Time Projection Chambers mainly consist of gas which accounts for a moderate material budget.

− One of the major drawbacks of a TPC is its slow readout compared to for example silicon detectors. Since the ILD TPC will have a maximal drift length of about 2.15 m it will take about 43 μs to completely read out the tracks of an event generated in the central part of the TPC, for typical electron drift velocities of 5 cm/μs. But, during this period the ILC produces some hundred bunch crossings, compare figure 2.3, and the created electrons of trajectories from different events are overlaid in the readout.

− Since ions drift about a factor 1000 slower compared to electrons, they are not useful for the measurement of the trajectory and it is not possible to remove them from the drift volume in the time between the ILC bunch crossings. These ions cause space charges that can disturb the electron drift.

− In TPC volumes where the electric $\vec{E}$ and magnetic $\vec{B}$ fields are not absolutely parallel, the drift velocity gets a component in the $\vec{E} \times \vec{B}$-direction and the

created electrons are deflected and arrive on displaced points on the anode. During the track reconstruction it is possible to apply a correction for these $\vec{E} \times \vec{B}$ effects, but only if the magnetic field and the electron mobility of the gas are very precisely known. However, it is not possible to measure the electric field very accurately, because a measuring device would by itself modify the field. Therefore it is utterly important that the TPC field cage provides a very homogeneous electric field.
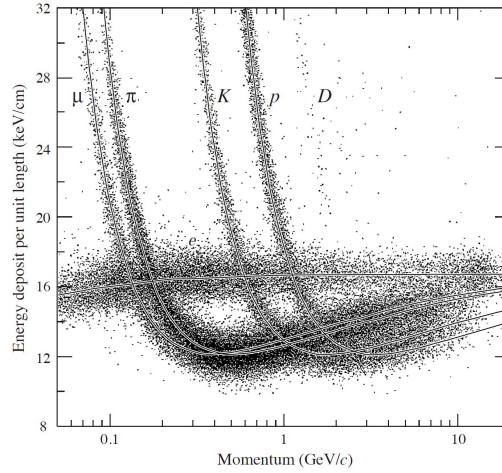

Fig.7.6: Particle identification with a TPC. From the energy deposit measurements with the PEP4/9-TPC it is possible to distinguish between muons μ, pions π, kaons K, protons p and deuterons D [4].

7.4.2 Amplification Technology

An ionising particle traversing the TPC volume creates, depending on the used gas mixture and the particle's type and momentum, approximately 100 electron-ion pairs per centimetre. These are too few electrons to produce a sufficiently strong signal on the pad plane. Therefore an amplification structure is needed in front of the readout plane, which typically provides an amplification between 10^3 and 10^4.

For most Time Projection Chambers in the past, proportional wires were used as amplification stage in front of the TPC anode. The high voltage applied to the wires attracts the drifting electrons, which get amplified before they reach the wire surfaces due to the strong electric field. For the track reconstruction both, the signals measured on the wires and the induced signals on the pad plane are used. There are four reasons, why it is not possible to fulfil the ILD requirements with proportional wires:

1. The required spatial resolution is not reachable, because the strong electrostatic forces between the wires prohibit to place them at a closer distance than 1 mm. This limits the obtainable resolution since it is not only defined

by the width of the induced signal on the pad plane but also by the distance of the wires.

2. The achievable resolution is also reduced by $\vec{E} \times \vec{B}$ effects caused by the strong electric field of the wires in combination with the external magnetic field.

3. To avoid a sagging of the wires they have to be tightened with high tension, which requires robust structures that introduce a lot of unwanted dead material into the detector volume.

4. To prohibit the ions, created in the electron avalanche near the wires, from drifting back into the sensitive TPC volume an additional plane of gating wires, located in between the sense wires and the drift region, is needed. During the readout phase of an event, these gating wires have to be set on equal potential to open the gate and in between the events on alternating potential to close the gate and catch the ions. At the ILC the time between the bunch crossings is too short for this switching of the gate and therefore not possible.

Therefore Micro Pattern Gaseous Detectors (MPGDs) are the technology of choice which offers the following advantages:

+ spatial resolutions down to approximately $100 \, \mu$m are possible

+ they are more robust than wires

+ the nearly homogeneous surface causes no $\vec{E} \times \vec{B}$ effects

+ fast signal collection combined with high gains

+ low ion back drift

+ better ageing properties

+ easier to manufacture

In the last few years Gas Electron Multiplier (GEMs) [38] and MICROMEsh GAseous Structures (Micromegas) [37] have begun to replace wire chambers in some experiments and they are in the focus of the R&D for the ILD TPC.

Micromegas

MICROMEsh GAseous Structures are amplification systems that use a thin metal mesh with a typical pitch of $50 \, \mu$m, which can be as simple as a wire grid. Typically it is hold in place by insulation pillars with a height between $50 \, \mu$m and $150 \, \mu$m. Due to the strong electric field, caused by the applied potential difference of about $400 \, $V between the mesh and the anode, the incoming electrons produce

an avalanche of secondary electrons that drift to the anode, as shown in the left schematic of figure 7.7. When operating very close to readout pads, the RMS of the avalanche size is approximately 15 μm [37]. The main advantages of Micromegas are the simple technology and the high gain achieved with only one stage of amplification. In addition Micromegas have a natural ion feedback suppression and discharges are non destructive.
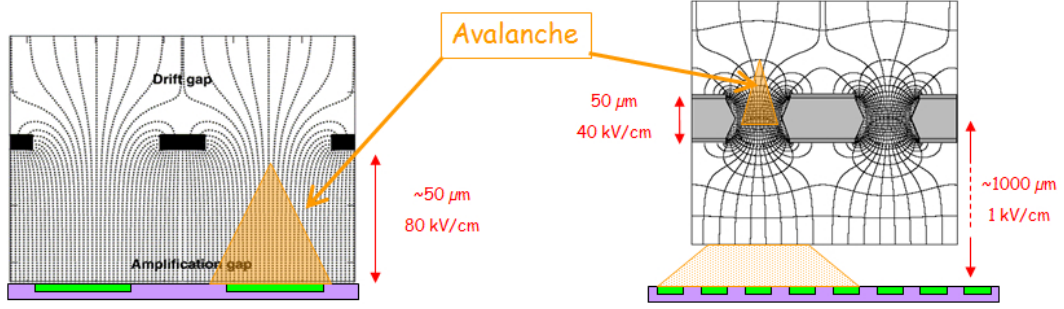

Fig. 7.7: TPC amplification technologies: Micromegas (left) and GEMs (right) [84].

GEMs

Gas Electron Multiplier consist of two metal foils separated by an isolation layer with a thickness of typically 50 μm, as displayed in the right schematic of figure 7.7. The electron amplification takes place in holes which are etched through the isolating layer. Most GEMs have bi-conical holes with a pitch of 140 μm and an external and internal diameter between 50 μm and 70 μm. The metal foils are charged to a potential difference of a few hundred volts and thus creating a strong electric field of a few ten thousand V/cm inside the holes. To compensate for the relatively low gain and to reach a higher multiplication factor GEMs are often cascaded in two or three stages, so-called double or triple GEMs. In such a setup it is possible to operate the topmost GEM with a moderate amplification so that only few ions are produced which could drift back into the sensitive TPC volume. At the same time, most of the ions coming from a lower GEM are caught on the bottom layer of an upper GEM. The main advantages of GEMS are the easy operation, the very small field above the electronics and the very low discharge probability.

7.4.3   LP Readout Technology

The readout electronics used for the pad panels equipped with Micromegas is based on the AFTER chip [86], initially developed for the T2K experiment [83]. The readout panels designed for the Large TPC Prototype contain 1728 channels which are arranged in 24 rows of 72 pads with an average pad size of $3.2 \times 7\,\text{mm}^2$. It provides a full wave sampling over 511 time buckets and each sample is digitised by a 12 bit ADC. The sampling frequency of the readout can be chosen between

10 MHz and 100 MHz and the peaking time of the shaper can be adjusted between 0.1 μs and 2 μs.

The GEMs are combined with readout electronics based on the ALICE TPC Read Out (ALTRO) chip [87] which was initially developed for the ALICE experiment [88] at the LHC. The ALTRO chip is a CMOS chip which contains eight channels and is able to perform tail cancellation, pedestal subtraction, zero suppression, formatting and buffering of the data. In order to work with a Micro Pattern Gaseous Detector (MPGD) based TPC this chip had to be slightly adapted: a new charge sensitive pre-amplifier was developed, the time of arrival is measured with a time to digital converter (TDC) and the signal charges on the pads are measured indirectly with the help of a charge-to-time converter. The system used for the LP is based on 200 ALTRO chips, containing 3200 readout channels, which digitise the TPC signals with a sampling frequency of 40 MHz. It is foreseen to extend the readout system with 1600 chips that are capable of a sampling rate of 25 MHz.

7.4.4 LP End-Plate
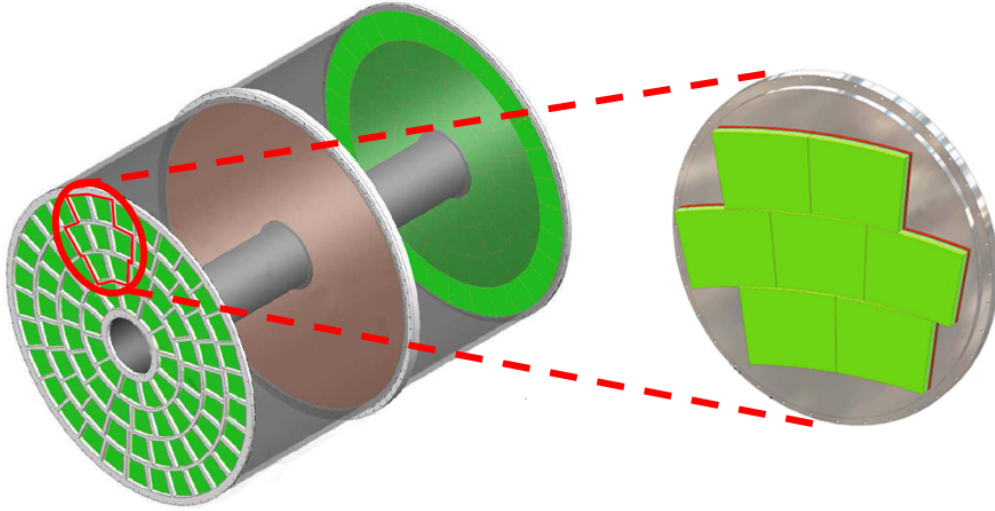
Fig. 7.8: The LP end-plate is designed as a section of the ILD TPC.

The anode of the Large TPC Prototype is formed as end-plate which contains seven identical cut-outs. Special care has been taken that the design of the openings enables an easy mounting of the pad panels containing different readout technologies. Within the LCTPC collaboration a variety of such panels were produced, equipped with GEMs, Micromegas and CMOS pixel (TimePix) readout. In addition six panels containing just a plane surface were build, which can be used as dummy anodes in unused openings.

Additional cut-outs in the end-plate allow to implement further devices, which can be tested with the LP, as for example laser insertion holes. During the de-

sign of the end-plate it was paid attention that a change of the LP end-plate is straightforward to enable tests of different end-plate prototypes. At the moment a new end-plate, improved in terms of material budget, is in production.

7.4.5 LP Field Cage

The LP field cage is a composite of lightweight materials with the aim of highest possible rigidity combined with the lowest possible material budget. Its layout is shown in figure 7.9 and including the end-cap it has a length of 610 mm and an outer diameter of 770 mm. The field cage walls of the LP consist of nine different layers, including the field and mirror strips, as illustrated on the left side of figure 7.9. Table 7.2 summarises the thickness d and radiation length X_0 of the field cage and its components. The total radiation length of the LP field cage is $X_{0,material} = 1.24\,\% \pm 0.30\,\%$, which is close to the aimed design goal of 1 % as aspired for the inner wall of the ILD TPC.
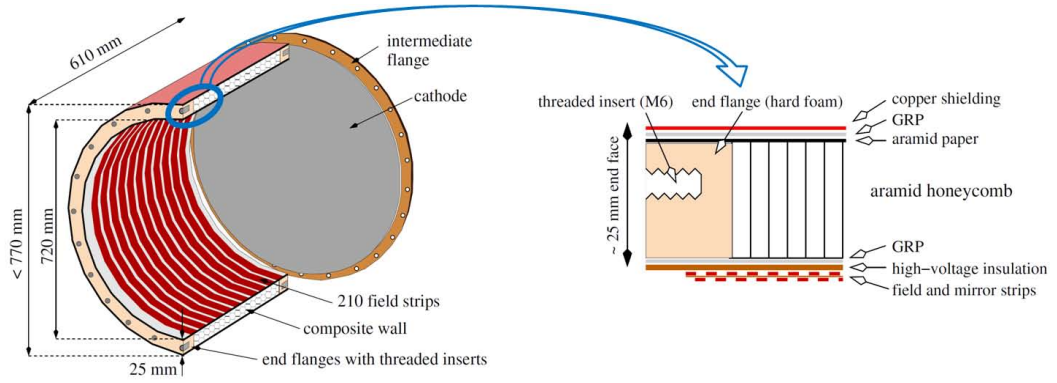
Fig. 7.9: Cut view of the LP field cage (left) and cross-section of the field cage wall and its end flange (right) [85].

material	d [cm]	molecule	X_0 [cm]	$X_{0.material}$ [%]
copper	0.007	Cu	1.47	0.45
polyimide	0.016	$C_{22}N_2O_5H_{10}$	29.2	0.07
glass fibre	0.04	SiO_2	10.5	0.38
aramid paper	0.007	$C_{14}O_2N_2H_{10}$	29.7	0.02
honeycomb	2.35		1480	0.15
epoxy	~ 0.06	C_2NH_4	~ 35.4	~ 0.17
total	~ 2.5		~ 20.2	~ 1.24

Tab. 7.2: Radiation length of the LP field cage [85].

7.4.6 LP Chamber Gas

Time projection chambers can be operated with gas at atmospheric pressure or pressurized, and also with liquids, for example with liquid Argon. In general a TPC uses a gas mixture consisting primary of a noble gas that has a low ionization potential. During operation, the noble gas is enriched with so-called quencher gases in a ratio of a few percent. The molecules of such quencher gases absorb UV photons that are created in the avalanche process inside the strong electric field of the amplification stages. Specific quencher gases can also influence the electron drift properties of the gas, and for example increase the electron drift velocity and thus improve the spatial resolution of the TPC.

For the Large TPC Prototype a premixed gas mixture from bottles containing $Ar : CF_4 : iC_4H_{10}$ in the rate of $95 : 3 : 2$ is used. The gas system is implemented into the slow control of the LP setup and is capable to change the complete LP volume of about 290 litres in one hour. The water and oxygen contents of the gas are continuously measured and controlled.

7.5 Trigger System

Fig. 7.10: The coincidence signal of two overlapping pairs of scintillators, in front of the setup, is used as trigger signal.

The coincidence signal of four scintillator counters, arranged in two overlapping pairs, as displayed in figure 7.10, in front of the setup is used as trigger signal. The trigger signal is centrally distributed to the different DAQ systems, that of the silicon and that of the LP, using a Trigger Logic Unit (TLU) [71] in combination with a Distributor Box (DB) [89]. In addition, the TLU and the DB provide a time stamp and the trigger number, which can be included into the output data files of the data acquisition systems. This enables the correct matching of the recorded events of the different DAQ systems during the off-line data analysis after the test

beam. With a busy signal, sent from the DAQ systems to the DB, it is possible to inhibit a subsequent trigger signal from the DB. This feature ensures, that the Distributor Box waits for the readiness of all DAQ systems.

7.6   Silicon Detectors for the LP Experiment

The initial idea to build a complete envelope of silicon sensors surrounding the barrel part of the large prototype TPC was discarded, because the needed amount of silicon sensors was not affordable. In addition the needed amount of readout electronics was not available. Therefore the final choice is to build two silicon detector modules which can be moved to the desired place inside the gap between the magnet and the TPC. These movements must be performed by the support structure of the silicon modules, which has to compensate for all movements of the surrounding magnet and ensure that the silicon sensors stay inside the beam line.
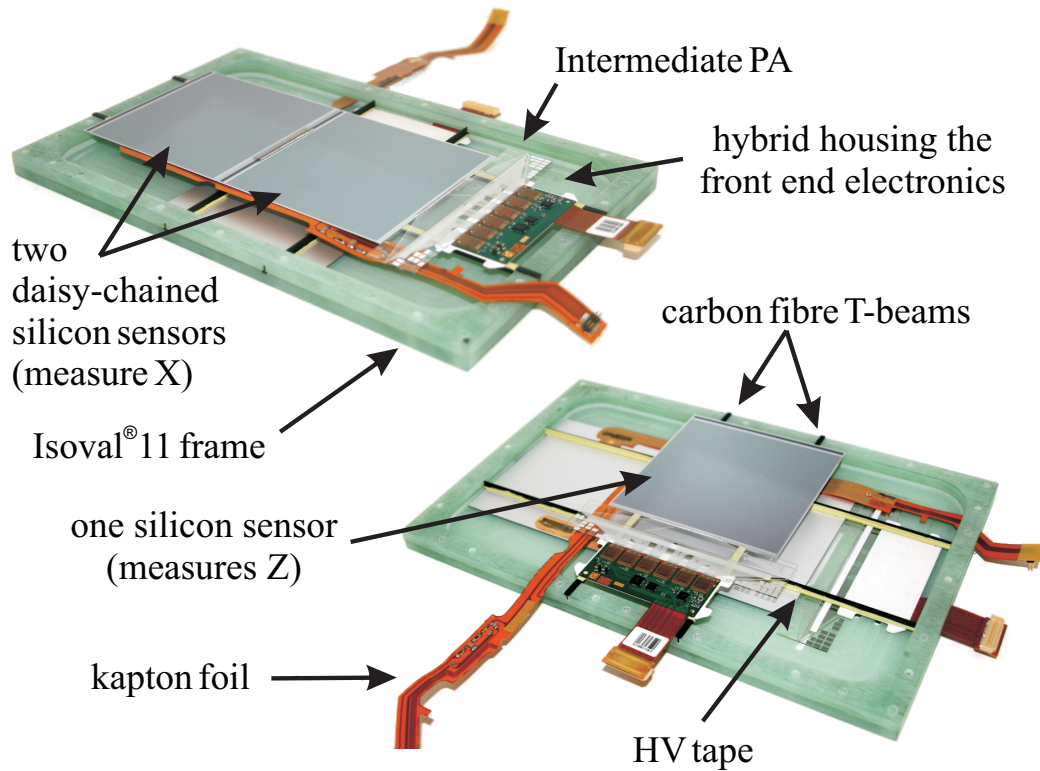
Fig. 7.11: Silicon detector modules without top cover.

The silicon detector modules on each side of the Large TPC Prototype consist of two silicon detectors, containing three single sided, silicon micro - strip sensors each. To enable the precise measurement of both coordinates orthogonal to the beam axis, the silicon detectors of each module are mounted in a way that the

readout strips of their silicon sensors are arranged with an angle of 90 degrees with respect to each other. The detector measuring the x - coordinate, compare figure 7.1, contains two daisy - chained sensors and is located closer to the magnet than the silicon detector measuring the z - coordinate, which contains only one silicon sensor. From the results of the test beam described in chapter 6 the spatial resolution of the sensors can be estimated to be about $9\,\mu$m. Figure 7.11 shows the finalised silicon detectors with labelled components, as described in this section.
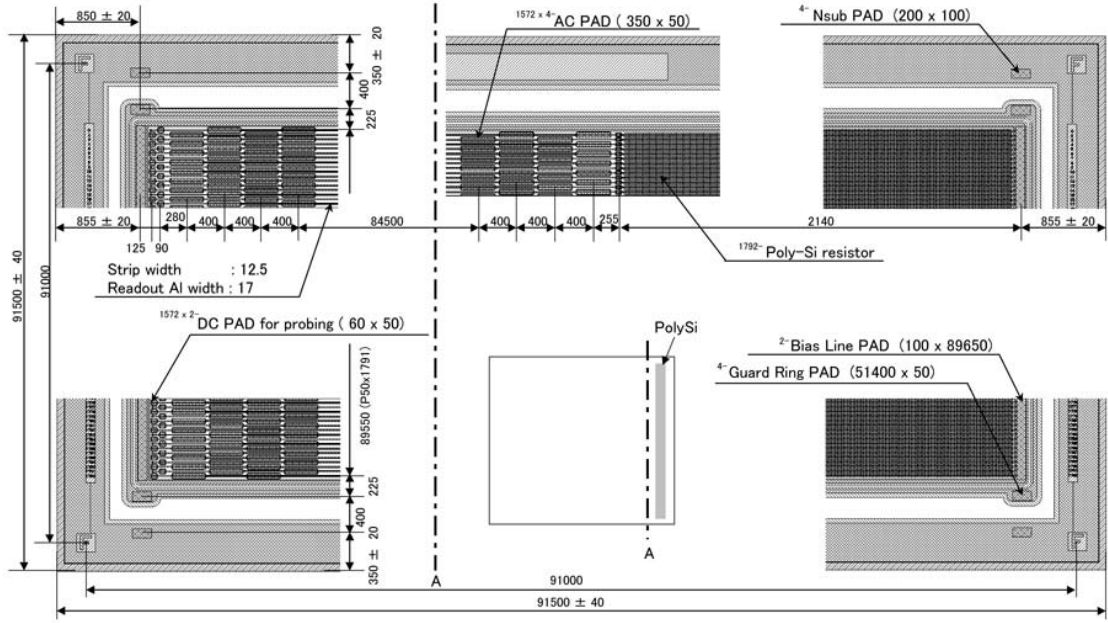
Fig. 7.12: Technical drawing of the silicon strip sensors used for the LP experiment (dimensions are given in μm).

7.6.1   Silicon Sensor Layout

The single sided AC coupled silicon strip sensors were designed by HEPHY and manufactured by Hamamatsu Photonics, Japan, on the silicon wafers described in chapter 5.1.1. The geometrical properties of the sensors are displayed in figure 7.12. The two photos in figure 7.13 show the opposite sides of a strip sensor where the small DC - and long AC - pads can be seen. On the right picture also the long poly - silicon resistors are visible. The sensitive area is surrounded by a thin bias ring, surrounded by two guard rings, whereof the outer contains reference marks and the strip numbering on the surface. The main characteristics of the silicon sensors follow the ILD sensor baseline as described in section 5.1 with the following additional specifications:

- sensor size: $91.5 \times 91.5\,\mathrm{mm}^2$

- sensor thickness: $320\,\mu$m

- bulk material: n-type silicon with $\langle 100 \rangle$ lattice orientation

- full sensor depletion in the range of $50\,\mathrm{V} < V_{depl} < 100\,\mathrm{V}$, which corresponds to a wafer resistivity of about $6-7\,\mathrm{k\Omega cm}$

- leakage current smaller that $10\,\mu\mathrm{A}$ per sensor

- number of readout strips: 1792

- strip pitch: $50\,\mu\mathrm{m}$ without intermediate strips

- the p$^+$-strips are biased individually with poly-silicon resistor with a resistance of $20\,\mathrm{M\Omega} \pm 5\,\mathrm{M\Omega}$

- p$^+$-strip width: $12.5\,\mu\mathrm{m}$ - resulting in a strip width to pitch ratio of $25\,\%$

- the p$^+$-implants are electrically isolated from the aluminium strips by a layer of a dielectric sandwich structure of silicon dioxide $\mathrm{SiO_2}$ and silicon nitride $\mathrm{Si_3N_4}$ with a thickness as used in CMS [51]

- metal overhang: $17\,\mu\mathrm{m}$ for the readout strips which is about $15\,\%$ wider than the width of the implants underneath

- each side of the aluminium strips have two metallised AC-pads with a size of $350 \times 50\,\mu\mathrm{m}$

- on each side of the p$^+$-strip one metallised DC-pad directly connects to the p$^+$-implant underneath - on the side without poly-silicon resistor it has a size of $60 \times 50\,\mu\mathrm{m}$ to ensure convenient contacting with probe needles
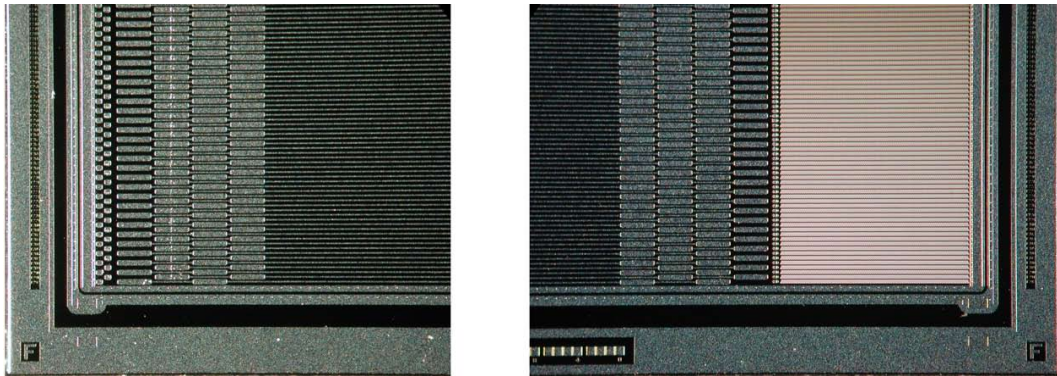
Fig. 7.13: Two opposite corners of a silicon strip sensor.

7.6.2 Electrical Sensor Tests

To build the two silicon layers all together six silicon strip sensors are needed. Prior their assembly into the detector modules the silicon strip sensors were electrical tested in the clean room at HEPHY with the measurement setup shown in figure 7.14. In this section only short overviews of the measurement procedures are presented, which are described in more detail in [52]. As expected, the electrical measurements verified the excellent quality of the sensors and ensured that they can safely be operated, slightly over‑depleted, with a bias voltage of 100 V.
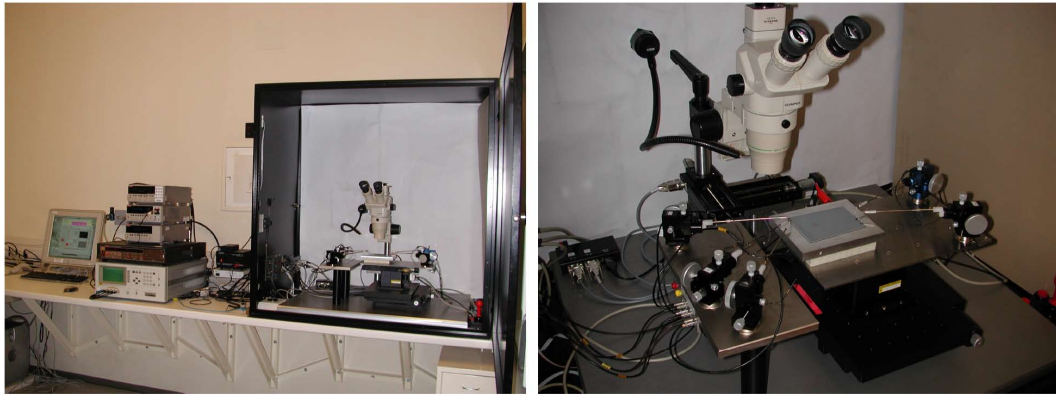
Fig. 7.14: Sensor measurement setup in the clean room of the HEPHY Vienna and a look inside the light‑tight test box.

7.6.2.1 Measurement Setup

During the measurements the sensors are sucked to a vacuum support which is mounted on a motorised xyz‑table inside a light‑tight box, visible on the right picture in figure 7.14. The sensors can be contacted with test needles, hold by micro positioners, with the help of a microscope. A computer running LabView controls the environmental conditions, like temperature and relative humidity, inside the box and also the measurements via a General Purpose Interface Bus (GPIB). The setup includes two source measure units (SMUs), one Keithley 237 and one Keithley 2410, a Keithley 6514 electrometer, an Agilent 4284A high frequency capacitance meter (LCR), a Keithley 595 quasi‑static capacitance meter (QCV) and a Keithley 7001 switching matrix frame equipped with two 7153 matrix cards.

7.6.2.2 IV and CV Curves

Figure 7.15 and figure 7.16 show the IV and $1/C^2$ curves of the six used silicon strip sensors. The IV curves were measured in 5 V steps from 0 V to 800 V, except for sensor 01 where the measurement was only done up to 550 V. No sensor showed a breakdown during these measurements, which indicates their excellent
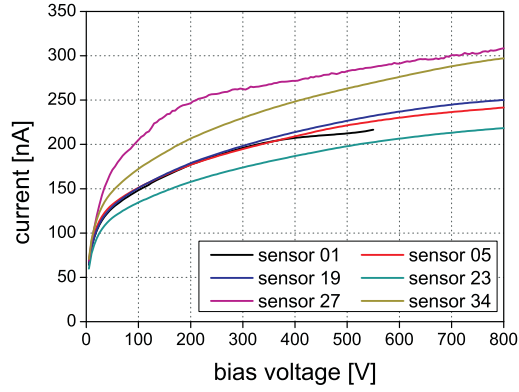
Fig. 7.15: IV curves of the used silicon sensors.

quality. The current values for each used sensor at 300 V and 450 V are also displayed in table 7.3. The total sensor capacitance C_{tot} is measured at different bias voltages between 0 and 200 V in steps of 5 V. For a better visualisation of the CV -behaviour, instead of the total capacitance $1/C^2$ is plotted versus the bias voltage. The $1/C^2$ curves rise linear until the sensor is fully depleted and a plateau is reached. From the position of the kink the full depletion voltage of the sensor can be determined. In practice this is done by calculating the intersection point of the linear fits of the two linear parts of the $1/C^2$ curve, as displayed in the left plot of figure 7.16. The mean values C_{tot} for the measured total capacitances between 100 V and 200 V and the full depletion voltages of the silicon sensors are displayed in table 7.3.
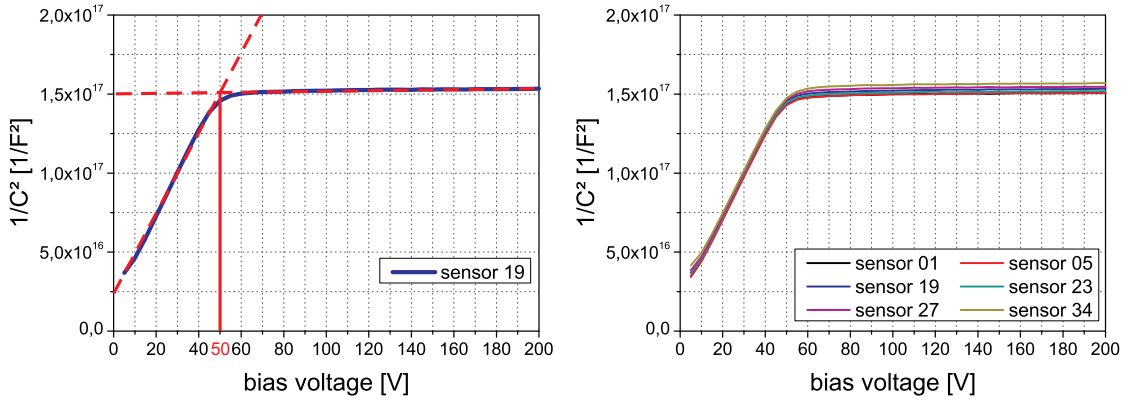
Fig. 7.16: $1/C^2$ curve of one sensor with linear fits (dashed red lines) to determine the depletion voltage (left) and $1/C^2$ curves of the six used sensors (right).

With the measurements of the sensor capacitance

$$2.5282\,\mathrm{nF} \ \leq \ C_{tot} \ \leq 2.5790\,\mathrm{nF}$$

sensor no.	C_{tot} [nF]	V_{depl} [V]	$I_{300\,V}$ [nA]	I_{450V} [nA]	d_{active} [μm]	ρ_{bulk} [kΩcm]
01	2.579	53	196	210	312.03	7.71
05	2.579	53	195	216	312.03	7.71
19	2.558	50	198	221	314.72	7.84
23	2.569	50	174	193	313.31	7.77
27	2.546	55	262	277	316.28	7.91
34	2.528	58	230	256	318.64	8.03

Tab. 7.3: Total sensor capacitance, full depletion voltage, current values at an applied reverse bias voltage of 300 V and 450 V, the calculated active sensor thickness and the bulk resistivity of the six used sensors.

and by transforming equation 4.20 to

$$d_{active} = \epsilon_0 \epsilon_r \cdot \frac{p}{C_{tot}} - p \cdot f(w/p) \tag{7.6}$$

with the strip pitch p and the function $f(w/p)$ from equation 4.18, it is possible to calculate the active sensor thickness d_{active} to:

$$312\,\mu m \lesssim d_{active} \lesssim 318\,\mu m$$

With the knowledge of the full depletion voltage and the thickness of the sensor it is possible to calculate the resistivity of the bulk material ρ_{bulk}. This is possible when starting from the thickness of an ideal diode d_{diode}:

$$d_{diode} = \sqrt{\frac{2 \cdot \epsilon_0 \epsilon_r}{e \cdot N_D} \cdot V_{FD,diode}} \tag{7.7}$$

and the assumption that the doping concentration N_D can be calculated from the resistivity of an extrinsic semiconductor, which is in good approximation valid for medium temperatures:

$$\rho = \frac{1}{e \cdot \mu_e \cdot N_D} \quad \text{for } N_D \; << \; N_A \tag{7.8}$$

and we get:

$$d_{diode} = \sqrt{2 \cdot \epsilon_0 \epsilon_r \cdot \mu_e \cdot \rho \cdot V_{FD,diode}} \tag{7.9}$$

Because of the non-linear electric field inside the bulk, caused by edge effects of the segmented pn-junctions, the solutions for the Poisson equation describing the voltage drop in a silicon strip sensor are quite complicated, but the full depletion voltage of a strip sensor can be calculated from that of an ideal diode with the help of [46]:

$$V_{FD,sensor} = V_{FD,diode} \cdot [1 + 2 \cdot p/d \cdot f(w/p)] \tag{7.10}$$

Inserted into equation 7.9 and after transformation it is possible to calculate the bulk resistivity:

$$\rho_{bulk} = \frac{d^2 + 2 \cdot d \cdot p \cdot f(w/p)}{2 \cdot \epsilon_0 \epsilon_r \cdot \mu_e \cdot V_{FD,sensor}} \tag{7.11}$$

With an electron mobility of $\mu_e = 0.135\,\text{m}^2/\text{Vs}$ and the values for the function f(w/p) from equation 4.18 we get:

$$7.71\,\text{k}\Omega\text{cm} \lesssim \rho_{bulk} \lesssim 8.03\,\text{k}\Omega\text{cm}$$

for the bulk resistivity of the six used silicon strip sensors.

7.6.2.3 Single Strip Scan

A single strip scan was performed for all 1792 channels of one sensor. These measurements were done at one of the probe stations in the HEPHY clean room where a moveable xyz‑table enables the automatically contacting of each of the 1792 sensor strips consecutively. Nevertheless these measurements were quite time consuming and one run took a few hours. During the measurements one needle has to contact the DC‑pad and one the AC‑pad of the measured strip and a third needle has to contact the AC‑pad of the next strip. Due to the geometry of the bond pads, only one DC‑pad per strip exists, the measurement had to be done separately for even and odd strips.

During the measurements the sensors are biased with 300 V and four different parameters of the strip can be measured with the same contacting: the single strip current I_{strip}, the dielectric current I_{diel}, the coupling capacity C_{ac} and the poly‑silicon resistor R_{poly}. This is possible because the available switching matrix allows to switch between the different needed circuit schematics. The measurements are explained below and displayed in figure 7.17 and figure 7.18.
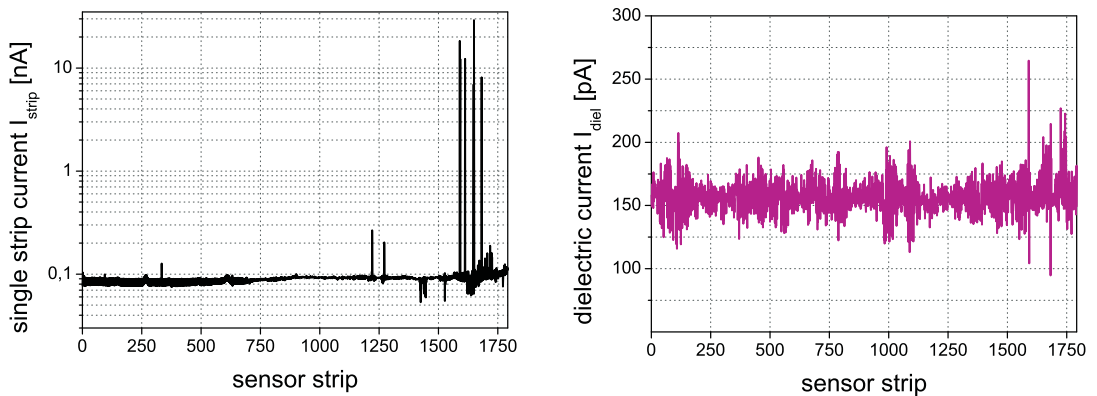
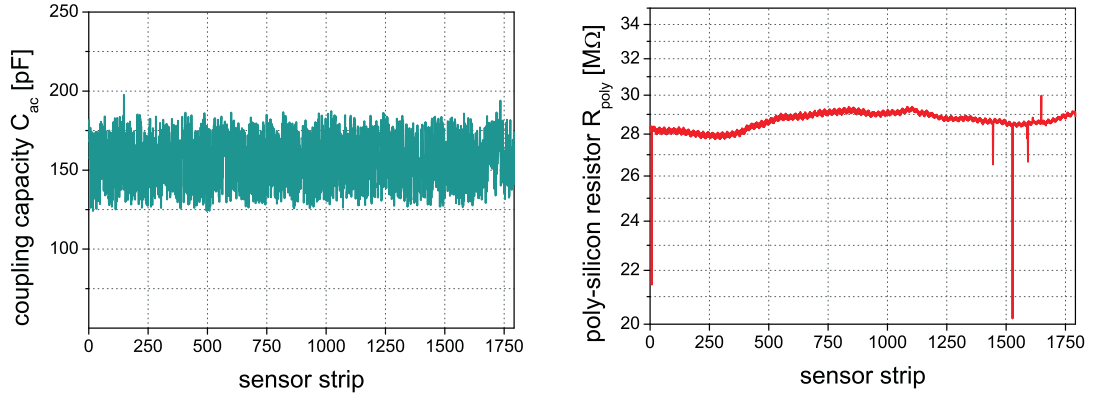Fig. 7.17: Single strip scan: strip current I_{strip} and dielectric current I_{diel}.

Fig. 7.18: Single strip scan: coupling capacity C_{ac} and poly-silicon resistor R_{poly}.

Single Strip Current (I_{strip})

With the measurement of the single strip current, done at a reverse bias voltage of 300 V, noisy strips can be identified. Such strips show a higher current than normal strips, possibly caused by scratches or other impurities induced during the sensor production, and can cause problems in the readout chip. During this measurement, the DC-pad of the strip is directly connected to the electrometer which measures the current against the external ground, thus by-passing the normal current path through the poly-silicon resistor. The measurements shown in the left of figure 7.17 revealed some noisy strips and an average single strip current of 0.138 nA.

Dielectric Current (I_{diel})

This measurement can reveal inhomogeneities of the dielectric layer between the p$^+$-strip implant and the overlying aluminium readout strip. The dielectric current is the electric current passing the dielectric layer when a voltage of 10 V is applied between DC-pad and AC-pad. So-called pinholes, electric shorts between the p$^+$-implant and the overlying aluminium, are the most severe strip damages in an AC-coupled strip sensor. Such strips have to be identified and left unconnected to the readout electronics, because pinholes cause the reverse bias current of the strip to flow through the pre-amplifier of the readout chip. Readout chips, like the APV25 chip, designed for AC-coupled strip sensors cannot cope with this increase in current and stop working properly when connected to a few of such defects. As visible in the right plot of figure 7.17 no pinhole was detected and the measurement revealed an average dielectric current below 160 pA.

Coupling Capacity (C_{ac})

The coupling capacitance is the capacity between the p$^+$-strip implant and the overlying aluminium readout strip and its measurement allows to electrically de-

termine single strip failures like opens or shorts. Figure 7.19 shows pictures of such faults detected at other sensors. The coupling capacity can be measured with a LCR meter connected between the DC- and AC-pad of the strip which reveals opens in the strip metallisation, e.g. caused by scratches, which decreases the effective area of a strip and thus reduces the measured capacitance. Opens lead to insensitive parts of the strip, because not the whole aluminium strip is connected to the readout electronics. Shorts between neighbouring channels can easily be detected by an increase in the measured capacitance. The number of connected strips in a short can be determined by dividing the measured capacitance by the average single strip capacitance. The measurements of the coupling capacitance are displayed on the left side in figure 7.18 and reveal a mean coupling capacity of 156 pF and no single strip failures.
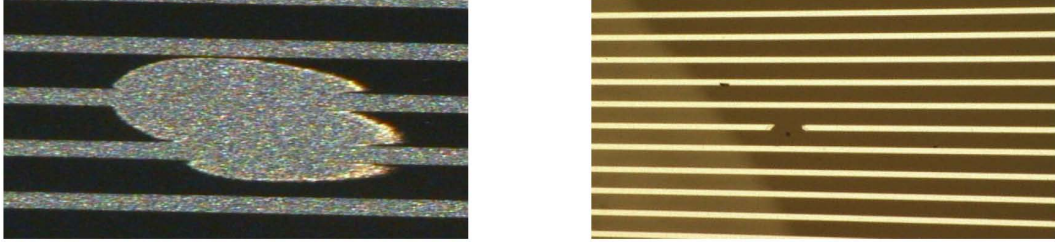
Fig. 7.19: Sample photos of single strip failures: left: a short between two strips - right: an open in the aluminium metallisation.

Poly-Silicon Resistor (R_{poly})

The poly-silicon resistors, as visible in the right picture of figure 7.13, connect each p$^+$-implant individually to the bias line of the sensor. Variations of R_{poly} lead to voltage differences among individual strips and to a non-uniform field distribution inside the silicon bulk. The measurements, shown in the right plot of figure 7.18, revealed very stable values well above the requested 20 MΩ.

7.6.3 Front-End Hybrid

The readout chip initially foreseen for the silicon layers at the LP setup, which is described in section 5.2.2 and still under development, was not available at the time of the module construction. Luckily this was predictable and with quite some effort it was possible to find an alternative.

The silicon detectors are designed and build with front-end hybrids remaining from the module production of the CMS Tracker End Caps [90]. These hybrids are already fully assembled and equipped with six APV25 chips [69], a 2:1 multiplexer (MUX), a phase locked loop (PLL) chip and a detector control unit (DCU), as shown in figure 7.20. All chips can be programmed and red out via an I^{2}C interface. Each APV25 chip has 128 readout channels and therefore one front-end hybrid

provides a total of 768 readout channels. Since the available clearance at the LP setup is not sufficient to use two of those hybrids side by side or on the opposite sides of the silicon sensors the read out sensor surface of the silicon detectors is reduced to a width of 38.4 mm.

Right from the start of the silicon layer design it was paid attention that it is possible to replace the used CMS hybrids when front‑end hybrids containing the newly designed readout chips are available.
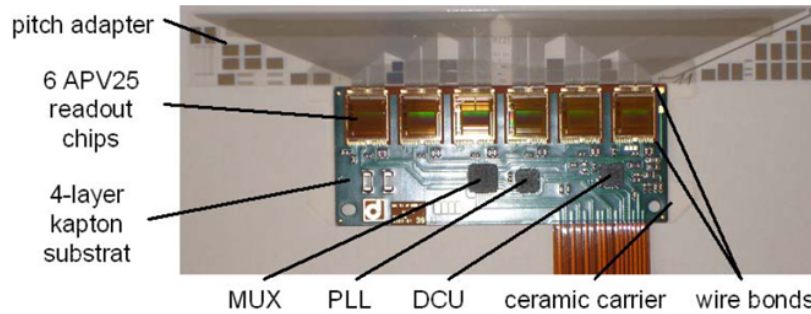

Fig. 7.20: Hybrid from the module production of the CMS Tracker End Caps.

Printed Circuit Board

The printed circuit board (PCB) of the front‑end hybrid is composed of a four layer circuit in Kapton technology and brings power and control lines to the integrated electronics.

APV25 Chip

This Analogue Pipeline Voltage chip is designed by the CMS collaboration and built on $0.25\,\mu$m CMOS technology. Figure 7.21 shows a block diagram of one of its 128 readout channels, which comprises a low noise amplifier, a 192 element deep analogue pipeline, operating with a default clock frequency of 40 MHz, and a deconvolution readout circuit. The incoming analogue signal from the silicon sensors gets amplified, shaped and stored in the pipeline every 25 ns. The deconvolution readout circuit can either form a weighted sum of three consecutive samples, effectively reducing the shaping time, in deconvolution mode or directly hand over the pipeline signal in peak mode. Running in deconvolution mode requires a clock‑synchronous beam, and thus cannot be used with the quasi‑continuous beam available at DESY. Therefore the APV is used in peak mode and all electrical tests shown are also performed in peak mode. Via an analogue 128:1 multiplexer the output data of each APV is transmitted on a single differential current output. The APV25 has an adjustable shaping time of about 50 ns and its equivalent noise charge (ENC) is $250\,e^- + 36\,e^-/$pF. The APV requires two operation voltages of 1.25 V and 2.5 V plus ground.
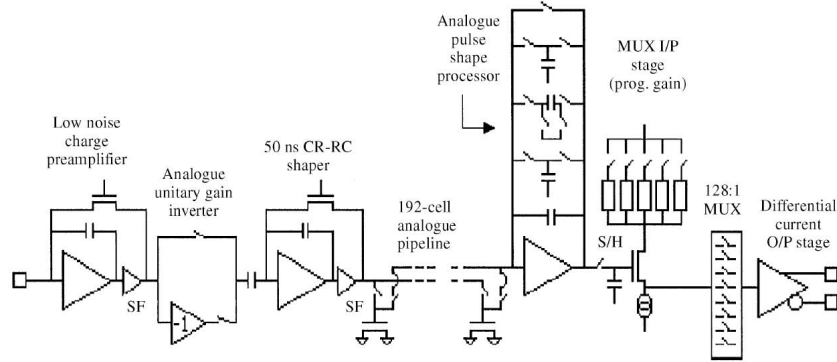
Fig. 7.21: Block diagram of one channel of the APV25 chip [69].

Phase Locked Loop

The PLL chip decodes the signal, containing clock and trigger information, for the MUX and the APV chips. For an accurate measurement of the analogue data from the APV chip it is crucial that the time jitter does not exceed 0.5 ns. Additionally to clock recovery and trigger decoding the PLL chip can also compensate clock delays, which can be introduced for example by cables of different lengths leading to variations in the runtime of different signals.

APV Multiplexer

The MUX chip multiplexes the signals from two APV25 chips and converts the current signal of the APV25 into a voltage signal.

Detector Control Unit

The DCU chip contains a 12‑bit ADC with an I^2C interface and allows to monitor the sensor temperatures, the leakage current and the low voltages of the APV25 chips and the hybrid.

Electrical Hybrid Tests

Before the hybrids were integrated into the silicon detectors all of them were electrically tested to verify their functionality. This was done with the ARC System at the HEPHY, which is described in section 7.6.10, which provides an automatic test routine. After a short self test of the test system, nine basic functionality tests are performed, which incorporate the validation of the I^2C communication, basic chip functionalities, and the power consumption of the hybrid. Afterwards the pedestal and the noise of each channel are measured, as shown in figure 7.22.
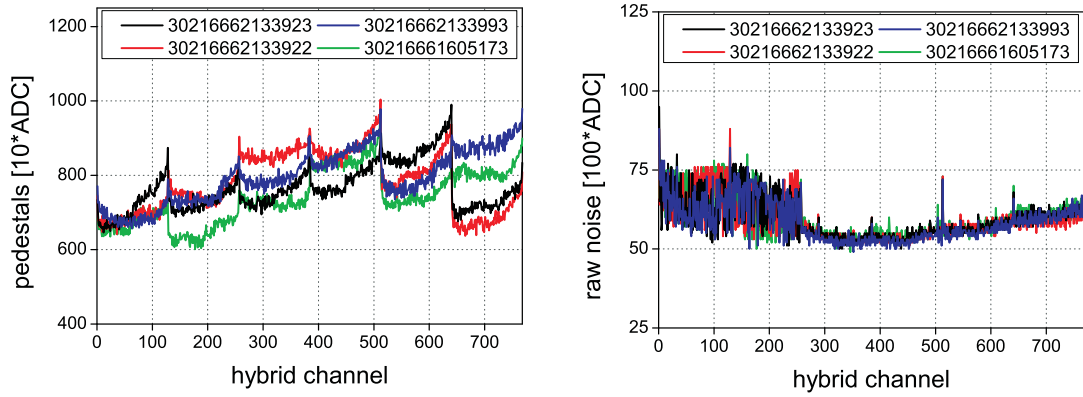
Fig. 7.22: Pedestal and noise measurements of each of the 768 channels of the used front‑end hybrids.

7.6.4 Intermediate Pitch Adapter (iPA)

The used CMS front‑end hybrids are already connected, mechanically and electrically, to a CMS pitch adapter (PA). This aluminium on glass PA connects the 768 channels of the six APV25 chips to the pitch of $143\,\mu$m, the readout pitch of the CMS Ring 2 strip sensors. Due to the size of the bond pads on the APV25 it is not possible to just disconnect the PA from the chips and contact a new one with wire bonds. Therefore the connected pitch adapter has to be used for the newly build silicon detectors. To connect the pitch of $143\,\mu$m with the readout pitch of $50\,\mu$m of the used silicon strip sensors a so‑called intermediate pitch adapter (iPA) had to be designed and produced. The intermediate pitch adapters were built in two different versions because shortly after the first version of iPA was produced by the company ILFA[6] also the Helsinki Institute of Physics (HIP) offered to produce a batch of pitch adapter:

1. ILFA

The first version of the iPA was designed with the program EAGLE[7] to be producible on a 4‑layer printed circuit board (PCB) by ILFA, an industrial company producing printed circuit boards. The design is defined by the fact, that ILFA cannot reliably process a pitch below $100\,\mu$m between two copper‑lines. Therefore the iPA is split on two PCB layers, each with Cu‑lines of $100\,\mu$m pitch, glued on top of each other. With this design an effective pitch of $50\,\mu$m can be obtained. Figure 7.23 shows the design of the intermediate pitch adapter, where the Cu‑lines on the top layer are indicated with red and that on the bottom layer with blue lines. A photo of such an iPA is shown in figure 7.24.
The production of these pitch adapters was on the limit for the company at the time

---

[6]ILFA Feinstleitertechnik GmbH: http://www.ilfa.de/
[7]Easily Applicable Graphical Layout Editor: http://www.cadsoftusa.com/

of production, but since the PA were produced successfully, such pitch adapters made on PCB are a cheap alternative to glass pitch adapters, especially interesting for future detector prototypes. The biggest advantage of such pitch adapters is, that the company electronically tests the functionality of every single channel on each PA and only delivers PAs which have a yield of 100 %.
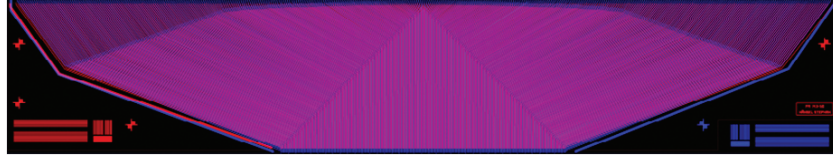

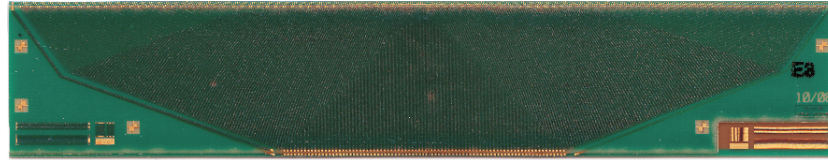Fig. 7.23: Layout of the intermediate pitch adapter produced by ILFA.

Fig. 7.24: Photo of the intermediate pitch adapter produced by ILFA.

2. HIP

The Helsinki Institute of Physics (HIP), Academy of Finland, designed and produced aluminium on quartz pitch adapter as shown in figure 7.25. The big advantage of this technology is, that it is possible to produce very fine conductive lines with a width of $10 \, \mu$m. Consequential the area needed for the PA is smaller and the size of the silicon detectors can be reduced. Because of the tough constraints in space at the LP setup, and because no problems with the production were expected, it was decided to design the silicon detectors with the pitch adapters produced by HIP, which have a width of only 10 mm. Compared to the width of 21 mm of the PAs from ILFA this is a huge gain. As described below, the PA from the HIP are unfortunately not of the expected high quality, but since all other parts of the silicon detectors were already produced when the PA from HIP arrived at the HEPHY it was too late to use the PA from ILFA.

Fig. 7.25: Intermediate pitch adapter produced by HIP.

Problems with the Pitch Adapter from HIP

- 1st batch
  Optical inspections at the HEPHY revealed, that all seven PA of the first
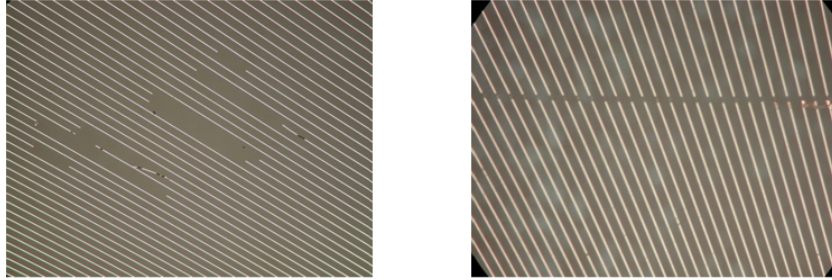

Fig. 7.26: 1st batch of iPAs from HIP.

batch of pitch adapters from the Helsinki Institute of Physics were faulty. Some of them had problems with the aluminium metallisation, figure 7.26 left, and the others had a lot of open lines or even long scratches as shown on the right photo of figure 7.26.
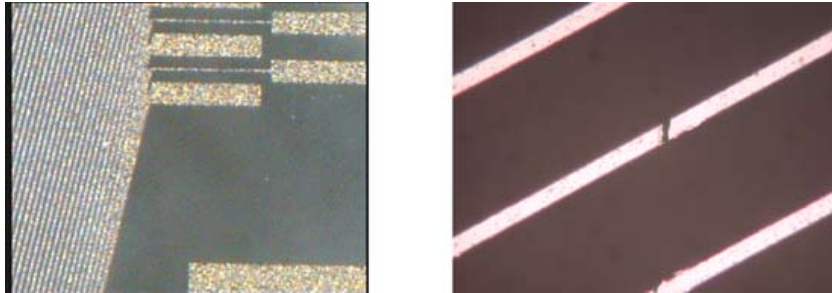
- 2nd batch
  A second batch containing 20 intermediate pitch adapters was produced

Fig. 7.27: 2nd batch of iPAs from HIP.

by HIP. According to the HIP the severe metallisation problems during the production could be corrected, but, nevertheless during an optical inspection with a microscope only two pitch adapters could be found with no visible faults. Important to mention is, that due to the very narrow lines it is not possible to detect all failures with a microscope, since opens of only one micron width, as displayed on the right photo in figure 7.27, can very easily be overlooked. Besides the opens in the metallisation, most of the PA had shorted aluminium lines at the outermost channels, as shown on the left picture in figure 7.27. An electrical measurement of the PA was not possible at the HEPHY, because the available automatic setup containing the moveable xyz-table does not allow to contact consecutive lines with different pitches at the same time.

Since it was not possible any more to use the PA from ILFA, it was decided to use the iPAs from HIP with the fewest visible failures for the production of the silicon detectors.

7.6.5   Carbon Fibre Support

The support structure of the silicon detectors is one of the major contributors to the material budget in the silicon detectors of the Tracker End-Caps of the CMS detector. For example, the support of the ring 7 detector modules containing two silicon sensors, which consists of two carbon fibre legs and one graphite plate, contributes with about 20 % to the relative radiation length of the total module. Because of the gained experiences, during the search for the ideal material and from tests with different material samples, the carbon fibre support of the two sensor detectors in the LP setup contributes only with about 7 % to the total radiation length of the detector, as visible in table 5.2. The backbone of each silicon detector consists of two carbon fibre T-beams. The material of the beams used for these detectors is not maximised in terms of radiation length and rigidity, but sufficient for the LP experiment and a first approach for future silicon strip modules for the ILD. Although there are companies which can produce carbon fibre U-, I- and T-profiles, it is not affordable for such a small quantity as needed here. SECAR[8] provided rectangular beams with a cross section of $3 \times 0{,}5\,\mathrm{mm}^2$. Since these beams do not provide enough stability for the needed lengths of 163 mm and 258 mm, two such beams were glued together with a thin film of epoxy adhesive[9]. To produce highly accurate T-beams with the needed length we designed and build an aluminium rail $(20 \times 20 \times 350\,\mathrm{mm}^3)$ with a Teflon insert, as shown in figure 7.28. After the glue is applied to the top surface of the vertical bar, the second bar is placed on top and weighted with another aluminium bar. The Teflon insert is important to ensure that overlapping glue does not adhere the beams to the rail and that excessive glue can easily be removed after the curing.
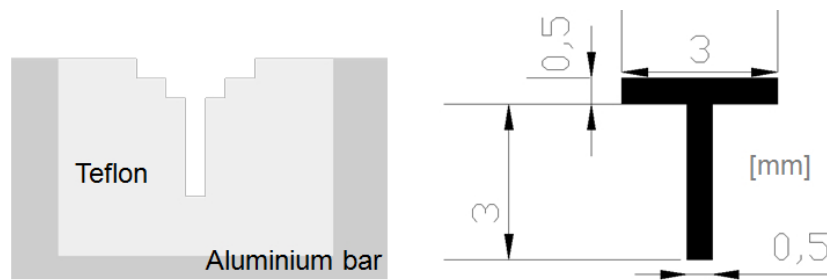

Fig. 7.28: Cross section of the aluminium rail with the Teflon insert (left) and profile of the carbon fibre T-beams (right).

---

[8]SECAR Technologie GmbH: http://www.secar.at/
[9]Epoxy AW 106: 2011 ARALDITE, Huntsman

Static Load Tests

The rigidity of the T‑beams was verified with static load tests and enabled the calculation of the Youngs modulus of the T‑beams with:

$$E = \frac{F \cdot L^3}{48 \cdot y_{max} \cdot I} \tag{7.12}$$

Here F is the applied force, L is the length of the beam, I is the moment of inertia, which can be calculated with the parallel axis theorem, and y_{max} is the measured deflection under load. The deflection was measured with the help of a coordinate measuring machine from the company Mitutoyo, available at the HEPHY Vienna. Figure 7.29 shows the measurement setup located on the table of the coordinate measuring machine with a load attached to the centre of the T‑beam, which is hold on each side by an aluminium piece containing a slot like that of the rail described above.

   The measurements revealed that the used carbon fibre beams have a Young's modulus of approximately 150 GPa and that the behaviour of the beam is stable in time, verified by measurements repeated after up to 4 hours with a load of 500 g. To approve these measurements, also the Young's modulus of a carbon fibre leg of a CMS Tracker End Cap ring seven module was measured. The Young's modulus was determined to be slightly above 300 GPa which matches exactly its production specifications [91].
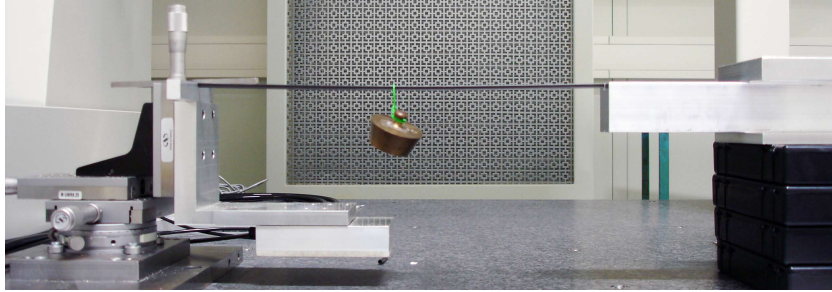

Fig. 7.29: Static load tests of the carbon fibre beams.

7.6.6   Kapton Foil

The bias voltage is delivered to the sensor backplane via copper lines of 17 μm height integrated on Kapton foils. The foils have a total height of approximately 100 μm and are modified leftovers of the CMS sensor recuperation campaign. These Kapton foils contain a lowpass filter to stabilize the HV line. In addition thermal probes are placed on the Kapton foil, which enable the measurement of the temperature very close to the silicon sensors. The electrical connection between the HV pad on the top surface of the Kapton foil and the sensor backplane is accomplished with a conductive glue[10].

---

[10]EPO‑TEK EE129‑4

7.6.7   Support Frame

The two silicon detectors of each detector modules are hold together by three frames made of Isoval®11[11] which are screwed together as shown in figure 7.30. This is also visible in figure 7.11 where the two photos show one module from both sides without top frame.

Isoval®11 is a composite of a resin epoxy reinforced with a woven fibreglass mat. It has a high rigidity, a low mass, is an insulator and rather easy to mechanically process. The only disadvantage of Isoval®11 is that it is not light tight. This makes it necessary to cover the detector modules with a light‑tight foil.

Since one requirement to the frame is, that it should be possible to exchange the silicon detector modules, the three support parts of each detector module are screwed together, and the carbon fibre beams and the HV and signal cables are not glued but only clamped between the frames. This makes it very easy to mount other detector modules, supported by carbon fibre beams of the same size, containing other sensors or different front‑end hybrids, into the frame.
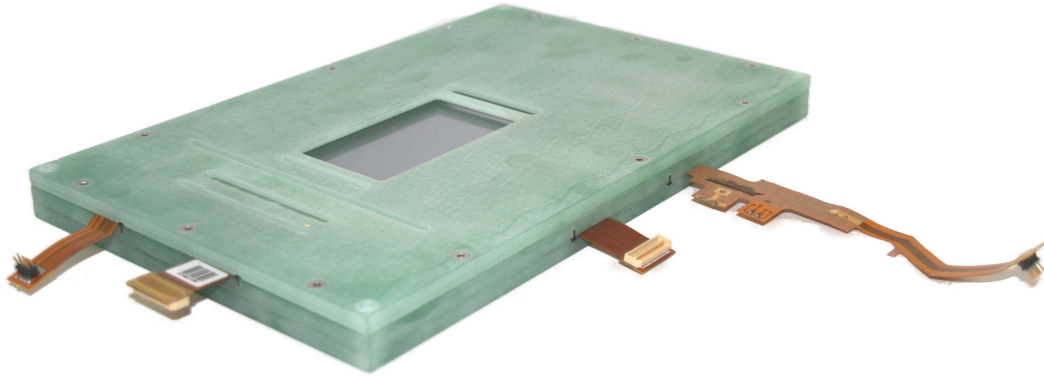

Fig. 7.30: Silicon detector module without light‑tight foil.

7.6.8   Assembly of the Silicon Detectors

The alignment of the different detector parts during the assembly was done with the help of the coordinate measuring machine at the HEPHY. Over the period of the gluing process, the sensors can be sucked by vacuum to the bottom side of a moveable xyz‑gibbet and positioned on the carbon fibre beams clamped onto the central support frame of the detector module. To electrically isolate the carbon fibre beams from the rest of the module their top surfaces are covered with a HV tape[12]. This tape has a thickness of 0.06 mm and can withstand up to 4.5 kV. The introduction of this tape also ensures, that the detector modules can be disassembled if necessary, like it had to be done for detector SiLC11, as described in

---

[11]Isovolta AG: www.isovolta.com
[12]TAPE POL. YELLOW, 4.5kV, 0.06 × 12 from the CERN store

section 7.6.10.4. The silicon sensors are glued onto this tape with a thin film of silicone glue[13] and the hybrid and intermediate pitch adapter with a thin film of the same epoxy adhesive as used to form the carbon fibre T-beams.

Wire Bonds

The different detector components are electrically connected to each other using ultrasonic wire bonding. This is a procedure, where small aluminium wires, including 1 % silicon, with a diameter of 25 μm, are soldered to the designated bonding pads. The bonding between the CMS PA and the iPA, the iPA and the near sensor and between the two sensors was done with the Delvotec 6400 automatic bonding machine available at the HEPHY.

The bonding for the near sensor was more or less unproblematic, since the sensor strips were connected on the side without poly-silicon resistor. But, due to the small readout pitch of the sensors and the 2.24 cm long poly-silicon resistors, visible in the right picture of figure 7.13, the connection of the two sensors of the long detectors was a very challenging task. The pitch of 50 μm prohibits the use of the same loop height for neighbouring bonds and therefore the bonds have to be arranged in two rows on top of each other. To connect the two bond pads closer and farer from the sensor edge a bond length of 4.6 cm and 5.4 cm, respectively, is needed. Nevertheless, bond tests performed on test structures, as shown in figure 7.31, including pull force tests, revealed that the bonding is feasible, but not advisable for a mass production.
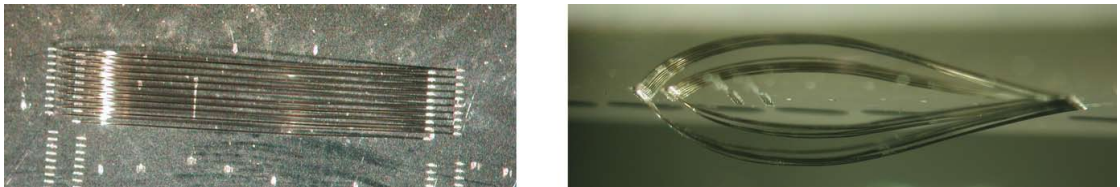

Fig. 7.31: Bonding tests performed on a test structure: the bonds are arranged in two rows on top of each other and have lengths of 4.6 cm and 5.4 cm.

7.6.9   Final Detector Modules

The finalised detector modules have a size of $165 \times 20 \times 260\,\text{mm}^3$, including a light-tight adhesive foil with a thickness of 1 mm on all sides. The components of the silicon detectors are listed in table 7.4. Here the near sensors are bonded to the intermediate pitch adapter and the far sensors are connected to the appropriate near sensors. The names of the hybrids come from the CMS module production. The silicon layers are named front and back, which indicates the position of the layer along the beam line with respect to the Large TPC Prototype. Inside the layers

---

[13]DOW CORNING, 3140 RTV COATING; non-corrosive Silicon Rubber, flow able

the silicon detectors containing two sensors are closer to the TPC than the detectors with one silicon sensor. Because of the problems described in section 7.6.10.4 the detector SiLC11 had to be disassembled and its silicon sensor was integrated into a new detector named SiLC11b.

layer	silicon detector	hybrid TEC_6D.2.1 /	near sensor HPK‑ILC‑6684‑	far sensors HPK‑ILC‑6684‑
back	SiLC01	30216662133923	01	
	SiLC02	30216662133993	19	05
front	SiLC11	30216662133922	23	
	SiLC11b	30216662133904	23	
	SiLC12	30216661605173	34	27

Tab. 7.4: Components of the silicon layers and silicon detectors.

7.6.10 Final Tests with the ARC System

Before the detector modules are wrapped into a light‑tight foil, the silicon detectors were tested at the HEPHY with an APV Readout Controller (ARC) System, displayed in figure 7.32. This system was initially developed by RWTH Aachen for the quality assurance during the production of CMS silicon strip modules [92]. It provides full hybrid support like power, trigger, clock and slow control and contains a dedicated software for a variety of electrical tests. Here only a very brief description of the APV Readout Controller (ARC) System is given, which is divided into a software and a hardware part:

- **software**
  The ARC System is controlled by a standard Windows PC running the APV Readout Controller Software (ARCS), which is a Labview 6i application and serves as graphical user interface to the hardware test setup. The registers of the APV25 chips, sitting on the front‑end hybrid, can be configured using an I^2C bus controlled by the software. With the ARC system it is possible to perform a variety of tests to verify the functionality of the integrated circuits of the front‑end hybrid and the mounted chips. To test the silicon strip sensors it is possible to take an IV curve, record the noise and make a calibration pulse shape measurement which uses an APV‑internal calibration signal circuit. These tests reveal severe sensor problems and also single channel faults like opens, shorts, pinholes and saturated channels, as described in detail in [93].

- **hardware**
  The PC acts as the control device of the ARC board, the main board of the setup, which is mounted into a common NIM crate. The ARC board

is connected to the front-end hybrid of the silicon detector via the ARC front-end adapter and the hybrid-to-VUTRI adapter, both located inside a light-tight, humidity controlled test box which also serves as Faraday cage. The two other boards located in the NIM crate are the Depletion Power (DEPP) board and the LED controller. The DEPP board provides high voltage up to 600 V to bias the silicon sensor and to measure its dark current. The LED controller steers 16 infrared light emitting diodes (LEDs). Via an array of 64 optical fibres, located above the detector under test, the LEDs can be used to induce charges into the silicon sensors.
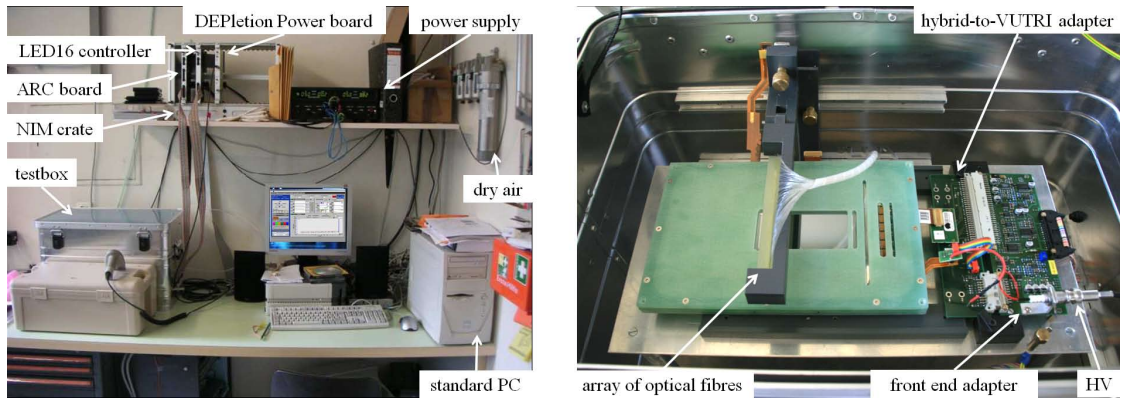
Fig. 7.32: Picture of the ARC setup (left) and look inside the test box with connected detector module (right).

7.6.10.1 IV Scan

During the IV scans of the silicon detectors the bias voltage of the sensor is ramped from 0 V to 450 V in steps of 10 V, while the current is recorded. A high bias current is an indication for sensor failures like scratches or pinholes. A breakthrough in the IV scan points towards serious failures that can be caused by heavy sensor damages or by micro discharges. The IV measurements of the detectors, displayed in figure 7.33, reveal, that all work perfect, except for detector SiLC11 which is discussed below. Naturally, the currents of the detectors containing two silicon sensors, SiLC02 and SiLC12, are about twice as high as that of a faultless detector containing just one sensor. All detectors can be used for the LP experiment without a concern at the foreseen operation voltage of 100 V.

The behaviour of detector SiLC11 containing sensor HPK-ILC-6684-23 is suspicious and the fact that the behaviour got worse after the sensor was dismounted and reused to build detector SiLC11b clearly points towards a sensor failure. Since the sensor did not show this behaviour during the IV scan before its assembly, compare figure 7.15, most probably the sensor was slightly damaged during the detector assembly. Nevertheless the current is not alarmingly high and the silicon detector SiLC11b can be used without solicitude.
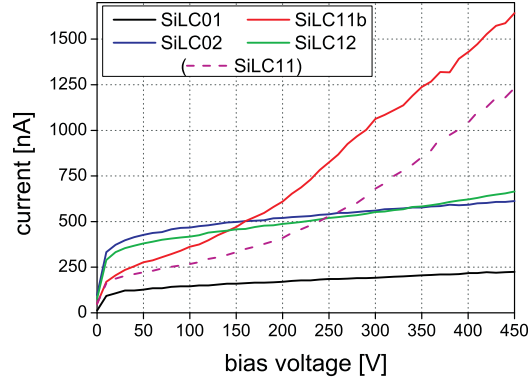
Fig. 7.33: IV curves of the silicon detectors.

7.6.10.2   Hybrid Tests

After the proper functionality of the test system itself is checked it is verified that the I^{2}C communication works proper. Then a series of electrical tests measure the operability of the front‑end hybrid. These tests verify the basic functionality of all the integrated circuits on the hybrid and the mounted chips described in section 7.6.3, namely the six APV25‑, DCU‑, MUX‑ and PLL‑chip. Any failure would indicate a major problem and would lead to the exchange of the hybrid.

7.6.10.3   Single Channel Noise

The raw noise of a channel is the root mean square fluctuation of its raw data around its pedestal. The pedestal of a channel is defined as the average strip output level without any particle or calibration signal. Because of electronic noise pick‑up at the inputs of the APV‑preamplifier an event by event baseline shift, common to groups of neighbouring channels or even all channels of an APV can occur. This effect is called common mode noise and used to evaluate the common mode subtracted noise for each channel, which is its raw noise corrected for these baseline shifts. This common mode subtracted noise assesses the quality of a channel with respect to its noise behaviour and is the value referred to as noise in the following.

From the noise of a channel, or the deviation from it with respect to the average noise, it is possible to see, if and why a channel is faulty. The displayed measurements in figure 7.34 show channels with opens, indicated by a lower than average noise. For the detectors containing two sensors it is easy to differentiate between opens on the pitch adapters or the pitch adapter to sensor connection and opens between the two sensors. This comes from the fact that the channel noise decreases with decreasing capacity and therefore the deviation from the normal noise gives information about the location of the open. Optical inspections revealed, that the majority of these opens are located on the intermediate pitch adapters. Since these opens are discrete in the centre regions and only concentrated on the sensor edges,
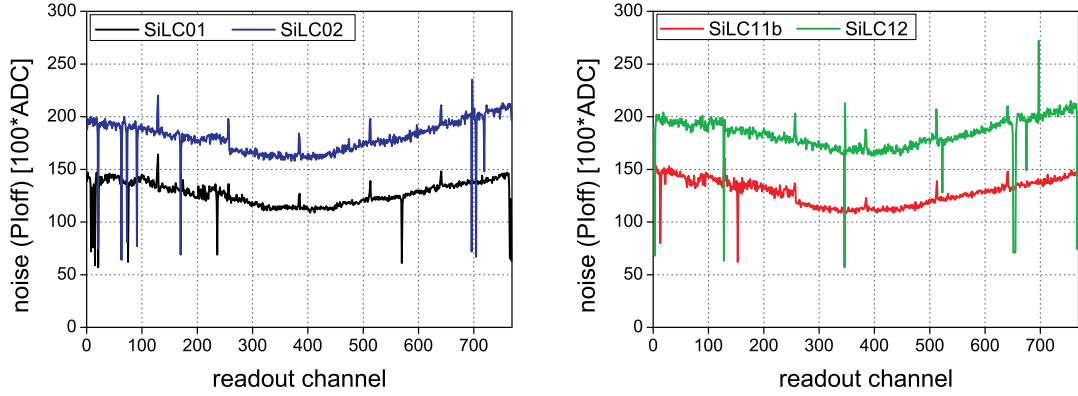
Fig. 7.34: Single channel noise of the silicon detectors $(1 \, \text{ADC} \cong 770 \, \text{e}^-)$.

and due to the lack of good iPAs it was decided to use these silicon detectors for the first LP studies.

7.6.10.4   SiLC11 and SiLC11b

Some problems occurred with the silicon detector SiLC11. This first detector had to be disassembled, which was rather easy because of the HV tape on top of the carbon fibre bars. Then the detector SiLC11b was assembled with the same sensor and carbon fibre bars, but a different front-end hybrid, intermediate pitch adapter and Kapton foil. The following list shortly describes the history of this silicon detector:

- The noise measurements of the silicon detector SiLC11 with the ARC system revealed a lot of channels containing opens. These channels are clearly visible in the noise plot shown in figure 7.35, as channels with a much decreased noise. In addition two very noisy channels, namely channel 2 and 3, can be seen.
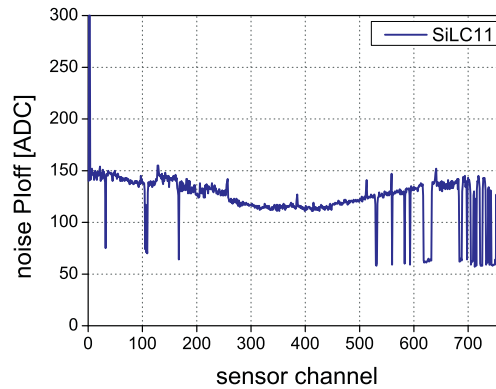

Fig. 7.35: Single channel noise of detector SiLC11.

- After the re - assembly of the usable components of SiLC11, detector SiLC11b also showed too many open channels, as shown in the left plot of figure 7.37.

- An optical inspection with the microscope revealed bonding failures on the bond pads of the intermediate pitch adapter, shown in figure 7.36, most probably caused by dirt on the bonding pads. The three pictures were taken with increasing focus heights from left to right: in the left picture the bond pads are brought into focus; in the centre picture the outer two connected bond feet; and in the picture on the right the inner two, unconnected bond feet are brought into focus.
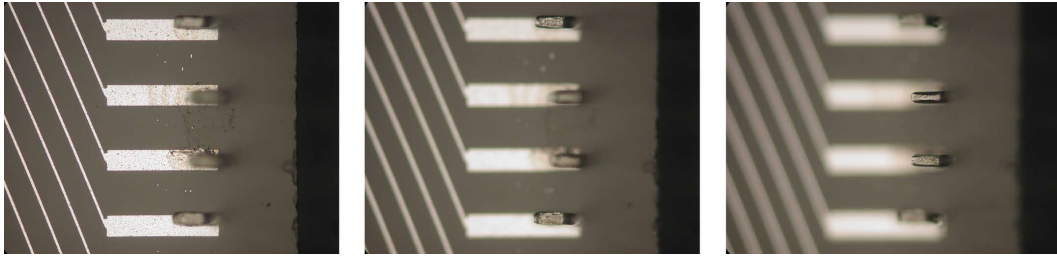

Fig. 7.36: Bonding failures: focus on the bond pads (left), focus on the outer, connected bond feet (centre) and focus on the inner, unconnected bond feet (right).

- After the faulty bonds were re - bonded the detector had only two remaining open channels, visible in the single noise measurement shown in the right picture of figure 7.37. An optical inspection revealed, that these two opens are caused by gaps in the aluminium lines of the intermediate pitch adapter.
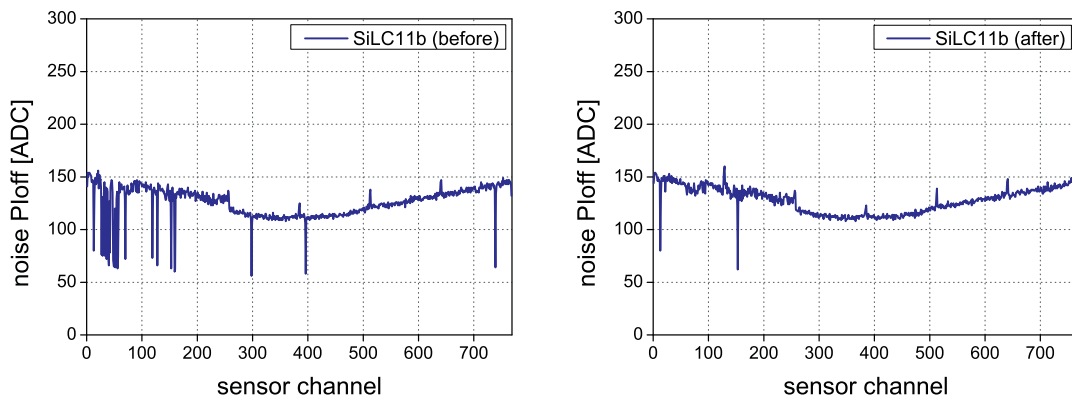

Fig.7.37: Single channel noise of detector SiLC11 before (left) and after re - bonding (right).

7.6.11 Adapter Cards

The available space in the gap between magnet and the TPC is not sufficient for the cards of the readout electronics which have to be connected to the front‑end hybrids, compare section 7.7. Therefore twisted pair cables with a length of two meters are needed to connect the silicon detectors inside the gap to the readout electronics located outside the magnet. To connect the plugs of the readout system with the twisted pair cable a set of three adapter cards is needed. They were designed with the program EAGLE[14] and produced on a 2‑layer printed circuit board by LeitOn[15]. The twisted pair cables are crimped on both ends to a commercial connector[16]. The first card connects the CMS hybrid, containing a special CMS connector[17], to the twisted pair cable. The other two cards connect the cable to the CMS connectors[18] on the ICC boards of the used data acquisition system. Because of spatial constraints two different cards are needed for the connection to the ICC board, as visible in figure 7.41.
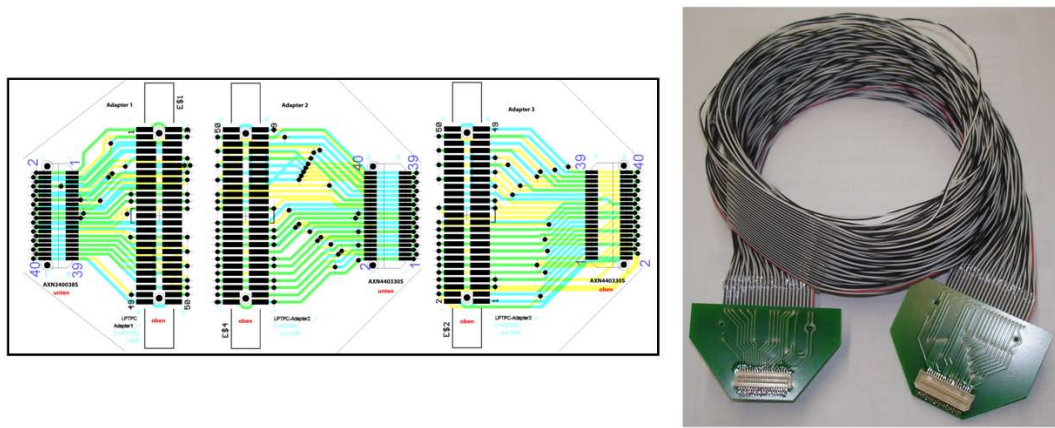

Fig. 7.38: Schematic of the three needed adapter cards (left) and photo of two adapter cards connected with the used 2 m long twisted pair cable (right).

Figure 7.38 shows the schematic of the three adapter cards and a picture of one of the four needed elongations, consisting of two adapter cards connected with a twisted pair cable. The left adapter card in the schematic is designed to connect the CMS hybrids to the twisted pair cables and the other two are used for the connection of the twisted pair cables to the ICC board.

Figure 7.39 shows a comparison of the single channel noise measured with and without extension and reveals, that the increase in noise is marginal. This test also verifies, that the adapter cards were designed correctly and that the different production steps like soldering and crimping of the connectors succeeded.

---

[14]Easily Applicable Graphical Layout Editor: http://www.cadsoftusa.com/
[15]LeitOn GmbH: www.leiton.de
[16]FTSH-125-01-L-DV-EJ-K-A
[17]AXN440330S
[18]AXN340038S
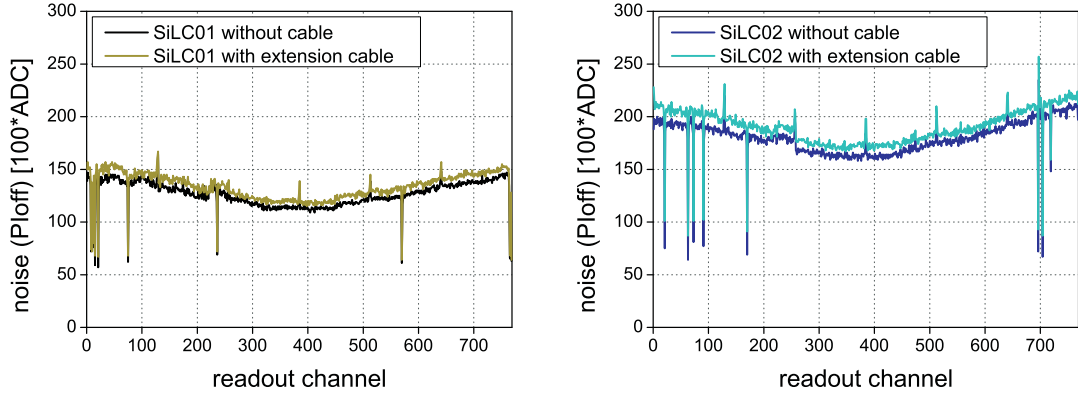
Fig. 7.39: Comparison of the single channel noise with and without extension cable $(1\,\mathrm{ADC} \widehat{=} 770\,\mathrm{e}^-)$.

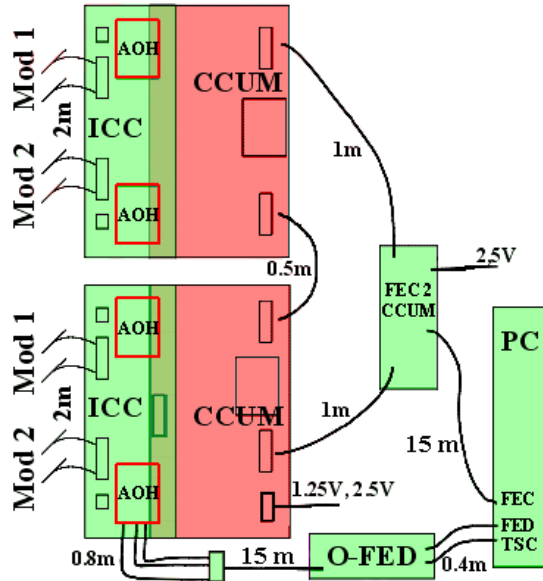## 7.7   Silicon Data Acquisition System

Fig. 7.40: Schematic of the silicon data acquisition system.

The data acquisition (DAQ) system of the silicon envelope is the subsystem which is used to gather the signals from the silicon sensors, save them to disc and to further process the data. It consists of a hardware and a software related part as described below. The initial foreseen DAQ system, working with the front-end readout chip currently under development for the ILD silicon tracker, was not available. Therefore we were forced to search for alternatives. Since both institutes, the IEKP and the HEPHY, were heavily involved in the production of the CMS Tracker, as short term solution it was possible to adapt a CMS silicon

detector test system and to provide a working silicon DAQ system. This system is based on the XDAQ system [94], a software product line that has been designed to match the diverse requirements of data acquisition application scenarios of the CMS experiment.

The data acquisition system is divided into a readout chain and a control sequence as shown in the figures 7.40, 7.41 and 7.42:
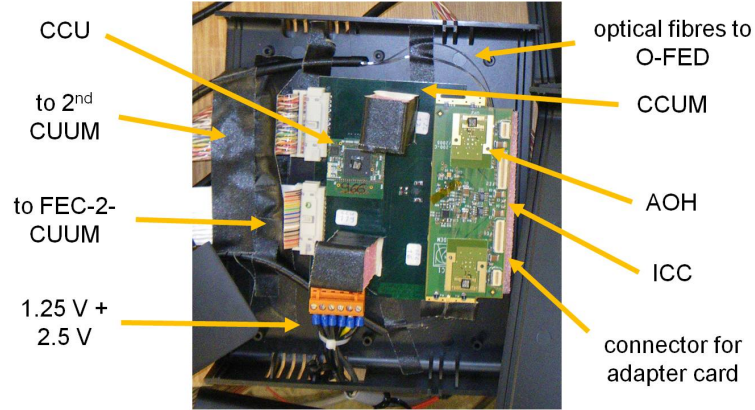

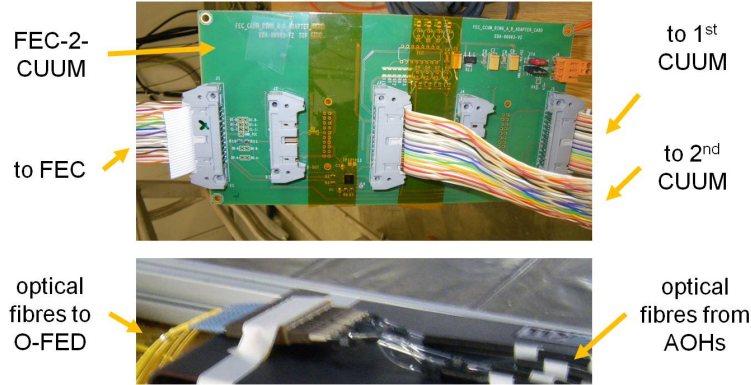Fig. 7.41: Silicon data acquisition system 1.

Fig. 7.42: Silicon data acquisition system 2.

- **readout chain:**
  After receiving a trigger, the signals from the silicon sensors, stored temporarily in the pipeline of the APV25 readout chip sitting on the front‑end hybrids of the silicon detectors, are read out. The amplified current signals of two APVs get multiplexed and transformed into voltage signals in the MUX, also located on the front‑end hybrid. These signals are transferred via four 2 m long twisted pair cables, one for each silicon detector, to the Inter Connect Cards (ICC) sitting outside the gap of the LP setup on top of the magnet. Each of the two ICCs host two Analogue Opto Hybrids (AOHs) [95] where the detector signals get converted into analogue optical signals.

This is done by three single pigtailed laser diodes with a Linear Laser Driver (LLD) ASIC. The optical signals are transferred via 15 m long optical links, each transferring the analogue signal of 256 channels, to the Optical Front End Driver (O‑FED) outside of the test beam area in the control hut. There they get re‑converted to electrical signals which are delivered to the Front End Driver (FED) [96] card in the DAQ PC.

- **control sequence:**
  The DAQ PC configures and controls the system via the Front End Control (FEC) [97] card. The trigger signals are produced by the Trigger Sequencer Card (TSC) in the PC, which receives the trigger signals from the Distributor Box (DB) [89] of the test beam trigger system, compare section 7.5. All digital signals, namely I^2C control, clock and trigger are transferred via 15 m long twisted pair cables to the Central Control Units (CCUs) [98], sitting on the Central Control Unit Modules (CCUMs) cards, located on top of the magnet inside the test beam area. From there these signals are brought via the ICCs and the 2 m long twisted pair cables to the front‑end hybrids of the silicon detectors.

7.8 Silicon Support

The moveable silicon support allows to position the silicon sensors of the detector modules inside the gap between magnet and TPC. It has to compensate all movements of the superconducting magnet to ensure that the sensitive silicon areas stay inside the electron beam. Such magnet movements are important to enable measurements with the beam traversing different regions of the inhomogeneous magnetic field. Since also rotations of the magnet are foreseen, to enable measurements with slanted tracks, the silicon support has to be composed of two independent parts, one for each silicon layer.
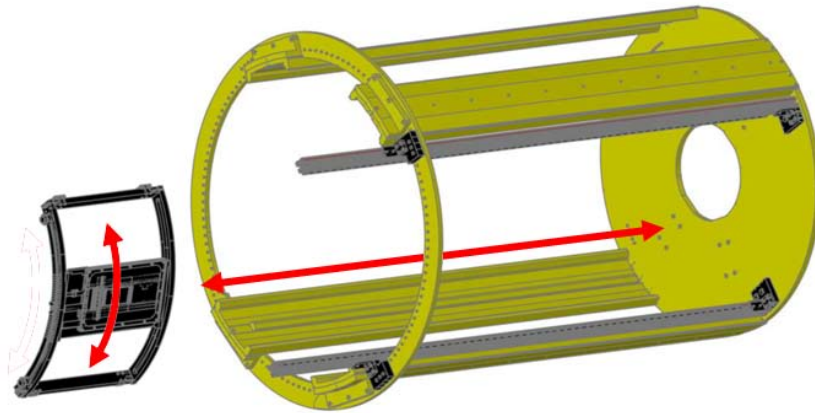

Fig. 7.43: One half of the silicon support mounted into the TPC support.

The moveable support structure was designed and built from the IEKP and the HEPHY. All parts are made of non‑magnetic materials, mainly aluminium, and screwed together with non‑magnetic screws. Each of the two halves consists of two long rails mounted into the support structure of the TPC. It is possible to move a curved sledge, holding the silicon detector modules, along those rails, in and out of the gap between magnet and TPC. The curved sledge is built in a way, that the detector modules can be moved along its curvature to position them vertically.

Figure 7.43 shows a technical drawing of one half of the silicon support system. Two long aluminium bars (grey) are mounted onto the inner and outer ring of the TPC support structure (yellow) with the help of four aluminium brackets (black). Sliding rails from the company igus[19] are mounted onto the side of each bar facing the other. The black curved sledge in front of the support is equipped with four slide bearings, also bought from igus, which enable movements along the sliding rails on the bars.
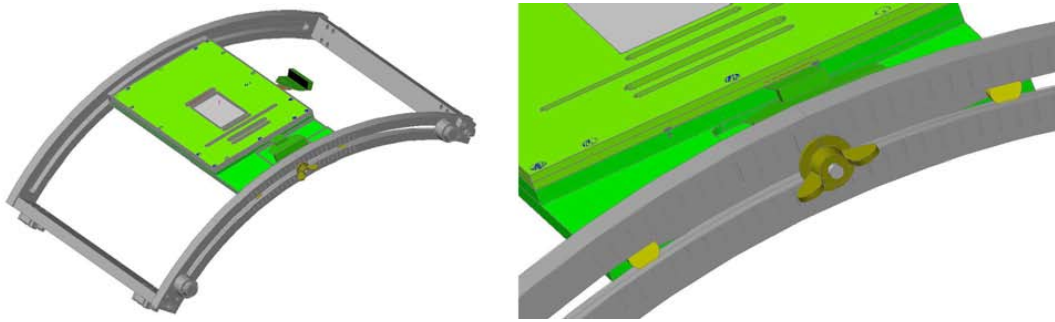

Fig. 7.44: Technical drawing of one silicon sledge.

Figure 7.44 shows a more detailed drawing of one silicon sledge containing one detector module. The adapter cards, described in section 7.6.11, are also included but not the twisted pair cables which are guided out of the sledge through the trench in its front side. The silicon detectors can be moved inside the curved sledges along the visible trenches, gliding on plastic rolls, shown in yellow in the right picture of figure 7.44, to the desired position and then fixed with a lining disc and a winged nut (gold) made of brass. The detector modules can be aligned with the help of a notch in the lining disc and 25 notches, in steps of one degree, milled into the front side of the sledge, which are visible on the right photo in figure 8.1.

7.9   Final Test with Cosmic Rays

After the functionality of the silicon modules was verified with the ARCs system in Vienna, they were brought to the IEKP where the silicon DAQ system has been built up. This test was very important to verify the silicon system before
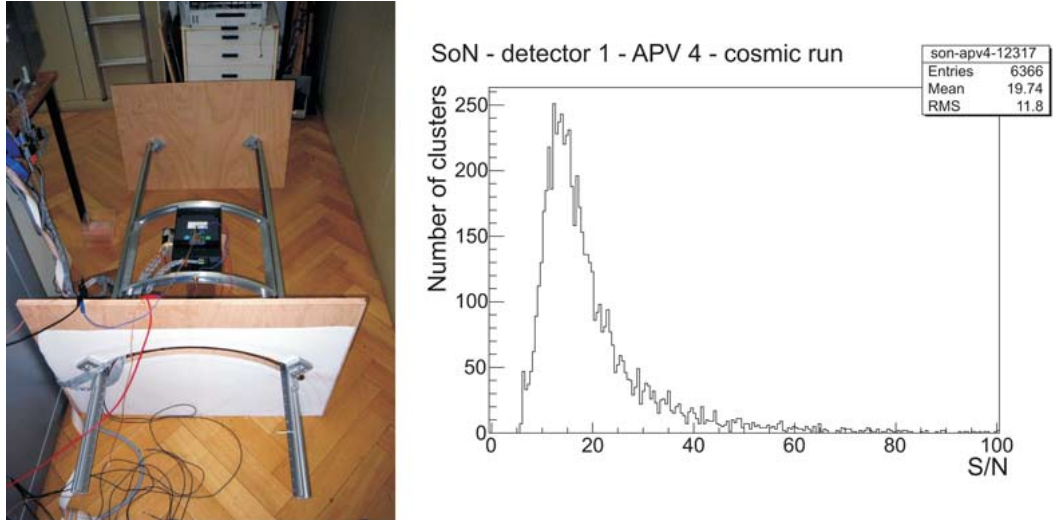
---

[19]igus® GmbH: www.igus.de

Fig. 7.45: Final test with cosmic rays at KIT.

its installation into the LP experiment at DESY. This was the first time that the different parts of the moveable support, see section 7.8, produced by the IEKP and the HEPHY, were built together and that the silicon detectors were read out using the final silicon data acquisition system, described in section 7.7. Since the TPC support of the LP was not available at the IEKP, the silicon system was mounted in between two wooden plates as shown on the left picture of figure 7.45. To be able to test the movements of the silicon layers a curved slot with the dimensions of the gap between magnet and TPC was cut into one wooden plate. This picture also views the setup as used during tests with cosmic rays, including all cables and the silicon DAQ system as used in the LP experiment. The coincidence signal of two quadratic scintillators, located on top and bottom of the silicon layer, was used as trigger signal. With the DAQ software pedestal subtraction, common mode correction and cluster search leading to the hit positions can be performed. The right picture of figure 7.45 shows the signal to noise ratio of the 128 channels of one APV chip recorded with cosmic rays. The measured mean signal to noise ratio is close to 20. This relative low signal to noise is caused by the signal reduction due to the use of two glass pitch adapters in the silicon detectors, the length of the extension cables and due to the fact that the environment in this setup is not optimised for low noise performance.

7.10   Installation in the LP Setup & Final Tests

To mount the silicon support into the support structure of the TPC it was necessary to dismount the TPC support out of the magnet. The left picture of figure 7.46 shows a photo of the first movement tests of the silicon sledge along the aluminium bars outside the TPC. This was a very important test, since it revealed that the end plates of the TPC are not mounted centrically, due to an offset of their hole

Fig. 7.46: Pictures of the silicon support mounted on the LP support.

patterns, so that the silicon sledges slightly touched the end plates during their movements. Fortunately it was possible to grind away small parts of the silicon sledges to enable smooth movements. Then the TPC support structure containing the bars of the silicon support was mounted into the magnet. The right picture of figure 7.46 shows the first movement tests of a silicon sledge inside the magnet. These movements can be done with a long pole, as visible in the picture, from outside the gap between TPC and magnet, which also acts as measuring stick for the positioning of the sledges. Final movement tests with also the TPC inserted proved that everything worked as expected. Also the installation of the silicon data acquisition system was smoothly and everything fitted into place. Finally it was possible to perform IV scans and pedestal runs of the silicon detectors located inside the gap between TPC and magnet from the electronics hut outside the test beam area without any problems.

Chapter 8

Combined Test Beam and Results

In November 2009 the first combined test beam of the silicon system and the Large TPC Prototype was performed in the test beam area at DESY. Since this is a first verification run and because of the studies presented in section 8.3, showing that it is not possible to align the LP with the silicon layers using just one TPC panel, it was decided to operate without magnetic field and to make the measurements with straight tracks. The possibility to use two TPC panels was not foreseen in the beginning and was not available before the last days of the test beam, far too late to start with the cooling of the magnet.

To minimise the average number of recorded tracks per event inside the TPC the beam intensity is reduced by setting the momentum of the electron beam to $5.6\,\mathrm{GeV/c}$ [99]. With this beam configuration about $28\,\%$ of the recorded events have exactly one cluster in all four silicon layers. The reason for this relative low amount of singe track events is mainly caused by multiple scattering in the magnet wall in front of the first silicon layer.
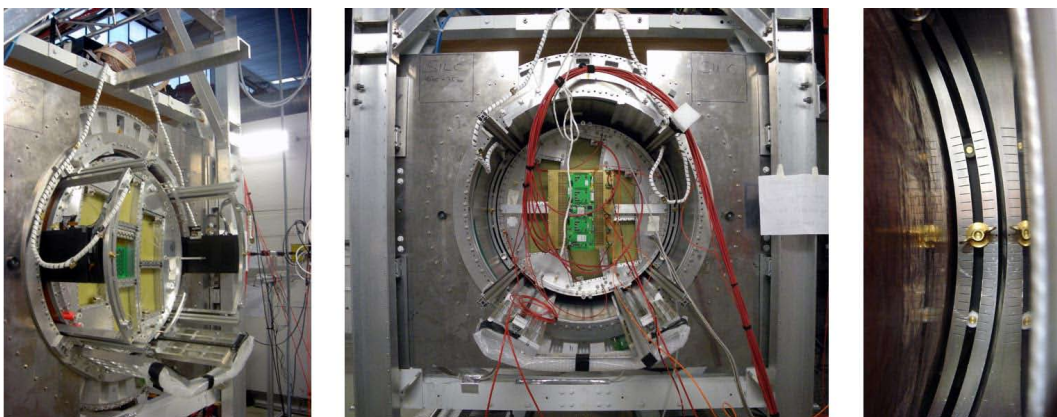

Fig. 8.1: Combined test beam: silicon sledges moved outside of the gap between magnet and the TPC (left), arrangement during data taking with one Micromegas panel in the centre position of the TPC end plate (centre) and silicon sledge inside the gap between TPC and magnet (right).

Figure 8.1 shows three pictures of the LP setup with the electron beam going from right to left. In the left picture one can see the silicon sledges moved out of the gap. In this position it is possible to loosen the winged nut, which fixes the silicon detectors inside the sledge, and adjust the height of the sensors. The signal and HV cables, running from the silicon detectors to the readout electronics located on top of the magnet, are protected by a white plastic spiral. The right picture of figure 8.1 views a close up of one silicon layer inside the gap between Large TPC Prototype and the surrounding magnet.

In a first run we collected about 20,000 triggered events with one Micromegas panel [86] mounted at the centre position of the LP end-plate, surrounded by six dummy modules, as visible on the central photo of figure 8.1. As described in section 7.4.3, the Micromegas are equipped with electronics based on the AFTER-chip.

To increase the number of measured track points inside the TPC a second run with two Micromegas panels was performed. The second panel was mounted on the top right position, compare the central picture of figure 8.1, of the LP end-plate. To ensure that the electron beam traverses the TPC volume in front of both TPC readout panels it was necessary to lower the magnet by 36 mm, which in turn had to be compensated by the silicon support. The alignment of the silicon layers worked perfect and with this second configuration about 60,000 triggered events were collected.

8.1   Trigger Logic

During the test beam it was not possible to use the trigger logic as initially proposed, described in section 7.5, because the DAQ system of the used TPC electronics was not able to write neither the trigger number nor the time stamp, provided from the Distributor Box (DB), into its output files. Furthermore the TPC DAQ could not provide a busy signal to communicate with the DB. Therefore it was required to adapt the trigger system as sketched in figure 8.2.
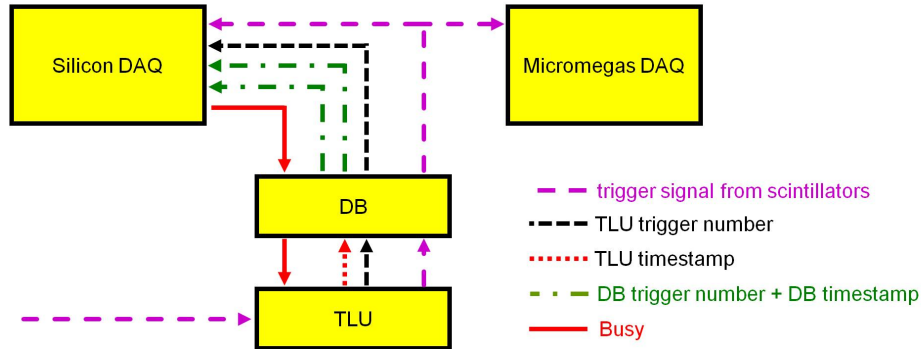

Fig. 8.2: Trigger logic during the combined test beam.

The time flow of the adapted trigger logic is as follows:

1. the Trigger Logic Unit (TLU) receives the coincidence signal from the four scintillators in front of the setup

2. the TLU sends trigger signal, TLU timestamp and TLU trigger number to the Distributor Box (DB) which immediately sends a busy signal to the TLU which prevents the TLU from passing further triggers

3. the DB sends the trigger signal to both DAQ systems and sends TLU trigger number, the DB trigger number and DB timestamp to the silicon DAQ system, which immediately sends back a busy signal to the DB, which prevents the DB to end its busy signal to the TLU

4. additionally, since the silicon DAQ system needs less time to record an event than the TPC DAQ system, the DB was advanced with an intern adjustable delay that was set to 100 ms during the measurements, which ensured that the TPC readout has enough time to process the events

5. after the silicon DAQ system stops its busy and the DB intern delay is over, the DB ends its busy to the TLU and waits for the next trigger

Since we have no common numbering to allocate the events of the silicon with those of the TPC it was utterly important, that both DAQ systems start with the same triggered event. Therefore each run was started with a busy signal sent from the silicon DAQ to the DB. Then the TPC DAQ was set ready and the silicon DAQ ended its busy so that the first trigger could be send.

Unfortunately there is no guarantee that triggers get lost, but with the used DAQ systems the possibility for such a failure is very small. The first object to verify with the recorded data is that consecutive events in the data files of the two DAQ systems refer to the same event. This can be done by matching the frequency of events with just one track in both DAQ systems. During the test beam this was done for a couple of events by hand using the online monitoring display of the TPC electronics and looked fine. It is important that this is verified for the full data set.

8.2   Results from the Silicon Layers

In the presented analysis the TPC data collected with the Micromegas panels is not included and only results from the silicon layers are presented. The data analysis of the silicon layers was done with the AC1 - Analysis software [100], which was developed for offline analyses of the CMS Tracker Outer Barrel. It is a collection of root classes[1] that ease the analysis of data taken with the CMS tracker XDAQ application [94].

---

[1] root is a collection of object - oriented programs and libraries developed by CERN: http://root.cern.ch/
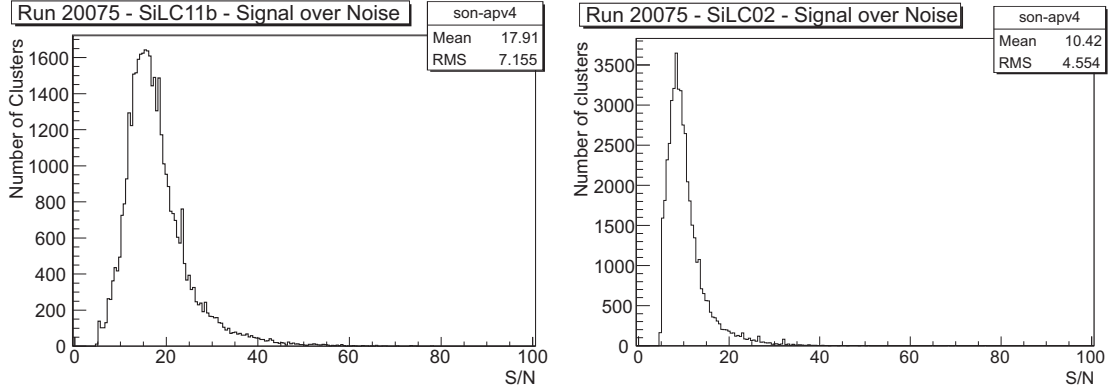
Fig. 8.3: Signal over noise ratio of SiLC11b (left), containing one silicon sensor, and of SiLC02 (right), containing two silicon sensors.

For the plots the data of the longest run, with number 20075, containing 42,434 triggered events is used. The measured cluster signal to noise ratio of two silicon detectors are shown in figure 8.3. It is between 17 and 18 for the detectors containing one silicon sensor and between 9.5 and 10.5 for detectors with two daisy-chained sensors. The smaller signal over noise ratio of the silicon detectors containing two silicon sensors is caused by the increased capacity of the readout strip. These values are not as high as desired, caused by the second pitch adapter and the length of the cables needed in the LP setup, but sufficient for the LP experiment.
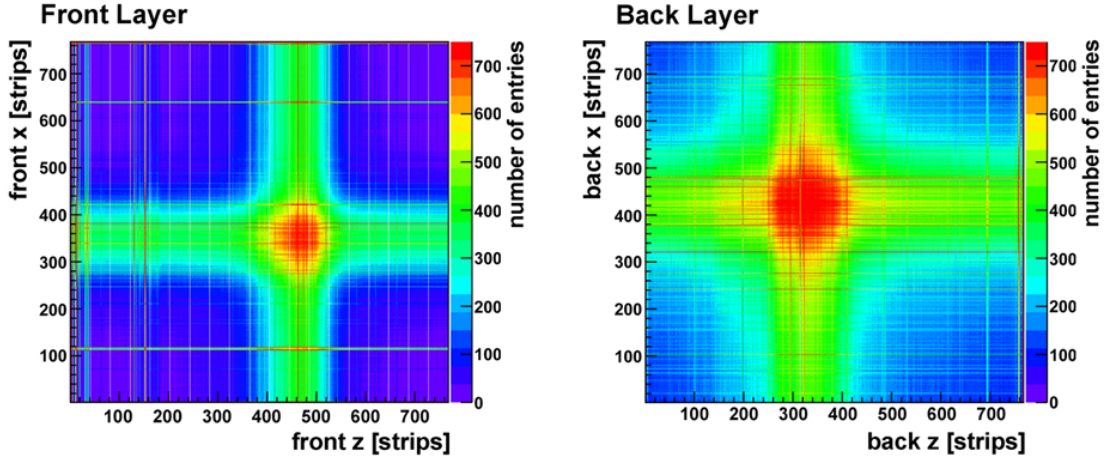
Fig. 8.4: Hit profile of the single track events in run 20075.

The plots in figure 8.4 show the hit profiles for run 20075. For each cluster only the readout channel with the highest signal is counted. The axes show the 768 readout strips of the four silicon modules. The left plot shows the hit profile of the silicon double layer in front of the TPC where the beam spot is much smaller compared to the beam profile in the double layer in the back, displayed on the right side. Since the silicon sensors have 768 readout strips with a pitch of $50 \, \mu$m

we can estimate the diameter of the beam spot from the profile in the front layer to be about 5 mm. The small shift between the location of the beam spots on the silicon detectors comes from imprecisions in the alignment of the silicon layers, but the fact that there was no readjusting of the positions proves again the high quality of the manual alignment.

Fig. 8.5: Number of clusters per event in the four silicon detectors.
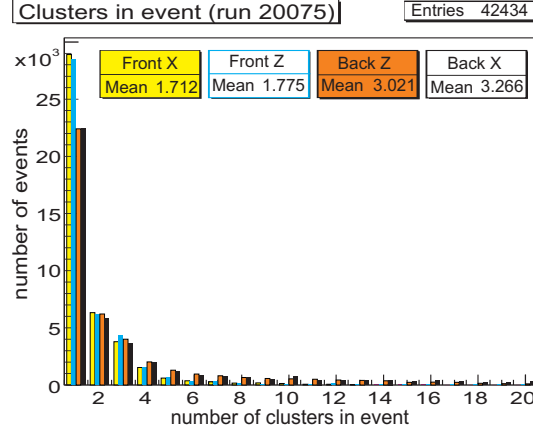
The magnet wall in front of the first silicon layer has a radiation length of $20\% X_0$ [78]. Therefore we have a high number of secondary particles passing the TPC and the silicon layers. But at the position of the silicon layer in front of the TPC, in the majority of the events these secondary particles produced in the magnet wall are too close to their corresponding beam particle to be seen as a separate cluster in the silicon sensors. This effect is clearly visible from the blurring of the two distributions in figure 8.4. It is also observable when the mean value of clusters per event in the two silicon layers is compared, as displayed in figure 8.5. In the back layer nearly twice as many clusters per event (~ 3.14) than in the front layer (~ 1.74) were recorded. Because of the high secondary emission yield and due to the multiple scattering only 12,058, about 28 %, of the 42,434 triggered events in run 20075 have exactly one cluster in all four silicon sensors. These so-called single track events are very important as starting point for the alignment of the TPC with respect to the silicon layers.

Figure 8.6 shows the correlation of the hits in the front layer with the hits in the back layer for all single track events in run 20075. First the centre of gravity of all single track events in each sensor was determined and the individual offset for each of these tracks was calculated. Then the difference of the hit-offset in the front layer and the corresponding offset in the back layer is plotted. This plot shows clearly, that the majority of the single tracks are rather straight with a RMS of 1.28 mm in x and 1.42 mm in z, which reflects a beam spread of 1.66 mrad and 1.84 mrad, respectively. This is in very good agreement to the results from the characterisation of the test beam line described in [99].

The next possible step, when the analysis software for the Micromegas is ready,
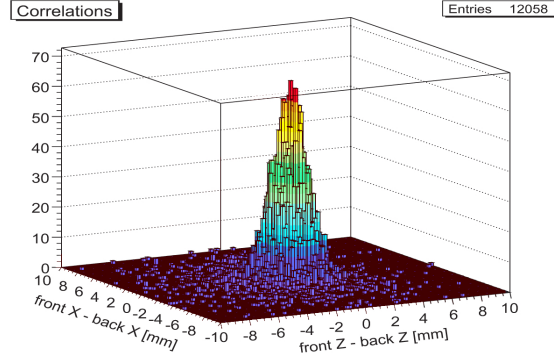
Fig. 8.6: Correlation plot of the front and back layer.

is the combined data analysis of the single track events. This will start from the
tracks in the silicon sensors and align them with the tracks recorded in the TPC.
Afterwards this first alignment can be used to eliminate all ghost hits of the events
with more than one cluster in the silicon layers by matching the clusters to the
corresponding TPC tracks. Then the total combined data can be used for a final
analysis of this first combined test beam. The results are then comparable with
the data of future test beams, collected with different TPC readout electronic
prototypes.

The really interesting analyses will start when enough TPC readout panels,
including the appropriate analysis software, are available to equip the full, or
at least the total diameter of the end‑plate of the Large TPC Prototype. The
preparations for such tests are ongoing as for example the construction of seven
Micromegas modules and the development of the dedicated software.

8.3   Alignment Study

To enable a proper analysis of the combined data of the silicon sensors and the
Large TPC Prototype, the alignment of the different parts of the setup has to
be better than one fifth, ideally one tenth, of the measured resolutions [101]. To
profit from the spatial resolution of the silicon sensors of less than $10\,\mu$m, the setup
should be alignment with a precision in the order of $2\,\mu$m or better.

For curved tracks in the magnetic field it is not possible to make a proper
alignment with just one TPC readout module, unless it is used orthogonal as
shown in section 8.3.2.1, because of the large distance between TPC readout and
silicon sensors. The only realistic possibility is a track based alignment, where
each single track of the TPC is extrapolated to the silicon layers and compared to
the positions measured with the silicon sensors.

8.3.1   Parametrisation of the LP Readout Panels

Table 8.1 gives the geometrical properties of the two readout panels, equipped with the GEM and the Micromegas technologies. For the calculations and simulations it was assumed, that the tracks pass the TPC volume in front of the centre of the panels, meaning that the average values for the measured path, the number of pads per row, 184 for the GEM, and for the readout pitch, 2.95 for the Micromegas, are used.

TPC readout	# measured points (pad rows × pad / row)	readout pitch [mm] (height × width)	measured path [m]
GEM	28 × 176 – 192	5.4 × 1.2	0.15 × 0.2
Micromegas	24 × 72	6.8 × 2.7 – 3.2	0.16 × 0.21

Tab. 8.1: Geometrical properties of the GEM and Micromegas panels.

The spatial resolutions of the readout panels were measured in former test beams with a magnetic field of 1 Tesla, but are still preliminary [102]. These measurements follow equation:

$$\sigma^2 = \sigma_0^2 + D^2/N_{eff} \cdot \Delta z \tag{8.1}$$

and are shown in figure 8.7. The measured values for σ_0, the spatial resolution at a drift distance of $\Delta z = 0$, and the number of effective electrons N_{eff} are displayed in table 8.2. Unfortunately no values for the resolution in drift direction were found and therefore the analyses in this section is restricted to the spatial resolution in x, the vertical axis of the LP setup as defined in figure 7.1. All values in this section are calculated and simulated for a spatial resolution of $100\,\mu$m, which represents a drift distance of about 250 mm for both readout options.
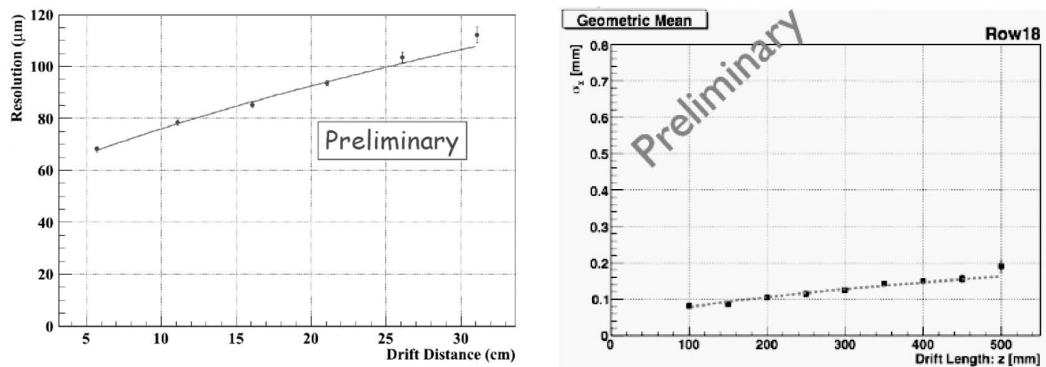

Fig. 8.7: Measurements of the spatial resolution for the LP equipped with Micromegas (left) and GEMs (right) with B = 1 T [102].

TPC readout	TPC resolution σ_0 at $\Delta z = 0$ [μm]	effective electrons N_{eff} [cm^{-1}]
GEM (B = 1 T)	51.9 ± 1.6	55.5 ± 1
Micromegas (1 T)	54.8 ± 1.6	54.4 ± 2

Tab. 8.2: $\Delta z = 0$ and N_{eff} for the GEM and Micromegas panels.

8.3.2 Estimations of the Alignment Precision

To get an idea about the precision achievable for a track based alignment at the LP setup, the resolutions for the extrapolated tracks, measured with the LP, on the plane of the silicon sensors are calculated. The resolution on the sensor plane can be calculated from the asymptotic error E on the plane with:

$$\sigma_{onSi} = \sqrt{E} \tag{8.2}$$

If a constant error and uniform spacing of the readout panels is assumed, it is possible to calculate the asymptotic error E on the sensor plane with

$$E = C_{11} + 2 \cdot \Delta x \cdot C + 2 \cdot \frac{\Delta x^2}{2} \cdot C_{13} + \Delta x^2 \cdot C_{22} + 2 \cdot \Delta x \cdot \frac{\Delta x^2}{2} \cdot C_{23} + \left(\frac{\Delta x^2}{2}\right)^2 \cdot C_{33} \tag{8.3}$$

where Δx^2 is the distance from the silicon plane to the last measured point of the readout panel and C_{ij} are the elements of the asymptotic covariance matrix that can be calculated with [103]:

$$C_\infty = \sigma^2 \cdot \begin{pmatrix} \frac{9}{n+5} & \frac{-36}{L(n+5.5)} & \frac{60}{L^2(n+6)} \\[2mm] \frac{-36}{L(n+5.5)} & \frac{192}{L^2(n+4.875)} & \frac{-360}{L^3(n+5)} \\[2mm] \frac{60}{L^2(n+6)} & \frac{-360}{L^3(n+5)} & \frac{720}{L^4(n+5)} \end{pmatrix} \tag{8.4}$$

Here σ is the resolution of measurements along the track, L is the length of the measured track and n = N_P - 1, the number of measured points N_P minus one.

It is important to mention, that this calculation neither includes systematic errors nor errors due to multiple scattering in the TPC gas and field cage. When systematic errors are neglected the achievable spatial resolution improves with the number of measurements N by the factor $1/\sqrt{N}$. In this way the number of needed measurements to achieve a resolution of $1 \, \mu$m and $2 \, \mu$m are calculated for each configuration. Further, the calculations were done with an assumed spatial resolution of $100 \, \mu$m for the measured track points with the TPC, which corresponds to a drift distance of roughly 25 cm for both readout options, as displayed in figure 8.2. Needless to say, for some of the configurations described below the position of the TPC and the silicon sensors have to be adjusted to ensure that they are inside the beam line.

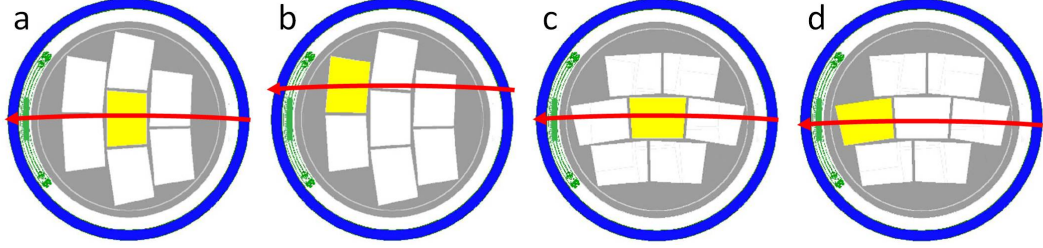### 8.3.2.1   Calculations for one Readout Panel

Fig. 8.8: Different configurations for the LP end plate (grey) equipped with one readout panel (yellow) - the red line indicates the beam, the blue circle the magnet, the silicon layer is coloured green and the dummy readout panels white.

configuration	readout	extrapolated resolution at silicon [μm]	number of measurements needed to reach a precision of	
			2 μm	1 μm
a	GEM	1,580	624,000	2,496,000
	Micromegas	1,450	524,000	2,096,000
b	GEM	490	60,000	240,000
	Micromegas	450	50,000	200,000
c	GEM	330	27,000	108,000
	Micromegas	550	75,000	300,000
d	GEM	62	1000	4,000
	Micromegas	106	3,000	12,000

Tab. 8.3: Alignment study in x - direction with one readout panel at different positions, compare figure 8.8, and a magnetic field of 1 T, taking neither systematic errors nor multiple scattering into account.

Table 8.3 shows the calculations described above made for the LP equipped with only one readout panel at different positions on the LP end plate, as indicated in figure 8.8. Here only the extrapolation of the track to the closer silicon sensor is considered, since the obtained resolution on the other silicon plane is smaller due to the larger distance between the silicon and the closest LP measurement.

Only the configurations a and b are realistic scenarios, since here the electron beam traverses the TPC relative to the readout panel in a similar direction as the tracks in a TPC at the ILD. Due to multiple scattering and systematic errors it seems impossible to make a proper alignment of the TPC and the silicon layers with configurations a and b, compare figure 8.3. Therefore, to evaluate if the inclusion of the magnetic field makes sense in the first combined test beam, described in

section 8, also the other two configurations c and d, where the TPC panels are rotated by 90°, are examined. The reasons why configurations c and d perform better are the longer measured path lengths and the smaller distances between the last measured track point and the closer silicon plane. The calculations show, that with a magnetic field of 1 T and a realistic amount of statistic only configuration d would allow a proper alignment of the TPC and the closer silicon sensor.

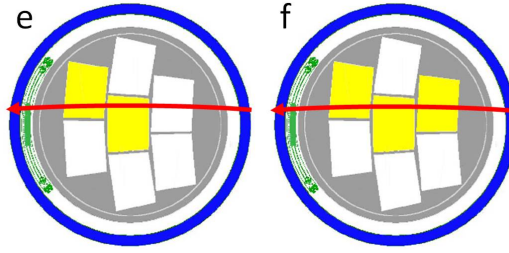### 8.3.2.2   Calculations for more Readout Panels

Fig. 8.9: Readout configurations of the Large TPC Prototype (grey) with two and three readout panels (yellow) - the red line indicates the beam, the blue circle the magnet, the silicon layer is coloured green and dummy readout panels white.

configuration	readout	extrapolated resolution at silicon $[\mu m]$	number of measurements needed to reach a precision of	
			$2\,\mu m$	$1\,\mu m$
e	GEM	130	4,250	17,000
	Micromegas	125	3,900	15,600
f	GEM	90	2,000	4,000
	Micromegas	88	2,000	8,000

Tab. 8.4: Alignment study in x-direction with two (e) and three (f) readout panels, as shown in figure 8.9, and a magnetic field of 1 T, taking neither systematic errors nor multiple scattering into account.

Table 8.4 shows the calculations described above made for the LP equipped with two, configuration e, and three, configuration f, readout panels, as shown in figure 8.9. In the table only the extrapolation of the track to the closer silicon sensor is considered, because after this first alignment it should be no problem to also align the second silicon detector.

The calculations show, that it is definitely possible to align the LP and the silicon detectors when the whole length of the TPC is read out. Also with just two equipped readout panels it should be possible to make a good enough alignment to

combine the measurements. Although a beam test with three GEM modules was already performed, they were, till now, not available for combined measurements.

8.4   Summary & Outlook

The first successful test beam allowed to verify the functionality of all different components of the silicon system at the Large TPC Prototype experiment. It was proven that the silicon double layers are working as specified and that they record useful data. The communication of the silicon data acquisition system with the trigger distribution system at the LP setup works perfect and the silicon DAQ is able to write the trigger numbers and the time stamp into its output files. This is utterly important to allocate the recorded events with the events from the TPC readout system in the data analysis. Also the moveable silicon support works as expected and without problems. The alignment of the silicon sensors, with a precision of a few mm with respect to the electron beam, after movements of the magnet is easy to achieve and can be provided in a very short time. The performed alignment study demonstrates that it is possible to usefully connect the data recorded with the data acquisition system of the TPC and that of the silicon.

For the future it is foreseen that the double silicon layers are exchanged with detector modules containing the readout electronics currently under development for the ILD tracking system and also the next generations of silicon strip sensors. In the coming years, combined test beams with and without magnetic field including different TPC readout technologies will be performed at the LP setup. These test beam experiments should allow to define the optimal technology for the ILD TPC readout and to verify the possibilities of the silicon system to monitor distortions and inhomogeneities of the magnetic field inside the TPC. In parallel, the combination of the silicon and TPC readout systems into one combined data acquisition system will be developed, including also a combined data analysis framework. This is an important step towards combined test beams with other sub‑detectors, like vertex detectors and calorimeters, which are foreseen in the coming years.

Chapter 9

Optimisations of the Silicon Tracking System

The fundamental decision, defining the basic geometry of the detector system, is the radius of the solenoid surrounding the tracking system and the calorimeter. Detectors at particle colliders would favour the highest possible magnetic field with the maximum possible radius of the coil, but unfortunately the magnetic field of a solenoid is inverse proportional to its radius. Considerations of momentum resolution favour a larger detector and a higher magnetic field. In addition, because of the background of charged particles with low momentum, the first layer of the vertex detector can move closer to the interaction point when the magnetic field is higher, which improves the resolution of the impact parameter. The main parameters of the ILD reference detector, described in section 3.2, are based on extensive simulation studies performed with three variations of both, the Large Detector Concept (LDC) [30] and the Global Large Detector (GLD) [31] concept, as described in [21]. These studies were used to merge the two detector concepts to form the ILD, with the main focus lying on the physics requirements at the ILC as described in chapter 2.5.

This chapter does not describe the simulation studies mentioned above, but investigates different variations of the ILD silicon tracking system by comparing the obtained resolutions for the normalized relative transversal momentum $\sigma(\Delta p_t/p_t^2)$, for the projected impact parameter (ip2) and for the z‑coordinate. Each point in the simulated curves is obtained by the simulation and reconstruction of the tracks of 1000 muons with the given angle and momentum. These studies are performed with the Vienna fast simulation tool "LiC Detector Toy" (LDT) [104]. First the parametrisation of the ILD tracking system used as starting point for the simulations are described. It is shown that the high requirements on the transversal momentum resolution demand the inclusion of the Silicon External Tracker, which is already included into the ILD - Letter of Intent [21]. Then different variations of the silicon tracking system are compared leading to an optimal layout within the given constraints.

9.1   Parametrisation of the ILD Tracking System
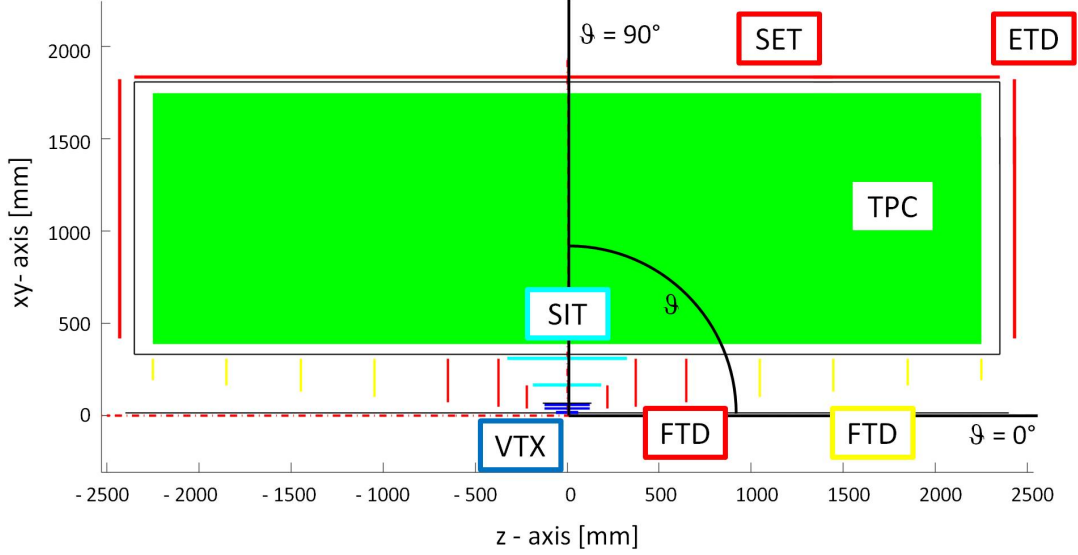
9.1.1   Global Layout

Fig. 9.1: 2D view of the ILD tracking system as used for the simulations.

As described in chapter 3, the tracking system of the ILD is azimuthally symmetric with respect to the z-axis and mirrored on the xy-plane, as visible in figure 3.4 and figure 9.1. It consists of a vertex detector and a large volume TPC, complemented by additional layers of silicon sensors. The barrel part of the detector is sensitive to tracks with polar angles in the range of $40° < \vartheta < 90°$, where a polar angle of $\vartheta = 90°$ refers to the plane orthogonal to the beam axis z, as indicated in figure 9.1. All detector layers in the barrel have a roughly cylindrical shape. The parametrisation of the ILD tracking system, used in this chapter, contains a vertex detector (VTX) with three double layers of silicon pixel detectors. The Silicon Internal Tracker (SIT) consists of two and the Silicon External Tracker (SET) of one double layer of silicon strip detectors. The forward region of the tracking system covers polar angles in the range of about $5° < \vartheta < 40°$ and consists of disk shaped layers, which are oriented perpendicular to the beam axis. The Forward Tracking Detector (FTD) consists of seven discs of silicon detectors and the End-cap Tracking Detector (ETD) of three discs covering the end-plates of the TPC.

Table 9.1 and table 9.2 define the barrel and forward geometry used in the simulations. The beam pipe, composed of beryllium covered with titanium, with a radius of 14 mm and a radiation length of $0.14\,\%X_0$ is not included in the tables. The detector layers in the barrel part cover a polar angle from $\vartheta < 90°$ down to the angle shown in table 9.1. The last column of the table shows the minimum transversal momentum a particle must have to reach the dedicated layer

component	r [mm]	z [mm]	polar angle ϑ [deg]	min. p_t [GeV/c]
VTX1	16.0	$\pm$ 62.5	14.36	0.02
VTX2	18.0	$\pm$ 125.0	8.19	0.02
VTX3	37.0	$\pm$ 125.0	16.49	0.04
VTX4	39.0	$\pm$ 125.0	17.33	0.04
VTX5	58.0	$\pm$ 125.0	24.89	0.06
VTX6	60.0	$\pm$ 125.0	25.64	0.06
SIT1$_{r\varphi}$	162.0	$\pm$ 185.5	41.13	0.17
SIT1$_z$	168.0	$\pm$ 185.5	42.17	0.18
SIT2$_{r\varphi}$	306.0	$\pm$ 322.5	43.50	0.32
SIT2$_z$	312.0	$\pm$ 322.5	44.05	0.33
TPC$_{wall}$ (i)	329.0	$\pm$ 2347.5	7.98	0.35
TPC$_{active}$ (i)	395.0	$\pm$ 2247.5	9.97	0.41
TPC$_{active}$ (o)	1739.0	$\pm$ 2247.5	37.73	1.82
TPC$_{wall}$ (o)	1808.0	$\pm$ 2347.5	37.60	1.90
SET$_{r\varphi}$	1831.0	$\pm$ 2347.5	37.95	1.92
SET$_z$	1837.0	$\pm$ 2347.5	38.04	1.93

Tab. 9.1: Barrel geometry of the ILD tracking system as used in the simulations.

component	z [mm]	r [mm]	polar angle ϑ [deg]
FTD1	220.0	39.0 − 164.0	10.05 − 36.70
FTD2	371.3	49.6 − 308.0	7.61 − 39.68
FTD3	644.9	70.1 − 308.0	6.20 − 25.53
FTD4	1046.1	100.3 − 309.0	5.48 − 16.46
FTD5	1447.3	130.4 − 309.0	5.15 − 12.05
FTD6	1848.5	160.5 − 309.0	4.96 − 9.49
FTD7	2250.0	190.5 − 309.0	4.84 − 7.82
TPC endplate	2350.0	329.0 − 1808.0	7.97 − 37.57
ETD1	2426.0	419.3 − 1822.7	9.81 − 36.92
ETD2	2428.0	419.3 − 1822.7	9.80 − 36.90
ETD3	2430.0	419.3 − 1822.7	9.79 − 36.87

Tab. 9.2: Forward geometry of the ILD tracking system as used for the simulations.

within a magnetic field of $3.5\,\mathrm{T}$, calculated with equation 9.3. For the double layers equipped with silicon strip sensors the measured coordinate is indicated with $r\varphi$ and z. TPC_{wall} and TPC_{active} stand for the TPC field cage and the sensitive TPC volume, with their inner and outer boundaries indicated with (i) and (o). The disc shaped layers of the forward part, defined in table 9.2, are spanned between their inner and outer radii defining their angular coverage.
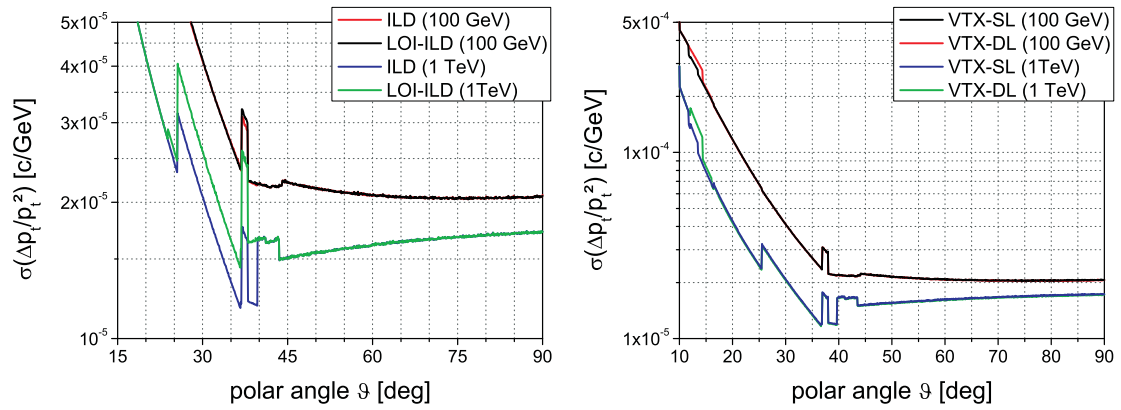
9.1.2   Silicon Strip Tracker

Fig. 9.2: Angle scan of $\sigma(\Delta p_t/p_t^2)$ for two different outer radii of the FTD2 (left) and for the two vertex geometries (right).

The silicon strip sensors are assumed to have a readout pitch of $50\,\mu\mathrm{m}$ with one intermediate strip. As evaluated in the test beam described in chapter 6, such sensors provide a spatial resolution of $6\,\mu\mathrm{m}$ perpendicular to their readout strips. The layers equipped with strip sensors are considered to have a radiation length of $0.4\%\,X_0$, averaged over their surface as described in section 5.

Compared to the ILD - Letter of Intent [21] one minor change is introduced into the layout of the strip tracker: the outer radius of the Forward Tracking Detector layer 2 (FTD2) is increased from $164.0\,\mathrm{mm}$ (LOI - ILD) to $308.0\,\mathrm{mm}$ (ILD). This slightly increases the asymptotic value of the transverse momentum resolution in the region of $25\,^\circ < \vartheta < 40\,^\circ$, as shown in the left plot of figure 9.2 for muons with an absolute momentum of $100\,\mathrm{GeV/c}$ and $1\,\mathrm{TeV/c}$.

9.1.3   Vertex Detector

For the simulations the vertex detector geometry VTX - DL containing three double layers, as described in section 3.2.1, is used. Each of the six layers of the VTX - DL is equipped with $50\,\mu\mathrm{m}$ thick silicon pixel sensors providing a spatial resolution of $2.8\,\mu\mathrm{m}$ in both directions of the sensor plane. Including support and electronics an average radiation length of $0.8\,\%X_0$ is assumed for each layer. The vertex detector

is enclosed with a beryllium support, a light foam cryostat and a thin aluminium foil adding up to a radiation length of $0.75\,\%X_0$.

The VTX‑DL geometry was chosen over the VTX‑SL because it provides slightly better resolutions for the impact parameters in the barrel region, as shown in figure 9.3 for muons with an absolute momentum of $100\,\mathrm{GeV/c}$ and $1\,\mathrm{TeV/c}$. Only in the forward region below $\vartheta\,<16.07\,^\circ$ the geometry VTX‑SL with five single layers shows better impact parameter resolutions. This comes from the fact that the second layer of the VTX‑SL reaches down to a polar angle of $11.75\,^\circ$, not covered by the second layer of the VTX‑DL. Nevertheless, the decision of the vertex geometry has no big influence on the momentum resolution of the whole tracking system, which only differs noticeable in the region of $11.7\,^\circ \lesssim \vartheta \lesssim 14.4\,^\circ$, where the VTX‑SL shows a slightly improved normalised transversal momentum resolution, visible on the right plot of figure 9.2. This is again caused by the length and radius of the second layer of the VTX‑SL, as shown in table 3.2.
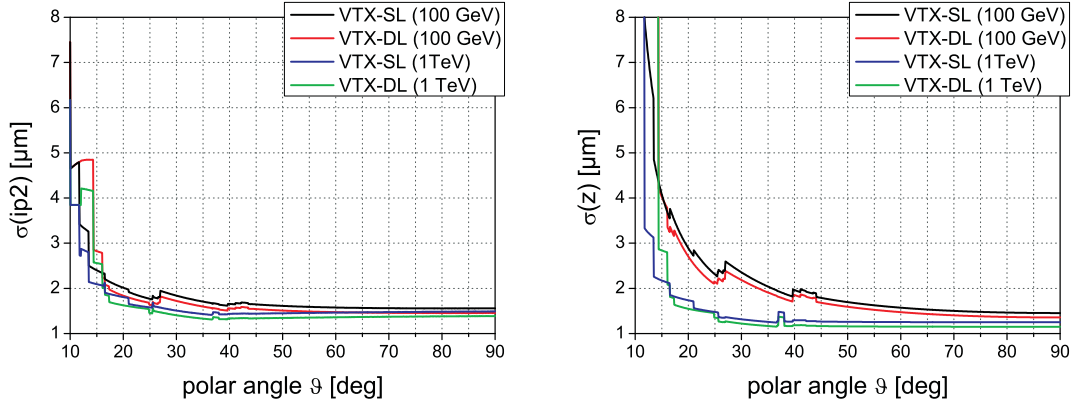

Fig. 9.3: Impact parameter resolutions for the two vertex detector geometries.

9.1.4   Time Projection Chamber

The properties of the ILD TPC are summarised in table 3.3. The resolution of the Time Projection Chamber is depending on the drift distance Δz, as described in section 7.4.1, and defined by two parameters: its resolution in the transversal plane, parallel to the readout panels on the TPC end‑plates, $\sigma_{r\varphi}$ and its resolution in drift direction σ_z, as defined by equations 7.4 and 7.5. For the simulations in this chapter the TPC parametrisation as defined in the ILD LOI [21] is used:

$$\sigma_{r\varphi}^2/\mu m^2 = 50^2 + 900^2 \cdot sin^2\varphi + ((25^2/22) \times (4/B)^2 \cdot sin\vartheta) \cdot \Delta z \qquad (9.1)$$

$$\sigma_z^2/\mu m^2 = 400^2 + 80^2 \times \Delta z \qquad (9.2)$$

For the material budget the TPC design goals as shown in table 3.3 are assumed.

9.2   The Vienna Fast Simulation Tool LiC Detector Toy

The LiC Detector Toy (LDT) [104] is a program written in MATLAB, which allows for a rather uncomplicated comparison of different tracker geometries. This tool was completely conceived and developed at the HEPHY Vienna. The reliability of the LDT was validated against a variety of other simulation tools and showed very comparable results [105]. Unfortunately, till now energy loss of minimum ionising particles passing matter is not included in the simulation algorithm. Therefore detector material and passive material layers only cause multiple Coulomb scattering leaving the absolute momentum $|\vec{p}|$ of traversing particles unaffected. Also the simulation and reconstruction of electrons and positrons is excluded. Their inclusion would require a new approach to the track fitting, which must be able to correctly handle energy loss by bremsstrahlung. This is foreseen to be implemented in future upgrades and therefore all simulations presented in this chapter are performed with muons.

9.2.1   Detector Geometry

The LDT is only able to handle detector geometries which have a cylindrical symmetry with respect to the beam axis z. In the barrel region the detector consists of cylindrical layers with the radius r and the length z_{higher} - z_{lower}. In the forward region it is composed of discs located at a distance z from the interaction point which range from r_{lower} to r_{higher}. A right-handed orthogonal frame is defined by the axes x, y and z, whereas the x-axis is horizontal and the y-axis is pointing upwards, as displayed in figure 9.4. In addition cylinder coordinates are defined for space points and momenta, as used in the results of the simulations. The absolute momentum $\vec{p} = [p_t, \varphi, p_z]$ is composed of $p_t = |p| \cdot cos(\pi/2 - \vartheta)$ and $p_z = |p| \cdot sin(\pi/2 - \vartheta)$ with $|\vec{p}|^2 = p_t^2 + p_z^2$. The polar angle reaches from $0 \leq \vartheta \leq \pi$ and the azimuth angle $\varphi = arctan(p_y/p_x)$ is limited by $0 \leq \varphi \leq 2\pi$.

For a particle with momentum $|p|$ [GeV/c] and charge q [e], the radius r_H [mm] of the helix and its signed inverse κ can be calculated using [106]:

$$r_H = \frac{1}{K} \cdot \frac{|p| \cdot cos(\pi/2 - \vartheta)}{|q \cdot B_z|}, \tag{9.3}$$

$$\kappa = -sign(q \cdot B_z) \cdot \frac{1}{r_H} \tag{9.4}$$

with the polar angle ϑ [rad], the magnetic field $\vec{B} = (0,0,B_z)$ [T] and the constant factor

$$K = 10^{-15}c = 2.99792458 \cdot 10^{-4} \frac{GeV/c}{T \cdot mm} \tag{9.5}$$
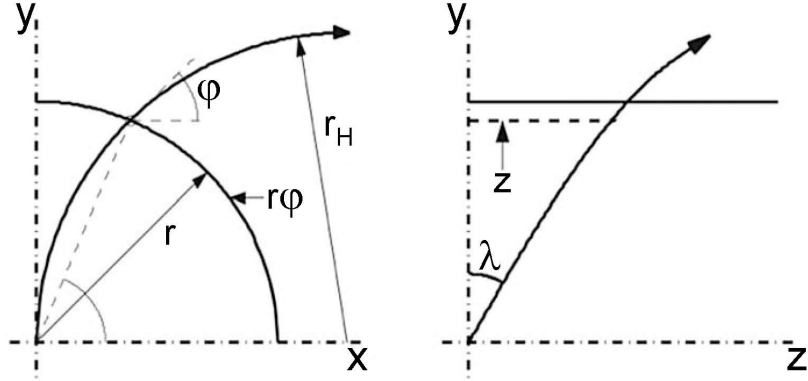
Fig. 9.4: Coordinates and track parameters as used in the LDT.

9.2.2 Simulation and Reconstruction

The simulation software propagates each particle from its primary vertex, the point of its creation defined in the input sheet, through the virtual detector, defined by two geometry files, one each for the barrel and the forward part. The charged particles follow helix tracks of radius r_H, as defined in equation 9.3, inside the homogeneous magnetic field with breakpoints due to multiple scattering at discrete thin layers, where the sensitive and insensitive material of the detector is concentrated and averaged over their surface. The simulated measurements of the sensitive detector material include systematic or stochastic inefficiencies and uniform or Gaussian observation errors, but no other degradation of data. A Gaussian distribution of the scattering angles is assumed, according to the Rossi-Greisen-Highland formula. The track reconstruction is based on single tracks using the Kalman filter [107] with a linear approximation to the track model, without pattern recognition. The simulated measurements are used to fit the parameters of the track and to calculate their corresponding 5×5 covariance matrix at the innermost layer of the geometry file, which is the beam pipe in the simulations presented here.

The detector resolutions of the z-coordinate, the projected impact parameter ip2 and of the normalized transversal momentum resolution $\sigma(\Delta p_t / p_t^2)$ are computed using the difference between the fitted track parameters and the Monte Carlo truth at the inside of the beam pipe. Because of multiple scattering particles with tracks traversing a layer suffer a change in direction by an angle ϑ_r in space, which leads to a change of their transversal momentum p_t. The scattering angle ϑ_r consists of λ_r in the zy-plane, and φ_r in the xy-plane, the two independent scattering angles of the two orthogonal planes with the track tangent as intersection, as shown in figure 9.4. Since the particle momentum $|p|$ is preserved in the scattering process the absolute value for ϑ_r does not change.

9.3 Inclusion if the Silicon External Tracker into the ILD

The first proposal of a Silicon External Tracker (SET) surrounding a tracking system, consisting of silicon sensors surrounded by a Time Projection Chamber, was made in 2001 [108] for a multi-purpose detector at the TeV-Energy Superconducting Linear Accelerator (TESLA) [16]. This proposal was followed by a wide discussion if the benefits legitimate the additional costs. This discussion ended with the inclusion of the SET into the baseline design of the International Large Detector [21].

This section demonstrates the reasons for the inclusion of the SET and investigates the behaviour of the ILD tracking system for four different cases:

- ILD - refers to the ILD as described in section 9.1

- no SET - refers to the ILD without Silicon External Tracker

- no SIT - refers to the ILD without Silicon Internal Tracker

- VTX + TPC - refers to the ILD concept without the Silicon External Tracker nor the Silicon Internal Tracker, leaving only the vertex detector and the Time Projection Chamber

9.3.1 Normalised Transversal Momentum Resolution
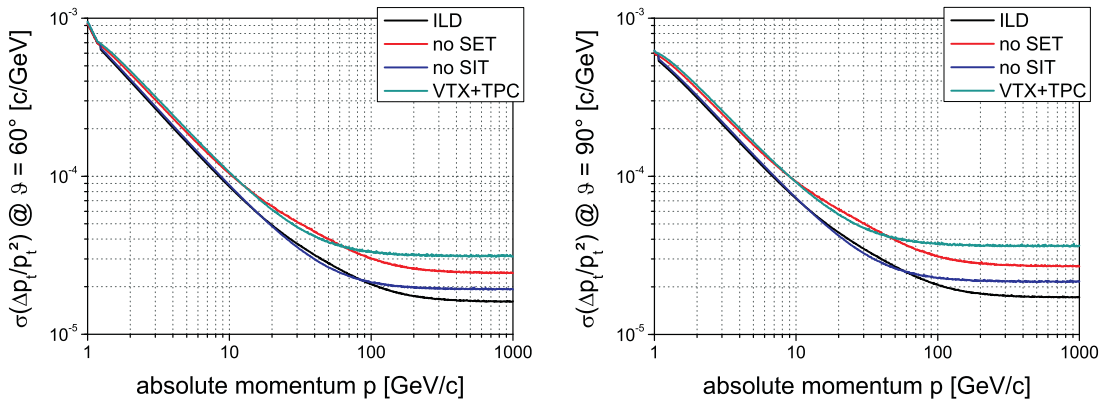
9.3.1.1 Momentum Scan

Fig. 9.5: Comparison of $\sigma(\Delta p_t/p_t^2)$ as function of the absolute muon momentum p for polar angles of $\vartheta = 60\,^\circ$ (left) and $\vartheta = 90\,^\circ$ (right).

Figure 9.5 displays the normalised transversal momentum resolution $\sigma(\Delta p_t/p_t^2)$ as function of the absolute momentum p for single muons in the four different ILD barrel configurations. Looking at the simulations it is obvious, that the resolution

of the tracking system without Silicon External Tracker does not reach the required asymptotic momentum resolution of $\sigma(\Delta p_t/p_t^2) \leq 2 \cdot 10^{-5} (\text{GeV/c})^{-1}$, which is important to reach the physics goals of the ILD as described in section 1.3. This comes from the precise rφ measurement at the large lever arm provided by the SET. The inclusion of the SIT only improves the resolution at low and high momenta and has a negative influence at medium momenta:

- $\text{p} < 1.23\,(1.06)\,\text{GeV/c}$ for $\vartheta = 60\,°\,(90\,°)$:
  The inclusion of the Silicon Internal Tracker improves $\sigma(\Delta p_t/p_t^2)$ by about 3%.

- $1.23\,(1.06)\,\text{GeV/c} < \text{p} \lesssim 80\,(50)\,\text{GeV/c}$ for $\vartheta = 60\,°\,(90\,°)$:
  In this range, the resolution is visibly worsened due to the material of the SIT, which introduces additional multiple scattering. The offset between the two polar angles is caused by the different amount of material traversed by the particles. The silicon sensors appear thicker for smaller polar angles.

- $80\,(50)\,\text{GeV/C} \lesssim \text{p}$ at $\vartheta = 60\,°\,(90\,°)$
  For high momenta the inclusion of the SIT considerably increases the resolution and starts to push $\sigma(\Delta p_t/p_t^2)$ considerably below $2 \cdot 10^{-5} (\text{GeV/c})^{-1}$.
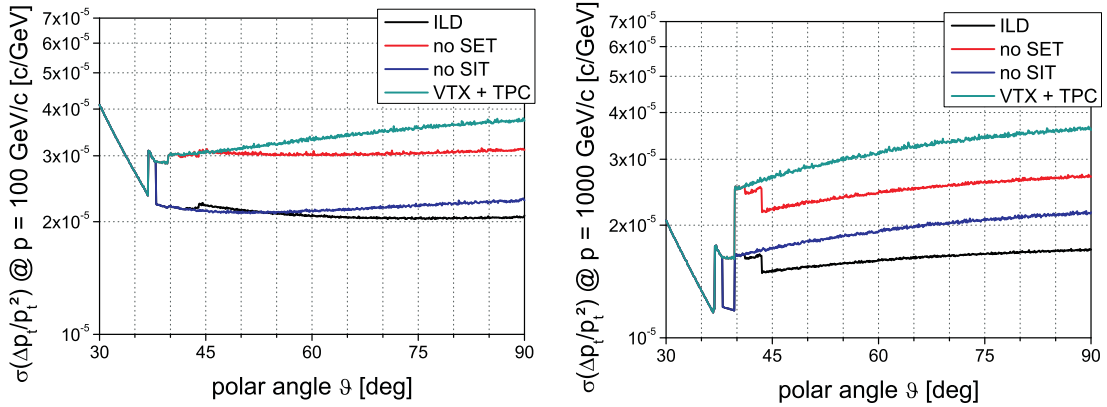
9.3.1.2   Polar Angle Scan

Fig. 9.6: Comparison of $\sigma(\Delta p_t/p_t^2)$ as function of the polar angle ϑ for the absolute momenta of $\text{p} = 100\,\text{GeV/c}$ (left) and $\text{p} = 1000\,\text{GeV/c}$ (right).

Figure 9.6 compares the normalised transversal momentum resolution as function of the polar angle ϑ for single muons within the four different ILD barrel configurations. It is important to remember that $p_t = |p| \cdot cos(\pi/2 - \vartheta)$ and therefore p_t rises with the polar angle when looking at muons with constant absolute momenta, as shown in table 9.3. Again it is clearly visible, that the requirement for the asymptotic value of $\sigma(\Delta p_t/p_t^2)$ can only be reached with the inclusion of the SET. The simulations also show, that with decreasing momenta the negative

polar angle ϑ [°]	p_t for $p = 100\,\mathrm{GeV/c}$	p_t for $p = 1000\,\mathrm{GeV/c}$
30	50.00	500.00
40	64.28	642.79
50	76.60	766.04
60	86.60	866.03
70	93.97	939.69
80	98.48	984.81
90	100.00	1000.00

Tab. 9.3: $p_t = |p| \cdot cos(\pi/2 - \vartheta)$.

influence of the SIT material rises and reduces its benefit. The influences of the different components of the tracking system on the transversal momentum resolution are distinguishable by the kinks in the curves:

- $\vartheta < 36.7\,°$
  The forward region of the ILD detector is not subject of this thesis and an optimisation study can be found in [105].

- $\vartheta > 36.7\,°$
  Here the FTD1 ends, which is hardly visible for muons with a momentum of 1 TeV. For 100 GeV muons the negative effect of the additional material and the benefit of the additional measurement are in balance and the FTD1 could in principal be shortened.

- $\vartheta \gtrsim 36.8\,°$
  The ETD starts and improves the resolution by about 30% (45%) for muons with an absolute momentum of $100\,(1000)\,\mathrm{GeV}$. The absence of a kink at $\vartheta \sim 37.6\,°$ proves that the ETD and the TPC are able to compensate for the large amount of material introduced by the TPC end-plate.

- $\vartheta \gtrsim 38\,°$
  The SET improves the resolution by about 25%.

- $\vartheta > 39.7\,°$
  The end of the FTD2 worsens the resolution by about 20% for 1 TeV muons, but is hardly influencing the resolution for muons with an absolute momentum of 100 GeV. This again shows, that the gain with the additional measured point of the track is negated by the introduced material at low momenta, compare also the left plot of figure 9.2.

- $\vartheta \gtrsim 42\,°$
  For 1 TeV muons the inner layer of the Silicon Internal Tracker, SIT1$_{r\varphi}$ starting at $\vartheta = 41.13\,°$, slightly improves the resolution which is further improved

by $SIT2_{r\varphi}$ starting at $\vartheta = 43.50\,^\circ$ to a total of $\sim 12\%$.

For muons with an absolute momentum of $100\,\mathrm{GeV}$ the SIT is disadvantageous for low angles and starts to become beneficial, for the configurations including the SET, not before $\vartheta \sim 53\,^\circ$, where the traversed material of the SIT is smaller.

9.3.2   Impact Parameter Resolution

As expected, the resolutions of the impact parameters, the projected impact parameter (ip2) and the z-coordinate, are dominated by the vertex detector and are far below the requested values, indicated by equation 2.1. As shown in figure 9.7 variations of the outer parts of the tracking system have no remarkable influence and only slightly alter the values. Nevertheless, above an absolute momentum of about $50\,\mathrm{GeV/c}$ the configurations containing the SET perform visibly better.
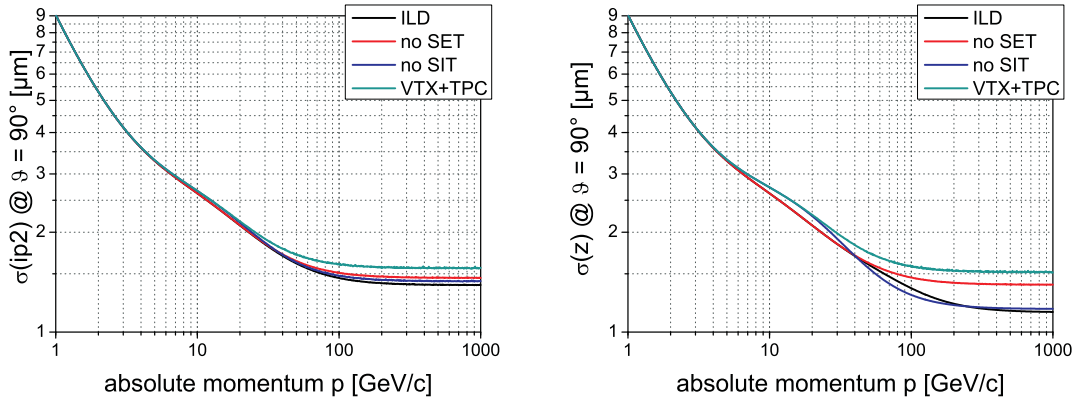

Fig. 9.7: Comparison of the impact parameter resolutions as functions of the absolute muon momentum for a polar angle of $\vartheta = 90\,^\circ$.

When looking at the impact parameter resolutions as functions of the polar angle, shown in figure 9.8, it is clearly visible that the requirements are fulfilled for the whole angular range of the barrel part. Nevertheless, the ip2-resolution for polar angles below $\vartheta < 10.05\,^\circ$, the end of FTD1, and the z-resolution for angles below $\vartheta < 14.36\,^\circ$, the end of the VTX1, the requirements for the impact parameter resolutions are not met any more.

9.3.3   Conclusion

The simulations show that the resolutions of the impact parameters are only marginal affected by variations of the silicon tracking system. On the other hand, only with the inclusion of the Silicon External Tracker it is possible to meet the requirement on the asymptotic transversal momentum resolution of $\sigma_\infty(\Delta p_t / p_t^2) \leq 2 \cdot 10^{-5} (\mathrm{GeV/c})^{-1}$, as displayed in table 9.4.

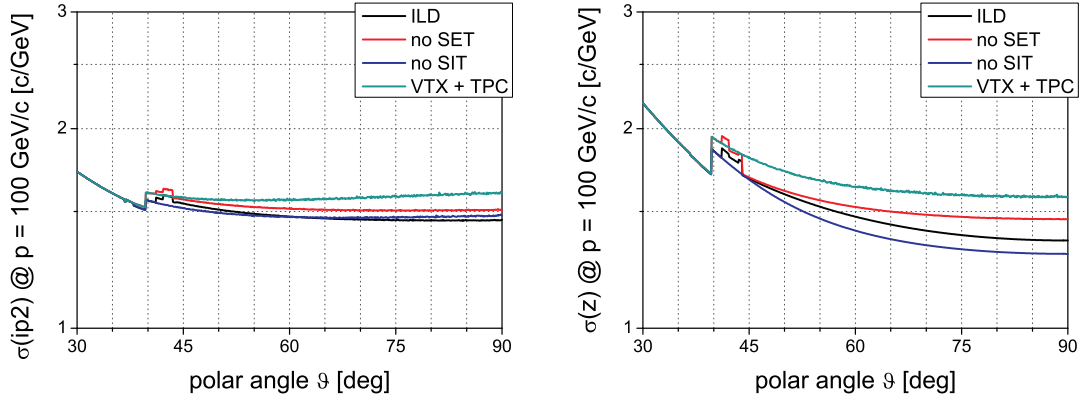Besides this, the introduction of the SET has some more benefits:

Fig. 9.8: Comparison of the impact parameter resolutions as functions of the polar angle for an absolute muon momentum of $p = 100\,\mathrm{GeV/c}$.

configuration	polar angle ϑ	
	$60\,^\circ$	$90\,^\circ$
only VTX + TPC	$3.10 \cdot 10^{-5}$	$3.64 \cdot 10^{-5}$
no SIT	$1.92 \cdot 10^{-5}$	$2.17 \cdot 10^{-5}$
no SET	$2.44 \cdot 10^{-5}$	$2.70 \cdot 10^{-5}$
ILD	$1.62 \cdot 10^{-5}$	$1.72 \cdot 10^{-5}$

Tab. 9.4: $\sigma_\infty(\Delta p_t / p_t^2)$ $[(\mathrm{GeV/c})^{-1}]$ for muons with an absolute momentum of $p = 1\,\mathrm{TeV/c}$.

- It provides a precise entry point to the barrel part of the ECAL, external to the outer wall of the TPC with a radiation length of $\sim 3\,\% \, X_0$. This is especially important to reach the double track resolution needed for the particle flow approach. In the forward region this task is fulfilled by the Endcap Tracking Detector (ETD), located just behind the Endplate of the TPC with a radiation length of $\sim 15\,\% \, X_0$.

- Although a TPC laser system is foreseen, an accurate tracking point external to the TPC volume is beneficial for the TPC calibration.

- With the combination of the data from the SIT and the SET it is possible to monitor tracking systematics inside the TPC volume during operation. This is especially important since the TPC is sensitive to variations of the ambient temperature, the atmospheric pressure and inhomogeneities in the electrical field of its field cage and of the external magnetic field.

- The addition of the precise measured track point at large lever arm also improves the absolute alignment of the overall tracking system.

9.4 Simulations for different SET Resolutions

The spatial resolution of the silicon strip sensors is directly proportional to the pitch of the readout strips, as outlined in section 4.3.4, which defines the number of readout channels and therefore the quantity of the needed readout electronics and cables. Therefore, with increasing sensor resolution not only the amount of insensitive material rises but also the power consumption and the heat production, increasing the need for cooling. All these factors raise the material budget which decreases again the resolutions obtainable with the tracking system. In addition, to guarantee for the best particle flow calorimetry, the material budget has to be as low as possible.

For the simulations in this section the radiation length of the silicon layers is fixed to $0.4\,\% X/X_0$, as used before, and is not modified with the spatial resolution, which is defined by the number of readout channels on the sensors. In my opinion this is a good approximation since:

- For the ILD tracking system, it should be possible to use a forced gas cooling system instead of a liquid cooling system, as outlined in section 5.3.4, which immensely reduces the material budget per readout channel.

- Since it is foreseen to use up to six daisy-chained sensors per detector, the effect of the different number of readout chips and wire bonds on the radiation length, averaged over the surface of the detectors, is very small.
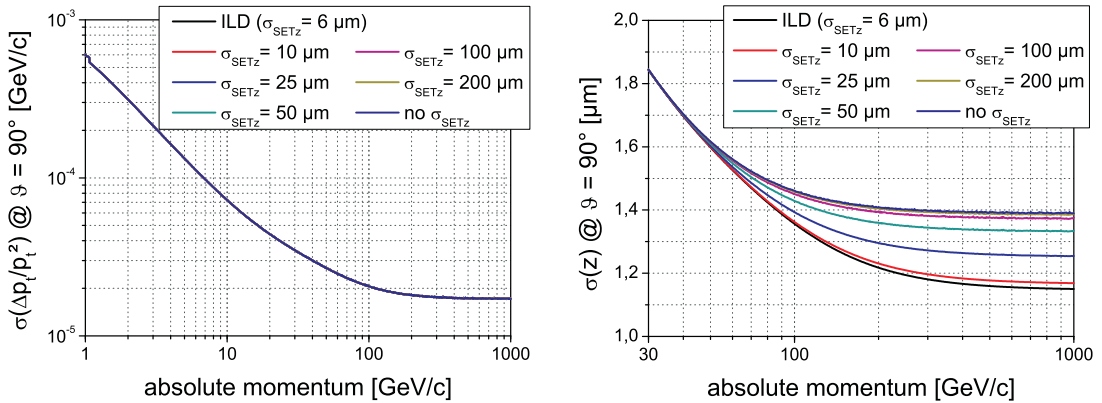
9.4.1 Resolution in z

Fig. 9.9: Variation of the SET$_z$ resolution: $\sigma(\Delta p_t/p_t^2)$ (left) and σ_z (right) as functions of the absolute momentum at a polar angle $\vartheta = 90\,^\circ$.

Obviously, as shown in the left plot of figure 9.9, the z-resolution of the Silicon External Tracker has no influence on the resolution of the transversal momentum. Also the effect on the resolutions of the impact parameters, shown for the z-coordinate in the right plot of figure 9.9, is minimal, since they are mainly defined

by the vertex detector. These simulations show that it is not important to max-imise the z‑resolution of the SET, which allows to reduce the number of readout channels with the use of a larger readout pitch on the silicon sensors. To monitor tracking systematics of the TPC and to deliver an entry point for the ECAL, a z‑resolution of $50\,\mu$m is adequate, which can be achieved with a readout pitch of about $200\,\mu$m to $250\,\mu$m, including one intermediate strip.
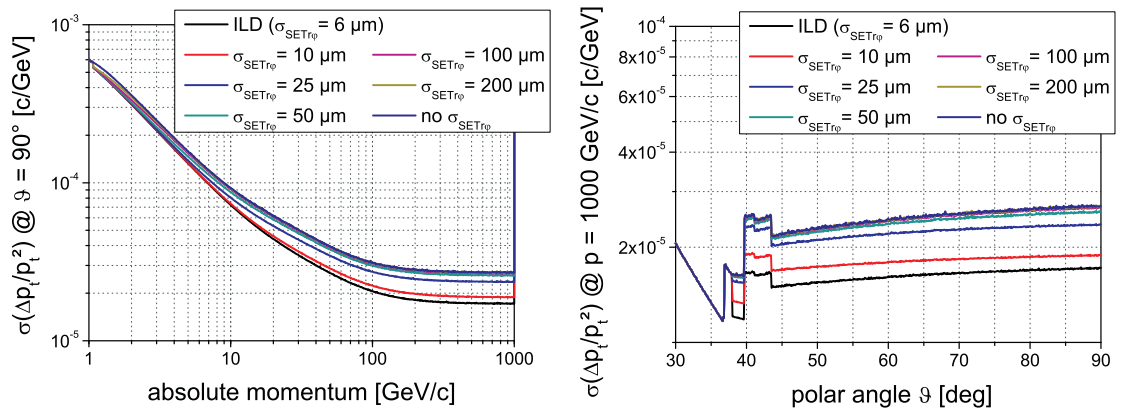
9.4.2 Resolution in $r\varphi$

Fig. 9.10: Variation of the SET$_{r\varphi}$ resolution: $\sigma(\Delta p_t/p_t^2)$ as function of the absolute momentum for $\vartheta = 90\,^\circ$ (right) and of the polar angle for $\mathrm{p} = 1000\,\mathrm{GeV/c}$ (right).

As described before, the variation of the SET resolution in $r\varphi$ has only small in-fluence on the resolution of the impact parameters. But the simulations, displayed in figure 9.10 show, that, in order to meet the requirement on the transversal momentum resolution of $\sigma_\infty(\Delta p_t/p_t^2) \leq 2\cdot 10^{-5}(\mathrm{GeV/c})^{-1}$, the Silicon External Tracker has to provide a $r\varphi$‑resolution of at least $10\,\mu$m.

9.4.3 Conclusion

The presented simulations clearly show, that for the Silicon External Tracker it is important to aim for the best possible resolution in $r\varphi$. As described in chapter 6 it is possible to achieve a spatial resolution of $6\,\mu$m with silicon strip detectors mature for mass production. The demands on the z‑resolution are not as stringent and mainly defined by the needs of the TPC and the particle flow approach, which requires a very accurate double track resolution. A resolution of $50\,\mu$m should be sufficient for these requirements.

9.5   Double Sided Silicon Sensors

As outlined in section 5.3.7 it is possible to also implement readout strips on the back side of a silicon strip sensor which enables the measurement of two dimensions with only one silicon sensor. When comparing a layer of double sided sensors with a double layer of single sided sensors the differences are:

+ decreasing the material budget
  The major advantage of double sided sensors is the decrease of the material budget, because the needed number of sensors halves. Advanced silicon detectors will consist only of the silicon sensors, readout chips, cables and support material, and therefore the sensors are the biggest contributors to the material budget. But, since silicon sensor with a thickness between $200\,\mu$m and $300\,\mu$m are mechanically rigid, they can be used as an integral part of the support structure, especially when integrated in double silicon layers, where both sensor layers share one support. Therefore the benefit of double sided sensors is lessened a bit because it is necessary to slightly increase the support material when removing one half of the sensors.

− sensor costs
  The manufacturing prize of the double sided sensors is about four times the prize of single sided sensors and also the production yield is much lower.

− assembly of the detectors
  It makes a huge difference in terms of complexity to build detector modules where readout strips have to be connected on both sides of the silicon strip sensor. Especially for a mass production like needed for the SET the module production should be as insusceptible to failures as possible.

− sensor temperature
  Special care has to be taken when using double sided silicon sensors with a forced gas cooling system, especially when the readout chips directly sit on the sensors. The effect of the cooling system is reduced when the sensor surface halves while the heat dissipation stays constant.

In the simulations the radiation length of the layers containing double sided sensors is assumed to be $0.56\,\%\,X/X_0$, which is a considerable reduction compared to the used radiation length of $0.8\,\%\,X/X_0$ for the double layers equipped with single sided sensors. The simulations of the ILD tracking system for three different cases: only the SIT, only the SET and both equipped with double sided silicon strip sensors compared to the ILD-configuration using only single sided sensors show no remarkable differences. The differences are hardly visible even when zoomed into the regions with the largest offset, as shown in figure 9.11. This can be explained by the fact that in the current available version of the LDT, as described in section 9.2, the simulation of energy loss of minimum ionising particles passing matter is not included and therefore the simulations are performed for muons.
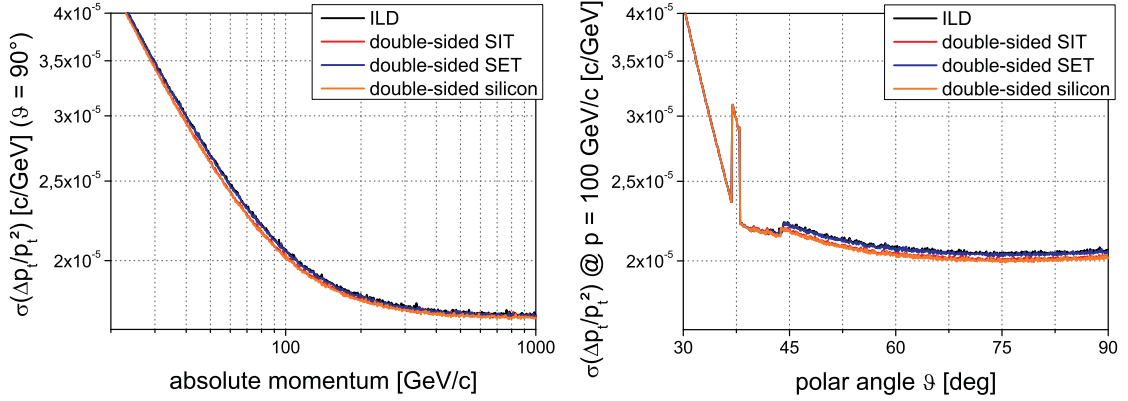
Fig. 9.11: Comparison of $\sigma(\Delta p_t/p_t^2)$ for the inclusion of double sided silicon strip sensors as function of the absolute momentum at $\vartheta = 90\,^\circ$ (left) and as function of the polar angle for $\mathrm{p} = 100\,\mathrm{GeV/c}$ (right).

9.5.1   Conclusion

The simulations with muons clearly show that the advantages of the use of double sided sensors in the Silicon Internal Tracker and the Silicon External Tracker do not outweigh the drawbacks. But for the final decision a full simulation with electrons and photons is mandatory since then the effect of the decreased material will start to play a significant role. When these simulations show the necessity it would be conceivable to introduce double sided sensors in the SIT.

9.6   Stereo Angle between the Silicon Strip Sensors

When using a double layer of silicon strip sensors (or one layer of double sided sensors) it is not mandatory to arrange the sensor strips of the two layers (of the two sides of the sensor) rotated by an angle of $90\,^\circ$ with respect to each other. Although a silicon strip sensor has its best resolution orthogonal to its strips σ_{ortho}, it is also possible to measure an inclined coordinate. The spatial resolution of a strip sensor tilted by a stereo angle α is:

$$\sigma_\alpha = \frac{\sigma_{ortho}}{tan\,\alpha}\sqrt{1 + \frac{1}{cos^2\,\alpha}} \qquad (9.6)$$

Figure 9.12 shows σ_α as function of the stereo angle α for a silicon strip sensor with an orthogonal resolution of $\sigma_{ortho} = 6\,\mu$m.

The advantage in introducing a stereo angle for one sensor is, compared to case of a double layer with orthogonal sensors, that the inclined sensor measures both, the z- and $r\varphi$- coordinate and therefore adds another measured track point to one coordinate while worsening the spatial resolution along the other. As determined
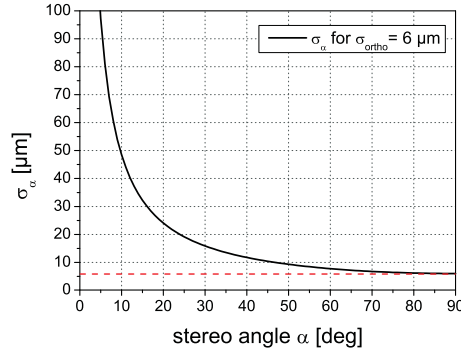
Fig. 9.12: Resolution of a silicon strip sensor with a spatial resolution of $6\,\mu m$ orthogonal to its strips as function of the stereo angle α.

in section 9.4 the resolution of the silicon strip layers have no big impact on the resolution of the impact parameters, and only the $r\varphi$ - resolution is important for the measurement of the transversal momentum. So it is interesting to look at simulations for different stereo angles using silicon strip sensors with a resolution of $6\,\mu m$. When such a sensor is tilted by a stereo angle of $\alpha = 10\,^\circ$, the angle between its strips and the z - axis, it provides a resolution of $6.2\,\mu m$ in $r\varphi$ and $48.5\,\mu m$ in z. Figure 9.13 shows simulations of the ILD tracking system with the introduction of a stereo angle $\alpha = 10\,^\circ$ for the different layers, with the following configurations:

- ILD - reference tracking system of the ILD as defined in section 9.1

- only SET_z $10\,^\circ$ - the sensors of the SET_z layer, which initially measured the z - coordinate, are rotated by $80\,^\circ$ so that their strips enclose now an angle of $10\,^\circ$ with the z - axis

- SET $10\,^\circ$ - the inner SET layer is rotated by $80\,^\circ$ and the outer by $-80\,^\circ$, so that both layers provide $\sigma_z = 48.5\,\mu m$ and $\sigma_{r\varphi} = 6.2\,\mu m$

- SIT $10\,^\circ$ - the two inner SIT layers are rotated by $80\,^\circ$ and the outer two by $-80\,^\circ$

- SIT + SET $10\,^\circ$ - all three double layers of the silicon strip tracker are rotated, the inner three by $80\,^\circ$ and the outer three by $-80\,^\circ$

When comparing the different cases with the ILD tracking system it is clearly visible that the resolution of the normalized transversal momentum improves for all of them. Unsurprisingly there is no difference for the configurations "only SET_z $10\,^\circ$" and "SET $10\,^\circ$". Alone with the introduction of a stereo angle in the SIT, "SIT $10\,^\circ$", an improvement of about 11% is achievable and obviously configuration "SIT + SET $10\,^\circ$" performs best with an improvement of about 15%.
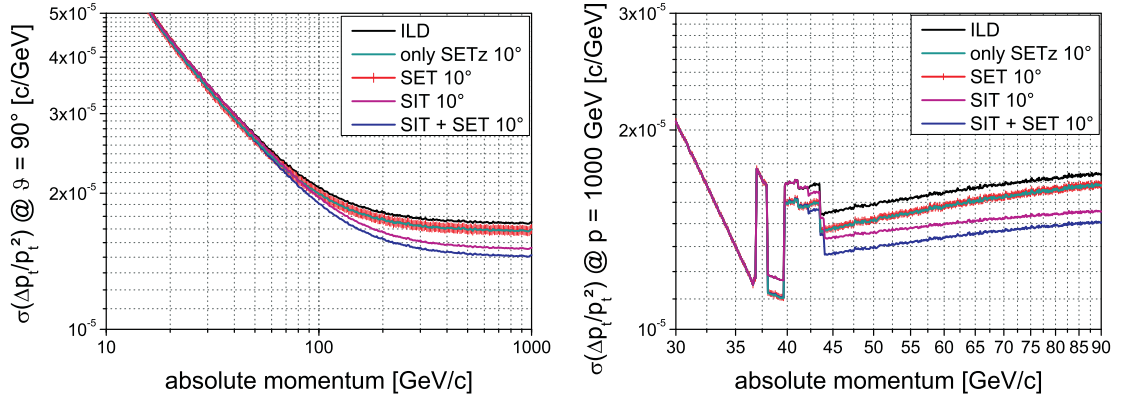
Fig. 9.13: Silicon sensors containing a stereo angle $\alpha = 10\,^\circ$.

9.6.1 Conclusion

The introduction of a stereo angle in the silicon sensors of the double layers would considerably increase the transversal momentum resolution of the ILD tracking system. Unfortunately the construction of silicon layers with a stereo angle of as big as $10\,^\circ$ is very challenging and some effort would have to be invested to design such double layers, especially for the case when two or more silicon strip sensors are used daisy - chained, as discussed in section 5.3.1. This, and the fact that it is not necessary to measure the $r\varphi$ - coordinate with both layers in each double layer to achieve the physics requirements, will lead to the use of the initial proposed orthogonal sensor strips.

9.7 Summary & Conclusions

As shown in this chapter, fast simulations are a very useful approach to quickly analyse different configurations and to get a good approximation for the optimal detector layout. The simulations presented clearly show, that the inclusion of the Silicon External Tracker is absolute necessary to reach the required transversal momentum resolution. It is also clear that the resolution of the silicon layers in $r\varphi$ must be below or equal $10\,\mu$m. To reach the requirements on the impact parameter resolutions the silicon tracking system is not needed, and therefore the silicon resolution in z of about $50\,\mu$m is adequate to monitor the TPC and the particle flow approach. To evaluate if the Silicon Internal Tracker should be build with single layers of double sided silicon strip sensors simulations with electrons and photons are utterly important, which could be done with the upgraded version of the Vienna fast simulation tool LiC Detector Toy. Regarding muons, the gain for using double sided sensors is too low to legitimate the increased costs and complexity in the silicon detector production. For the Silicon External Tracker one double layer of single sided sensors is the best solution. The simulations for the silicon tracking system with the inclusion of a stereo angle of $10\,^\circ$ between

the readout strips shows that it is possible to even increase the performance of the tracking system. Unfortunately this concept with such a large stereo angle is not very easy to implement, from the technical point of view, but if future studies show that the current requirement on the transversal momentum is not stringent enough this would be a possibility.

Although fast simulations are ideal for first optimisation studies, for the final evaluation of the ideal geometry of the ILD tracking system full simulations are mandatory. This should be done not only for the vertex detector and the tracker, but also including the calorimeter system. The performed simulations also show, that for different absolute particle momenta the optimisations can lead into different directions and the ILD tracking system should not be optimised for the asymptotic value of the transversal momentum, but for the momentum regions of the interesting physics channels. Therefore the requirement on the transversal momentum resolution should be modified with a term depending on the absolute particle momentum. Like already introduced in the requirement on the impact parameter resolutions, compare equation 2.1, also for the momentum requirements the inclusion of such a term depending on the polar angle would be interesting, especially for the optimisation of the forward region.

Chapter 10

Conclusion & Outlook

As outlined in the introduction of this thesis, the International Linear Collider (ILC) will be the logical follow‑up project after the Large Hadron Collider (LHC). The ILC will enable precision measurements of the known physics but also the discoveries made with the LHC, important to verify the physic theories. The high demands on the detector systems operating at the ILC require the use of the particle flow approach and the most up to date technologies for all sub‑systems. As verified with fast simulations the tracking system of the International Large Detector (ILD) can meet the required transversal momentum resolution with a combination of a large Time Projection Chamber surrounded by three double layers of silicon strip detectors.

It was understood that, in order to provide the required performance, for the $r\varphi$‑resolution of the silicon detector layers it is necessary to use silicon strip sensors with the best possible spatial resolution. For a reliable mass production of silicon detectors, regarding quality assurance tests and detector assembly, it is not advisable to use a readout pitch below $50\,\mu$m. A special designed multi‑geometry sensor with a readout pitch of $50\,\mu$m was tested in a test beam at the SPS at CERN and the ideal strip geometry in terms of spatial resolution could be evaluated. The analysis shows, that with the introduction of one and two intermediate strips and a strip width between $12.5\,\mu$m and $17.5\,\mu$m a spatial resolution below $6\,\mu$m is achievable. The next step is to verify that silicon detectors containing four daisy‑chained large area silicon strip sensors with such strip geometries have a reasonable signal to noise ratio and can provide the same spatial resolution.

The demands on the z‑resolution of the silicon layers are not as stringent, since it does not contribute to the measurement of the transversal momentum and the resolutions of the impact parameters are defined by the vertex detector. Therefore a spatial resolution of $50\,\mu$m is proposed, which is sufficient for the monitoring of TPC inhomogeneities, to improve the overall alignment of the tracking system and to provide a precise entry point for the calorimeter system. As shown in former test beam experiments such a resolution can easily be provided by silicon strip sensors with a readout pitch of $200\,\mu$m, containing one intermediate strip. To reduce the number of readout channels, which is important to keep the overall

power consumption at a low level, it is required to build ladders with up to four daisy-chained sensors along the z-axis of the detector system. Since the readout strips resolving the z-coordinate are orthogonal to z these sensors must contain a second metal layer routing that guides the signals from the readout strips to the sensor side parallel to the readout strips. The sensor production for such ladders is even more difficult, since the signals from the sensors, not directly connectible to the readout electronics, have to be routed via the second metal layer routing of the other sensors of the ladder. This is in principle possible with a sensor readout pitch of $200\,\mu$m and a pitch of $50\,\mu$m for the second metal layer routing. The alternatives are the development of convex ladders or the introduction of a shallow stereo angle.

To reach the requirements on spatial resolution the Time Projection Chamber of the ILD must be read out using Micro Pattern Gas Detectors (MPGD). Since this technology is relatively new, and different possibilities exist, it is subject of current R&D activities. Therefore a Large TPC Prototype (LP) was designed, constructed and installed in a superconducting magnet in a test beam area at the DESY. At the LP setup the different MPGD technologies, including different readout electronics, can be tested and evaluated. To enable the comparison of the different readout options a set of silicon strip detectors was installed in the gap between LP and magnet, providing a precise external measurement of traversing particles, important as reference point. The design and production of these silicon layers, including an appropriate data acquisition system and a moveable support structure, was successful and the functionality of the silicon system was verified in a first combined test beam with the Large TPC Prototype. In the coming years, combined test beams, with and without magnetic field, including different TPC readout technologies will be performed at the LP setup. These test beam experiments are an important step to define the optimal technology for the ILD TPC readout. They will also help to verify the possibilities of the silicon system to monitor distortions and inhomogeneities of the electric and magnetic field inside the TPC. In parallel, the combination of the silicon and TPC readout systems into one combined data acquisition system will be developed, including also a combined data analysis framework.

On the basis of the silicon detectors, designed and constructed for the LP experiment it was possible to verify, that the required material budget for the silicon layers of the ILD tracking system can be met. This is possible even with the use of the current state of the art technologies. Different concepts to further decrease the material of the silicon detectors are described and the ultimate silicon detector design, where the readout chips are directly connected to the silicon sensor, is presented.

Bibliography

[1] L. Evans, P. Bryant, *"LHC Machine"; JINST 3, S08001 (2008)*

[2] L. Teng, *"Particle Accelerators - Outlook for the twenty‑first century."; Proceeding of the Second Asian Particle Accelerator Conference, Beijing, China (2001)*

[3] F. Hartmann, *"Evolution of Silicon Sensor Technology in Particle Physics"; ISBN 978-3-540-44774-0, Springer‑Verlag Berlin Heidelberg 2009*

[4] Particle Data Group, *"The Review of Particle Physics"; Physics Letters B, Vol. 667, 1 (2008) and (2009): partial update for the 2010 edition*

[5] T. S. Virdee, *"The LHC project: The accelerator and the experiments"; Nucl. Instr. and Meth. A (2010), doi:10.1016/j.nima.2010.02.142*

[6] ILC Collaboration, *"ILC Reference Design Report - 1: Executive summary; 2: Physics at the ILC; 3: Accelerator; 4: Detectors"; ILC-REPORT-2007-001 (2007)*

[7] The LEP Collaborations, *"A Combination of Preliminary Electroweak Measurements and Constraints on the Standard Model"; CERN-PH-EP/2005-051 (2005)*

[8] A. Djouadi and J. Baglio, *"Predictions for Higgs production at the Tevatron and the associated uncertainties"; arXiv:1003.4266v1 [hep-ph] (2010)*

[9] E. Accomando et al., *"Physics with e^+e^- linear colliders"; DESY 97(100), arXiv:hep-ph/9705442 v1 (1997)*

[10] J. Mnich, *"Detectors for a linear collider"; Nucl. Instr. and Meth. A 581 (2007) 48-56*

[11] The Tevatron Electroweak Working Group for the CDF and DØ Collaborations, *"Combination of CDF and DØ Results on the Mass of the Top Quark"; arXiv:0803.1683v1 [hep-ex] (2008)*

[12] W. de Boer et al., *"Consistency Checks of GUT's with LEP Data"; CERN-PPE/91-190 (1991)*

[13] BELLE Collaboration, *"Belle Experiment"*;
web - page: http://belle.kek.jp/

[14] CMS Collaboration, *"The Compact Muon Solenoid Experiment"*;
web - page: https://cms.web.cern.ch/cms/

[15] R. Galea, *"A Muon Collider scheme based on Frictional Cooling"*; *Nucl. Instr. and Meth. A 546 (2005) 356375*

[16] TESLA Collaboration, *"TESLA Technical Design Report"*; *CERN/LHCC 2000 - 38, CMS TDR 6.1 (2001)*

[17] CMS Collaboration, *"Technical Design Report, Volume 1: The Trigger Systems"*; *CERN/LHCC 2000 - 38, CMS TDR 6.1 (2000)*

[18] ILC Collaboration, *"http://www.linearcollider.org"*; *(webpage)*

[19] ILC Collaboration, *"Parameters for the Linear Collider (update of the document 'ICFA - Parameters of the linear collider')"*; *(2006)*

[20] H. Videau, *"ILD dimensional constraints"*; *talk at ILD Workshop 2010 (2010)*

[21] The ILD concept group, *"International Large Detector - Letter of Intent"*; *DESY 2009-87, FERMILAB-PUB-09-682-E, KEK Report 2009-6 (2010)*

[22] S. Hillert and C. Damerell, *"Physics Potential of Vertex Detector as Function of Beam Pipe Radius"*; *2005 ALCPG & ILC Workshops, ECONF C050:ALCPG1403 (2005)*

[23] A. Nomerotski, *"Silicon detectors for tracking and vertexing"*; *Nucl. Instr. and Meth. A 598 (2009) 33–40*

[24] F. Meier on behalf of the CMS collaboration, *"First alignment of the complete CMS tracker"*; *Nucl. Instr. and Meth. A (2010), doi:10.1016/j.nima.2010.04.106*

[25] M. A. Thomson, *"Particle flow calorimetry and the Pandora PFA algorithm"*; *Nucl. Instr. and Meth. A 611 (2009) 25–40*

[26] G. Franzoni, *"Performance of CMS ECAL with first LHC data"*; *Nucl. Instr. and Meth. A (2010), doi:10.1016/j.nima.2010.06.291*

[27] M. Battaglia, *"The Vertex Tracker at future e^+e^- linear colliders"*; *Nucl. Instr. and Meth. A 530 (2004) 33–37*

[28] M. Vos, *"Tracking at the International Linear Collider"*; *Nucl. Instr. and Meth. A 596 (2008) 29–31*

[29] ILC Global Design Effort, *"ILC Research and Development Plan for the Technical Design Phase"*; *ILC-EDMS Doc. # 813385, Release 5 (2010)*

[30] LDC Working Group, *"Detector Outline Document for the Large Detector Concept"; (2006)*

[31] GLD Concept Study Group, *"GLD Detector Outline Document"; arXiv:physics/0607154v1 (2006)*

[32] C. Clerc and M. Joré, *"Note on the integration of the ILD detector"; (2009)*

[33] ILD Joint steering board, *"Definition of the ILD reference detector"; (2008)*

[34] A. Savoy - Navarro et al. *"The SiLC Collaboration"; Proposal to the ILCSC R&D Panel on Tracking for the ILC, Submitted on January 29, 2007*

[35] A. Savoy - Navarro, *"Development of Semiconductor Tracking: the Future Linear Collider Case"; Nucl. Instr. and Meth. A (2010), doi:10.1016/j.nima.2010.04.088*

[36] ILC Detector R&D Panel, *"ILC Vertex Detector R&D - Report of Review Committee"; ILC-Report-2008-016 (2008)*

[37] Y. Giomataris et al., *"Micromegas: A High Granularity Position Sensitive Gaseous Detector for High Particle Flux Experiments"; Nucl. Instr. and Meth. A 376 (1996) 29–35*

[38] F. Sauli, *"GEM: A New Concept for Electron Amplification in Gas Detectors"; Nucl. Instr. and Meth. A 386 (1997) 531–534*

[39] LCTPC Collaboration, *"TPC R&D for an ILC Detector - Status Report"; LC-DET-2007-005 (2007)*

[40] CALICE Collaboration, *"https://twiki.cern.ch/twiki/bin/view/CALICE/"; (webpage)*

[41] C. Cârloganu et al., *"Response of the CALICE Si - W electromagnetic calorimeter physics prototype to electrons"; Nucl. Instr. and Meth. A 608 (2009) 372-383*

[42] T. Buanes et al., *"The CALICE hadron scintillator tile calorimeter prototype"; Nucl. Instr. and Meth. A (2010), doi:10.1016/j.nima.2010.02.242*

[43] M. Friedl, T. Bauer, M. Krammer, *"A Simple Model of Charge Collection in Silicon Detectors"; Nucl. Instr. and Meth. A 461, 192–196 (2001)*

[44] W. de Boer et al., *"Lorentz angle measurements in irradiated silicon detectors between 77 and 300 K"; Nucl. Instr. and Meth. A 461, 200–203 (2001)*

[45] M. Friedl, PhD thesis, *"The CMS Silicon Strip Tracker and Its Electronic Readout"; University of Technology, Vienna (2001)*

[46] E. Barberis et al., *"Capacitances in silicon microstrip detectors"; Nucl. Instr. and Meth. A 342 (1994) 90–95*

[47] G. Lutz, *"Semiconductor Radiation Detectors"; Springer (1999)*

[48] S. Hänsel, diploma thesis, *"Quality of the CMS Tracker End Cap Silicon Strip Modules"; University of Technology, Vienna (2007)*

[49] V. Radicci et al., *"A comparison on radiation tolerance of microstrip detectors built on <100> and <111> silicon substrates after proton irradiation"; Nucl. Instr. and Meth. A 485, 109–115 (2002)*

[50] A. Frey, et al., *"Optimization of the silicon sensors for the CMS tracker"; Nucl. Instr. and Meth. A 466 (2001) 300-307*

[51] M. Krammer, et al., *"The silicon sensors for the Compact Muon Solenoid tracker design and qualification procedure"; Nucl. Instr. and Meth. A 517 (2004) 77-93*

[52] T. Bergauer, PhD thesis, *"Design, Construction and Commissioning of the CMS Tracker at CERN and Proposed Improvements for Detectors at the Future International Linear Collider"; University of Technology, Vienna (2008)*

[53] M. Dragicevic, PhD thesis, *"The New Silicon Strip Detectors for the CMS Tracker Upgrade"; University of Technology, Vienna (2010)*

[54] M. Dragicevic et al., *"Results from a first production of enhanced Silicon Sensor Test Structures produced by ITE Warsaw"; Nucl. Instr. and Meth. A 598 (2009) 86-88*

[55] RD50 Status Report 2007, *"Radiation hard semiconductor devices for very high luminosity colliders"; CERN-LHCC-2008-001 (2008)*

[56] SiLC Collaboration, *"SiLC R&D: Design, present status and perspectives"; Nucl. Instr. and Meth. A 579 (2007) 750-753*

[57] Z. Dolez et al., *"SiLC R&D: Design, present status and perspectives"; Nucl. Instr. and Meth. A 579 (2007) 750-753*

[58] T. H. Pham et al., *"A 130 nm CMOS mixed mode front end readout chip for silicon strip tracking at the future linear collider"; Nucl. Instr. and Meth. A (2010), doi:10.1016/j.nima.2010.03.049*

[59] M. Krammer and H. Pernegger, *"Signal collection and position reconstruction of silicon strip detectors with 200 μm readout pitch"; Nucl. Instr. and Meth. A 397 (1997) 232-242*

[60] C. Troncon et al., *"The DELPHI silicon strip microvertex detector with double sided readout"; Nucl. Instr. and Meth. A 386, 314–332 (1996)*

[61] H. Miyata et al., *"Load capacitance of single-sided silicon strip detectors with double-metal layers"; Nucl. Instr. and Meth. A 383, 110–115 (1996)*

[62] E. Verbitskaya et al., *"Electrical properties of the sensitive side in Si edgeless detectors"; Nucl. Instr. and Meth. A 604, 246–249 (2009)*

[63] H. G. Moser et al., *"Thinned Silicon Detectors"; Proceedings of Science - (Vertex 2007) 013 (2007)*

[64] J. Fernandez, on behalf of the CMS Tracker Collaboration, *"The CMS silicon strip tracker"; Nucl. Instr. and Meth. A 573, 257–259 (2007)*

[65] SiD Concept Group, *"SiD Letter of Intent"; arXiv:0911.0006v1 (2009)*

[66] K.-H. Hoffmann et al., *"R&D on novel sensor routing and test structure development"; Nucl. Instr. and Meth. A doi:10.1016/j.nima.2010.06.333 (2010)*

[67] M. Friedl et al., *'The silicon vertex detector of the Belle II experiment"; Nucl. Instr. and Meth. A doi:10.1016/j.nima.2010.06.295 (2010)*

[68] ATLAS Colaboration, *"ATLAS: letter of intent for a general-purpose pp experiment at the large hadron collider at CERN"; CERN-LHCC-92-004; LHCC-I-2 (1992)*

[69] M. French et al., *"Design and results from the APV25, a deep sub-micron CMOS front-end chip for the CMS tracker"; Nucl. Instr. and Meth. A, 466 (2001) 359–365*

[70] A. Bulgheroni for the EUDET-.JRA1 Consortium, *"Results from the EUDET telescope with high resolution planes"; Nucl. Instr. and Meth. A 623 (2010) 399-401*

[71] D. Cussans, *"Description of the JRA1 Trigger Logic Unit (TLU), v0.2c"; Eudet Memo 2009-04*

[72] W. Kiesenhofer et al., *"Beam test results for fine pitched multigeometry silicon strip detectors"; Proceedings of the 11th Conference on ICATPP-11 (2009)*

[73] M. Dragicevic et al., *"Optimising the strip geometry for very fine pitch silicon strip sensors"; Nucl. Instr. and Meth. A 617 (2010) 532-533*

[74] W. Kiesenhofer, diploma thesis, *"Performance studies on Silicon Strip Sensors with 50 µm pitch"; University of Technology, Vienna (2010)*

[75] R. Frühwirth et al., *"Data Analysis Techniques for High-Energy Physics"; Cambridge Monographs on Particle Physics, Nuclear Physics and Cosmology (2000)*

[76] W. Adam et al., *"Performance studies of the CMS Strip Tracker before installation"; JINST 4 P06009 (2009)*

[77] P. Schade and J. Kaminski, on behalf of the LCTPC collaboration, *"A Large TPC Prototype for a Linear Collider Detector"; Nucl. Instr. and Meth. A (2010), doi:10.1016/j.nima.2010.06.300*

[78] A. Yamamoto et al., *"Superconducting Magnet for Long Duration Flights"; KEK Proceedings 94 - 11, (March 1995)*

[79] Deutsches Elektronen - Synchrotron, *"(http://desy.de)"*

[80] K. Dehmelt for the LCTPC Collaboration, *"A large prototype of a time projection chamber for a linear collider detector"; Nucl. Instr. and Meth. A (2010), doi:10.1016/j.nima.2010.02.160*

[81] D. R. Nygren, *"The Time Projection Chamber: A New 4 π Detector for Charged Particles"; Proceedings of The 1974 PEP Summer Study, Berkeley, California (1974)*

[82] K. H. Ackermann et al., *"The STAR time projection chamber."; Nucl. Instr. and Meth. A 661 (1999) 681-685*

[83] D. Karlen, *"Time projection chambers for the T2K experiment."; Nucl. Instr. and Meth. A (2010), doi:10.1016/j.nima.2010.02.164*

[84] D. Attie, Talk at INSTR08, *"TPC Review"; Nucl. Instr. and Meth. A 598 (2009) 89-93*

[85] P. Schade, PhD thesis, *"Development and Construction of a Large TPC Prototype for the ILC and Study of τ Polarisation in $\widetilde{\tau}$ Decays with the ILD Detector"; Universität Hamburg (2009)*

[86] P. Colas, on behalf of the LCTPC collaboration, *"First Test Results from a Micromegas Large TPC Prototype"; Nucl. Instr. and Meth. A (2010) doi:10.1016/j.nima.2010.02.161*

[87] ALICE Collaboration, *"ALICE - Technical Design Report of the Time Projection Chamber"; printed at CERN, Geneva, Switzerland, December 1999, ISBN 92-9083-155-3*

[88] ALICE Collaboration, *"A Large Ion Collider Experiment";* web - page: *http://aliceinfo.cern.ch/*

[89] Y. Yang et al., *"A trigger distributor box for the LP - TPC"; EUDET Memo 2008-18*

[90] M. Krammer, *"Module production for the CMS Tracker: Problems and achieved quality"; Nucl. Instr. and Meth. A 582 (2007) 766-770*

[91] P. Petagna et al., *"Technical specification for the CMS Tracker silicon module carbon fibre composite frames"*; IT-2434D/EP/CMS (2005)

[92] T. Franke, PhD Thesis, *"Development and Evaluation of a Test System for the Quality Assurance during the Mass Production of Silicon Microstrip Detector Modules for the CMS Experiment"*; University of Technology Aachen (2005)

[93] M. Axer et. al., *"Testing of FE Hybrids and Si detector modules for the CMS Tracker"*; Nucl. Instr. and Meth. A 485 (2002) 73–77

[94] M. Kozlovszky et al., *"A TCP/IP transport layer for the DAQ of the CMS experiment"*; Nucl. Instr. and Meth. A, 534(1-2): 125–129 (2004)

[95] M. Friedl, On behalf of the CMS Tracker Collaboration, *"Analog optohybrids for the readout of the CMS silicon tracker"*; Nucl. Instr. and Meth. A, 518 (2004) 515–518

[96] C. Foudas et al., *"The CMS tracker readout front end driver"*; IEEE Trans. Nucl. Sci. 52 (2005) 2836–2840

[97] K. Kloukinas et al., *"FEC-CCS: A common front-end controller card for the CMS detector electronics"*; 12th Workshop on Electronics For LHC and Future Experiments, Valencia, Spain (2006) 179-184

[98] C. Paillard, C. Ljuslin and A. Marchioro, *"The CCU25: a network oriented communication and control unit integrated circuit in a 0.25 μm CMOS technology"*; 8th Workshop on Electronics for LHC Experiments, Colmar, France (2002) 174-178

[99] I.-M. Gregor et al., *"Characterisation of the Test Beam Lines T21 and T24 at DESY II"*; EUDET Memo 2007-50

[100] R. Brauer et al., *"http://brauer.web.cern.ch/brauer/Ana"*

[101] R. Frühwirth, private communication

[102] K. Dehmelt, *"A Large TPC Prototype for an ILC Detector"*; European Physical Society Europhysics Conference on High Energy Physics, Krakow, Poland 2009, PoS (EPS-HEP 2009) 155

[103] R. Frühwirth and M. Regler, *"Generalization of the Gluckstern formulas I: Higher orders, alternatives and exact results"*; Nucl. Instr. and Meth. A 589 (2008) 109-117

[104] M. Regler, M. Valentan, R. Frühwirth, *"The LiC detector toy program"*; Nucl. Instr. and Meth. A 581 (2007) 553-556

[105] M. Valentan, diploma thesis, *"Tracking detector optimization for collider experiments with fast simulation and by analytical methods"; University of Technology, Vienna (2009)*

[106] M. Valentan, M. Regler, R. Fruühwirth, *"Generalization of the Gluckstern formulas II: Multiple scattering and non‑zero dip angles"; Nucl. Instr. and Meth. A 606 (2009) 728-742*

[107] M. Regler, R. Frühwirth, W. Mitaroff *"Filter methods in track and vertex reconstruction"; Int. J. Mod. Phys. C 7 (4) (1996)*

[108] J. Augustin, M. Berggren, A. Savoy‑Navarro, *"Study of a Silicon External Tracker: SET"; LC-DET-2001-075 (2001)*